UNIVERSITY OF CALIFORNIA SAN DIEGO

Functionalized Porous Silicon for Applications in Chemical Sensing, Tumor Imaging and Drug Delivery

A Dissertation submitted in partial satisfaction of the requirements
for the degree Doctor of Philosophy

in

Materials Science & Engineering

by

Sanahan Vijayakumar

Committee in charge:

Professor Michael Sailor, Chair
Professor F. Akif Tezcan, Co-Chair
Professor Gerry Boss
Professor Seth Cohen
Professor Partha Ray

2022

The Dissertation of Sanahan Vijayakumar is approved, and it is acceptable in quality and form for publication on microfilm and electronically.

University of California San Diego

2022

DEDICATION

To Kanna

TABLE OF CONTENTS

DISSERTATION APPROVAL PAGE iii

DEDICATION iv

TABLE OF CONTENTS v

LIST OF FIGURES x

LIST OF TABLES xvi

ACKNOWLEDGEMENTS xvii

VITA xxi

ABSTRACT OF THE DISSERTATION xxiii

CHAPTER 1 1

1.1 General Overview of Porous Silicon 1

1.2 Functionalized Porous Silicon & Surface Chemistries 5

1.3 Porous Silicon Materials for Sensing 11

1.4 Porous Silicon Materials for Biomedical Applications 15

REFERENCES – CHAPTER 1 18

CHAPTER 2 20

2.1 Abstract 20

2.2 Introduction 21

2.2 Results and Discussion 24

2.2A Preparation of pSi Photonic Crystal Sensors 24

2.2B Surface Modification and Loading of Indicator Dyes 26

2.2C Sensing of HF Using RDI-pSi(C_{18}) Photonic Crystal Sensors 30

2.2D Sensing of DFP Using RDI-pSi(C_{18}) Photonic Crystal Sensors 35

2.2E Sensing of HCN Using MCBI-pSi(C_{18}) Photonic Crystal Sensors 37

2.2F Sensing of HF and HCN in a Complex Air Mixture 39

2.2G Remote Sensing Demonstration 40
2.3 Conclusion 42
2.4 Experimental Section 44
2.4A Materials 44
2.4B Instrumentation 44
2.4C Preparation of pSi Photonic Crystals 45
2.4D Synthesis of Rhodamine 6G Imidazole (RDI) 46
2.4E Synthesis of Monocyanocobinamide 47
2.4F Loading of Colorimetric Indicators 47
2.4G Vapor Dosing Experiments 48
2.5 Supporting Information 50
2.6 Supporting Information – Literature Cited 65
2.7 Acknowledgements 66
REFERENCES – CHAPTER 2 67
CHAPTER 3 71
3.1 Abstract 71
3.2 Main Text 72
3.3 Conclusion 89
3.4 Materials & Instrumentation 90
3.5 Methods 91
3.5A Preparation of Porous Silicon (pSi) Photonic Crystals 91
3.5B Surface Functionalization of pSi Photonic Crystals 92
3.5C Synthesis and Loading of Monocyanocobinamide (MCbi) 93
3.5D Synthesis, Preparation and Deposition of Gatekeeper Crystals onto pSi Photonic Crystals 93
3.5E Vapor Dosing Experiments 95

3.6 Supplementary Information 96
3.7 Acknowledgements 110
REFERENCES - CHAPTER 3 111
CHAPTER 4 113
4.1 Abstract 113
4.2 Introduction 113
4.3 Results & Discussion 119
4.3a Development of Aptamer-Conjugated Nanoparticles 119
4.3b *In vitro* Cellular Targeting 123
4.3c *In vivo* & *ex vivo* cellular targeting of nanoparticles 125
4.3d Biosafety of nanoparticles 131
4.4 Experimental Section 134
4.4a Materials 134
4.4b Preparation of Porous Silicon Nanoparticles (pSiNP) 135
4.4c Surface Modification of pSiNPs 136
4.4d Loading of Fluorophores to pSiNPs 137
4.4e Attachment of Poly-Ethylene Glycol (PEG) to pSiNPs 137
4.4f Attachment of DNA Aptamer Ligands to pSiNPs 138
4.4g Characterization of pSiNPs 138
4.4h Cell Culture 139
4.4i *In Vitro* Toxicity 139
4.4j *In vitro* Flow Cytometry Experiments and Confocal Microscopy 140
4.4k Establishing the Spleen-to-liver GIST Metastases Model 140
4.4l *In vivo* Experiments 141
4.4m *Ex vivo* Imaging 142

4.4N *IN VIVO* TOXICITY & HISTOLOGY STUDIES 142
4.4O LIVER SECTION IMAGING 143
4.4P IMAGE ANALYSIS 143
4.4Q STATISTICAL ANALYSIS 144
4.5 CONCLUSIONS 144
4.6 SUPPORTING INFORMATION – LITERATURE CITED 151
4.7 ACKNOWLEDGEMENTS 151
REFERENCES - CHAPTER 4 152
CHAPTER 5 155
5.1 ABSTRACT 155
5.2 MAIN TEXT 155
5.3 CONCLUSIONS 167
5.4 MATERIALS & METHODS 168
5.4A MATERIALS 168
5.4B PREPARATION OF POROUS SILICON NANOPARTICLES (PSINP) 168
5.4C SURFACE MODIFICATION OF PSINPS 170
5.4D LOADING OF FLUOROPHORES TO PSINPS 170
5.4E LOADING OF ERUCAMIDE TO PSINPS 170
5.4F CHARACTERIZATION OF PSINPS 171
5.4G CELL CULTURE 171
5.4H *IN VITRO* TOXICITY 172
5.4I MICE AND ANIMAL EXPERIMENTAL PROCEDURES 173
5.4J IMMUNOHISTOCHEMISTRY OF WHOLE-MOUNT RETINAS 173
5.4K RETINAL MICROGLIA ISOLATION BY FLOW CYTOMETRY 174
5.4L RNA ISOLATION AND REAL-TIME PCR 174

5.4M STATISTICAL ANALYSIS 175
5.5 ACKNOWLEDGEMENTS 182
REFERENCES - CHAPTER 5 183
APPENDIX A 186
A.1 METHODS 186
A.1A PREPARATION OF POROUS SILICON MICROPARTICLES (PSIMPS) 186
A.1B SURFACE FUNCTIONALIZATION OF PSIMPS 187
A.1C LOADING OF COBINAMIDE TO FUCTIONALIZED PSIMPS 187
A.1D EXTRACTION METHODOLOGY OF CBI-DYE FROM PSIMPS 188
A.2 RESULTS & DISCUSSION 192
A.2A CHARACTERIZATION OF PSIMPS 192
A.3 CONCLUSIONS 194
REFERENCES – APPENDIX A 196
APPENDIX B 197
B.1 OVERVIEW 197
B.2 RESULTS & DISCUSSION 198
B.2A SOLUTION BINDING OF BIO-MOF TO PSIMPS 198
B.2B DROP-CASTING" OF BIO-MOF ONTO PSIMPS 201
B.3 CONCLUSIONS 206

LIST OF FIGURES

Figure 1.1: Physical characteristics and etching tools of porous silicon (pSi).... 3

Figure 1.2: Unique optical properties of porous silicon. 5

Figure 1.3: Surface species and common functionalization techniques to react to silicon hydrides..... 7

Figure 1.4: Surface species and common functionalization techniques to react to silicon oxides. 8

Figure 1.5: Schematic of dehydrocoupling reactions using trihydridosilanes to graft long-chain functional groups onto the surface of porous silicon hydrides. 9

Figure 1.6: Schematic of ring-opening "click" reactions of heterocyclic silanes to graft various functional groups onto the surface of porous silicon oxides..... 10

Figure 1.7: Oxidants to alter the pSi substrate both chemically and physically.11

Figure 1.8: Photonic crystal properties of pSi. 12

Figure 1.9: Various etch types can yield different reflectance spectra..... 13

Figure 1.10: pSi photonic crystals change color when the etched film is infiltrated with a medium of different refractive index. 14

Figure 1.11: Biomedical applications of porous silicon nanoparticles (pSiNPs).17

Figure 2.1: Sensor and sensing approach used in this work. 24

Figure 2.2: Morphology of pSi photonic crystal sensors and their optical response to analyte vapor challenges. 28

Figure 2.3: $HF_{(g)}$ sensing performance of RDI – pSi-Si(C_{18}) photonic crystal sensor. 33

Figure 2.4: Performance of MCbi – pSi-Si(C_{18}) photonic crystal sensor for HCN detection. 36

Figure 2.5: Detection of analytes within complex air mixture. 42

Figure 2.S1: UV-vis Absorbance Spectra of Indicator Dyes. 50

Figure 2.S2: Characterization of surface chemistry of RDI-pSi and MCbi-pSi photonic crystal sensors. 51

Figure 2.S3: Reaction scheme used for preparation of the rhodamine 6G-imidazole complex. 52

Figure 2.S4: ESI-MS spectrum of RDI. Ion at m/z = 507.35 is assigned to $[RDI+H]^+$ parent ion. 53

Figure 2.S5: ESI-MS spectrum of cobinamide. 54

Figure 2.S6: Cobinamide's structure and absorbance properties. 55

Figure 2.S7: Attenuated total reflectance Fourier-transform infrared (ATR-FTIR) spectra. 56

Figure 2.S8: Schematic of vapor dosing setup for HF, HCl, NH_3, and octane vapor sensing experiments. 57

Figure 2.S9: Reported mechanism of HF detection by Rhodamine (RDI). 59

Figure 2.S10: Optical reflectance spectrum of RDI-photonic crystal. 60

Figure 2.S11: Temporal response curve of RDI – pSi photonic crystal sensors to 100 ppb of DFP vapor. 61

Figure 2.S12: Schematic of vapor dosing setup for HCN and DFP sensing. .. 62

Figure 2.S13: Representative temporal response curve of a MCbi – pSi photonic crystal sensor to sequential exposure of vapors. 63

Figure 2.S14: Optical reflectance spectrum of MCbi-photonic crystal sensor before and after exposure to 600 ppm Octane. 64

Figure 2.S15: Experimental setup and representative data for remote sensing of HF vapor. 65

Figure 3.1: Properties of HCN-selective ^{CEE}RhuA protein crystals gatekeeper coated onto a pSi photonic crystal. 76

Figure 3.2: ^{CEE}RhuA protein crystals gatekeeper coated onto a pSi photonic crystal. 80

Figure 3.3: Optical response of gatekeeper-coated pSi photonic crystal sensors to analyte vapor challenges. 84

Figure 3.4: HCN sensing performance of Cbi-dye impregnated, gatekeeper-coated pSi photonic crystal sensors. 89

Figure 3.S1: Characterization and morphology of pSiNP surfaces of pSi and Gatekeeper-Cbi-pSi photonic crystal sensors. 96

Figure 3.S2: Cobinamide structures and absorbance measurements..... 97

Figure 3.S3: Vapor dosing set-up and photonic crystal testing-chamber. 98

Figure 3.S4: Temporal responses of interferant vapors**.** 99

Figure 3.S5: All-atom molecular dynamics (MD) of infinitely periodic ^{C98}RhuA lattices. 100

Figure 3.S6: Transport rates in terms of total hexane molecules. 101

Figure 3.S7: Behavior of Cbi-dye impregnated pSi photonic crystal sensors without a ^{CEE}RhuA gatekeeper. 102

Figure 3.S8: Behavior of $CoCl_2$ coated pSi photonic crystal sensors. 103

Figure 3.S9: Behavior of Cbi-dye impregnated pSi photonic crystal sensors with disassembled ^{CEE}RhuA proteins, co-incubated with $CoCl_2$..... 104

Figure 3.S10: Behavior of Cbi-dye impregnated photonic crystal sensors with a ^{CEE}RhuA protein (without $CoCl_2$ incubation) coating. 105

Figure 3.S11: Behavior of Cbi-dye impregnated photonic crystal sensors with a ^{CEE}RhuA protein (without $CoCl_2$ incubation) coating and vigorously mixed prior to deposition on the sensors. 106

Figure 3.S12: Behavior of Cbi-dye impregnated photonic crystal sensors with a ^{C98}RhuA protein (without $CoCl_2$ incubation)..... 107

Figure 3.S13: Behavior of Cbi-dye impregnated photonic crystal sensors with a ^{C98}RhuA protein (without $CoCl_2$ incubation) and vigorously mixed prior to deposition. 108

Figure 3.S14: Behavior of Cbi-dye impregnated photonic crystal sensors with a ^{C98}RhuA protein co-incubated $CoCl_2$ prior to deposition..... 109

Figure 4.1: Preparation of silane-modified pSiNPs for the attachment of PEG and aptamers. 120

Figure 4.2: KIT-Aptamer conjugated porous silicon nanoparticles. 122

Figure 4.3: Investigation of cellular targeting of pSiNP constructs in a model GIST-T1 cancer cell line. 125

Figure 4.4: *in vivo* evaluation of targeted pSiNPs in GIST-T1 model.. 126

Figure 4.5: *ex vivo* imaging of abdominal organs following injection of pSiNP constructs..... 129

Figure 4.6: *ex vivo* imaging of frozen liver tissues..... 130

Figure 4.7: Histopathology of extracted organs 5 hours following injection of nanoparticles..... 133

Figure 4.S1: Characterization of pSiNP constructs. 146

Figure 4.S2: Characterization of dye-conjugated pSiNPs. 146

Figure 4.S3: Standard curve of 6-FAM-conjugated KIT-aptamer. 147

Figure 4.S4: Thermogravimetric analysis (TGA) measurements..... 147

Figure 4.S5: Investigation of cellular targeting of aptamer-conjugated pSiNPs in a model HMC-1.2 cancer cell line. 148

Figure 4.S6: Temporal *in vivo* IVIS imaging. 149

Figure 4.S7: Biosafety Analysis of pSiNP constructs. 150

Figure 5.1: Preparation of silane-modified pSiNPs for erucamide loading. ... 159

Figure 5.2: Characterization of Erucamided-loaded, silane-functionalized nanoparticles**.**..... 161

Figure 5.3: *in vivo* behaviour of pSiNP constructs.. 162

Figure 5.4: Vascularization of pSiNPs constructs to identify activated cells.. 164

Figure 5.5: Proangiogenic factors activated by Eru-C_{18}-pSiNPs injection. 165

Figure 5.6: Proangiogenic factors activated by Eru-C_{18}-pSiNP and AFK-187-C_{18}-pSiNP injections. 167

Figure 5.S1: Model for how erucamide may function within the retina. 176

Figure 5.S2: Characterization of pSiNP constructs. 176

Figure 5.S3: Thermogravimetric analysis (TGA) measurements..... 179

Figure 5.S4: *in vitro* toxicity of pSiNP constructs. 180

Figure 5.S5: Erucamide is neutrophic due to phenotypes changes. 180

Figure 5.S6: Fluorescence measurement of bodipy-labelled erucamide-loaded, silane-functionalized pSiNP. 181

Figure 5.S7: Schematic illustration of erucamide derivatives within the same class of long chain fatty acids..... 181

Figure 5.S8: Vascularization of loaded pSiNPs constructs to identify activated CD11b+ cells..... 181

Figure 5.S9: Proangiogenic factors activated by erucamide-derivative loaded pSiNPs constructs. 182

Figure A.1: Schematic of methodology in extracting cobinamide from pSiMPs for HCN measurements. 188

Figure A.2: Removing Cbi-loaded pSiMPs from thermal desorption tube. 189

Figure A.3: Transferring Cbi-loaded pSiMPs into Eppendorf™ tube. 189

Figure A.4: Adding ethanol to Cbi-loaded pSiMPs. 190

Figure A.5: Vortexing pSiMPs to remove Cbi from the particles. 190

Figure A.6: Centrifuging the tube to remove the Cbi solution from pSiMPs. . 191

Figure A.7: Measuring the absorbance intensity of Cbi solution. 191

Figure A.8: Schematic of the characterization of cobinamide-loaded porous silicon microparticles. 192

Figure A.9: Schematic of thermogravimetric analysis (TGA) tests of the Cbi-pSi microparticles. 193

Figure A.10: Schematic of BET N_2 Adsorption/Desorption tests for porous silicon microparticles. 194

Figure B.1: SEM images of pSiMPs after overnight solution binding to Bio-MOF crystals. 199

Figure B.2: SEM images of 10:1 (0.2 mg:20 µg) pSiMP:Bio-MOF samples under different mixing conditions. 199

Figure B.3: SEM images of various mass ratios of 0.5 mg pSiMP vs Bio-MOF mixed via rotating wheel. 200

Figure B.4: 30 mg pSiMPs mixed with 10 or 2.5 mg Bio-MOF via rotating wheel mixer. 200

Figure B.5: 5 mg pSiMPs mixed with varying amounts of Bio-MOF. 202

Figure B.6: SEM images of 30 µg Bio-MOF in different solvents drop-cast onto 2 mg pSiMPs. 202

Figure B.7: Double application of Bio-MOF (2x 45 µg) onto 2 mg pSiMPs. .. 204

Figure B.8: 30 µg Bio-MOF in different solvents drop-cast onto pSiMPs. 204

Figure B.9: Sandwich method on Teflon substrates 205

Figure B.10: Scale up of “sandwich method” on Teflon substrates. 205

Figure B.11: Schematic of the FTIR peaks of the Bio-MOF-pSi samples. 206

Figure B.12: Optical reflectance peaks of the Bio-MOF-pSi samples. 206

LIST OF TABLES

Table **2.S1**: Conversion of molar HF concentrations to its associated partial pressure (mmHg). 58

Table **2.S2**: Conversion of molar HCl concentrations to its associated partial pressure (mmHg). 58

Table **2.S3**: Conversion of molar NH_3 concentrations to its associated partial pressure (mmHg). 58

Table **3.S1**: Table of gatekeeper variations coated onto the photonic crystals.101

Table **4.S1**: Characteristics of pSiNP constructs for pore structure and internal surface area as calculated from cryogenic nitrogen adsorption isotherms..... 145

Table **4.S2**: Size & Surface Charge of pSiNP Constructs as assessed through Dynamic Light Scattering. 145

Table **4.S3**: Histopathological analysis of harvested organs, liver, spleen, and kidneys of pSiNP injected mice compared to PBS controls..... 151

Table **5.S1**: Size & Surface Charge of pSiNP Constructs as assessed through Dynamic Light Scattering. 177

Table **5.S2**: Characteristics of pSiNP constructs for pore structure and internal surface area as calculated from cryogenic nitrogen adsorption isotherms..... 177

ACKNOWLEDGEMENTS

My journey to completing my PhD started when I was young, and for that I must thank my family. First and foremost, this thesis is dedicated to my mother, who has guided me throughout this process, through all the ups and downs, while always providing me with the support, guidance, encouragement, and love, at the times that I needed it the most. I would not have been able to get where I am without her, and I owe all my success to her. I would also like to thank my late father who instilled in me the drive to challenge and push myself to work towards something beyond what I ever imagined in achieving. His love for inquiry is what inspired me to pursue a PhD. In addition, my grandmother has always supported me to work hard and do well since I was a child, something which I always admired. She always valued higher education, something she was not fortunate to have experienced, and it fills me with great pride that I am able to complete this degree for her. I would also like to thank my grandfather who always encouraged me to pursue a field that would benefit the advancement of knowledge and always viewed things with a larger scope. I also would like to thank my uncle, Mithrakumar, who helped me with life adjustments after my father's passing. Finally, I would especially like to thank my stepfather, Murray, who at times, I felt, was the only person who understood all the challenges my studies put me through. He was always a source of positive encouragement and was instrumental in helping me realize how to communicate my ideas clearly and effectively. I appreciate his willingness to always help me out with my work, even when he was extremely busy.

I want to express my gratitude to my supervisor Prof. Michael Sailor. I am extremely grateful that he took a chance on a high school student from Canada who

had limited knowledge about working in a lab setting and provided me with the guidance and the opportunity to become a well-rounded researcher while giving me the freedom to explore a wide scope of research projects. His constant help, support and patience enabled me to succeed throughout my time as an undergraduate and graduate student. I have gained invaluable opportunities being a part of the Sailor Group and the larger porous silicon family.

I would also like to thank all of my mentors and supervisors throughout my many internships and work terms. I have learned so much from them, which has enabled me, I hope, to become a well-rounded scientist. This included Dr. Thomas Defforge, Prof. Gaël Gautier, Prof. Marta Cerruti, Prof. J. Matt Kinsella, Prof. Nicolas Voelcker, Dr. Soundar Chandrasekaran, Dr. Jimnyoung Joo, Prof. Elena Varoni, Dr. Jinke Xu, and Dr. Hesam Mahjoubi.

I would like to thank my committee members for their helpful advice and suggestions throughout our various collaborative projects and for my thesis as well. These are: Prof. Akif Tezcan, Prof. Seth Cohen, Dr. Gerry Boss and Dr. Partha Ray.

I would also like to thank my other project collaborators who have been of immeasurable help. These were: Dr. Jason Sicklick, Dr. Guoqin Wei, Dr. Rob Alberstein, Dr. Kyle Bentz, Dr. Brian Pimentel, and Dr. Martin Friedlander.

I would like to thank both past and present members of the Sailor Group generally, and specifically Eason Lu, Dr. Jon Zuidema, Ricardo De Luna and Dr. Mehdi Nasr. Their countless discussions, advice and suggestions helped me throughout my many projects. In addition, they were great colleagues and our common interest in

basketball and getting coffee helped ease the stress whenever experiments did not go according to plan.

Finally, I would like to thank all my friends whom I met in San Diego and Boston, where I initially started my PhD, as well as my friends from Montreal. They were always supportive of my work in my busy schedule, always provided a great list of activities for me and were always there to chat whenever I needed it. I am grateful for their friendship. This included Rob Dooley, The “Helmholtz Study Group”, Hunter Kimmett and Joel Grant.

Chapter 2, in full, is a reprint of the material as it appears in *ACS Sensors*, 2020. Lu, Y.S., Vijayakumar, S., Chaix, A., Pimentel, B., Bentz, K., Li, S., Chan, A., Whal, C., Ha, J., Hunka, D., Boss, G., Cohen, S., Sailor, M. “Remote Detection of HCN, HF, and Nerve Agent Vapors Based on Self-Referencing, Dye-Impregnated Porous Silicon Photonic Crystals”. The dissertation author was a primary investigator and an author of this paper.

Chapter 3, in full, is currently being prepared for submission for publication of the material *Nature Nanotechnology*, 2022. Vijayakumar, S*., Alberstein, R.G*., Lu, Y.S., Chan, A., Wahl, C.E., Ha, J.S., Hunka, D.E., Boss, G.R., Tezcan, F.A., Sailor, M.J. “Photonic porous silicon sensor with integrated biological gatekeeper for remote detection of HCN vapors”. The dissertation author was the primary researcher and author of this paper.

Chapter 4, in full, has been submitted for publication of the material as it may appear in *Nanoscale*, 2022. Vijayakumar, S., Nasr, S.H., Davis, J.A., Wang, E., Zuidema, J.M., Lu, Y.S., Lo, Y-H., Sicklick, J.K., Sailor, M.J., Ray, P. “Anti-KIT DNA

Aptamer-conjugated Porous Silicon Nanoparticles for the Targeted Detection of Gastrointestinal Stromal Tumors". The dissertation author was the primary researcher and author of this material.

Chapter 5, in part, is currently being prepared for submission for publication of the material in *Science*, 2023. Wei, G*., Chatterjee, S.*, Vijayakumar, S.*, Aguilar, E., Giles, S., Boger, D., Sailor, M.J., Friedlander, M. "Erucamide targets microglia to regulate the retinal angiogenic microenvironment and function as a neurotrophic factor". The dissertation author was a primary researcher and author of this chapter.

VITA

2017 Bachelor of Engineering in Materials Engineering (Co-Op), McGill University

2017-2018 Graduate Student Researcher, Northeastern University

2017-2018 Teaching Assistant, Northeastern University

2018-2022 Graduate Student Researcher, University of California San Diego

2019 Master of Science in Materials Science & Engineering, University of California San Diego

2019-2021 Teaching Assistant, University of California San Diego

2022 Doctor of Philosophy in Materials Science & Engineering, University of California San Diego

PUBLICATIONS

1. Wei, G., Chatterjee, S.*, **Vijayakumar, S.***, Aguilar, E., Giles, S., Boger, D., Sailor, M.J., and Friedlander, M. (2023) *Erucamide targets microglia to regulate the retinal angiogenic microenvironment and function as a neurotrophic factor*. Science. (In Preparation).

2. **Vijayakumar, S***., Alberstein, R.G*., Lu, Y.S., Chan, A., Wahl, C.E., Ha, J.S., Hunka, D.E., Boss, G.R., Tezcan, F.A., and Sailor, M.J. (2022) *Photonic porous silicon sensor with integrated biological gatekeeper for remote detection of HCN vapors.* Nature Nanotechnology. (In Preparation).

3. Lu, Y.S., Vugs, W., Biewenga, L., Zhou, Z., **Vijayakumar, S.**, Merkx, M and Sailor, M. (2022) *Harnessing the Chemistry of Mesoporous Silicon to Prepare "Armor-Clad" Enzyme Nanoparticles with Improved Catalytic Performance*. Chemistry of Materials. (In Preparation).

4. **Vijayakumar, S.**, Nasr, S.H., Davis, J.A., Wang, E., Zuidema, J.M., Lu, Y.S., Lo, Y-H., Sicklick, J.K., Sailor, M.J., and Ray, P. (2022) Anti-KIT DNA *Aptamer-conjugated Porous Silicon Nanoparticles for the Targeted Detection of Gastrointestinal Stromal Tumors*. Nanoscale. (Submitted).

5. Waggoner, L., Kang, J., Zuidema, J., **Vijayakumar, S**., Hurtado, A., Sailor, M., and Kwon, E. (2022) *Porous Silicon Nanoparticles Targeted to the Extracellular Matrix for Therapeutic Protein Delivery in Traumatic Brain Injury*. Bioconjugate Chemistry. (Submitted).

6. Lu, Y.S., **Vijayakumar, S.**, Chaix, A., Pimentel, B., Bentz, K., Li, S., Chan, A., Whal, C., Ha, J., Hunka, D., Boss, G., Cohen, S., and Sailor, M. (2021) *Remote Detection of HCN, HF, and Nerve Agent Vapors Based on Self-Referencing, Dye-Impregnated Porous Silicon Photonic Crystals*. ACS Sensors, 2021, 6, 418-428.

7. Singh, B., Shankar, N., **Vijayakumar, S.**, Abdelhalim, M., Cormack, Makrigiorgos, M.G., van de Ven, A.L., Sridhar, S. (2019) *Scalable, solvent-free extrusion of implantable docetaxel for sustained chemotherapy*. Biomaterials. (Under Review, 2019/11/29).

8. Jiang, T., Mungia-Lopez, J., Gu, K., Bavoux, M., Flores-Torres, S., Kort-Mascort, J., Grant, J., **Vijayakumar, S.**, Rodriguez, A.D., Ehrlicher, A., and Kinsella, J.M. (2019) *Engineering bioprintable alginate/gelatin composite hydrogels with tunable mechanical and cell adhesive properties to modulate tumor spheroid growth kinetics*. Biofabrication, 2019, 12, 015024.

9. Jiang, T., Mungia-Lopez, J., Flores-Torres, S., Grant, J., **Vijayakumar, S.**, Rodriguez, A.D., and Kinsella, J.M. (2018) *Bioprintable Alginate/Gelatin Hydrogel 3D In Vitro Model Systems Induce Cell Spheroid Formation*. Journal of Visualized Experiments. e57826.

10. Varoni E. M., **Vijayakumar, S.**, Canciani, E., Cochis, A., Nardo, L.D., Lodi, G., Rimondini, L., and Cerruti, M. (2018) *Chitosan-Based Trilayer Scaffold for Multitissue Periodontal Regeneration.* Journal of Dental Research. 97(3): 303-311.

11. Jiang, T., Mungia-Lopez, J., Flores-Torres, S., Grant, J., **Vijayakumar, S.**, Rodriguez, A.D., and Kinsella, J.M. (2017) *Directing the Self-assembly of Tumour Spheroids by Bioprinting Cellular Heterogeneous Models within Alginate/Gelatin Hydrogels*. Scientific Reports. 7(1): 4575.

12. Chandrasekaran, S., **Vijayakumar, S**., Nann, T., and Voelcker, N. H. (2016). *Investigation of porous silicon photocathodes for photoelectrochemical hydrogen production*. International Journal of Hydrogen Energy. 41(44): 19915-19920.

13. Joo, J., Cruz, J. F., **Vijayakumar, S.**, Grondek, J., and Sailor, M. J. (2014) *Photoluminescence: Photoluminescent Porous Si/SiO2 Core/Shell Nanoparticles Prepared by Borate Oxidation*. Advanced Functional Materials. 24(36): 5687-5687.

ABSTRACT OF THE DISSERTATION

Functionalized Porous Silicon for Applications in Chemical Sensing, Tumor Imaging and Drug Delivery

by

Sanahan Vijayakumar

Doctor of Philosophy in Materials Science & Engineering

University of California San Diego, 2022

Professor Michael Sailor, Chair
Professor F. Akif Tezcan, Co-Chair

For over 30 years, porous silicon as a material has been leveraged for its usefulness in biomedical and sensing applications. Its tunable structural features, low toxicity profile and readily modifiable surface render this material extremely useful for a wide variety of applications. By chemically modifying surface species, such as silicon hydrides and silicon oxides with silanes, the properties of porous silicon can be enhanced for its use for chemical sensing, biomedical imaging, and drug delivery.

After a brief introduction to porous silicon materials, the first part of this dissertation details surface-modified porous silicon photonic crystals for the chemical sensing of toxic vapors and nerve agents. Chapter 2 utilizes a dual-peak porous silicon photonic crystal embedded with specific for the selective detection of hydrogen fluoride (HF), hydrogen cyanide (HCN), and the chemical nerve agent diisopropyl fluorophosphate (DFP). The pore walls are rendered hydrophobic with octadecylsilane to aid with the loading of the colorimetric molecules while being insensitive to humidity fluctuations. This provides a robust means to develop a remote detection system for chemical agents. Chapter 3 employs the same photonic crystal, modified, however, with a specialized protein-based gatekeeper that is rendered semi-permeable only in the presence of HCN. This is one of the first novel designs of a bio-inorganic sensor capable of detecting chemical agents with high specificity and precision.

The second portion of the dissertation describes how surface-modified porous silicon nanoparticles can be applied in biomedical applications. The first project details the use of Anti-KIT protein DNA-aptamers decorated onto a fluorescently labelled porous silicon nanoparticle for the *in vitro* and *in vivo* imaging of gastrointestinal stromal tumors. This work provides an effective platform in which aptamer-conjugated porous silicon nanoparticle constructs can be used for the targeted imaging of KIT-expressing cancers. The final project utilizes hydrophobic porous silicon nanoparticles for the delivery of erucamide, a highly hydrophobic fatty acid amide, within the retina. By harnessing the versatility of porous silicon, erucamide's target cells and mechanism of neurotrophic action can be identified.

CHAPTER 1

FUNCTIONALIZED POROUS SILICON AND ITS APPLICATIONS

Porous silicon (pSi) is a particular alteration of silicon, whose key feature is that minute pores of a micro- to macro- size have been deliberately created in the element's substrate, hence the term "porous".

This porous structure at the nanoscale turns out to confer pSi with a surprising number of very diverse and valuable uses, features, and applications. This chapter will first summarize why that is so, and then focus on the chemical fuctionalization of pSi as well as its particular applications in chemical sensing and biomedicine.

1.1 GENERAL OVERVIEW OF POROUS SILICON

Porous silicon (pSi) is a material that is prepared by the electrochemical or chemical etching of crystalline silicon at the nanoscale level.[1, 2] pSi was accidently discovered at Bell Labs in 1956 but was not significantly studied until the 1980s.[1] However, over time, pSi garnered some interest as a precursor material for generating oxide layers on silicon and as a dielectric material for capacitance-based chemical sensors. In the late 1980s and early 1990s, a significant breakthrough was the discovery of the photoluminescent properties of pSi, causing increased interest in pSi in the broader scientific community.[1, 3] Over time, pSi became more widely studied, particularly for its potential use in sensors, due to its optical properties, and for its potential biomedical applications, due to the material's minimal toxicity *in vivo*.[2, 4]

The etching of silicon for the creation of pSi follows the chemical equation shown below:

$$Si + 6\ HF + 2\ h^+ \rightarrow SiF_6^{2-} + 4\ H^+ + H_2$$

One important effect of the nanostructuring of pSi in this way is that the resulting material has a variety of tunable structural properties, that is, characteristics that can be modified in a controlled and purposeful way. This is shown in **Figure 1.1a**. These tunable pore characteristics, together with pSi's large specific surface area (which can average around 200 m^2/g), make pSi extremely versatile.[1] In addition, pSI can be given different physical properties or forms, such as thin films or particles.

The set of controllable and tunable pore characteristics includes the pore size, porosity, and pSi film thickness.[1, 2] These can all be modulated by changing variables in the electrochemical etching process, such as the electrolyte solution composition, the applied current, the etch time and the type of doped silicon that is used.[1, 2]

The production of porous silicon involves the use of a Teflon etch-rig with a silicon wafer sandwiched between an aluminum electrode and a platinum counter electrode, as seen in **Figure 1.1b**. A mixture of hydrofluoric acid (HF) and ethanol-based electrolyte solution is commonly used to etch the pores within the silicon wafer. The applied etch current and etch time are all controlled using a computer and a modulating current source.[1]

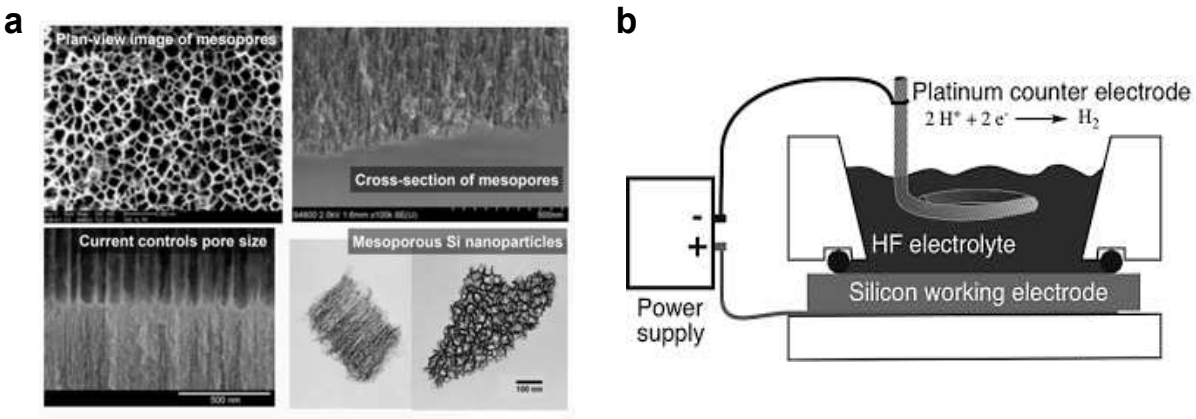

Figure 1.1: Physical characteristics and etching tools of porous silicon (pSi). (a) Tunable morphological properties of nanostructured porous silicon. The scanning electron microscope (SEM) and transmission electron microscope (TEM) images show a tunable pore size and physical properties of pSi.[1] (b) Common set-up utilized for the etching of silicon.[1] A Teflon etch rig is used to house an electrolyte solution of hydrofluoric acid and ethanol while the silicon substrate is in contact between an aluminium electrode and a platinum counter electrode. The electrodes are connected to a power supply which is used to apply current towards this electrochemical etch.

Two major and broad categories of current pSi application consist of various types of chemical sensors, and a variety of biomedical applications. Both categories of applications take advantage of the modifiable physical characteristics of pSi. In the case of sensors, the etching of silicon yields an SiF_6^{2-} species on the substrate surface which can either be readily oxidized to form SiO_2 or be functionalized with many organic, inorganic, and biological molecules.[1] The etched surface is highly reactive to many different chemicals, allowing its use in many kinds of sensors. The biomedical applications of pSi make use of its biocompatibility and biodegradability in the body and include uses in *in vivo* imaging and in the delivery of treatment payloads to sensitive and hard-to-reach tissues. Once introduced *in vivo*, pSi eventually oxidizes and hydrolyzes to form silicic acid, a non-toxic material that is commonly present within the human body.[1, 2, 4, 5]

Another important characteristic of pSi are its aforementioned optical properties, which are unique and distinguish pSi from other nanostructured semiconductor materials and are a major factor in its usefulness. As previously alluded to, in the late 1980s two researchers, Leigh Canham and Ulrich Goesele, each independently discovered that pSi displays both photoluminescence and electroluminescence properties when the pore walls of pSi are thinned to less than 5 nm, due to quantum confinement effects.[1, 2] When excited with a UV light, pSi can glow with a red-orange color (**Figure 1.2a**). It was further discovered that pSi can be etched to make photonic crystals with tunable optical reflectivity spectra (**Figure 1.2b**). Both optical features can be utilized in unique applications as sensors due to the exhibited pSi signals that change in a predictable way when exposed to external environmental changes.

As a result of this set of features, pSi has been utilized in a broad variety of applications, such as systems that incorporate pSi's optical and porous features for medical therapeutic or diagnostic uses, or in applications that take advantage of the chemical and electrical propertiesi to create devices for thermoelectric, photovoltaic and energy storage uses.[1, 2]

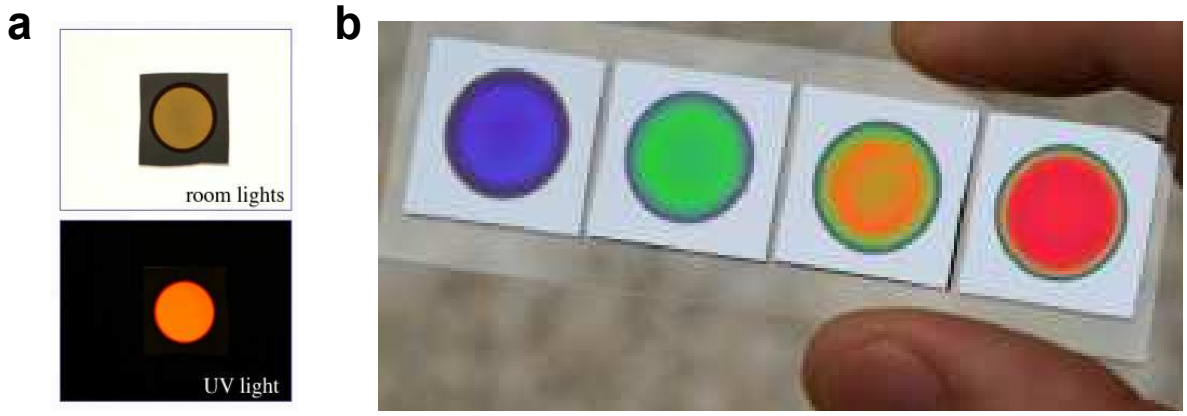

Figure 1.2: Unique optical properties of porous silicon. (a) pSi displays photoluminescent properties which can enable the material to display a red-orange color when illuminated with a UV-light.[1] (b) pSi can also be tuned to make photonic crystal structures that can display various colors within the visible spectrum.[1]

1.2 Functionalized Porous Silicon & Surface Chemistries

The readily modifiable surface of pSi opens the door for this material to be used in various very specific applications based on different surface functionalization chemistries. Depending on the particular use case, from sensing to drug delivery, the material is treated with different chemical, mechanical and electrical processes to create the desired surface features. For example, in the development of sensors, real-world use situations entail sensors being exposed to many different chemical analytes, so the pSi material requires high chemical stability, so as not to be degraded by external stimuli. At the same time, these sensors need to maintain their optical functionality for their intended use and therefore modifications to create such stability must not limit or interfere with its engineered optical properties.[1, 2]

Similarly, in silicon thermoelectrics, a long lifespan is needed, with both high mechanical and chemical stability, while maintaining other factors such as high electrical conductivity and low phonon conductivity.[1] The applications of pSi in LEDs and Li-Ion

batteries share similar features, but with LEDs, features such as a high emission quantum yield is required, while for Li-Ion batteries high ionic conductivity is necessary.[1]

Interestingly, the feature of stability which pSi importantly provides for sensing and thermoelectrics uses contrasts with biomedical applications where the opposite characteristics, such as a short lifespan, are needed.[1] In particular, pSi particles can offer controlled degradability as a primary feature in medical settings so that pSi materials carrying payloads such as oligonucleotides or small-molecule drugs can release their payload at an extended time to targeted tissues or cells of choice. As an additional benefit, these delivery particles, having served their purpose, can then easily degrade, and clear out of the body within a short time frame to avoid toxicity.[1, 2, 5] This large variety of applications of pSi shows the value and importance of the surface modification and functionalization of the pSi substrate.

When pSi is freshly etched several common surface species are present, including silicon hydrides and silicon oxides.[1] Over the course of the last 20 years, many methods have been devised of grafting various silanes onto the hydride and oxide surfaces, through techniques such as hydrosilylation and radical coupling.[1, 2, 6-10] These processes have been a mainstay in the field because of the ease in which functional species can be incorporated onto the pSi surface and the low hydrolytic reactivity of the resulting modified Si-C bonds (**Figure 1.3**). The major drawback with these methods is that both sets of reactions require scrupulous exclusion of air and water to avoid any oxidative side reactions with Si-H.[1] Though these methods are still used today, they are not the most efficient, and common problems such as low reactivity do exist.

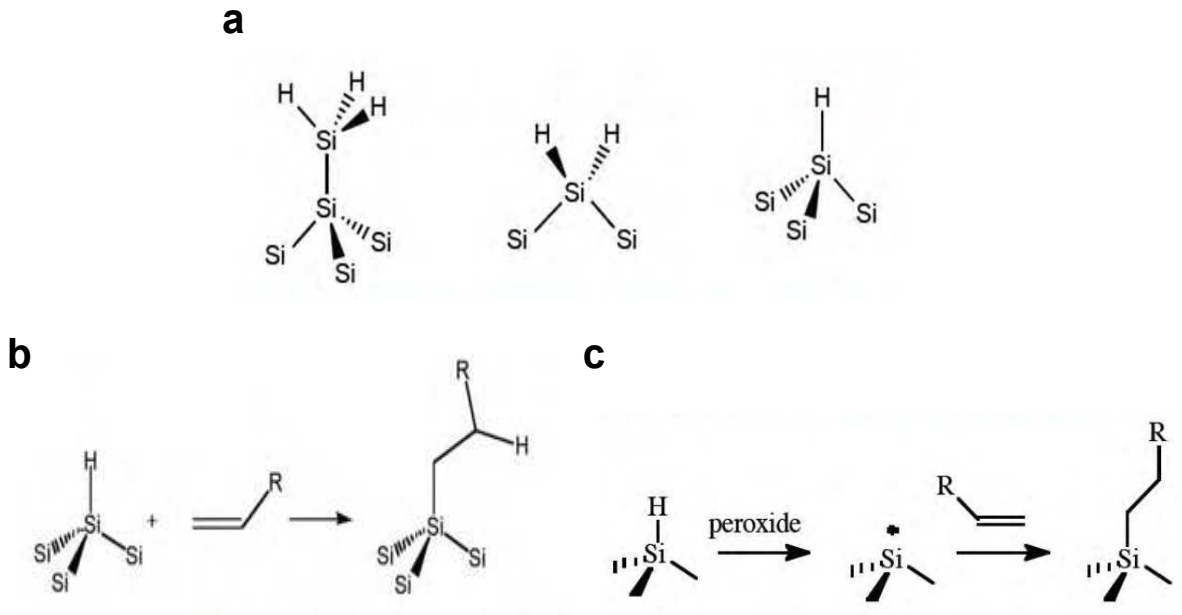

Figure 1.3: Surface species and common functionalization techniques to react to silicon hydrides. (a) Schematic of various silicon hydride species that can exist on pSi.[1] (b) Hydrosilyation of silicon hydrides that is used to graft functional species onto the surface of pSi.[8] (c) Schematic of radical coupling reactions to functionalize the surface hydride species with Si-C bonds.[9, 10]

With respect to silicon oxides, the most common means to functionalize such surfaces is to graft organotrialkoxysilanes, as they react to hydroxyl-rich surfaces on pSi through hydrolytic condensation (**Figure 1.4**).[1, 11] These reactions are commonly associated with (3-Aminopropyl)triethoxysilane (APTES) or 3-Aminopropyl(diethoxy)methylsilane (APDMES). These have been the most common ways to create amine- or thiol- based surfaces on pSi for use in sensor, energy, and biomedical applications.[11] However, these reactions have their limitations as they require long reaction times or high temperatures to obtain an efficient coverage, and any alcohol or water by-products can negatively impact the final product, specifically by clogging the pores within the pSi substrate.[1]

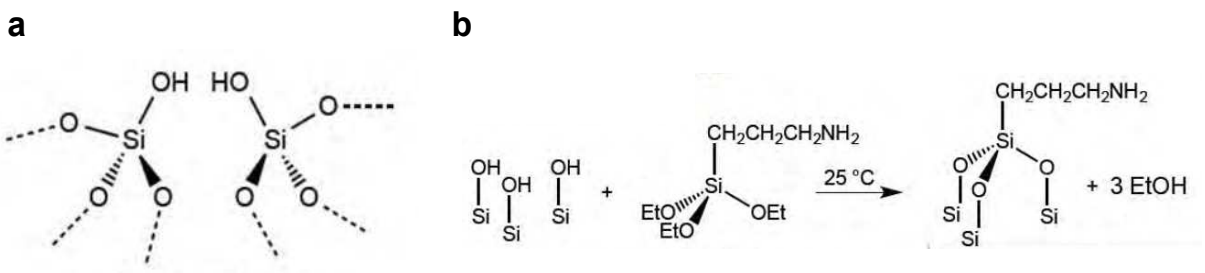

Figure 1.4: Surface species and common functionalization techniques to react to silicon oxides. (a) Schematic of various silicon oxide species that can exist on pSi.[1] (b) Alkoxysilane grafting onto silicon oxides that is used to graft functional species onto the surface, commonly utilizing silanes such as APTES or APDMES.[11]

Recently other alternative methods of functionalizing silicon surfaces have been developed, which provide similar surface species functionalization to the aforementioned methods, but which ameliorate some of their disadvantages. One method involves the catalyst-free dehydrocoupling reaction of various hydridosilanes to silicon hydride surfaces (**Figure 1.5**).[12] This allows for the addition of grafting long-chain hydrocarbons at mild thermal conditions to generate a stable, functional coating with minimal oxidation on the pSi surface, while maintaining functional optical characteristics (which is important for its use for sensors, as the nanostructure is not destroyed). This is an alternative to radical coupling and these reactions work with great efficiency and ease. Chapters 2 and 5 describe this specific dehydrocoupling chemistry for functionalizing the surface of pSi substrates to render them hydrophobic for sensing usages (Chapter 2) and drug delivery applications (Chapter 5).

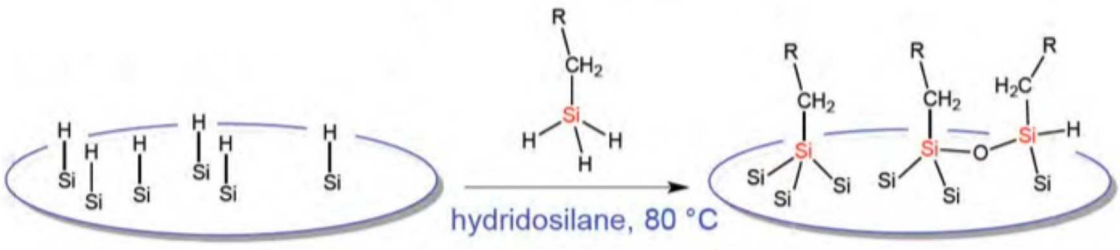

Figure 1.5: Schematic of dehydrocoupling reactions using trihydridosilanes to graft long-chain functional groups onto the surface of porous silicon hydrides.[12]

One novel oxide functionalization is the use of heterocyclic compounds with Si-S or Si-N motifs that can undergo a ring opening reaction to modify surface hydroxyl groups.[13, 14] This follows a "Click" chemistry which is faster and milder than the alkoxysilanes that are commonly used (**Figure 1.6**). Due to the immediate reaction and simplicity of this process, and the ability to perform these reactions on the benchtop, one can quite easily use these reactions to functionalize the surface of pSi with multiple terminal groups, including, amines, and thiols.[13] These reactions yield minimal by-products and can also maintain the optical properties of silicon while preventing pore clogging calculated by surface area calculations from N_2 adsorption/desorption isotherms.[13] These reactions are seen in chapters 3 and 4, in which the surface of the oxidized pSi substrate is functionalized with NH_2-terminal groups for the attachments of protein-based gatekeepers (Chapter 3) and (poly)ethylene glycol (PEG) (Chapter 4).

Figure 1.6: Schematic of ring-opening "click" reactions of heterocyclic silanes to graft various functional groups onto the surface of porous silicon oxides.[13]

There are also other chemistries which utilize oxidants to both chemically and physically alter the surface of silicon. These include borate buffer (borax), tris buffer, and dimethyl sulfoxide (DMSO).[15-17] These oxidants can create a Si/SiO_2 core shell which both yields surface oxides while physically thinning the pore walls of the material. The pore wall thinning can be used to physically trap payloads in a porous surface. In addition, this can be used to generate an electronically passivated material, leading to defects in the $Si\text{-}SiO_2$ interface and therefore cause an increase of the photoluminescent quantum yield up to 23-32% (λ_{ex} = 365 nm) (**Figure 1.7**).[17] These oxides have been used in biomedical applications, particularly for developing nanoparticles for drug delivery and biosensors.

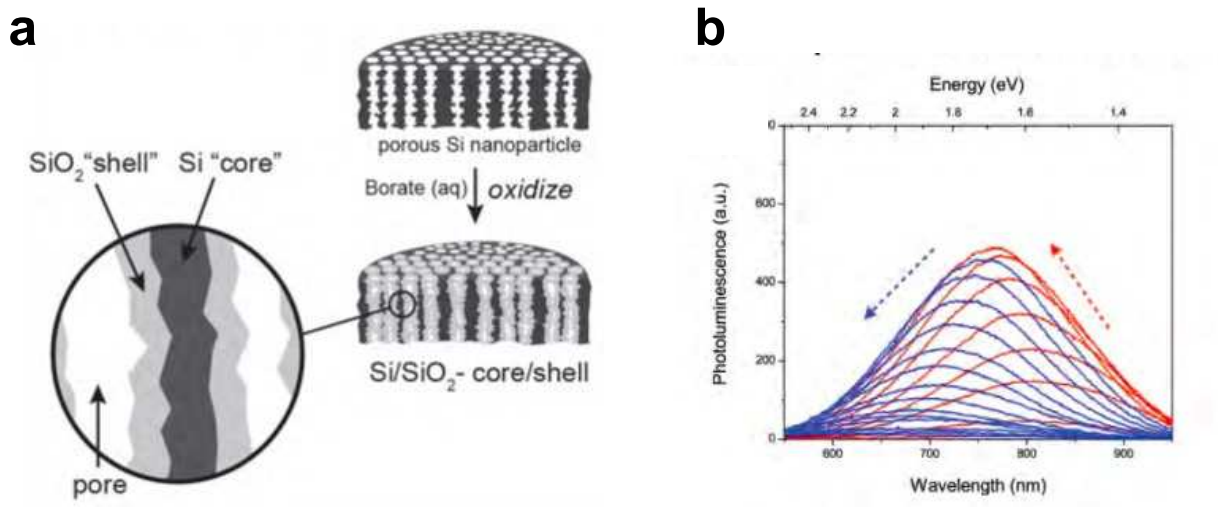

Figure 1.7: Oxidants used to alter the pSi substrate both chemically and physically. (a) Schematic of borate oxidation of porous silicon to create a Si/SiO_2 core shell.[17] (b) The core shell material shown an increase in photoluminescent quantum yield within the pSi substrate.[17]

1.3 Porous Silicon Materials for Sensing

As introduced above, one of the key categories of uses of pSi is in the field of sensing and sensors, due to the ability to electrochemically tune pSi to have different optical characteristics. By modulating a current applied to a silicon substrate, different optical properties can be created on the surface. **Figure 1.8a** shows a rugate etch, which embeds photonic crystal properties within the pSi substrate.[1, 18, 19] The simplicity of this process creates the ability to tune the reflectance spectrum of the thin, porous film relatively easily. This rugate etch is the foundation for the pSi sensors described in Chapters 2 and 3. **Figure 1.8b** details various pSi photonic crystal samples with different rugate etches applied onto their surfaces. The difference in color of the reflected wavelength of the "stop-band" or reflectance peak is due to the period of a sine wave of the current that is applied to the pSi substrate. With a shorter period, a reflected blue color is seen, while with an increase in period, a reflected red color is shown.

a

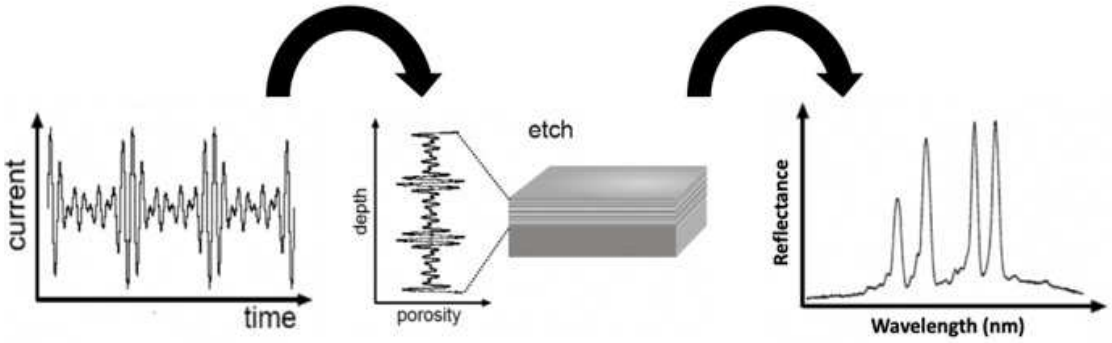

b

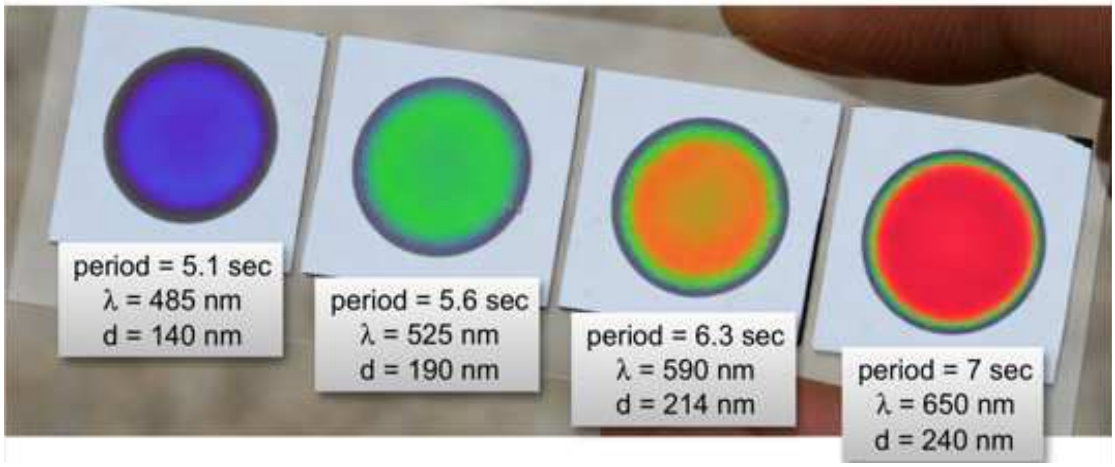

Figure 1.8: Photonic crystal properties of pSi. (a) Schematic of applying photonic crystal properties onto a pSi substrate. A sinusoidal "rugate" waveform of current is applied onto the pSi wafer thereby yielding specific "stop-bands" based on the periodicity of the current.[1] (b) pSi photonic crystals displaying various colors based on the applied period of the "rugate" waveform.[1]

Figure 1.9a below details various etch currents which embed different reflectance properties onto the pSi thin film. The reflected read-out is measured using a light source focused on the pSi film. The reflected light leads back into the fibre optic cable, which is bifurcated and connected to a charged coupled device (CCD) spectrometer (**Figure 1.9b**). This provides a useful measurement tool by which the photonic crystals can be observed and utilized as a sensor, with quantitative measurement properties. The

modulation of current enables pSi to be used from sensors to barcodes, with specifically coded reflected wavelengths.[1]

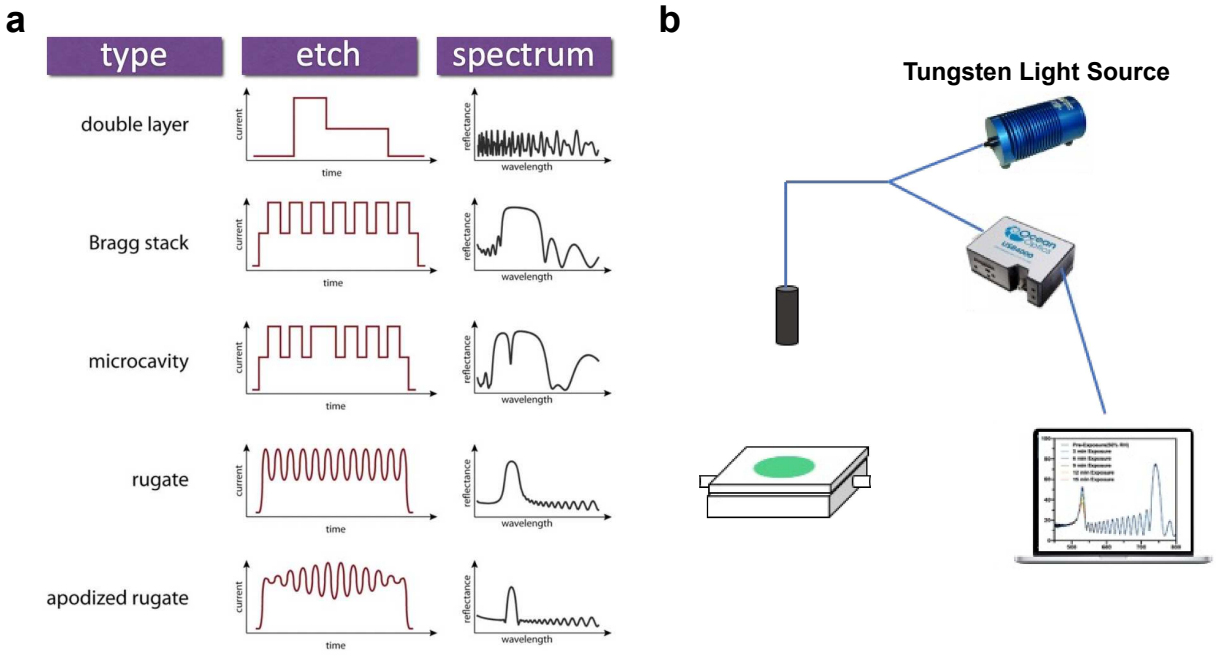

Figure 1.9: Various etch types can yield different reflectance spectra. (a) List of different etch types along with their corresponding etching waveform and reflectance spectrum.[1] (b) Schematic of set-up yest to measure the reflectance spectra of pSi photonic crystals.

Once these photonic crystals are created, interference from various compounds in the surrounding environment can modify the refractive index of the porous, thin film. This is what creates the usefulness of pSi for sensing. **Figure 1.10** shows that these crystals, in air, display a green color, but when infiltrated with a liquid, such as water or ethanol, with a different refracted index from air, a red color is seen. This is because the reflectance spectrum has shifted towards red, known as “red-shifting”.[1] This change is reversible - if the liquid were to evaporate, without destroying the photonic crystal, the color would return to green. That particular reflectance spectral shift is known as “blue-shifting”.[1]

Importantly, this feature of photonic crystals in pSi can be exploited by embedding various compounds that have specific absorbance properties within the nanostructured film. By tuning the reflectance peaks of the sensor, to overlapping absorbance peaks within externally administered compounds into the substrate, the measured reflectance signal of the pSi photonic crystal could be either masked or enhanced.[19] This opens many possible applications using these pSi crystals as sensors.

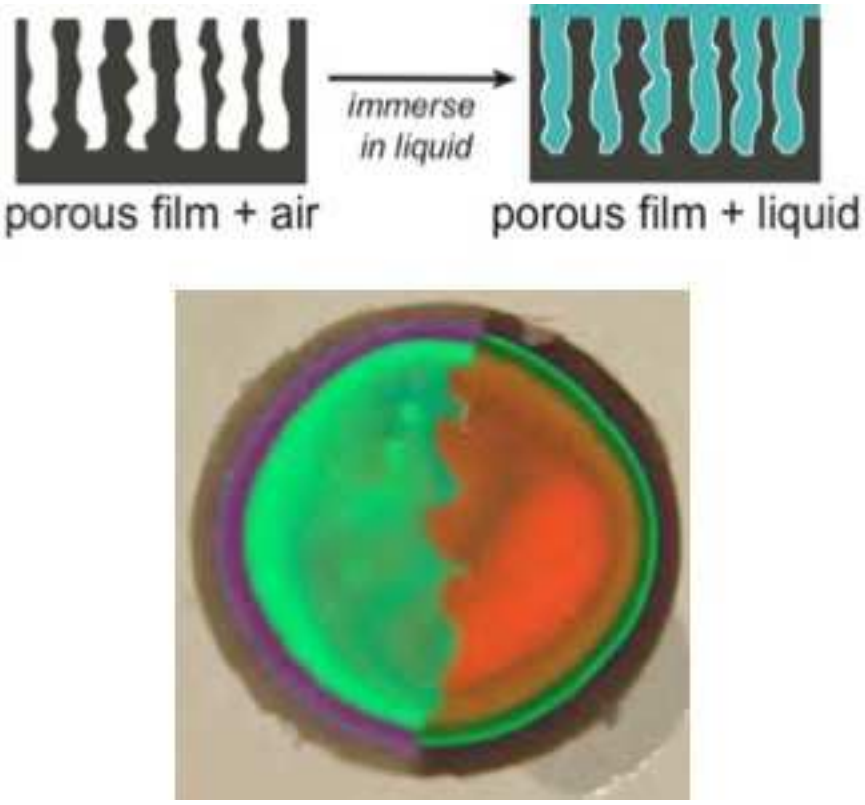

Figure 1.10: pSi photonic crystals change color when the etched film is infiltrated with a medium of different refractive index. The pSi crystal displays a green color in air, but when immersed with a liquid, the color changes to red. This feature can be exploited for the use of these photonic crystals as sensors.[1, 20]

These chemical properties of pSi allow for the creation of sensors that can detect toxic industrial chemicals (TICs), chemical warfare agents (CWAs) and volatile organic compounds (VOCs), with many important uses in industrial and military settings. In

particular, these sensing technologies and modalities are potentially portable, provide a real-time readout, maintain a small form factor, and are cheap and easy to manufacture, an ideal combination.

However, to be workable and useful in real-world settings these sensors would need to meet other criteria as well. They should be sensitive enough to detect compounds at levels below the IDLH (immediate danger to life and health). They would need to detect a specific compound of choice, which however would often exist within a larger mixture "cluttered" with other compounds.[1] They would need to be robust so as to not degrade from the effects of impurities or clutter. Very importantly, they should not provide false positive readings due to shifts in environmental factors or lighting conditions. This list of challenges is a major reason why some sensors with theoretical potential do not in fact have much real-world use. Chapters 2 and 3 go into further detail as to how functionalized porous silicon can be used for sensing of TICs, CWAs, and VOCs.

1.4 Porous Silicon Materials for Biomedical Applications

The potential of porous silicon nanoparticles (pSiNPs) in biomedical applications has been recognized for over 20 years. Early studies, making use of the important biocompatibility advantage of pSi, used pSiNPs for treatments of both liver and pancreatic cancers. pSiNPs are biodegradable and are easily biologically processed by the body into inert orthosilicic acid ions, which then clear through the kidneys, within one week.[1, 2, 5, 21, 22] Studies have shown that pSiNPs have yielded no evidence of toxicity in animal models. The inherent near infrared (IR) photoluminescent property of these nanoparticles makes them very convenient for monitoring both the distribution of the particles in the body and

the subsequent degradation of the particles *in vivo*.[6] The result is that pSiNPs have many clear advantages over conventional nanoparticles in biomedical usages.

This combination of pSiNPs properties make them a remarkably versatile delivery vehicle in biomedical applications. pSiNPs can be modified with various surface chemistries to obtain the optimal loading of a wide range of payloads, including drugs, small biologics, and imaging contrast agents. The highly reactive and versatile surface chemistry of pSiNPs makes them compatible for the conjugation to various polymeric and liposomal coatings, while a novel calcium-silicate trapping chemistry can be used to condense anionic payloads effectively to achieve higher loading efficiencies than lipid and silica-based nanoparticles (**Figure 1.11**).[23] Chapter 5 details the use of functionalized pSiNPs for the delivery of hydrophobic payloads. In that specific example, pSiNPs are modified with a hydrophobic chemistry to load primary lipid fatty acid amides for delivery of these materials within the eye.

By coating pSiNPs with biologically inert polymers, such as (poly)ethylene glycol (PEG), the nanoparticle can be protected from degradation, that can also reduce unwanted non-specific uptake of the particles by the liver and spleen, and can prolong circulation in the blood.[1, 2, 5, 6] Another important characteristic of pSiNPs is the ability to "decorate" the surface of these particles with targeting moieties (e.g., peptides, antibodies, aptamers), to increase the specific targeting and penetration to selected tissues. Multiple targeting ligands can be decorated onto the surface of a single particle, which can provide greater targeting efficiency than the free molecule.[1, 2, 5, 21, 23, 24] This allows a modular nanosystem to act as a long-circulating formulation that effectively targets hard-to-bind tumors and tissues. Chapter 4 explores this concept for the imaging

of tumors using aptamers conjugated onto pSiNPs. By utilizing multiple aptamer-ligands conjugated onto a PEG-coated nanoparticle, pre-loaded with an imaging fluorophore, this system can specifically image gastrointestinal stromal tumors with high effectiveness within the liver and spleen.

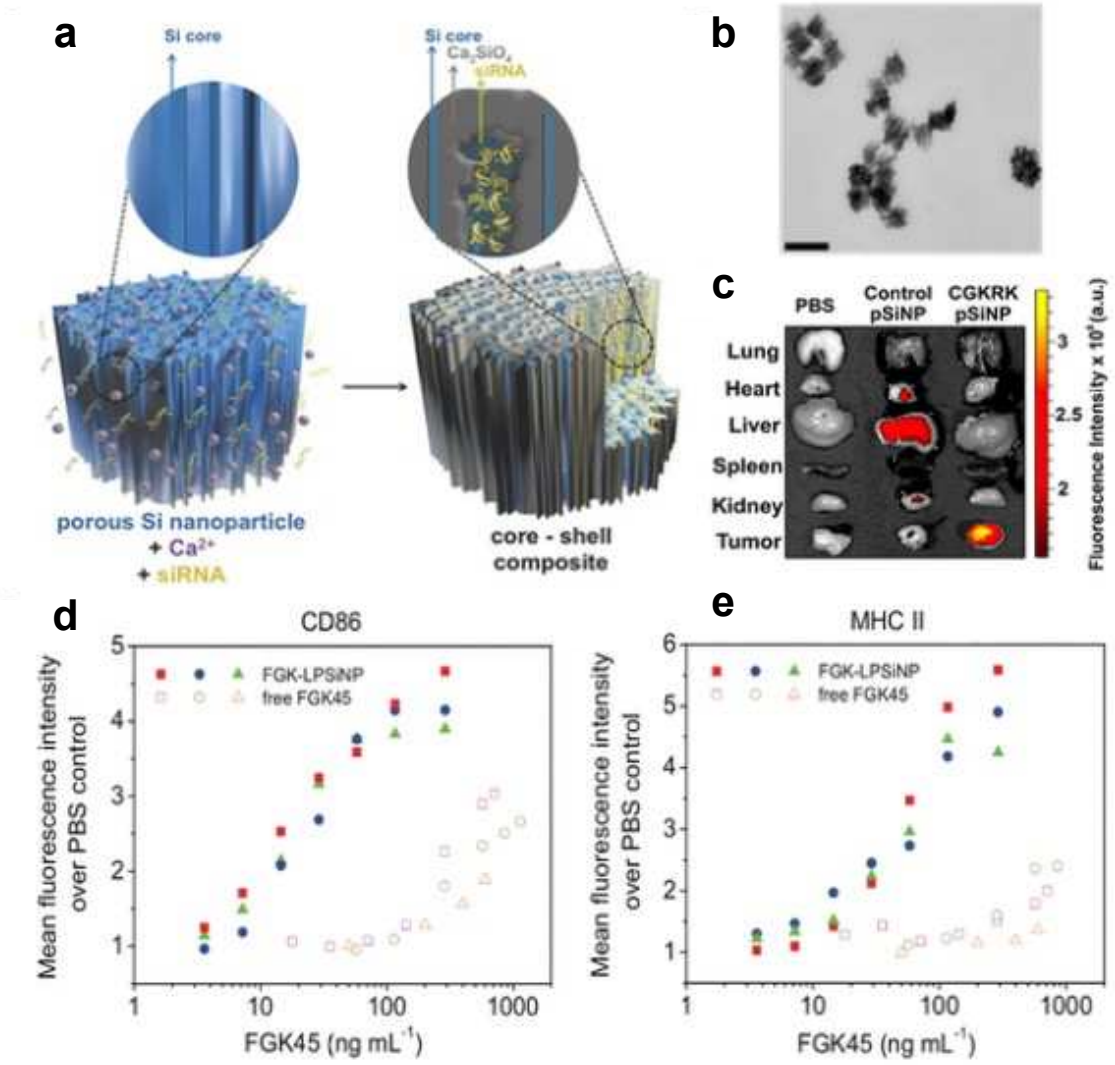

Figure 1.11: Biomedical applications of porous silicon nanoparticles (pSiNPs). (a) Schematic of the preparation of calcium-silicate pSiNPs for the trapping of payloads.[23] (b) Transmission electron microscopy (TEM) image of pSiNPs.[23] Scale bar = 200 nm. (c) Fluorescence images of harvested organs of ovarian cancer-bearing mice after intravenous injection of PBS, control pSiNPs conjugated with nontargeting peptide and tumor-targeting CGKRK-conjugated pSiNPs.[25] Antibody-conjugated pSiNPs (FGK-pSiNP) show amplified activation potency compared to free FGK45 antibody as seen through flow cytometry analysis of the expression of B cell activation markers (d) CD86 and (e) MHC II8.[21]

REFERENCES – CHAPTER 1

1. M. J. Sailor, *Porous Silicon in Practice: Preparation, Characterization, and Applications*, Wiley-VCH, Weinheim, Germany, 2012.

2. L. T. Canham, *Handbook of Porous Silicon*, Springer, Switzerland, 2014.

3. J.-H. Park, L. Gu, G. von Maltzahn, E. Ruoslahti, S. N. Bhatia and M. J. Sailor, *Nature Materials*, 2009, **8**, 331-336.

4. C. Chiappini, E. Tasciotti, J. R. Fakhoury, D. Fine, L. Pullan, Y.-C. Wang, L. Fu, X. Liu and M. Ferrari, *Chemphyschem*, 2010, **11**, 1029-1035.

5. H. A. Santos, ed., *Porous Silicon for Biomedical Applications*, Elsevier, Amsterdam, 2014.

6. J. Wang, T. Kumeria, M. T. Bezem, J. Wang and M. J. Sailor, *ACS Applied Materials & Interfaces*, 2018, **10**, 3200-3209.

7. Y.-H. Li and J. M. Buriak, *Inorganic Chemistry*, 2006, **45**, 1096-1102.

8. M. P. Stewart and J. M. Buriak, *Angewandte Chemie International Edition*, 1998, **37**, 3257-3260.

9. M. R. Linford, P. Fenter, P. M. Eisenberger and C. E. D. Chidsey, *Journal of the American Chemical Society*, 1995, **117**, 3145-3155.

10. A. Bansal and N. S. Lewis, *The Journal of Physical Chemistry B*, 1998, **102**, 4058-4060.

11. G. T. Hermanson, in *Bioconjugate Techniques*, ed. G. T. Hermanson, Academic Press, San Diego, 1996, DOI: https://doi.org/10.1016/B978-012342335-1/50000-2, pp. xxi-xxiii.

12. D. Kim, J. Joo, Y. Pan, A. Boarino, Y. W. Jun, K. H. Ahn, B. Arkles and M. J. Sailor, *Angewandte Chemie International Edition*, 2016, **55**, 6423-6427.

13. D. Kim, J. M. Zuidema, J. Kang, Y. Pan, L. Wu, D. Warther, B. Arkles and M. J. Sailor, *Journal of the American Chemical Society*, 2016, **138**, 15106-15109.

14. B. Arkles, Y. Pan, Y. Mi Kim, E. Eisenbraun, C. Miller and A. E. A. Kaloyeros, *Journal of Adhesion Science and Technology*, 2012, **26**, 41-54.

15. J. H. Song and M. J. Sailor, *Inorganic Chemistry*, 1998, **37**, 3355-3360.

16. N. L. Fry, G. R. Boss and M. J. Sailor, *Chemistry of Materials*, 2014, **26**, 2758-2764.

17. J. Joo, J. F. Cruz, S. Vijayakumar, J. Grondek and M. J. Sailor, *Advanced Functional Materials*, 2014, **24**, 5688-5694.

18. A. M. Ruminski, B. H. King, J. Salonen, J. L. Snyder and M. J. Sailor, *Advanced Functional Materials*, 2010, **20**, 2874-2883.

19. B. H. King, A. Gramada, J. R. Link and M. J. Sailor, *Advanced Materials*, 2007, **19**, 4044-4048.

20. E. Segal, L. A. Perelman, F. Cunin, F. Di Renzo, J. M. Devoisselle, Y. Y. Li and M. J. Sailor, *Advanced Functional Materials*, 2007, **17**, 1153-1162.

21. L. Gu, L. E. Ruff, Z. Qin, M. Corr, S. M. Hedrick and M. J. Sailor, *Advanced Materials*, 2012, **24**, 3981-3987.

22. J. Salonen, A. M. Kaukonen, J. Hirvonen and V. P. Lehto, *J Pharm Sci*, 2008, **97**, 632-653.

23. J. Kang, J. Joo, E. J. Kwon, M. Skalak, S. Hussain, Z.-G. She, E. Ruoslahti, S. N. Bhatia and M. J. Sailor, *Advanced Materials*, 2016, **28**, 7962-7969.

24. J. Joo, X. Liu, V. R. Kotamraju, E. Ruoslahti, Y. Nam and M. J. Sailor, *ACS Nano*, 2015, **9**, 6233-6241.

25. A. Bertucci, K.-H. Kim, J. Kang, J. M. Zuidema, S. H. Lee, E. J. Kwon, D. Kim, S. B. Howell, F. Ricci, E. Ruoslahti, H.-J. Jang and M. J. Sailor, *ACS Applied Materials & Interfaces*, 2019, **11**, 23926-23937.

CHAPTER 2

REMOTE DETECTION OF HCN, HF AND NERVE AGENT VAPORS VASED ON SELF-REFERENCED, DYE-IMPREGNATED POROUS SILICON PHOTONIC CRYSTALS

2.1 ABSTRACT

A one-dimensional photonic crystal is prepared from porous silicon (pSi) and impregnated with a chemically specific colorimetric indicator dye to provide a self-referenced vapor sensor for the selective detection of hydrogen fluoride (HF), hydrogen cyanide (HCN), and the chemical nerve agent diisopropyl fluorophosphate (DFP). The photonic crystal is prepared with two stop bands: one that coincides with the optical absorbance of the relevant activated indicator dye and the other in a spectrally "clear" region, to provide a reference. The inner pore walls of the pSi sample are then modified with octadecylsilane to provide a hydrophobic interior, and the indicator dye of interest is then loaded into the mesoporous matrix. Remote analyte detection is achieved by measurement of the intensity ratio of the two stop bands in the white light reflectance spectrum, which provides a means to reliably detect colorimetric changes in the indicator dye. Indicator dyes were chosen for their specificity for the relevant agents: rhodamine-imidazole (RDI) for HF and DFP, and monocyanocobinamide (MCbi) for HCN. The ratiometric readout allows detection of HF and HCN at concentrations (14 and 5 ppm, respectively) that are below their respective IDLH (immediately dangerous to life and health) concentrations (30 ppm for HF; 50 ppm for HCN); detection of DFP at a concentration of 114 ppb is also demonstrated. The approach is insensitive to potential interferents such as ammonia, hydrogen chloride, octane, and the 43-component mixture of VOCs known as EPA TO-14A, and to variations in relative humidity (20 – 80% RH). Detection of HF and HCN spiked into the complex mixture EPA TO-14A is demonstrated.

The approach provides a general means to construct robust remote detection systems for chemical agents.

2.2 Introduction

There is a longstanding need for simple systems that can remotely detect airborne toxic industrial chemicals (TICs) and chemical warfare agents (CWAs).[1, 2] Technologies that meet the criteria of portability, real-time response, and low false positives or false negatives include gas chromatography – mass spectroscopy (GC/MS),[3] ion mobility spectrometry (IMS),[4] and infrared and Raman spectroscopy.[5-8] When low power consumption, small form factor and low complexity are taken into consideration, point sensor technologies involving surface acoustic wave (SAW),[9] conducting polymers,[10] or metal oxide sensors[11] can provide good sensitivity but typically provide lower selectivity, compromising false alarm/false positive metrics. Colorimetric indicators, in which the target analyte is detected by a specific molecular interaction with a dye that responds to the event with a change in its electronic structure and thus its color, offers a simple yet powerful means to enhance specificity in point sensors. Many colorimetric indicators have been synthesized that provide high selectivity and sensitivity for the detection of a variety of important environmental analytes: volatile organic compounds (VOCs), explosives, TICs and CWAs.[12-14] An advantage of colorimetric indicators is that multiple dyes can be incorporated into spatially segregated arrays to allow detection of multiple analytes simultaneously or to increase fidelity by taking advantage of the cross-reactivity of the dyes to different agents.[14-16] Dyes can also show relatively low susceptibility to interference from environmental fluctuations in temperature and humidity—a particular challenge for many point sensors.[17] The increased availability of low power, high

resolution digital cameras in recent years has been an enabling feature of colorimetric indicators, which has led to increased interest in their use in remote sensing schemes.[18-23] In remote sensing, the sensor element is located a substantial distance from the optical reader, which places limitations on the system related to spatial resolution, extraneous "clutter" in the image field that can obscure the colorimetric signal, and uncontrolled lighting conditions.[23] The problem is compounded by the fact that most organic indicator dyes have broad absorbance bands that are not particularly distinctive compared to the broad range of pigments and dyes commonly present in the environment.

In prior work we showed that the fidelity of remote detection with an indicator dye can be substantially improved by impregnating the dye in a porous silicon (pSi)-based 1-D photonic crystal.[24] Using a standard pH indicator dye, bromothymol blue, a photonic crystal was prepared with two reflectance (stop) bands: one that overlapped with the absorbance band of the basic form of the dye (the "signal" channel) and the other that appeared in a spectral region where the dye showed minimal absorbance (the "reference" channel). We found that the intensity ratio of the reflectance bands accurately responded to a gas phase ammonia challenge, and this corrected for large changes in zero-point drift associated with fluctuating probe light intensity. Prepared using an electrochemical anodization process, the pSi system provides a convenient means to fabricate mesoporous 1-D photonic crystals for such applications, allowing the programmatic generation of complex spectral signatures that can be measured from a remote distance by optical reflectance spectroscopy or by hyperspectral imaging.[24-27] In addition, the pSi-based photonic structures enables very minor reflectance shifts at a large temperature range, providing accurate and robust readouts in varied conditions.[28]

While the earlier work demonstrated the remote detection concept for the pSi system, the reliability of the approach for use in “real-world” complex air samples and with changing humidity was not evaluated. Furthermore, it used a simple pH indicator dye and the question of how generalizable the approach might be to chemical agents other than simple acids and bases was not addressed. Here we evaluate the selective detection of hydrogen fluoride (HF), diisopropyl fluorophosphonate (DFP), and hydrogen cyanide (HCN) vapors using indicator dyes for which specificity is well established: a rhodamine-imidazole (RDI) complex for detection of HF and DFP, and monocyanocobinamide (MCbi) for detection of HCN. The sensors are tested for their sensitivity and selectivity relative to common environmental interferents and to changes in background relative humidity.

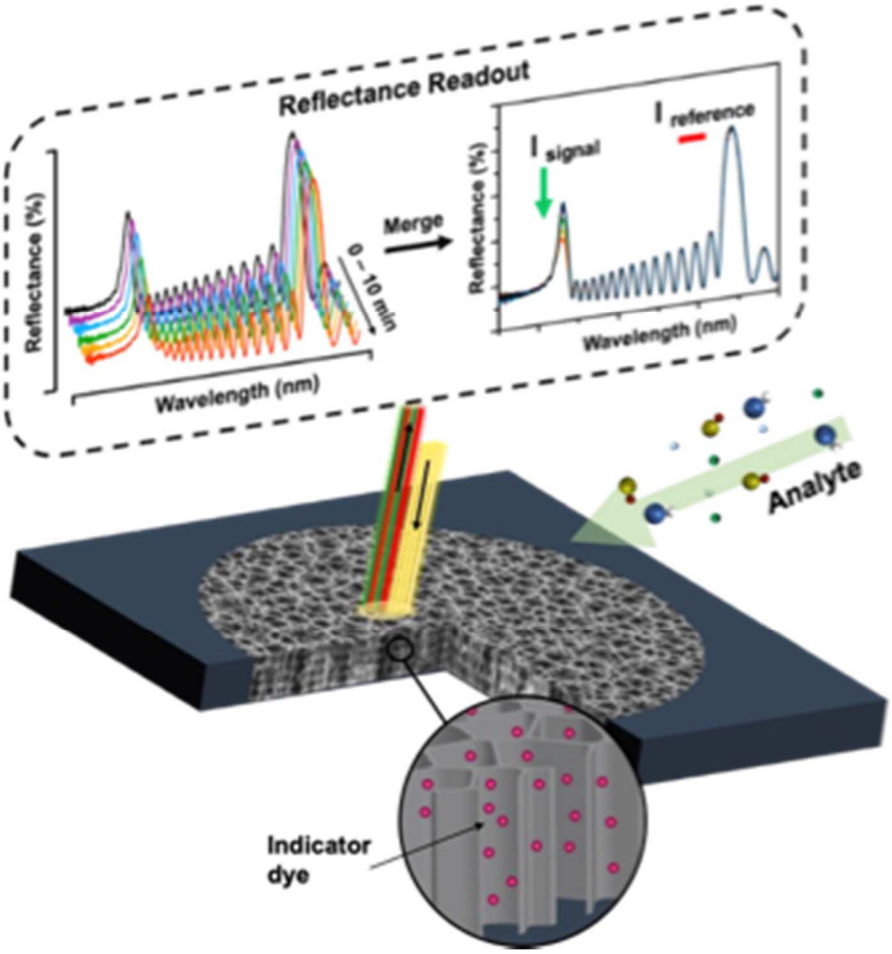

Figure 2.1: Sensor and sensing approach used in this work. A mesoporous Si photonic crystal is prepared with two stop bands: one that coincides with the optical absorbance of the relevant activated indicator dye (signal channel) and the other in a region of the spectrum where neither activated nor inactivated forms of the dye absorbs (reference channel). The inner pore walls are modified with octadecylsilane to provide a hydrophobic interior, and the indicator dye of interest is loaded into the mesoporous matrix. Analyte binding to the dye is quantified as $I_{signal}/I_{reference}$, where I_{signal} and $I_{reference}$ are the intensities of light reflected at the signal and reference wavelength bands, respectively.

2.2 Results and Discussion

2.2a Preparation of pSi Photonic Crystal Sensors

The sensor and detection concepts are outlined in **Figure 2.1**. The pSi photonic crystals were prepared by electrochemical anodization of single-crystal Si wafers in an aqueous ethanolic hydrofluoric acid solution using a composite current density – time waveform as previously described,[29] and then chemically modified to improve their

performance in ambient environments. For preparation of the photonic crystals, the etching waveform was composed of a sum of two sine waves, such that the photonic crystal that resulted from the process would display two stop bands in the reflection spectrum that could act as “reference” and “sample” channels due to their differing wavelengths (**Figure 2.1**). The time-dependent current density waveforms, J(t), used in this work were created following the relationship:

$$J(t) = \left[\frac{J_{\max} - J_{\min}}{4}\right]\left[\sin\left(\frac{t}{T_1}\right) + \sin\left(\frac{t}{T_2}\right)\right] + \left[\frac{J_{\max} + J_{\min}}{2}\right] \quad \textbf{(1)}$$

Where J_{max} and J_{min} represent the maximum and minimum current density values applied during the etch, and T_1 and T_2 are the periods of the two sine waves used, each of which determined the wavelength of one of the two stop bands in the resulting photonic crystal. These values were determined empirically based on the wavelength of the absorbance maximum for the particular indicator dye of interest. For the HF and DFP sensors (which use the RDI indicator dye), samples with stop bands centered at 520 and 730 ± 10 nm were designed, and for the HCN sensor (which uses the MCbi indicator dye), stop bands centered at 605 and 730 ± 10 nm were prepared (**Figure 2.2**). For both sample types the wavelength of 720-740 nm was chosen for the “reference” band because both of the indicator dyes showed minimal absorbance in this region, either before or after exposure to their intended analytes (**Figure 2.2**). The other stop band in each sample was the “Signal” band, whose wavelength was chosen to optimally overlap with the absorbance of the colorimetric indicator dye when it interacted with the analyte of interest (**Figure 2.S1**, Supporting Information).

2.2B Surface Modification and Loading of Indicator Dyes

After anodization and prior to loading the indicator dye of interest into the mesoporous matrix, the inner pore walls of the pSi samples were modified with octadecylsilane to provide a hydrophobic interior, referred to in this work as pSi-Si(C_{18}). The main motivation for this chemistry was to suppress the response of the materials to humidity. In particular, the wavelength maximum of the stop band in pSi photonic crystals is known to shift in response to capillary condensation of water vapor,[30, 31] and the hydrophobic chemistry was deployed to minimize spectral drift in the real-world sensing scenario, where RH is uncontrolled.

We used a thermal dehydrocoupling chemistry to prepare pSi-Si(C_{18}). As-anodized pSi samples contain a reactive surface chemistry composed of Si-H species that readily undergo dehydrocoupling with a wide range of organic species containing terminal -SiH_3 groups.[32] In the present case, the as-etched samples were chemically modified by reaction with octadecylsilane ($H_3Si(CH_2)_{17}CH_3$), which has been shown to impart a highly hydrophobic character.[32] Water contact angle increased from 89° to 128° upon conversion of pSi to pSi-Si(C_{18}) (**Figure 2.S2**, Supporting Information). Attenuated total reflectance Fourier transform infrared (ATR-FTIR) spectra confirmed the presence of organic signatures assigned to the surface-grafted octadecylsilane species in pSi-Si(C_{18}) (**Figure 2.S2**, Supporting Information): bands at 1470 and 2850 – 2930 cm^{-1} are assigned to the scissor and stretching modes of CH_2, respectively. A band at 1080 cm^{-1} is assigned to Si – O stretching; the dehydrocoupling reaction generally produces small quantities of adventitious silicon oxides.[32]

Representative plan-view scanning electron microscope (SEM) images of pSi-Si(C_{18}) (**Figure 2.2a**) revealed that the pSi photonic crystals retained their open porous nanostructure after surface functionalization. Furthermore, the cross-sectional SEM images (**Figure 2.2b**) revealed the periodic multilayered nanostructure characteristic of the porosity gradient that is generated by the electrochemical preparation and which is responsible for the photonic properties of the material.[29] Digital Analysis of the plan-view SEM images (**Figure 2.2a**) indicated a mean pore diameter of 12 $\pm$ 3 nm. The porosity and thickness of the octadecyl-modified porous photonic crystals were measured using the spectroscopic liquid infiltration method (SLIM),[29] which indicated a net porosity of ~30% and an overall thickness of ~7 μm for the pSi films.

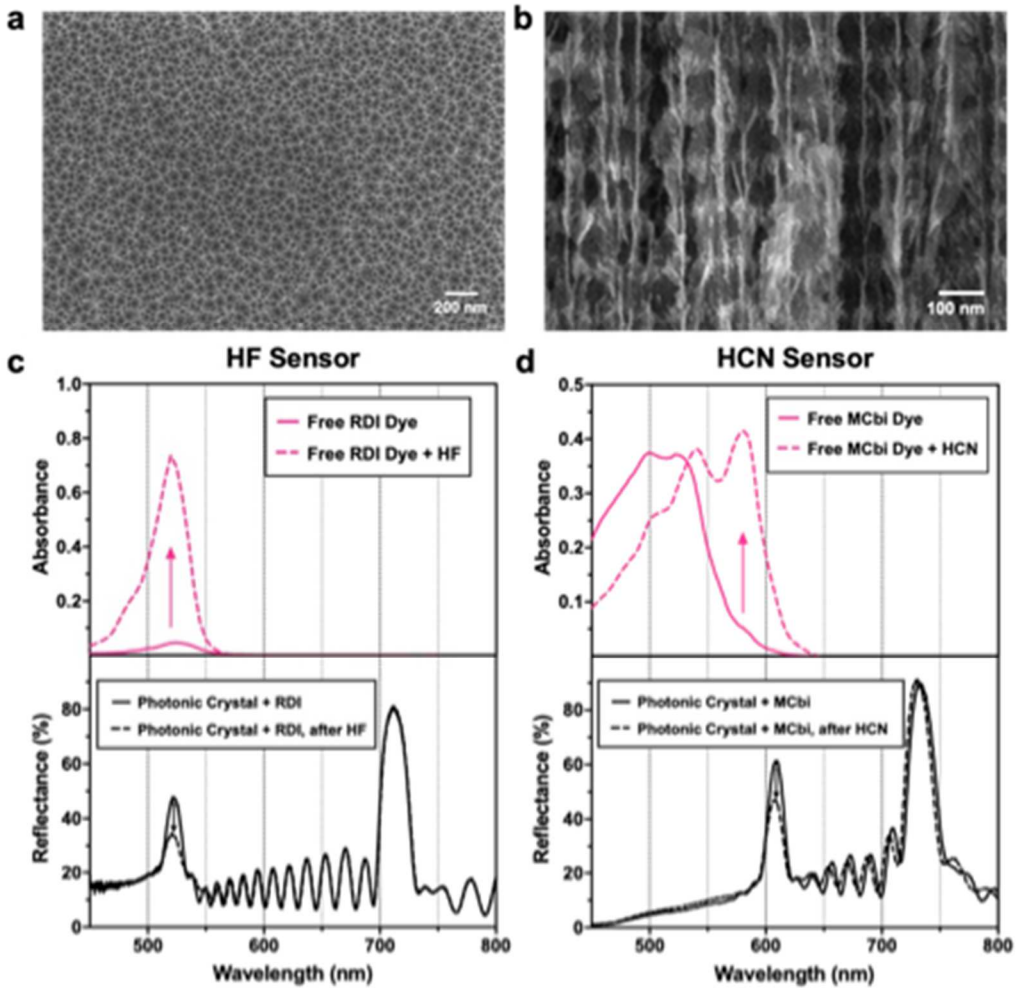

Figure 2.2: Morphology of pSi photonic crystal sensors and their optical response to analyte vapor challenges. Representative plan-view (a) and cross-sectional (b) scanning electron microscope (SEM) images of the octadecylsilane-modified porous Si photonic crystal, pSi-Si(C_{18}). (c) Representative visible absorbance spectrum of RDI dye in solution (top) and optical reflectance spectrum of RDI dye-impregnated pSi-Si(C_{18}) photonic crystal (bottom), before and after exposure to HF analyte. Absorbance spectrum measured in a 1-cm pathlength cuvette using RDI dye (2 mM) dissolved in 1:1 (v:v) acetonitrile:dichloromethane. Addition of HF performed by introduction of aqueous HF (48% by mass) sufficient to achieve final [HF] = 17 mM. Optical reflectance spectrum of RDI – impregnated pSi-Si(C_{18}) photonic crystal was measured before and after exposure to HF vapor as described in the text, resulting in the indicated decrease in intensity of the band at 520 nm. (d) Representative visible absorbance spectrum of monocyanocobinamide, MCbi, in solution (top) and optical reflectance spectrum of MCbi dye-impregnated pSi-Si(C_{18}) photonic crystal (bottom), before and after exposure to cyanide analyte. Absorbance spectrum measured in a microplate reader normalized to a 1-cm pathlength cuvette equivalent using MCbi dye (500 μM) dissolved in ethanol. Addition of cyanide performed by introduction of concentrated aqueous KCN sufficient to achieve final [CN^-] = 500 μM. Optical reflectance spectrum of MCbi – impregnated pSi-Si(C_{18}) photonic crystal measured before and after exposure to HCN vapor as described in the text, resulting in the indicated decrease in intensity of the band at 605 nm.

Two colorimetric indicators were chosen based on their known chemical specificity for the HF or HCN analytes of interest in this work. Based on a rhodamine-imidazole complex, RDI has been reported as a selective probe for fluoride that displays a marked change in color due the ability of fluoride to induce a spiro-ring-opening reaction on the rhodamine moiety. RDI was synthesized as previously reported.[33, 34] Briefly, the procedure involved reaction of rhodamine 6G with hydrazine to obtain rhodamine hydrazide, and incorporation of the imidazole group to the rhodamine 6G – hydrazide backbone (**Figure 2.S3** and 2.**S4**, Supporting Information). Cobinamide (Cbi), a cobalt-containing Vitamin B-12 analog, has been used both as an antidote for cyanide poisoning and for analytical applications due to its high affinity for CN^- and its rapid binding kinetics.[35] As-synthesized Cbi contains OH and H_2O ligands coordinated to the cobalt center, and these are sequentially replaced upon encounter with CN^- to generate a 1:2 Cbi:CN^- complex. The binding interactions produce noticeable color changes in Cbi, from orange (absorbance at ~510 nm) to violet (583 nm). The replacement of OH- with CN^- results in a strong trans-labilizing effect, and addition of the second CN^- ligand has been shown to provide a more rapid and more pronounced spectral change in the complex.[36] Thus in order to enhance the sensing response in this work, the as-synthesized Cbi(OH)(H_2O) complex was titrated with CN^- in a 1:1 molar ratio to generate the monocyano species MCbi, or Cbi(CN)(H_2O), (**Figure 2.S5** and **2.S6a**, Supporting Information). Calibration curves showing optical absorbance of the MCbi probe at 583 nm as a function of CN^- concentration in water, ethanol, and in a 1:1 mixture of water and ethanol are presented in **Figure 2.S6b**, Supporting Information. The probe showed no detectable

solvatochromism. The monocyano complex was diluted with ethanol and loaded into the pSi-Si(C_{18}) matrix to be used as the analyte-selective indicator.

In either case, the RDI or MCbi probes were embedded into the pSi-Si(C_{18}) samples by drop-casting and characterized using ATR-FTIR spectroscopy (**Figure 2.S2**, Supporting Information). The RDI – pSi-Si(C_{18}) samples showed additional weak bands at 1530 cm^{-1} and 1640 cm^{-1} assigned to C–N and amine groups of the RDI probe (**Figure 2.S7a**, Supporting Information). The MCbi – pSi-Si(C_{18}) samples displayed spectral characteristics of the MCbi probe, with a band at 1670 cm^{-1}, assigned to a C=O stretching mode, as the most distinctive feature (**Figure 2.S7b**, Supporting Information). The quantity of indicator dye loaded onto the porous samples was maximized to provide the fastest response to the analyte of interest while simultaneously controlled to prevent any significant spectral shift or decrease in the intensity of the reflectance stop bands prior to being triggered by the analyte of interest. The indicator dye, drop-cast onto the pSi-Si(C_{18}) samples, is assumed to be loaded onto the pSi-Si(C_{18}) without any loss. The mass loading of dye, defined as (mass of dye)/(mass of dye-loaded porous film), was gravimetrically quantified as 4.92 ± 0.94% and 2.93 ± 0.27%, for RDI and MCbi samples, respectively. The sensors are referred to in this work as "RDI – pSi-Si(C_{18})" or just "RDI – photonic crystal" (for the HF or DFP sensor) and "MCbi – pSi-Si(C_{18})" or "MCbi – photonic crystal" (for the HCN sensor).

2.2c Sensing of HF Using RDI-pSi(C_{18}) Photonic Crystal Sensors

The ability of the RDI – photonic crystal sensors to detect HF in the vapor phase was assessed using a vapor dosing setup fitted with a reflectance spectrometer (see **Figure 2.S8,** Supporting Information for a schematic and more detailed description of the

procedure). Prior to each dosing experiment, the sensors were exposed for 30 min to a flowing gas stream at a fixed value of %RH by premixing a ratio of dry compressed air and air saturated with water vapor, using digital mass flow controllers. The $HF_{(g)}$ analyte was then introduced to the flowing stream by bubbling laboratory air through an aqueous HF solution and diluting it as appropriate using mass flow controllers. The concentration of $HF_{(g)}$ was determined from the dilution ratio and using published partitioning values for $HF_{(g)}$ with $HF_{(aq)}$ at the relevant values of aqueous concentration and temperature, and assuming that the air in the bubbler reached equilibrium with the aqueous solution. Thus, the concentration values for $HF_{(g)}$ given in this work are likely under-estimates of the actual values. Based on flow rate and system volume, the time needed to reach steady state concentration in the sample chamber was ~8 min.

`The response of the RDI – photonic crystal sensor to an HF challenge, measured by optical reflectance spectroscopy, is shown in **Figure 2.3a**. As expected, exposure to HF triggered an irreversible increase in optical absorbance at ~521 nm from the RDI probe molecule due to opening of the spirolactam ring (**Figure 2.S9a,** Supporting Information), as previously described.[33, 34] This increase in absorbance resulted in a decrease in intensity of reflectance from the "Signal" band of the photonic crystal relative to the "Reference" reflectance band. The HF sensing response was quantified with a Response function defined in **Eq. 2**:

$$Response = \frac{R_t}{R_0} = \left(\frac{I_{signal}}{I_{reference}}\right)_t / \left(\frac{I_{signal}}{I_{reference}}\right)_0 \qquad \textbf{(2)}$$

Where R_t is the ratio of intensities of the signal band (I_{signal}) to the reference band ($I_{reference}$) measured at time t, R_0 is the ratio of intensities of the signal band (I_{signal}) to the reference band ($I_{reference}$) measured before exposure (time $t = 0$). The quantity R_0 therefore

provided a means to correct for instrumental response at the different wavelengths measured; this is referred to in the Figure axes as Normalized $I_{signal}/I_{reference}$. A decrease in the value of this response function corresponds to an increase in absorbance of the indicator dye that correlated with analyte exposure.

Figure 2.3b presents dose-response curves for the RDI – photonic crystal sensor exposed to $HF_{(g)}$ at concentrations of 14, 28, and 59 ppm, in an air carrier stream maintained at 50% relative humidity (RH). The sensor exhibited a significant decrease in the value of the response function, and the rate of decrease in this value scaled with analyte concentration. For all $HF_{(g)}$ concentrations tested, the responses reached the same (saturation) value after a sufficient period of time had passed (**Figure 2.S9b**, Supporting Information). This behavior is consistent with the irreversible chemistry of the indicator dye; the saturation level corresponds to a point at which essentially all of the indicator dye available had reacted with HF analyte. Therefore, the response function, and thus the limit of detection (LOD), was a function of both analyte concentration and time of exposure. For example, to reach an LOD (signal exceeding 3 standard deviations relative to the blank) of 28 ppm $HF_{(g)}$ required 3 min of exposure to the flowing analyte stream, while an LOD of 14 ppm required a 6 min exposure. The time required for the sensor to reliably detect the Immediately Dangerous to Life and Health (IDLH) level of 30 ppm for $HF_{(g)}$ exposure[1] was therefore < 3 min. Because of the irreversible kinetics of the spirolactam ring opening reaction of the indicator dye, the behavior of the RDI – photonic crystal system is perhaps more appropriately described as a dosimeter than as a sensor.

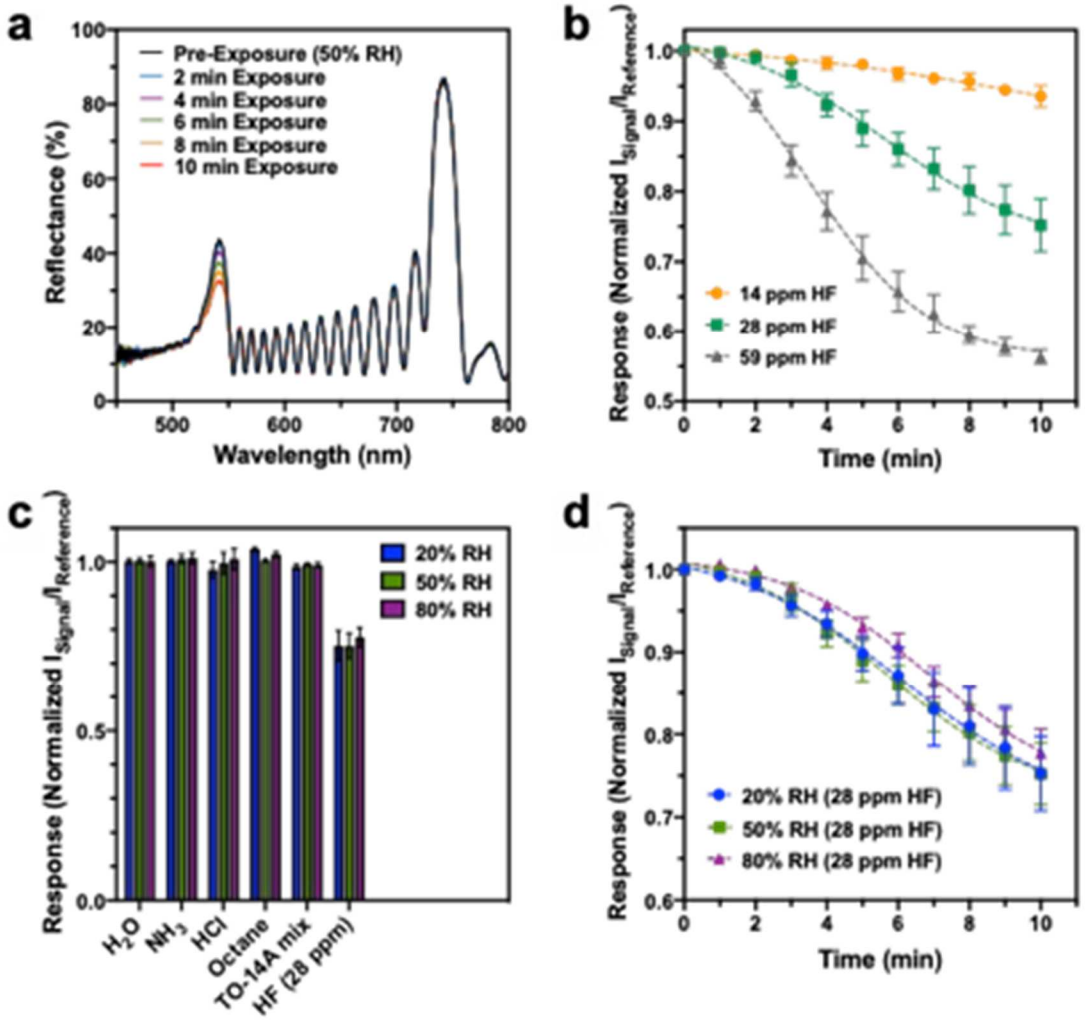

Figure 2.3: $HF_{(g)}$ sensing performance of RDI – pSi-Si(C_{18}) photonic crystal sensor. (a) Overlaid time series of reflectance spectra obtained from an RDI – pSi-Si(C_{18}) photonic crystal sensor exposed to 28 ppm of $HF_{(g)}$ (50% RH) at the indicated time points. The decrease in the signal peak (~520 nm) indicates detection of HF. (b) Temporal response curves of RDI – pSi-Si(C_{18}) photonic crystal sensors upon exposure to the indicated concentrations of $HF_{(g)}$ (14 – 59 ppm) at 50% RH. Response metric is defined in eq. 2. (c) Selectivity studies of RDI – pSi-Si(C_{18}) photonic crystal sensors challenged with vapors of the indicated potential interferents. Results of experiments performed with carrier gas at 20, 50 and 80% RH are shown. Interferent concentrations: NH_3, 100 ppm; HCl, 100 ppm; octane, 600 ppm; and TO-14A mixture of VOCs (0.5 ppm of each component). Bars labeled "H_2O" represent air blanks at the indicated values of RH. Data were acquired 10 min after introduction of the indicated analyte or interferent agents. (d) Temporal response curves for RDI – pSi-Si(C_{18}) photonic crystal sensors upon exposure to 28 ppm of $HF_{(g)}$, measured under varying humidity conditions, as indicated. Error bars shown are the standard deviation from triplicate trials.

We next evaluated the selectivity of the RDI – photonic crystal sensor by comparing the sensor response to $HF_{(g)}$ to the potential interferents ammonia (NH_3), hydrochloric acid (HCl), octane, and a complex air mixture containing 43 different volatile organic compounds defined in method TO-14A by the US Environmental Protection Agency (EPA),[37] referred to in this work as "TO-14A mix." The NH_3, HCl, octane, and TO-14A mix interferents were each diluted into a humidified air stream to achieve 20, 50 and 80% RH. The sensors were exposed to a flowing stream of the potential interferents for 10 minutes and the responses are presented and compared with a 28 ppm $HF_{(g)}$ challenge in **Figure 2.3c**. The sensor showed no significant response to the NH_3, HCl, and TO-14A mix interferents at all values of %RH tested whereas there was a slight sensor drift after the exposure of 600 ppm octane vapor at 50 %RH. The sensor drift was caused by the spectral shift of the stop bands upon the infiltration of octane vapor into the sensor, which leads to a change in total refractive index of the porous matrix of the sensor (**Figure 2.S10**, supporting information). While the chemical modification of octadecylsilane imparts a high level of hydrophobicity onto the sensor surface to suppress the response to humidity, it also generates a greater affinity to a range of hydrocarbon vapors, such as octane, that can potentially impact on the sensor response. However, it should be pointed out that the "Signal" reflectance band of the RDI – photonic crystal sensor remained within the region of the spectrum where the RDI dye absorbs and provides a detectable $HF_{(g)}$ response with the exposure of octane vapor.

To assess the effect of different RH values on the temporal response of the RDI – photonic crystal sensor, temporal dose-response curves were acquired for a 28 ppm $HF_{(g)}$ challenge at 20, 50 and 80% RH (**Figure 2.3d**). The responses of the sensor in 80% RH

air were slightly, but consistently suppressed by ~3% relative to the responses measured at 20 and 50% RH. Overall, the sensors displayed a good ability to discriminate HF from the interferents over a wide range of relative humidity values.

2.2D Sensing of DFP Using RDI-pSi(C_{18}) Photonic Crystal Sensors

Because it responds to the presence of HF, the RDI – photonic crystal sensor can potentially be used for detection of fluoride-based organophosphonate nerve agents such as sarin, soman, and diisopropyl fluorophosphonate (DFP), as all of these agents are subject to P-F bond hydrolysis, liberating HF as a byproduct.[38] We tested this hypothesis in the case of DFP, a nerve toxin that is considerably less toxic than the organophosphorus nerve agents sarin and soman.[39] The pilot experiments involved generation of DFP vapor using a permeation tube generation system with nitrogen carrier gas at 50°C. Prior to the dosing of DFP analyte, the sensors were exposed for 30 min to a flowing gas stream at 50% RH by premixing a ratio of nitrogen carrier gas and laboratory air saturated with water vapor. The DFP analyte generated from the permeation tube system (228 ppb) was then introduced into humidified laboratory air to provide the final concentration at 114 ppb DFP vapor at 50 %RH. No specific hydrolysis catalyst was used in these experiments, so the generation of the HF analyte needed to activate the RDI – pSi-Si(C_{18}) sensor resulted from the natural, slow rate of hydrolysis of DFP[40] in the mesoporous material,[41] which was not measured here. A ~3% change in the response was observed after 3h exposure to 114 ppb DFP vapor at 50% RH (**Figure 2.S11**, Supporting Information). The low level and slow response of the sensor is consistent with the substantially lower concentration of analyte used in these experiments, and the slow kinetics for DFP hydrolysis that can be expected to be present under the test conditions.

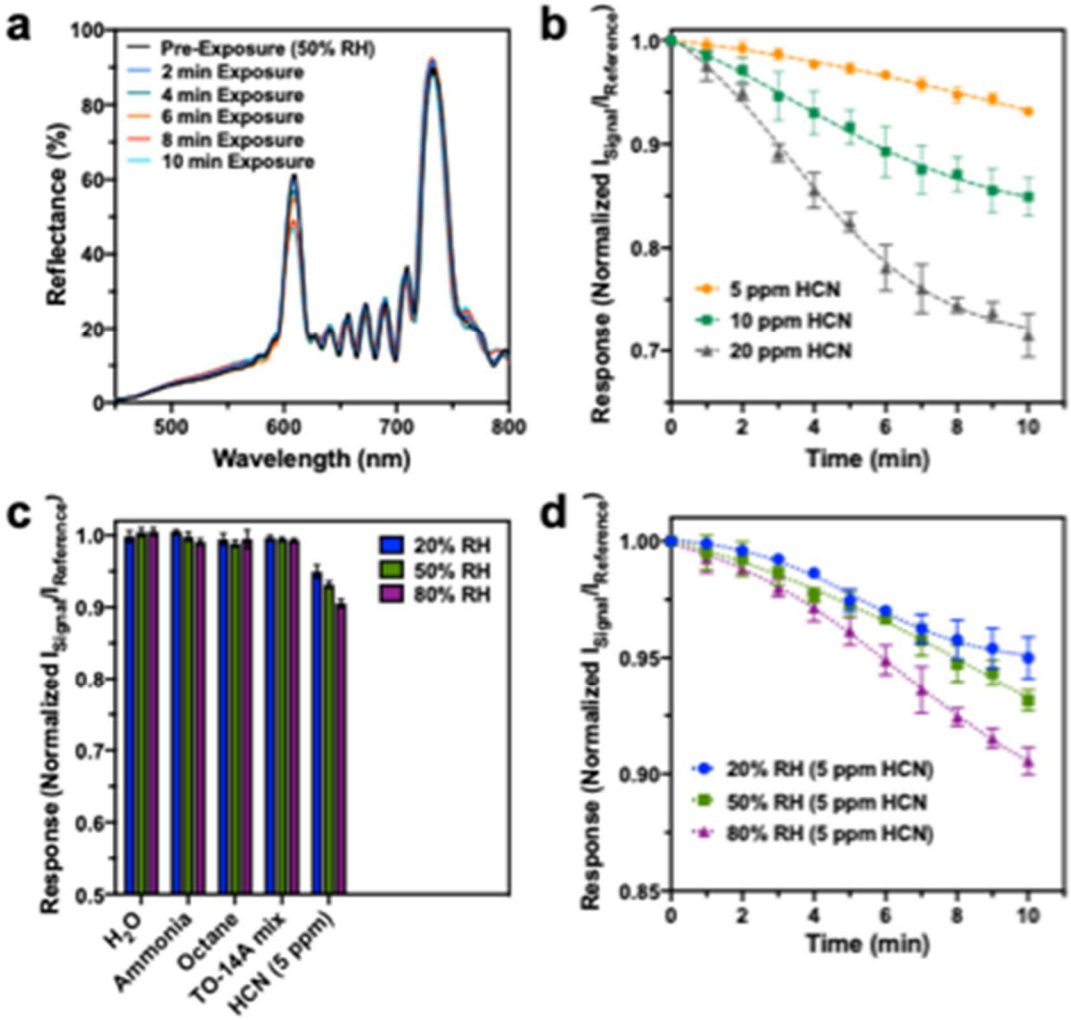

Figure 2.4: Performance of MCbi – pSi-Si(C_{18}) photonic crystal sensor for HCN detection. (a) Overlaid time series of reflectance spectra obtained from a MCbi – photonic crystal sensor exposed to 20 ppm of $HCN_{(g)}$ (50% RH) at the indicated time points. The decrease in the signal peak (~605 nm) indicates detection of HCN. (b) Temporal response curves of MCbi – photonic crystal sensors upon exposure to the indicated concentrations of HCN vapor under 50% RH. Response metric is defined in eq. 2. (c) Selectivity studies of MCbi – photonic crystal sensors challenged with vapors of the indicated potential interferents. Results of experiments performed with carrier gas at 20, 50 and 80% RH are shown. Interferent concentrations: NH_3, 100 ppm; octane, 600 ppm; and TO-14A mixture of VOCs (0.5 ppm of each component). Bars labeled "H_2O" represent air blanks at the indicated values of RH. Data were acquired 10 min after introduction of the indicated analyte or interferent agents. (d) Temporal response curves for MCbi–photonic crystal sensors upon exposure to 5 ppm of $HCN_{(g)}$, measured under varying humidity conditions, as indicated. Error bars shown are the standard deviation from triplicate trials.

2.2E Sensing of HCN Using MCBi-pSi(C_{18}) Photonic Crystal Sensors

The MCbi –photonic crystal sensor triggered on the colorimetric change that occurs when the MCbi indicator dye undergoes a binding interaction with cyanide. The response to an HCN vapor challenge is presented in **Figure 2.4**. The experiments were performed in a manner similar to that involving the RDI–photonic crystal sensors for DFP: the MCbi – photonic crystal sensors were first exposed for 30 min to a humid atmosphere at the desired RH value, and $HCN_{(g)}$ from a calibrated, certified gas cylinder was then introduced into the flow stream (**Figure 2.S12**, Supporting Information). Reaction of monocyanocobinamide with HCN to form the dicyanocobinamide species generated a broad absorbance band centered at 583 nm (**Figure 2.S1,** Supporting Information), which overlapped with the 605 nm stop band of the MCbi – photonic crystal sensor. As with the HF sensor, this increase in absorbance resulted in a substantial decrease in the intensity of the "Signal" reflectance peak upon exposure to 20 ppm $HCN_{(g)}$, with no significant change in the "Reference" reflectance peak of the sensor (**Figure 2.4a**). The HCN response was quantified using the Response function defined in eq. 2, and the results for the HCN concentration range 5 – 20 ppm and under 50% RH are presented in **Figure 2.4b**. An LOD of 5 ppm HCN was achieved within 2 min of exposure, whereas the LOD values of 10 and 20 ppm HCN were achieved within 1 min. Thus, the sensor could detect $HCN_{(g)}$ at the IDLH level (50 ppm)[1] in < 1 min.

Although both sensors measured optical absorbance from the indicator dye, the response of the MCbi indicator to $HCN_{(g)}$ differed from the response of the RDI indicator to $HF_{(g)}$ described above because the reaction of MCbi with HCN is reversible. While the equilibrium constant for binding of CN^- to monocyanocobinamide is quite large (10^8),[36] it

was previously demonstrated that the back-reaction is observed when HCN vapor is removed from the gas stream.[42] Consistent with its large binding constant, the rate of loss of CN^- from the dicyano complex of cobinamide was significantly slower than the rate of binding, thus substantial time was required for the sensor to recover to its original state (**Figure 2.S13**, Supporting Information).

The selectivity of the MCbi – photonic crystal sensor for $HCN_{(g)}$ relative to the potential interferents ammonia (NH_3), octane, and a mixture of VOCs (TO-14A mix) was quantified at different humidity levels following procedures similar to those described for the $HF_{(g)}$ sensor (i.e., the RDI–photonic crystal). Tests were performed in the absence of the $HCN_{(g)}$ analyte. The NH_3, octane, and TO-14A mix interferents were each diluted into a humidified air stream to achieve 20, 50 and 80% RH. The sensors were exposed to a flowing stream of the potential interferents for 10 min and the responses are presented and compared with a 5 ppm $HCN_{(g)}$ challenge in **Figure 2.4c**. The MCbi – photonic crystal sensor showed no significant response to the NH_3, HCl, and TO-14A mix interferents at all values of RH tested. While the response of the MCbi – photonic crystal sensor to octane vapor also underwent a spectral shift of the stop bands, the sensor displayed no significant response to the octane vapor. Similar to the RDI – photonic crystal sensor, the "Signal" reflectance band of the MCbi – photonic crystal sensor remained within the region of the spectrum where the MCbi dye absorbs and provides a detectable $HCN_{(g)}$ response after the exposure of octane vapor" (**Figure 2.S14**, Supporting Information).

The temporal response of the MCbi–photonic crystal sensor to the target HCN analyte was moderately dependent on RH. Temporal response curves acquired for a 5 ppm $HCN_{(g)}$ challenge at RH values of 20, 50 and 80% are presented in **Figure 2.4d**. The

rate of response of the sensor to $HCN_{(g)}$ increased somewhat with increasing RH, and the dependence of the temporal response on RH was substantial compared to what was observed with the $HF_{(g)}$ sensor (RDI–photonic crystal, **Figure 2.3d**). The observed increase in rate of response to HCN with increasing humidity has been observed previously for the MCbi probe.[34, 40] In that prior study, MCbi was dispersed on cellulosic and glass fiber-based paper supports, and it was concluded that the MCbi + HCN reaction chemistry is dependent on the availability of water. That study also found that the sensitivity of the probe to HCN increased with increasing RH. Both of these observations (increase in sensitivity and increase in response rate) are consistent with the present results. The role of water in this reaction is presumably to hydrate and stabilize the dye and to effect deprotonation of HCN into CN^-, in order to form the final cyano-complex with the MCbi probe. The fact that the sensor response is somewhat dependent on humidity imposes a practical limitation on the sensor. However, it should be pointed out that over the entire humidity range studied (20-80% RH), the sensor was able to detect 5 ppm HCN within 10 min.

2.2F Sensing of HF and HCN in a Complex Air Mixture

To simulate real-world environments, the photonic crystal sensors were challenged with their target analytes in the presence of a complex matrix containing multiple VOCs. The experiments described above (**Figures 2.3** and 2.**4**) established that the sensors did not respond to the VOCs in the EPA TO-14A calibration mixture (TO-14A mix), however an additional set of experiments is performed to determine if detection of the target analytes was obscured when they are in the presence of this more complex air matrix. The RDI – or MCbi – photonic crystal sensors were exposed to three different

conditions in a sequential order: laboratory air (50% RH), air + TO-14A mix at 50% RH, and finally the target analyte (HF or HCN) spiked into air + TO-14A mix at 50% RH (**Figure 2.5**). To reduce the spectral noise, a Gaussian peak fit with a width of 15 nm was applied onto the reflectance stop bands. The change in the peak amplitudes for both stop bands were then used to determine the temporal response of photonic crystal sensors in a complex air mixture, following eq. 2.

As expected, the ratiometric signal (eq. 2) from the RDI – and the MCbi – photonic crystal sensors showed no response to either laboratory air at 50% RH or to 50% RH air containing the TO-14A mix. The sensors then displayed a strong, but very slightly suppressed response upon introduction of their target analytes (28 ppm $HF_{(g)}$ or 10 ppm $HCN_{(g)}$) into a flowing stream containing the interferents, compared to the non-spiked analyte exposures shown in Figure 3b and Figure 4b. While it is not surprising that the indicator dyes showed such excellent performance in the complex sample matrix, as they were chosen for this study because of their previously established chemical specificities, these results demonstrated that incorporation of the colorimetric indicators into the mesoporous and hydrophobic environment of the photonic crystal-based sensor did not impair their selectivity.

2.2G Remote Sensing Demonstration

The motivation of this study was to improve the fidelity of colorimetric indicator dyes by providing a more distinctive spectral signature that could be discriminated at a distance and in an image field containing substantial spectral or physical “clutter”. In the present work the RDI and MCbi indicator dyes had substantial spectral overlap with each other (**Figure 2.2c** and 2.**2d**), such that it would be difficult to distinguish them in a remote

image—for example in a scenario where it was desired to monitor sentinels for multiple threat agents simultaneously. The photonic crystal host then provides an ability to distinguish one sentinel from another, either spectrally or in a hyperspectral image, as the characteristic reflectance band being monitored is artificially narrowed relative to the natural linewidth of the dye. To evaluate the ability of the approach to be used in a remote sensing scenario, a RDI – photonic crystal sensor was configured in a dosing chamber fitted with an optical window, and the reflectance spectrum was monitored by a source/detector system fitted to an optical telescope and positioned at a distance 2 m from the sensor (**Figure 2.S15a**, Supporting Information). The overlaid time-resolved reflectance spectra and temporal response to a 28 ppm $HF_{(g)}$ challenge (50% RH, in air) were obtained from the RDI–photonic crystal sensor (**Figure 2.S15b-c**, Supporting Information). Positive detection (95% confidence interval) was confirmed within 3 min of exposure.

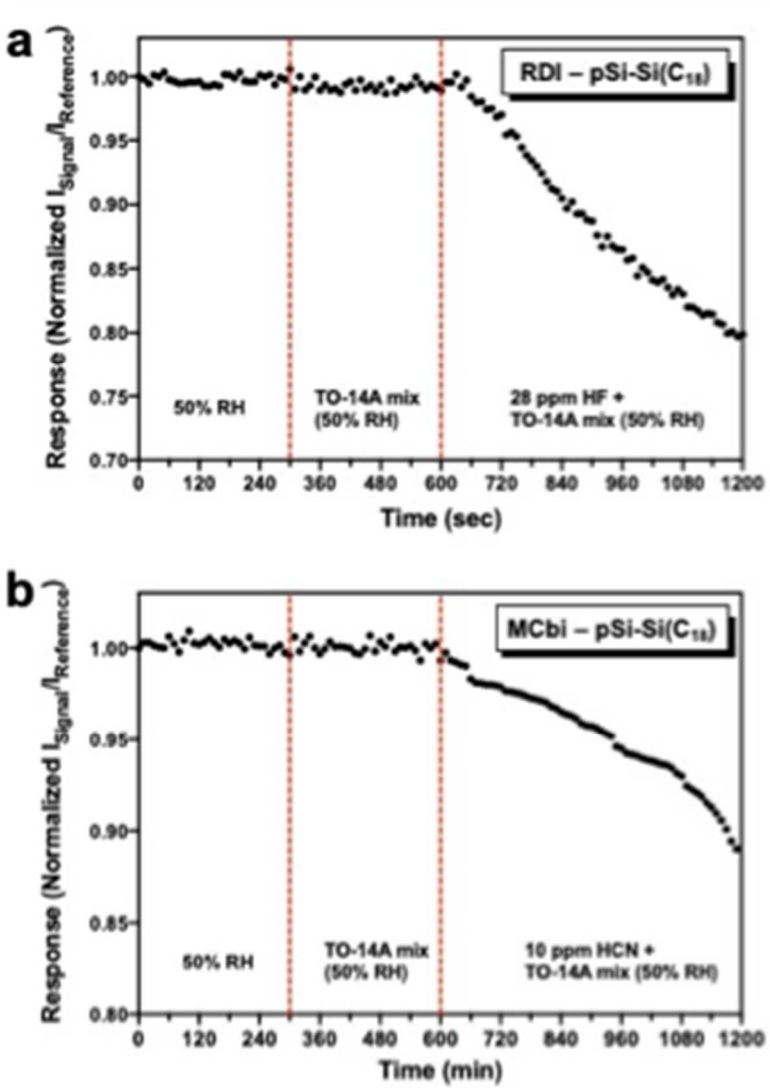

Figure 2.5: Detection of analytes within complex air mixture. Representative temporal response of (a) RDI – pSi-Si(C_{18}) and (b) MCbi – pSi-Si(C_{18}) photonic crystal sensors to sequential exposure of: 50% RH air (time = 0 to 300s); TO-14A analyte mixture in 50% RH air (time = 300 to 600s); 28 ppm HF (a) or 10 ppm HCN (b) in a carrier stream containing TO-14A analyte mixture in 50% RH air (time = 600 to 1200s). Each of the 43 VOC components of the TO-14A mixture was present in the air matrix at a nominal concentration of 0.5 ppm. The optical response (as defined in Eq. 2) were acquired every 10 sec.

2.3 Conclusion

In summary, this work showed that a colorimetric dye molecule can be embedded in a mesoporous photonic crystal to provide selective analyte detection that provides a higher degree of fidelity for remote detection by artificially narrowing the spectral

bandwidth of the dye. The synthesis of the photonic crystal allowed the creation of specific spectral reflectance signatures that could be engineered to match the dye and to provide a separate reflectance feature that was used as a reference channel in a ratiometric detection scheme. A hydrophobic surface chemistry based on dehydrocoupling of octadecylsilane provided a mesoporous nanostructure that retained sufficient porosity to host the indicator dye and to allow ingress of the gas-phase analytes, while suppressing zero-point drift due to fluctuations in relative humidity, which was established over the range 20-80% RH. The two types of sensors, RDI – pSi-Si(C_{18}) photonic crystal for HF and MCbi – pSi-Si(C_{18}) photonic crystal for HCN, were able to detect their analytes at levels below the NIOSH IDLH. Due to its similar indicator chemistry, which triggered on the presence of HF, the RDI – photonic crystal was also able to detect the fluorophosphonate nerve agent DFP at a level of 114 ppb. For irreversible indicator chemistries, such as the RDI dye used in this work to detect HF, the sensor displayed behavior similar to a dosimeter, where the rate of change in response scaled with concentration but reached a point of saturation at exposure times sufficiently long to allow reaction of the dye with the analyte to reach completion. Both types of sensors showed excellent selectivity for their target analyte over other interfering agents including NH_3, HCl, octane and a complex mixture of VOCs (EPA TO-14A).

2.4 Experimental Section

2.4A Materials

Single-crystal highly doped p-type (B-doped) silicon wafers of resistivity 0.8 – 1 mΩ-cm, polished on the (100) face, were purchased from Siltronix Corp. All reagents were used as received. Octadecylsilane ($H_3Si(CH_2)_{17}CH_3$) was purchased from Gelest, Inc. Diisopropyl fluorophosphonate was purchased from Sigma Aldrich, catalog #D0879 while the permeation tube was purchased from Kin-Tek Analytical, catalog # 143409, calibrated at a concentration of 0.228 ppm DFP (at a flow rate of 50 sccm). Pre-mixed hydrogen cyanide gas cylinders (10 and 20 ppm; balance gas nitrogen) were purchased from Gasco Inc. EPA TO-14A Calibration mix was purchased from Restek through Linde Spectra Environmental Gases, catalog # 34432 and contained 1 ppm of each component. All other chemical reagents were purchased from Sigma-Aldrich.

2.4B Instrumentation

Attenuated total reflectance Fourier transform infrared (ATR-FTIR) spectra were recorded on a Thermo Scientific Nicolet 6700 FTIR instrument fitted with a Smart iTR diamond ATR fixture. Scanning electron microscope (SEM) images were obtained with a Zeiss Sigma 500 in secondary electron imaging mode. Contact angles were measured using a Rame-Hart DROPimage CA v2.5 instrument. Reflected light spectra were obtained in the visible-NIR spectral range with an Ocean Optics USB-4000 CCD spectrometer and a tungsten-halogen illumination source (Ocean Optics LS-1) connected with a Y-branch 600 μm-diameter, bifurcated multimode optical fiber. The common end of the bifurcated fiber was focused with an objective lens to a ~1 mm^2 spot and positioned with the optic axis normal to the sample surface. UV-vis absorbance spectra were

obtained using a Molecular Devices SpectraMax 340PC384 Microplate Spectrophotometer with a 1-cm pathlength cuvette and 96-well microplate with normalized absorbance values to an equivalent 1-cm pathlength cuvette. 1H NMR analysis was performed on a Varian spectrometer running at 500 MHz, or a 300 MHz Bruker AVA. Mass spectrometry analysis was performed by the University of California San Diego Chemistry and Biochemistry Mass Spectrometry Facility (MMSF). The ESI-MS spectrum of Cbi was obtained using an Otribtrap Exactive mass spectrometer (Thermo Fisher, San Jose, CA, USA) with an ESI source at capillary temperature of 275 °C and spray voltage of 3.5 kV in positive ion mode. The spectra were acquired for m/z = 75-1500 using a maximum injection time of 50 ms and a resolution of 100,000. Prior to this, all the Cbi samples were diluted 50-fold with methanol containing 0.25% by mass formic acid. Diluted samples were directly infused into the mass spectrometer at a rate of 5 µL/min.

2.4C Preparation of pSi Photonic Crystals

The single-crystal Si wafers were diced into square chips of approx. 2 x 2 cm and mounted in a Teflon etching cell described elsewhere. The O-ring seal of the cell exposed 1.2 cm^2 of the Si surface to electrolyte. The chip was contacted on the backside with aluminum foil, and the counter-electrode consisted of a platinum coil. The chip was anodized in an electrolyte consisting of 3:1 (v:v) 48% aqueous hydrofluoric acid:ethanol (CAUTION: HF is highly toxic and can cause severe burns on contact with the skin or eyes). Prior to the preparation of the porous layers, the samples were cleaned using a “sacrificial etch” which consisted of etching a thin pSi layer into the chip (400 mA cm^{-2} applied for 50 s) in the above electrolyte, removing the electrolyte, rinsing the cell with

ethanol, and then dissolving this layer in strong base (2M aqueous KOH). The cell was then rinsed with water and ethanol, fresh aqueous HF:ethanol electrolyte was added, and the cleaned sample was anodized to prepare the photonic crystal. The anodization waveform for the photonic crystal was generated using LabView (National Instruments, Inc.), and the electric current was driven by a Keithley 2651A Sourcemeter power supply interfaced to the LabView program. The time-dependent current density waveforms, J(t), used in this work were created following the relationship of eq. 1, with J_{min} = 4.167 mA/cm^2, J_{max} = 60.0 mA/cm^2. For the HF and DFP sensors (RDI – pSi-Si(C_{18}) photonic crystal), values of T_1 = 6.6 s and T_2 = 9.8 s were used. For the HCN sensors (MCbi – pSi-Si(C_{18}) photonic crystal), values of T_1 = 8 s and T_2 = 9.8 s were used. The etching waveform was applied for 300 s. The as-etched samples were then chemically modified by subjecting them to a dehydrocoupling reaction with n-octadecylsilane: 500 µL of n-octadecylsilane, $H_3Si(CH_2)_{17}CH_3$, was introduced *via* microliter syringe to the pSi photonic crystal substrate in a 20 mL vial. The vial was sealed and immersed in a silicone oil bath at 80°C for 16 hours. The samples were then cooled, removed, and rinsed 3x with n-hexane and then 3x with ethanol.

2.4D Synthesis of Rhodamine 6G Imidazole (RDI)

Rhodamine 6G hydrazide was synthesized following the procedure previously described.[32, 33] Rhodamine 6G (2.40 g, 5 mmol) was dissolved in ethanol (60 mL). Hydrazine monohydride (8 mL, 160 mmol) was added and the reaction was maintained at reflux for 2 h then allowed to stir overnight at room temperature. The white precipitate was filtered and washed with water and ethanol to yield the product, rhodamine 6G hydrazide (1.68 g, 79%). The product was used for the next step without further

purification. To prepare rhodamine 6G imidazole (RDI), rhodamine 6G hydrazide (0.5 g, 1.17 mmol) was dissolved in methanol (10 mL). 2-formylimidazole was then added and the reaction was maintained at reflux overnight. The precipitate was filtered, washed with ethanol, and dried *in vacuo* (yield: 0.20 g, 35%).

2.4E Synthesis of Monocyanocobinamide

Pure aquohydroxocobinamide [$OH(H_2O)$Cbi], Co(III) was synthesized by base hydrolysis of hydroxocobalamin as described previously.[35] A stock solution of monocyanocobinamide ($CN(H_2O)$Cbi) was then prepared by reacting a 1:1 equimolar amount of aquohydroxocobinamide with KCN dissolved in deionized water in 1 M aqueous NaOH for 6h under mild agitation at room temperature, resulting in a dark red solution. Using a bench-top optical absorbance spectrometer (Molecular Devices Spectramax 340Pc384 Microplate Spectrophotometer), the distinct absorbance band at 475-520 nm confirmed the synthesis of monocyanocobinamide.

2.4F Loading of Colorimetric Indicators

For the RDI–photonic crystal sensors (HF or DFP analytes), the rhodamine–imidazole (RDI) complex was dissolved in a 1:1 (v:v) dichloromethane:acetonitrile mixture at a concentration of 1 mg/mL. A 100 µL aliquot of RDI was then drop-cast onto the pSi-Si(C_{18}) photonic crystal substrate and allowed to dry at room temperature. For HCN sensing, a monocyanocobinamide (MCbi) stock solution was diluted in ethanol until the concentration of the solution was 500 µM. A 100 µL aliquot of MCbi solution was subsequently drop-cast onto pSi-Si(C_{18}) photonic crystal substrates and allowed to dry at room temperature for ~5 h or until the ethanol solvent appeared fully evaporated.

2.4G VAPOR DOSING EXPERIMENTS

Analyte vapor challenges were prepared by dilution of analyte vapor streams of fixed concentration with dry or humidified compressed air, laboratory air, or nitrogen gas using digital mass flow controllers to obtain the desired concentration. For hydrogen fluoride, hydrogen chloride, and ammonia, aqueous solutions of these analytes were prepared at a given concentration, and the vapors were generated by bubbling the laboratory air through them. Details are provided in **Figure S8**, Supporting Information. Octane vapor was generated by bubbling the laboratory air though neat octane. For hydrogen cyanide and EPA TO-14A mix, the gas produced directly from the certified gas cylinder was mixed with humidified laboratory air to the desired concentration. The concentration of analytes were calculated based on their partial pressures at 25°C over the aqueous solution (for HF, HCl, and NH_3) or the neat liquid (for octane)[43-45]; the partial pressures of analyte vapors were then converted to concentration using eq 3:[46]

$$\text{Vapor concentration (ppm)} = \frac{P_{analyte}}{760\ mmHg} \times 10^6 \times \frac{F_{analyte}}{F_{analyte}+F_{dilution\ air}} \qquad (3)$$

Where $P_{analyte}$ is the partial pressure of the analyte vapor, in Torr, $F_{analyte}$ is the flow rate of the analyte vapor stream in sccm and $F_{dilution\ air}$ is the flow rate of the dilution air stream in sccm.

For the DFP experiments, the vapor was generated from a certified permeation tube (Kin-Tek Analytical, catalog # 143409) that was heated to 50 °C in a Metronics Inc. VICI Dynacalibrator Model 190 permeation oven, producing 228 ppb of DFP vapor in a nitrogen carrier gas. This was then mixed 1:1 (v:v) with humid laboratory air to achieve the desired humidity (50% RH) and analyte concentration (114 ppb). The RH values reported were verified with a probe hygrometer. The DFP sensing experiment was

conducted with a net flow rate of 100 sccm; all the other sensing experiments were conducted with a net flow rate of 300 sccm.

Reflectance spectra from the sensors were collected with a CCD spectrometer (Ocean Optics USB-4000) coupled to one branch of a bifurcated fiber optic cable. Light from a tungsten filament source was fed into the other branch of the fiber. The two branches were combined to a single fiber, and a focusing or a collimating lens was fitted to the distal end of this combined fiber and mounted 20 cm above or 2 m in front of the samples in the test chamber.

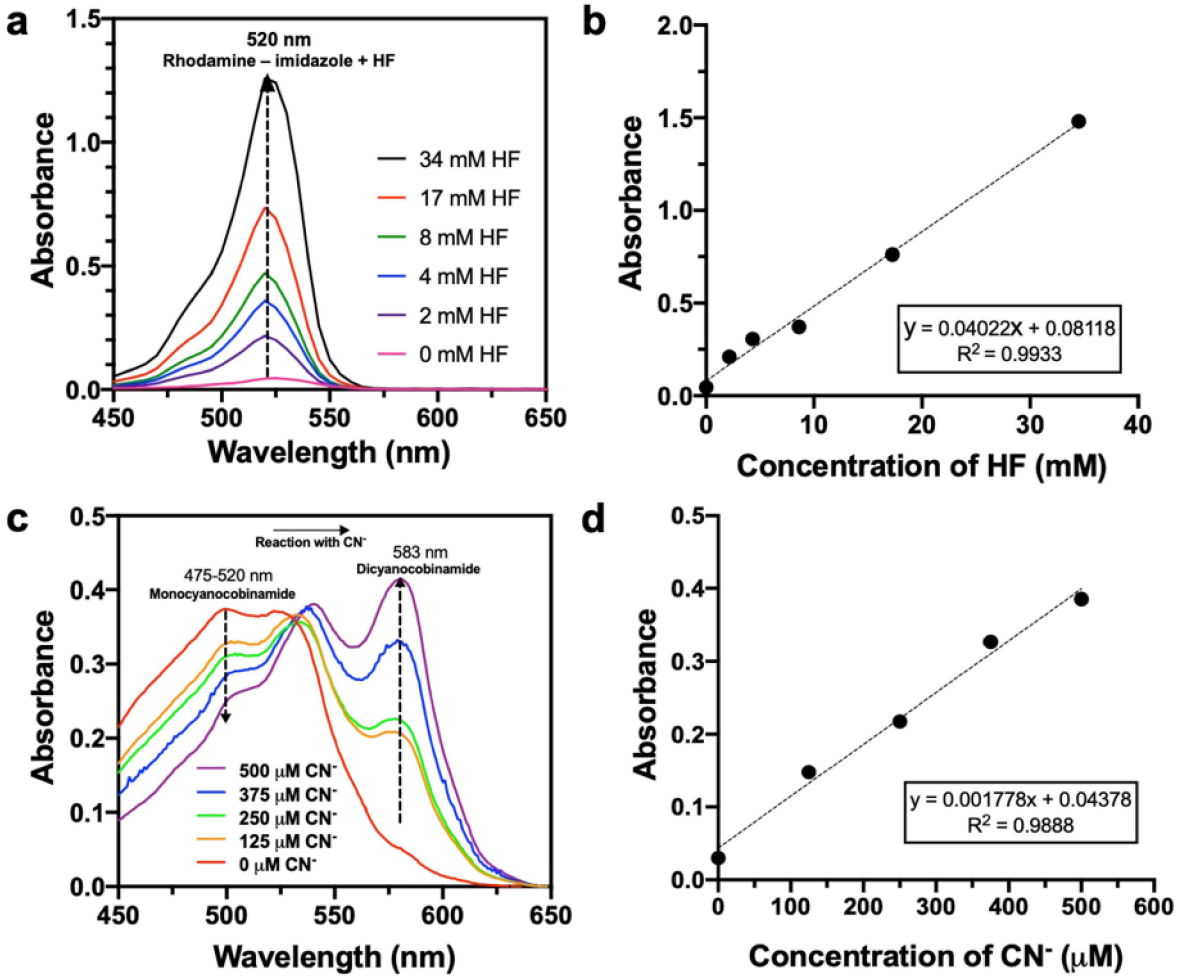

Figure 2.S1: UV-vis Absorbance Spectra of Indicator Dyes. (a) Series of UV-vis absorbance spectra of rhodamine – imidazole (RDI) indicator dye (2 mM) in 1:1 (v:v) acetonitrile:dichloromethane solution, upon titration with HF to the indicated values. (b) Dose-response curve extracted from (a), showing RDI absorbance at 520 nm as a function of HF concentration, over the range 0 – 34 mM. The measured molar extinction coefficient of RDI at 520 nm for the condition of [HF] = 34 mM is 40.22 M^{-1} cm^{-1}. (c) Series of UV-vis absorbance spectra of monocyanocobinamide (MCbi) indicator dye (500 μM) in water, upon titration with CN^- to the indicated values. (d) Dose-response curve extracted from (c), showing MCbi absorbance at 583 nm as a function of different concentrations of CN^- (0 – 500 μM). The measured molar extinction coefficient of MCbi at 520 nm for the condition of [CN^-] = 500 μM is 1778 M^{-1} cm^{-1}.

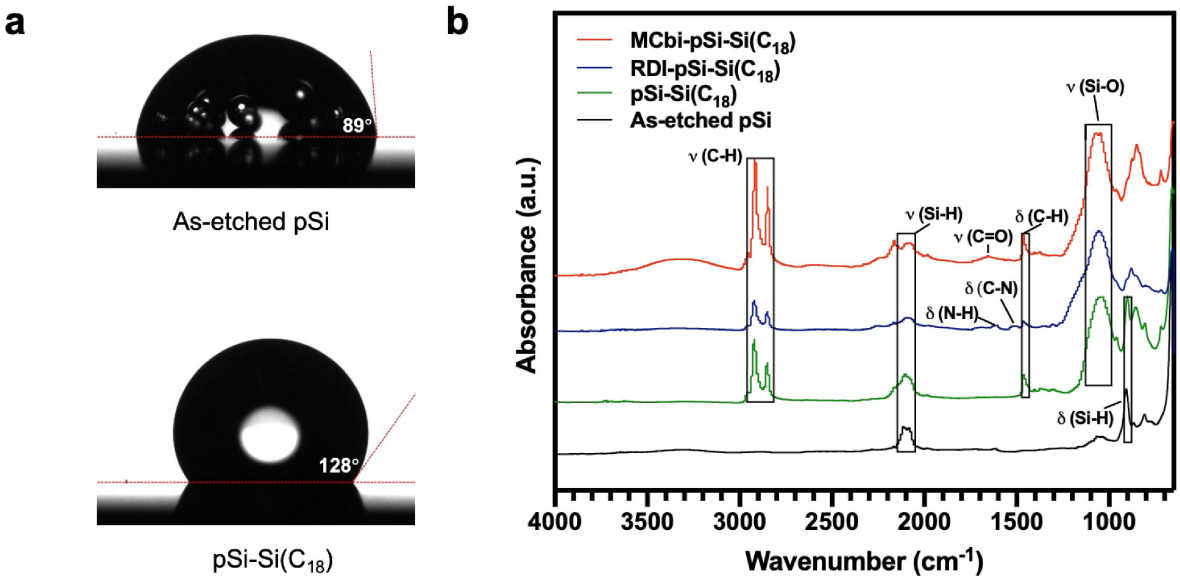

Figure 2.S2: Characterization of surface chemistry of RDI-pSi and MCbi-pSi photonic crystal sensors. (a) Images showing water contact angle on as-etched pSi and the chemically modified pSi-Si(C_{18}), prepared by thermal dehydrocoupling of octadecylsilane to pSi. Contact angle values reported are averages from 3 separate samples. Bubbles apparent in the image of the as-etched pSi sample are attributed to hydrogen, resulting from chemical reaction of pSi with water. (b) Attenuated total reflectance Fourier-transform infrared (ATR-FTIR) spectra of modified sensor samples, from bottom to top: As-etched pSi (black trace), pSi-Si(C_{18}) (green trace). RDI-pSi-Si(C_{18}) (blue trace) and Cbi-pSi-Si(C_{18}) (red trace). Symbols: $\boldsymbol{\nu}$ = stretching, $\boldsymbol{\delta}$ = bending.

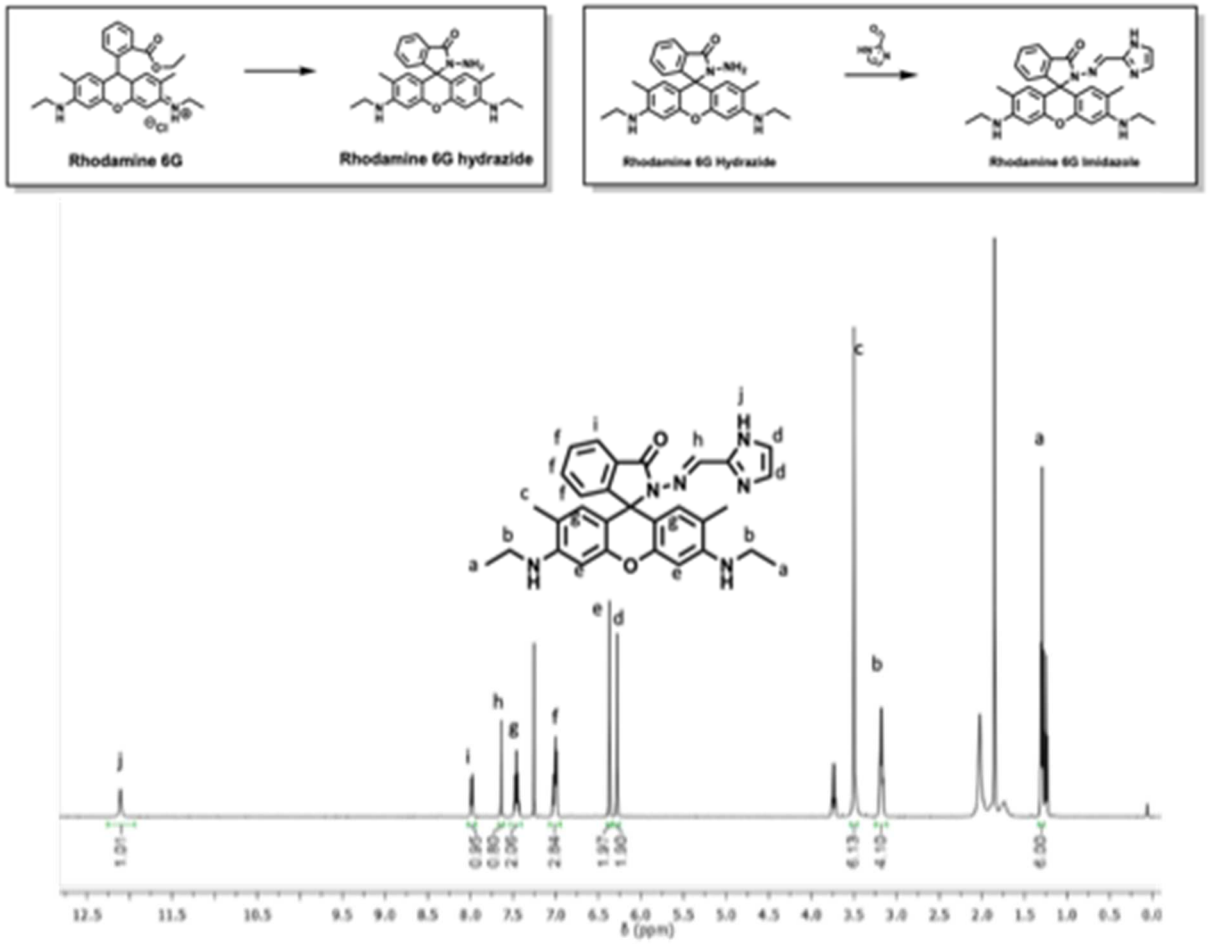

Figure 2.S3: Reaction scheme used for preparation of the rhodamine 6G-imidazole complex referred to in this work as "RDI" or "Rhodamine-imidazole" (above), and the ^{1}H NMR spectrum of the RDI product in $CDCl_3$ (below). Peak at 0 ppm is TMS reference. The synthesis of RDI followed the procedure described in the literature.[1, 2]

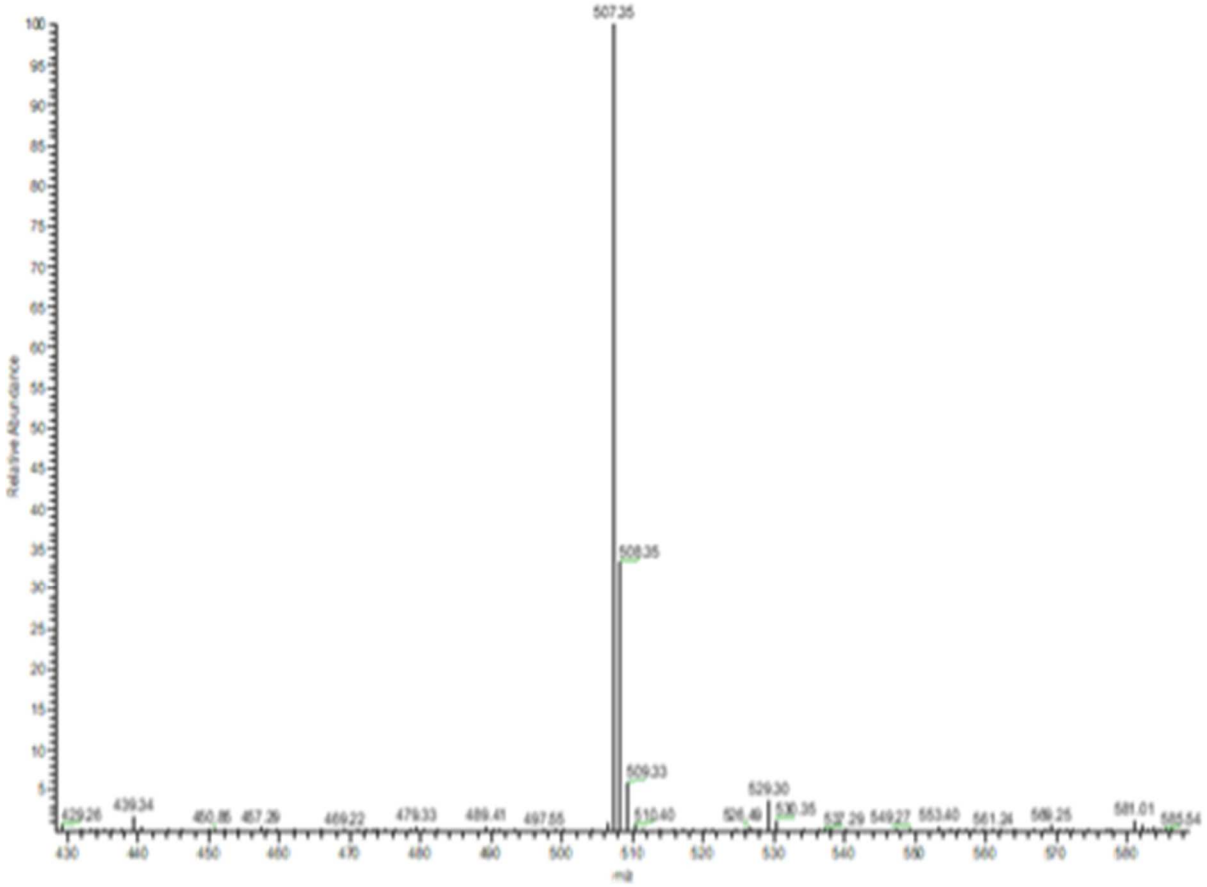

Figure 2.S4: ESI-MS spectrum of RDI. Ion at m/z = 507.35 is assigned to $[RDI+H]^+$ parent ion.

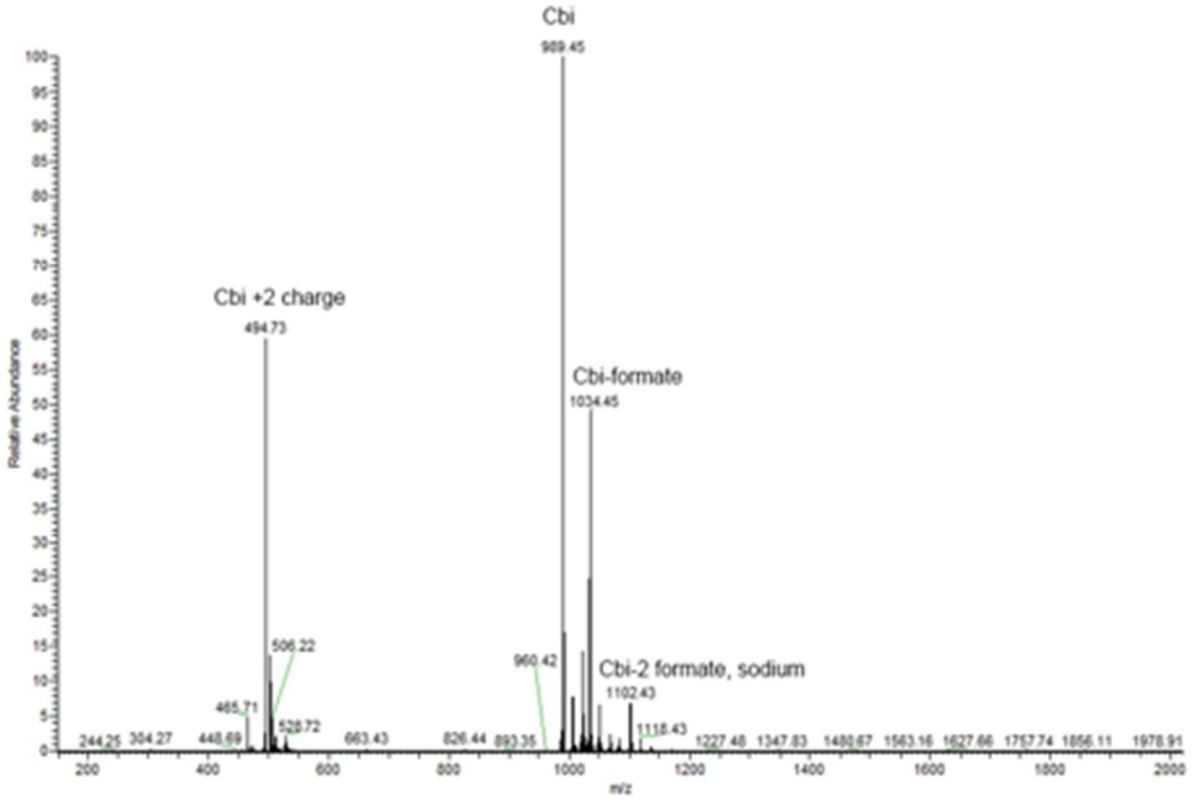

Figure 2.S5: ESI-MS spectrum of cobinamide, referred to in this work as “Cbi.” Parent ion, dipositive parent, and formate adducts assigned. Sodium formate was added to the sample prior to measurement to improve detection.

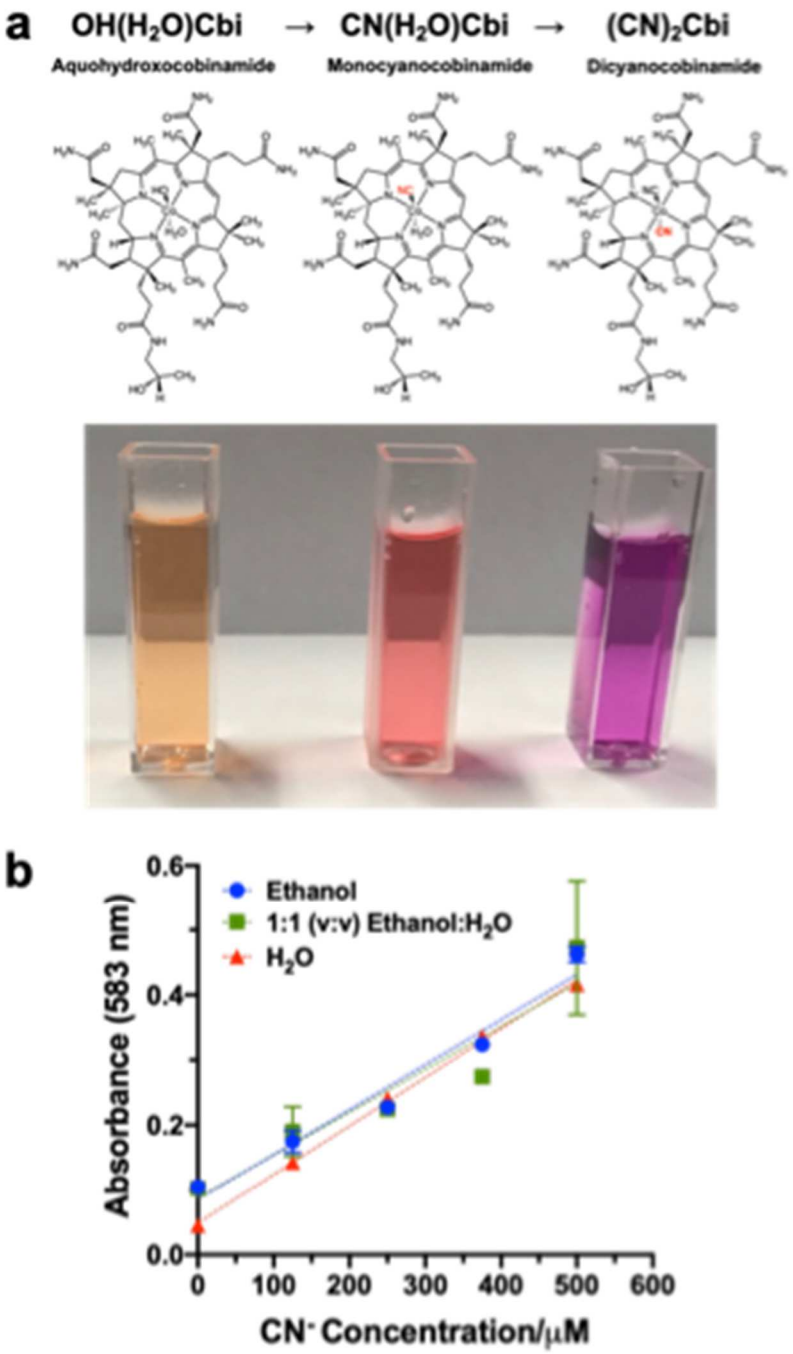

Figure 2.S6: Cobinamide's structure and absorbance properties. (a) Molecular structures of aquohydroxocobinamide, monocyanocobinamide and dicyanocobinamide. Photograph of corresponding cuvettes containing solutions of the three species is shown at the bottom. Monocyanocobinamide ("$CN(H_2O)Cbi$", or "MCbi") used in this work was prepared in-situ by reaction of an equimolar mixture of aquohydroxocobinamide and KCN. (b) Calibration curve showing MCbi absorbance at a wavelength of 583nm as a function of CN^- concentration (in micromolar; 0 – 500 μM) in water, 1:1 (v:v) ethanol:water mixture and ethanol. Data shown no significant solvatochromism. The error bars shown are the standard deviation of triplicate trials.

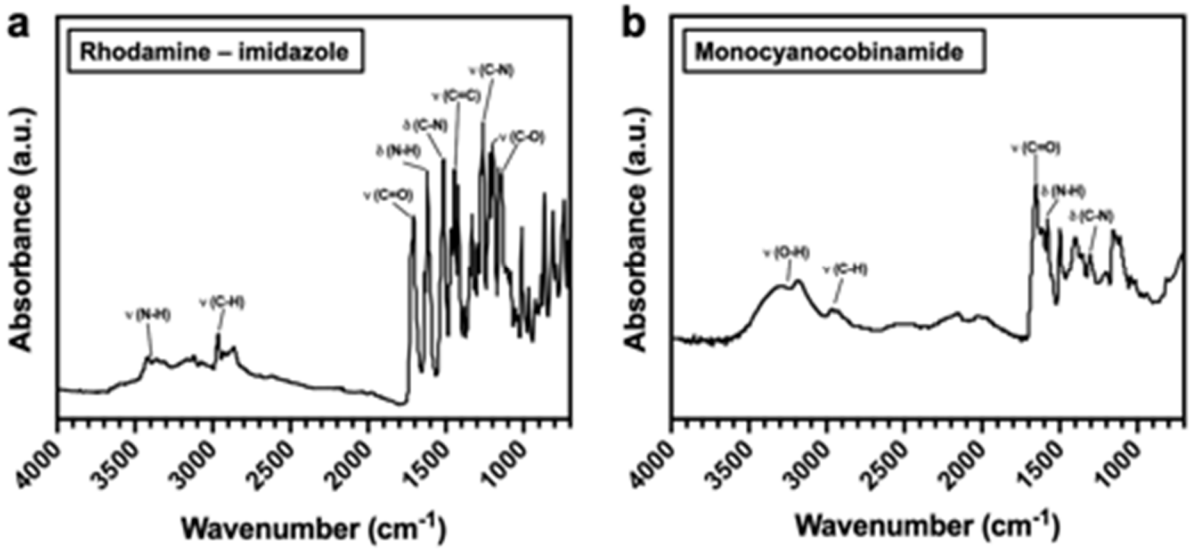

Figure 2.S7: Attenuated total reflectance Fourier-transform infrared (ATR-FTIR) spectra of (a) Rhodamine – imidazole (RDI) and (b) Monocyanocobinamide (MCbi). Spectra obtained from dry powder samples.

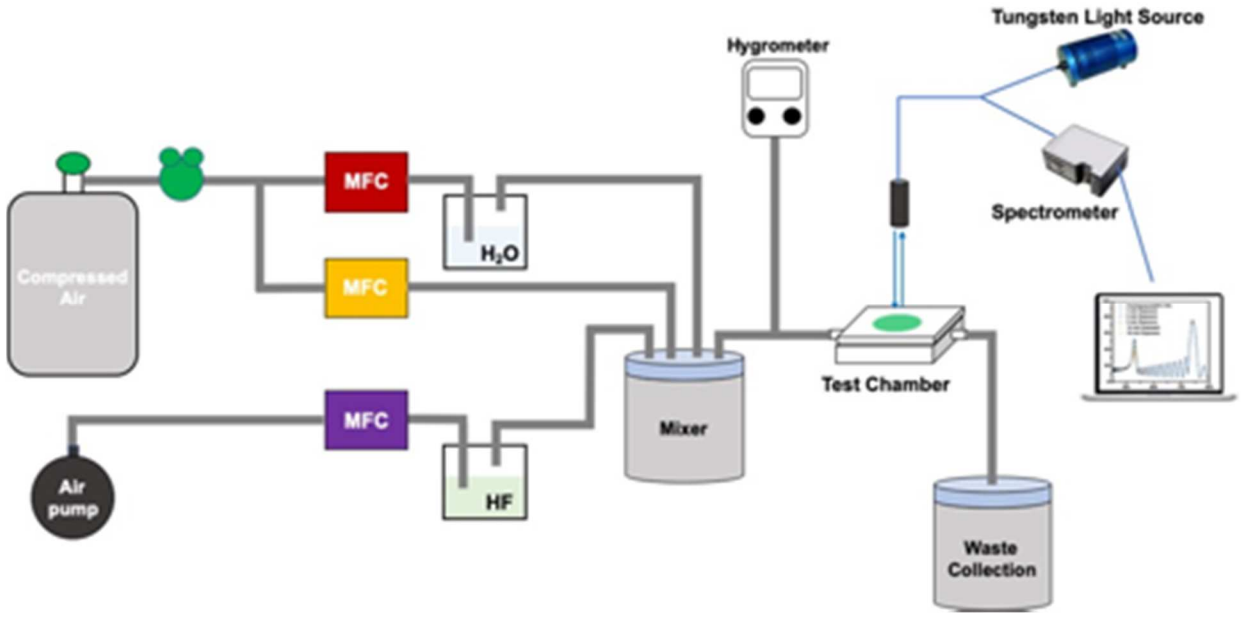

Figure 2.S8: Schematic of vapor dosing setup for HF, HCl, NH_3, and octane vapor sensing experiments (example for HF analyte is shown; the setup for the other analytes was similar). Mass Flow Controllers (MFC) enabled control of the overall analyte concentration, flow rate and % RH (which was measured with a commercial hygrometer). Mass flow rates of pure air, humid air (air bubbled through "H_2O" reservoir) and analyte (air bubbled through "HF" reservoir) were adjusted to obtain the desired values of humidity and analyte concentration in the "Mixer" chamber. The total flow rate of carrier gas for sensor dosing was 300 sccm. The volume of the mixer and testing chamber was approx. 500.0 cc; the concentration of analyte in the testing chamber was assumed to reach the steady-state, set-point concentration after 5 volumes had passed through the chamber, corresponding to 5 x 500.0/300sccm = 8.3 min.

Table 2.S1: Conversion of molar HF concentrations to its associated partial pressure (mmHg).

Concentration of HF solution (M)	Partial Pressure of HF Vapor (mmHg)
1.725	0.0598
0.575	0.0284
0.0575	0.0157

Table 2.S2: Conversion of molar HCl concentrations to its associated partial pressure (mmHg).

Concentration of HCl solution (M)	Partial Pressure of HCl Vapor (mmHg)
6	0.0903
7	0.231

Table 2.S3: Conversion of molar NH_3 concentrations to its associated partial pressure (mmHg).

Concentration of NH_3 solution (M)	Partial Pressure of NH_3 Vapor (mmHg)
0.00690	0.0844
0.00931	0.114
0.0310	0.380

The octane analyte was treated similarly, except that neat octane was used, and so the partial pressure of analyte in the carrier gas was assumed to be 11.8 mmHg[6] (the published vapor pressure of octane at 25 °C).

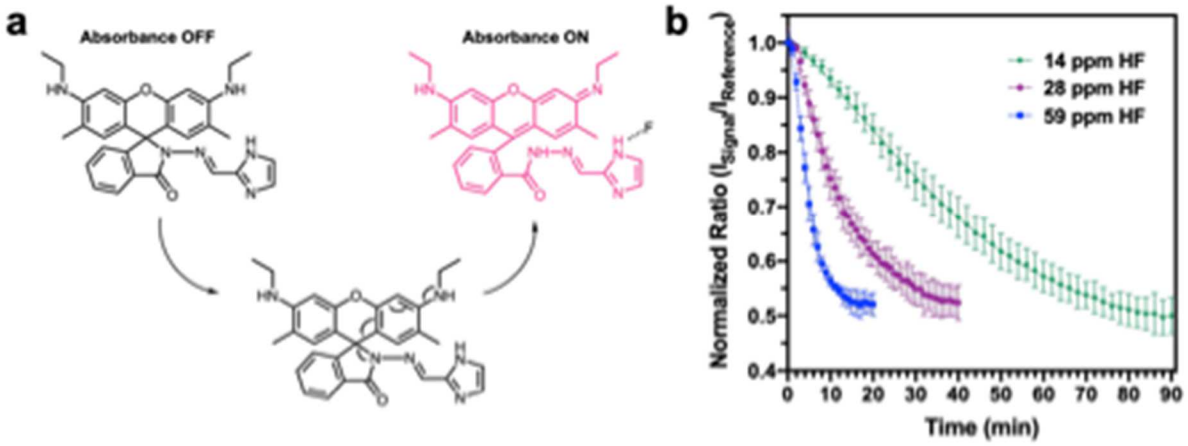

Figure 2.S9: (a) Reported mechanism of HF detection by Rhodamine (RDI)[2] and (b) Temporal response curves of RDI – pSi photonic crystal sensor with 14 – 59 ppm HF vapor under 50% RH. The data were acquired every two minutes and the error bars shown represent the standard deviation of triplicate trials.

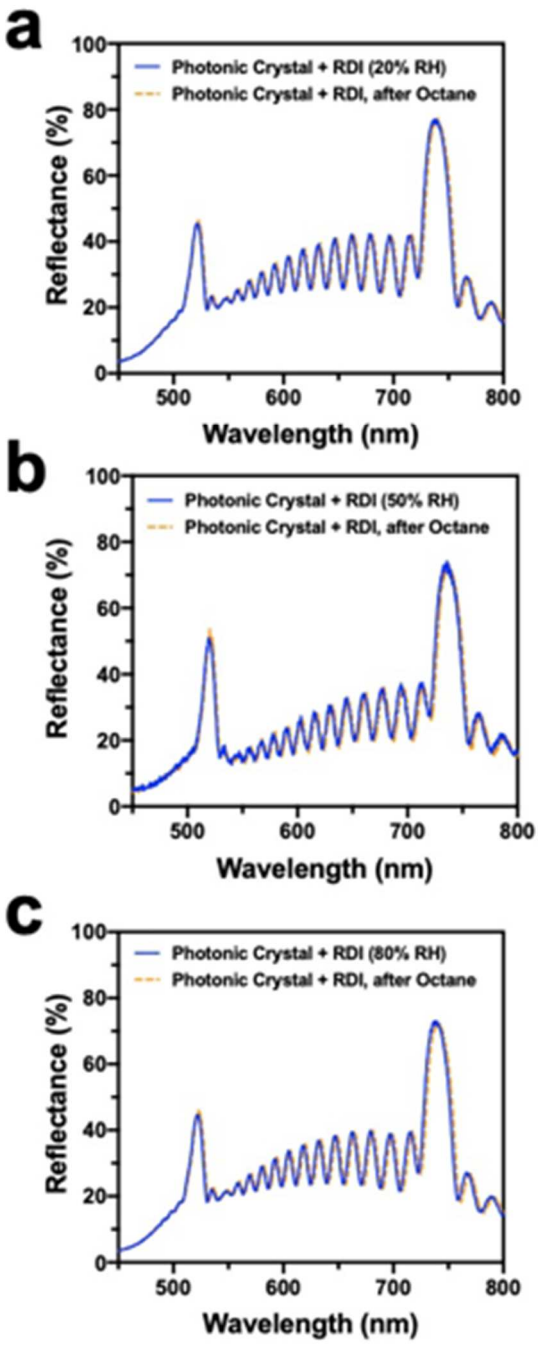

Figure 2.S10: Optical reflectance spectrum of RDI-photonic crystal sensor before and after exposure to 600 ppm Octane at (a) 20% RH, (b) 50% RH and (c) 80% RH for 10 minutes

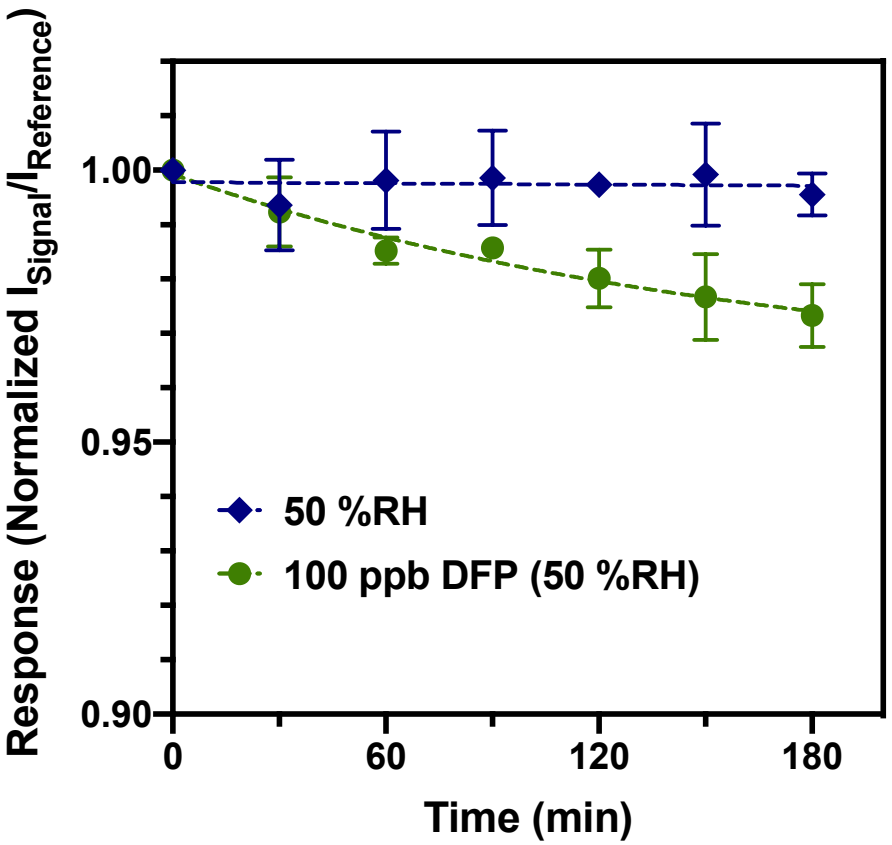

Figure 2.S11: Temporal response curve of RDI – pSi photonic crystal sensors to 100 ppb of DFP vapor under 50% RH. DFP vapor (228 ppb) was generated in a permeation tube oven at 50°C and diluted 1:1 v:v into humidified (100% RH) laboratory air, resulting in a final concentration of 114 ppb of DFP and 50% RH. The data were acquired every 30 minutes. The error bars shown are standard deviation of triplicate trials.

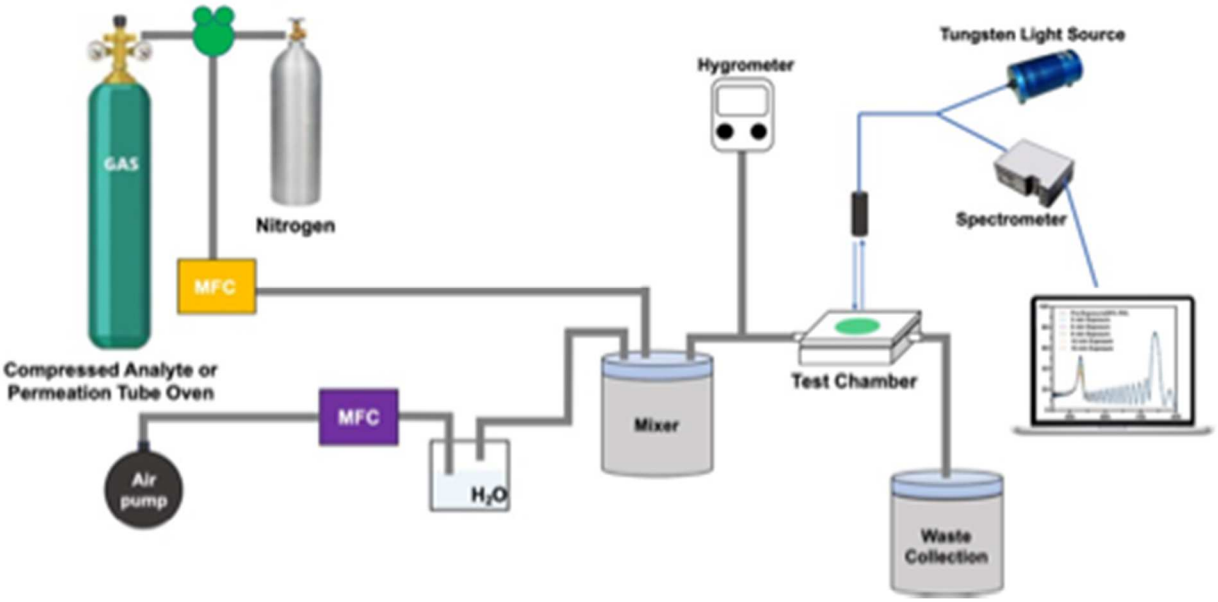

Figure 2.S12: Schematic of vapor dosing setup for HCN and DFP sensing. The source of HCN was a certified gas cylinder ("compressed analyte") containing either 10 or 20 ppm HCN in dry nitrogen. The source of DFP was a VICI Metronics Dynacalibrator Model 190 vapor generator that used certified permeation tubes from KIN-TEK Analytical, Inc. that contained DFP. The device was programmed to deliver 228 ppb of DFP vapor at 50 °C into dry nitrogen carrier gas. The RH values reported were monitored with a probe hygrometer. The HCN sensing experiments were conducted with a flow rate of 300 sccm, and the DFP sensing experiments were conducted with a flow rate of 100 sccm. The Mass Flow Controllers (MFC) enabled control of the overall analyte concentration, flow rate and % RH (which was measured with a commercial hygrometer). Mass flow rates of humid air (air bubbled through "H_2O" reservoir) and analyte (diluted with from calibrated gas cylinder or vapor generator as shown) were adjusted to obtain the desired values of humidity and analyte concentration in the "Mixer" chamber. The volume of the mixer and testing chamber was approx. 500.0 cc; the concentration of analyte in the testing chamber was assumed to reach the steady-state, set-point concentration after 5 volumes had passed through the chamber, corresponding to 5 x 500.0/300sccm = 8.3 min.

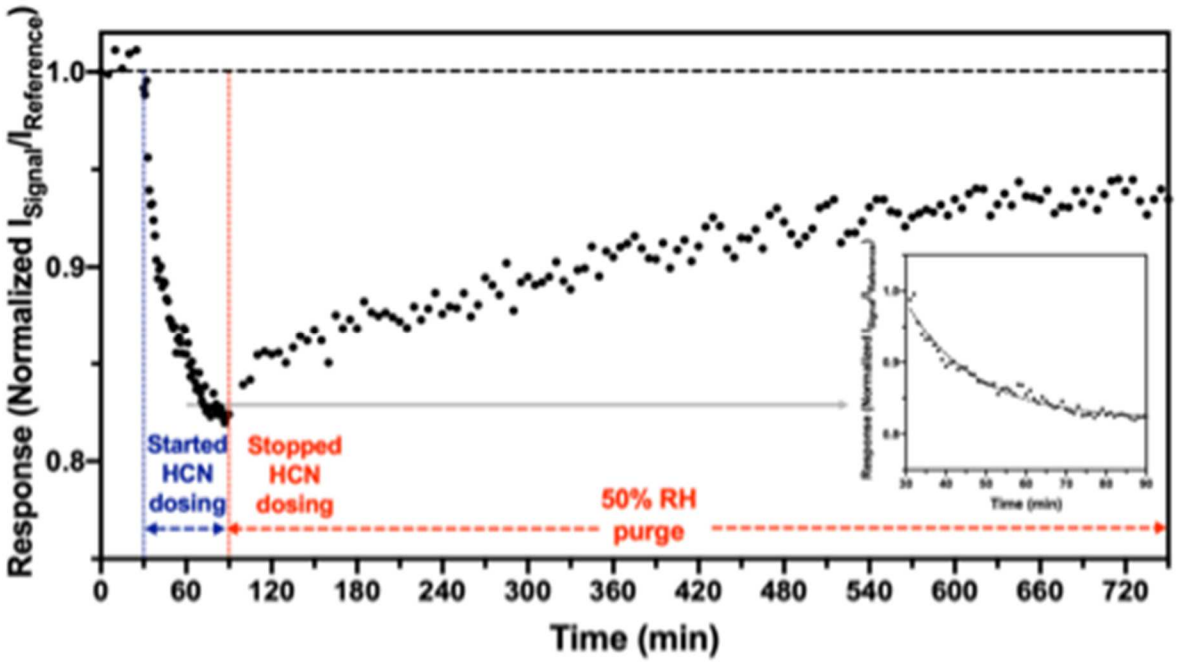

Figure 2.S13: Representative temporal response curve of a MCbi – pSi photonic crystal sensor to sequential exposure of 50% RH air (time = 0 to 30 min); 10 ppm of HCN vapor in 50% RH air; (time = 30 to 90 min); 50% RH purge (time = 90 to 750 min). The optical responses were acquired every min for the dosing of HCN vapor, and every 5 min for the conditions of 50% RH of air and 50% RH purge. The inset shows an expansion of the portion of the sensor response curve during exposure to 10 ppm HCN vapor in 50% RH (from time = 30 to 90 min).

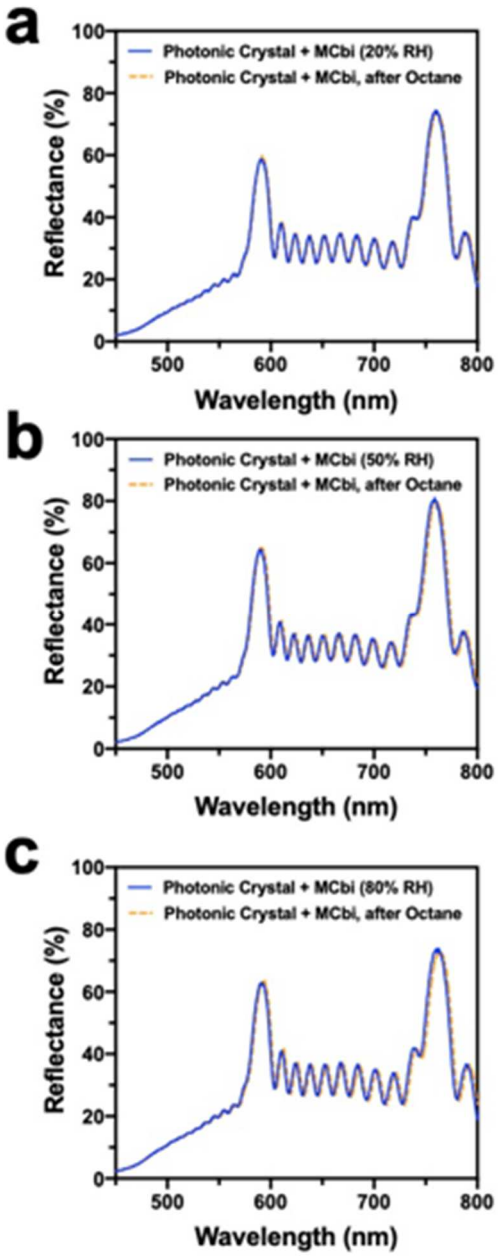

Figure 2.S14: Optical reflectance spectrum of MCbi-photonic crystal sensor before and after exposure to 600 ppm Octane at (a) 20% RH, (b) 50% RH and (c) 80% RH for 10 minutes.

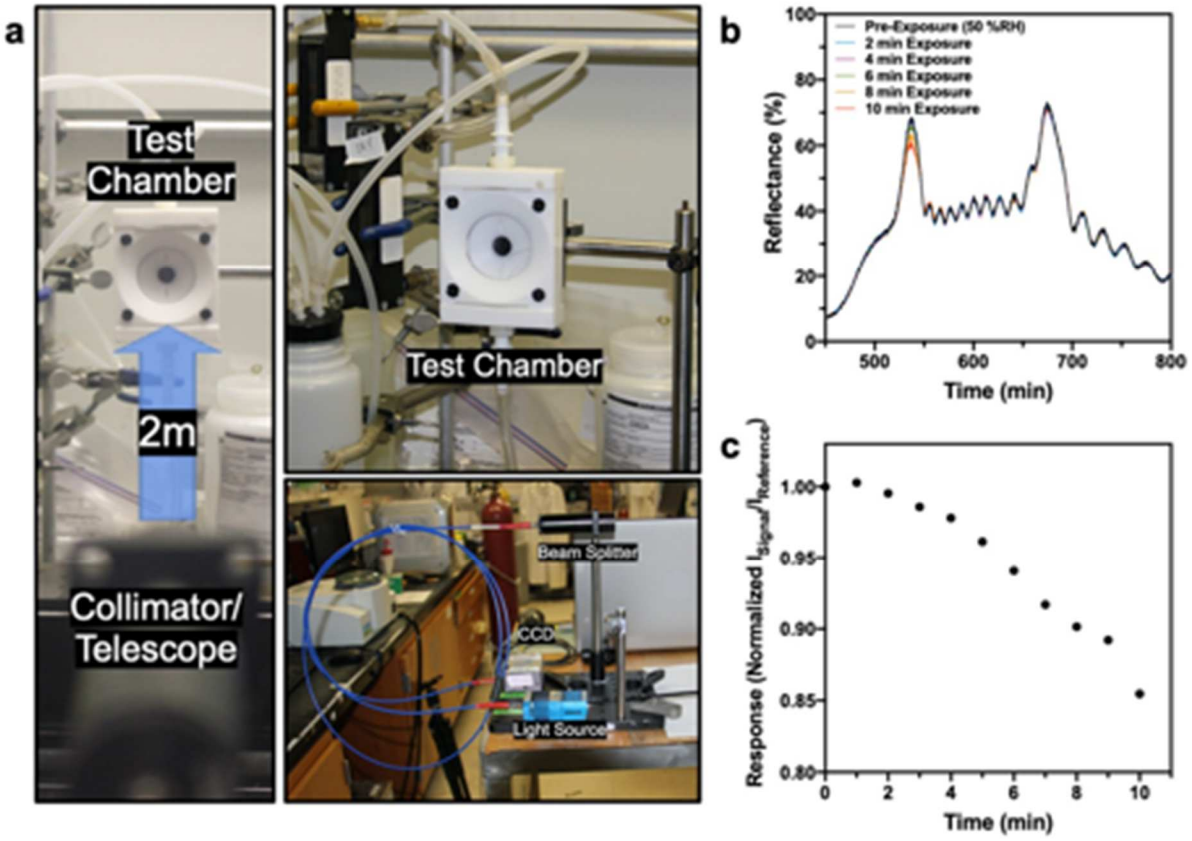

Figure 2.S15: Experimental setup and representative data for remote sensing of HF vapor. (a) Photographs of the remote sensing configuration. Fiber optic cables from a tungsten lamp (Light Source) and from a charge coupled device (CCD) spectrometer were combined into a dual bifurcated fiber, and the distal end was fed into collimator optics (Collimator/Telescope) positioned 2 meters from the pSi photonic crystal sensor, which was mounted in a test chamber fitted with an optical window. (b) Overlaid reflectance spectra, obtained at the indicated time points, for a RDI-pSi photonic crystal sensor exposed to 28 ppm of HF vapor at 0, 2, 4, 6, 8 and 10 minutes at 50% RH. (c) Temporal response (see eq. 2 in the text) of RDI – pSi photonic crystal sensor upon exposure to 28 ppm HF vapor in air at 50% RH.

2.6 Supporting Information – Literature Cited

1. Zhang, Z.; Zheng, Y.; Hang, W.; Yan, X.; Zhao, Y. Sensitive and selective off–on rhodamine hydrazide fluorescent chemosensor for hypochlorous acid detection and bioimaging. *Talanta* **2011,** *85*, 779-786.

2. Sivaraman, G.; Chellappa, D. Rhodamine based sensor for naked-eye detection and live cell imaging of fluoride ions. *J. Mater. Chem. B* **2013,** *1*, 5768-5772.

3. Brosheer, J.; Lenfesty, F.; Elmore, K. Vapor Pressure of Hydrofluoric Acid Solutions. *Ind. Eng. Chem.* **1947,** *39*, 423-427.

4. Fritz, J. J.; Fuget, C. R. Vapor Pressure of Aqueous Hydrogen Chloride Solutions, 0° to 50° C. *Ind. Eng. Chem. Chem. Eng. Data Series* **1956,** *1*, 10-12.

5. Clegg, S. L.; Brimblecombe, P. Solubility of ammonia in pure aqueous and multicomponent solutions. *J. Phys. Chem.* **1989,** *93*, 7237-7248.

6. Carruth, G. F.; Kobayashi, R. Vapor pressure of normal paraffins ethane through n-decane from their triple points to about 10 mm mercury. *J. Chem. Eng. Data* **1973,** *18*, 115-126.

2.7 Acknowledgements

Chapter 2, in full, is a reprint of the material as it appears in *ACS Sensors*, 2020. Lu, Y.S., Vijayakumar, S., Chaix, A., Pimentel, B., Bentz, K., Li, S., Chan, A., Whal, C., Ha, J., Hunka, D., Boss, G., Cohen, S., Sailor, M. "Remote Detection of HCN, HF, and Nerve Agent Vapors Based on Self-Referencing, Dye-Impregnated Porous Silicon Photonic Crystals". The dissertation author was a primary investigator and an author of this paper.

REFERENCES – CHAPTER 2

1. *NIOSH Pocket Guide to Chemical Hazards*; National Institute for Occupational Safety and Health of the United States: DHHS (NIOSH) Publication #2005-149: Cincinnati, Ohio, 2007.

2. Kim, K.; Tsay, O. G.; Atwood, D. A.; Churchill, D. G. Destruction and Detection of Chemical Warfare Agents. *Chem. Rev.* **2011,** *111*, 5345-5403.

3. Alcaraz, A., *Gas Chromatography/Mass Spectrometry in Analysis of Chemicals Relevant to the Chemical Weapons Convention Update based on the original article by Eric R.J. Wils. In Encyclopedia of Analytical Chemistry, Meyers, R.A.; Meyers, R.A., Eds. John Wiley & Sons, Ltd.: New Jersey, 2012*. DOI: 10.1002/9780470027318.a0405.pub2.

4. Mäkinen, M. A.; Anttalainen, O. A.; Sillanpää, M. E. T. Ion Mobility Spectrometry and Its Applications in Detection of Chemical Warfare Agents. *Anal. Chem.* **2010,** *82*, 9594-9600.

5. Mosier-Boss, P. A. Review of SERS Substrates for Chemical Sensing. *Nanomaterials* **2017,** *7*, 142.

6. Kondo, T.; Hashimoto, R.; Ohrui, Y.; Sekioka, R.; Nogami, T.; Muta, F.; Seto, Y. Analysis of chemical warfare agents by portable Raman spectrometer with both 785nm and 1064nm excitation. *Forensic Sci. Int.* **2018,** *291*, 23-38.

7. Hodgkinson, J.; Tatam, R. P. Optical gas sensing: a review. *Meas. Sci. Technol.* **2012,** *24*, 012004.

8. U.S. Department of Homeland Security, System Assessment and Validation for Emergency Responders (SAVER): Portable Infrared Spectroscopy Chemical Detectors Assessment Report. Richland, WA, 2016.

9. Grate, J. W. Acoustic Wave Microsensor Arrays for Vapor Sensing. *Chem. Rev.* **2000,** *100*, 2627-2648.

10. Janata, J.; Josowicz, M. Conducting polymers in electronic chemical sensors. *Nat. Mater* **2003,** *2*, 19-24.

11. Wetchakun, K.; Samerjai, T.; Tamaekong, N.; Liewhiran, C.; Siriwong, C.; Kruefu, V.; Wisitsoraat, A.; Tuantranont, A.; Phanichphant, S. Semiconducting metal oxides as sensors for environmentally hazardous gases. *Sens. Actuators B Chem.* **2011,** *160*, 580-591.

12. Zhou, X.; Lee, S.; Xu, Z.; Yoon, J. Recent Progress on the Development of Chemosensors for Gases. *Chem. Rev.* **2015,** *115*, 7944-8000.

13. Liu, Y.; Hu, Y.; Lee, S.; Lee, D.; Yoon, J. Fluorescent and Colorimetric Chemosensors for Anions, Metal Ions, Reactive Oxygen Species, Biothiols, and Gases. *Bull. Korean Chem. Soc.* **2016,** *37*, 1661-1678.

14. Chen, L.; Wu, D.; Yoon, J. Recent Advances in the Development of Chromophore-Based Chemosensors for Nerve Agents and Phosgene. *ACS Sens.* **2018,** *3*, 27-43.

15. Lim, S. H.; Feng, L.; Kemling, J. W.; Musto, C. J.; Suslick, K. S. An optoelectronic nose for the detection of toxic gases. *Nat. Chem.* **2009,** *1*, 562-567.

16. Davidson, C. E.; Dixon, M. M.; Williams, B. R.; Kilper, G. K.; Lim, S. H.; Martino, R. A.; Rhodes, P.; Hulet, M. S.; Miles, R. W.; Samuels, A. C.; Emanuel, P. A.; Miklos, A. E. Detection of Chemical Warfare Agents by Colorimetric Sensor Arrays. *ACS Sens.* **2020,** *5*, 1102-1109.

17. Liu, X.; Cheng, S.; Liu, H.; Hu, S.; Zhang, D.; Ning, H. A survey on gas sensing technology. *Sensors* **2012,** *12*, 9635-9665.

18. Hou, C.; Li, J.; Huo, D.; Luo, X.; Dong, J.; Yang, M.; Shi, X. A portable embedded toxic gas detection device based on a cross-responsive sensor array. *Sens. Actuators B Chem.* **2012,** *161*, 244-250.

19. Devadhasan, J. P.; Kim, D.; Lee, D. Y.; Kim, S. Smartphone coupled handheld array reader for real-time toxic gas detection. *Anal. Chim. Acta* **2017,** *984*, 168-176.

20. Askim, J. R.; Suslick, K. S. Hand-Held Reader for Colorimetric Sensor Arrays. *Anal. Chem.* **2015,** *87*, 7810-7816.

21. Kassal, P.; Horak, E.; Sigurnjak, M.; Steinberg, M. D.; Steinberg, I. M. Wireless and mobile optical chemical sensors and biosensors. *Rev. Anal. Chem* **2018,** *37*, 20170024.

22. Luka, G. S.; Nowak, E.; Kawchuk, J.; Hoorfar, M.; Najjaran, H. Portable device for the detection of colorimetric assays. *R Soc Open Sci* **2017,** *4*, 171025-171025.

23. Switkes, M.; Ervin, B. L.; Kingsborough, R. P.; Rothschild, M.; Sworin, M. Retroreflectors for remote readout of colorimetric sensors. *Sens. Actuators B Chem.* **2011,** *160*, 1244-1249.

24. King, B. H.; Gramada, A.; Link, J. R.; Sailor, M. J. Internally Referenced Ammonia Sensor Based on an Electrochemically Prepared Porous SiO2 Photonic Crystal. *Adv. Mater.* **2007,** *19*, 4044-4048.

25. Garcia Sega, A.; King, B. H.; Lee, J. Y.; Sailor, M. J.; Miskelly, G. M. Thermally Modulated Porous Silica Multispectral Filters and Their Application in Remote Imaging. *ACS Nano* **2013,** *7*, 7785-7794.

26. Ruminski, A. M.; Barillaro, G.; Chaffin, C.; Sailor, M. J. Internally Referenced Remote Sensors for HF and Cl2 Using Reactive Porous Silicon Photonic Crystals. *Adv. Funct. Mater.* **2011,** *21*, 1511-1525.

27. Leacock-Johnson, A.; Garcia Sega, A.; Sharief, A.; Sailor, M. J.; Miskelly, G. M. Real-time 1D hyperspectral imaging of porous silicon-based photonic crystals with one-dimensional chemical composition gradients undergoing pore-filling-induced spectral shifts. *Sens. Actuator A Phys.* **2013,** *203*, 154-159.

28. Weiss, S. M.; Molinari, M.; Fauchet, P. M. Temperature stability for silicon-based photonic band-gap structures. *Appl. Phys. Lett.* **2003,** *83*, 1980-1982.

29. Sailor, M. J. *Porous Silicon in Practice: Preparation, Characterization, and Applications*. Wiley-VCH: Weinheim, Germany, 2012.

30. Ruminski, A. M.; King, B. H.; Salonen, J.; Snyder, J. L.; Sailor, M. J. Porous Silicon-Based Optical Microsensors for Volatile Organic Analytes: Effect of Surface Chemistry on Stability and Specificity. *Adv. Funct. Mater.* **2010,** *20*, 2874-2883.

31. Ruminski, A. M.; Moore, M. M.; Sailor, M. J. Humidity-Compensating Sensor for Volatile Organic Compounds Using Stacked Porous Silicon Photonic Crystals. *Adv. Funct. Mater.* **2008,** *18*, 3418-3426.

32. Kim, D.; Joo, J.; Pan, Y.; Boarino, A.; Jun, Y. W.; Ahn, K. H.; Arkles, B.; Sailor, M. J. Thermally Induced Silane Dehydrocoupling on Silicon Nanostructures. *Angew. Chem. Int. Ed.* **2016,** *55*, 6423-6427.

33. Zhang, Z.; Zheng, Y.; Hang, W.; Yan, X.; Zhao, Y. Sensitive and selective off–on rhodamine hydrazide fluorescent chemosensor for hypochlorous acid detection and bioimaging. *Talanta* **2011,** *85*, 779-786.

34. Sivaraman, G.; Chellappa, D. Rhodamine based sensor for naked-eye detection and live cell imaging of fluoride ions. *J. Mater. Chem. B* **2013,** *1*, 5768-5772.

35. Greenawald, L. A.; Snyder, J. L.; Fry, N. L.; Sailor, M. J.; Boss, G. R.; Finklea, H. O.; Bell, S. Development of a cobinamide-based end-of-service-life indicator for detection of hydrogen cyanide gas. *Sens. Actuators B Chem.* **2015,** *221*, 379-385.

36. Ma, J.; Dasgupta, P. K.; Zelder, F. H.; Boss, G. R. Cobinamide chemistries for photometric cyanide determination. A merging zone liquid core waveguide cyanide analyzer using cyanoaquacobinamide. *Anal. Chim. Acta* **2012,** *736*, 78-84.

37. Manning, J. A.; Burckle, J. O.; Hedges, S.; McElro, F. F. *Compendium of Methods for the Determination of Toxic Organic Compounds in Ambient Air Second Edition, Compendium Method TO-14A*. Environmental Protection Agency: 1999.

38. Hammond, P.; Forster, J. A polymeric amine–copper(II) complex as catalyst for the hydrolysis of 1,2,2-trimethylpropyl methylphosphonofluoridate (soman) and bis (1-methylethyl) phosphorofluoridate (DFP). *J. Appl. Polym. Sci.* **1991,** *43*, 1925-1931.

39. Misik, J.; Pavlikova, R.; Cabal, J.; Kuca, K. Acute toxicity of some nerve agents and pesticides in rats. *Drug Chem. Toxicol.* **2015,** *38*, 32-36.

40. Kilpatrick, M.; Kilpatrick, M. L. The Hydrolysis of Diisopropyl Fluophosphate. *J. Phys. Colloid Chem.* **1949,** *53*, 1371-1384.

41. Baldwin, D. S.; Beattie, J. K.; Coleman, L. M.; Jones, D. R. Phosphate Ester Hydrolysis Facilitated by Mineral Phases. *Environ. Sci. Technol.* **1995,** *29*, 1706-1709.

42. Greenawald, L. A.; Boss, G. R.; Snyder, J. L.; Reeder, A.; Bell, S. Development of an Inexpensive RGB Color Sensor for the Detection of Hydrogen Cyanide Gas. *ACS Sens.* **2017,** *2*, 1458-1466.

43. Brosheer, J.; Lenfesty, F.; Elmore, K. Vapor Pressure of Hydrofluoric Acid Solutions. *Ind. Eng. Chem.* **1947,** *39*, 423-427.

44. Fritz, J. J.; Fuget, C. R. Vapor Pressure of Aqueous Hydrogen Chloride Solutions, O° to 50° C. *Ind. Eng. Chem. Chem. Eng. Data Series* **1956,** *1*, 10-12.

45. Clegg, S.; Brimblecombe, P. Solubility of ammonia in pure aqueous and multicomponent solutions. *J. Phys. Chem.* **1989,** *93*, 7237-7248.

46. Woodfin, W. J.; National Institute for Occupational, S.; Health; Division of Physical, S.; Engineering; United, S.; National Technical Information, S. *Gas and vapor generating systems for laboratories*. U.S. Dept. of Health, Education and Welfare, Public Health Service, Center for Disease Control, National Institute for Occupational Safety and Health, Division of Physical Sciences and Engineering: Cincinnati, Ohio, 1984.

CHAPTER 3

PHOTONIC POROUS SILICON SENSOR WITH INTEGRATED BIOLOGICAL GATEKEEPER FOR REMOTE DETECTION OF HCN VAPORS

3.1 ABSTRACT

The most common objectives of biological and synthetic gatekeeping systems include the containment and protection of sensitive cargo behind the “gate” until triggered by a specific external environmental stimulus. An inverted, and less common, perspective on these gatekeeping functions involves the selective entrance of a particular substance into a porous host. This idea, in which specific classes of target analytes are distinguished from external clutter, is of major utility in chemical sensors in real-world environments (i.e., outside of controlled laboratory settings). However, the stringency of the gatekeeping criterion becomes very important, for example, in industrial settings which require careful monitoring for the presence of noxious agents among chemically complex multi-component atmospheres, where sensing fidelity can become a determinant of life-or-death situations. Here we report the design and characterization of an HCN-selective, one-dimensional porous silicon (pSi) photonic optical sensor reinforced with a stimuli-responsive biological framework, which serves as a protective coating against a broad range of chemical species, that is rendered semi-permeable only in the presence of the prescribed target, hydrogen cyanide (HCN). Reliable detection was achieved for minute quantities (10 ppm) of HCN, even in the presence of significant quantities of non-target interferents, exhibiting a rapid temporal response that could be remotely quantified by optical measurement. These capabilities were achieved through the careful exploitation of both the highly tunable spectral properties of the pSi substrate embedded with a specific colorimetric dye, tuned to HCN, and the precision afforded by biomolecular re-

engineering of protein-based materials. This approach is insensitive to potential interferents such as hexane, nitrogen, ammonia, and the 43-component mixture of VOCs known as EPA TO-14A, and to variations in relative humidity (20−80% RH). Detection of HCN spiked into the complex mixture EPA TO-14A is demonstrated. The results suggest that this strategy should be broadly applicable for the rational design of new gatekeeper-coated bio-inorganic sensors capable of detecting arbitrary analytes with high precision.

3.2 Main Text

The ability to regulate permeability with high specificity is widespread in biological systems and a highly desirable property in many classes of functional materials, such as those used for drug delivery.[1-6] Recently, there has been great progress towards the development of synthetic “gatekeeper” modalities including polymers, inorganic nanomaterials, host-guest assemblies, and biomacromolecules that respond to stimuli such as changes in pH, redox potential, temperature, light irradiation, competitive binding, and catalytic degradation[6-12]. In drug delivery applications, where these gatekeepers have primarily been employed, therapeutic agents are sealed within porous structures that localize to targeted regions before releasing their payload into the surrounding tissue in response to environmental stimuli (**Figure 3.1a)**.[1, 2, 10] However, many of these triggers are quite general, and can be nonspecific depending on the environment. In contrast, biological gatekeepers are extremely specific, such as the protein channels and pumps that regulate ion transport across lipid bilayers, where the placement of chemical groups can selectively distinguish and differentiate ions with elemental accuracy based on properties of size differences and hydration structures.[3-5, 13] Thus, biomolecular

membrane systems could provide significantly greater stringency in their selective permeability to specific species of interest.

In contrast to the use of gatekeepers to regulate molecular release, the inverse approach of controlling entry of specific species could find direct application in the field of sensing, particularly in cases such as environmental monitoring, where passive sensors are continuously exposed to non-target analytes. This can lead to “cluttering” of the absorbent, compounding interference from temperature and humidity fluctuations and/or saturation of the sensor, leading to decreased performance over relatively short time periods. While reduced sensitivity or false-positive readings may be tolerable in specific use cases, these effects would significantly undercut real-world utility as passive sensors or environmental monitors. Thus, it should be possible to create robust passive sensors consisting of high-sensitivity detection modalities enveloped by physical, chemical, or biological gatekeeper functionalities that toggle their structural porosity to allow entry in response to a specified individual (or class of) analyte. In this way, sensing is initiated by the target, directly “activating” the device for molecular intake by permitting selective infiltration into the absorbent bed while ignoring ambient “clutter”.

Recent examples of gatekeeper modalities include synthetic polymer or lipid membranes, DNA, peptide and carbon nanotubes, transition metals and peptide-based membrane transporters and organic and metal-organic frameworks.[6-12, 14, 15] Despite the chemical and structural variety of these gatekeepers, their current use cases are limited towards the selective transport of protons and ions in specific solution-based settings. Although these synthetic gatekeepers are unable to rival the performance that is seen in their biological counterparts, they highlight the promising future applications in chemical

sequestering and sensing that has made this concept ideal for industrial and military applications, seeking improvement upon current sensors where selective gatekeepers are not used.

In our recent earlier work, we have developed a self-referenced vapor sensor for the selective detection of hydrogen cyanide (HCN) based on a one-dimensional photonic crystal prepared from porous silicon (pSi) impregnated with a colorimetric indicator dye, cobinamide (Cbi), that is highly specific for HCN.[16] These photonic crystal sensors were shown to detect HCN facilely and reliably at concentrations down to 5 ppm within 10 minutes of vapor exposure, with a readout visible from 2 m. Despite the convincing demonstration of this remote sensing concept for HCN, we observed that the presence of non-target clutter yielded nonspecific saturation and interference with the photonic crystals, leading to inconsistent responses to HCN in “real-world” complex air samples. We realized that this sensing system is ideal for developing an HCN-selective gatekeeper, as it provides a sensitive readout to the intrusion non-target analytes while otherwise providing high fidelity detection appropriate for deployment. Thus, we set out to augment this platform with a selectively permeable coating to gate entry to the sensor, preventing non-specific clutter from changing the index of the porous silicon substrates that produces false-positive and inconsistent read-outs from the photonic crystal sensor. Inspired by the specificity of biological systems, we elected to employ an engineered two-dimensional protein crystal (whose porosity can be toggled by specific analytes) as our gatekeeper to create a novel bio-inorganic heterojunction with robust sensing capabilities.[17]

Previous work with gatekeepers, as well as the relevant photonic crystal sensor and gatekeeper concepts described above, are outlined in **Figure 3.1**. Our HCN-sensing

pSi photonic crystals were prepared as described previously.[16] Briefly, electrochemical anodization of highly-doped p^{++} single crystal Si wafers in an aqueous ethanolic hydrofluoric acid solution using a composite current-density-time waveform produced two distinct optical peaks, or stop-bands, in the reflection spectrum of the crystal that would act as “reference” and “signal” channels due to their difference wavelengths.[16, 18, 19] The signal channel was determined empirically, per previous experiments, to match the Cbi indicator dye. Cbi is a Vitamin B12 analog with very high affinity and rapid binding kinetics for CN^- as an indicator dye. Upon complexation with CN^-, Cbi undergoes a colorimetric shift from red to purple, with a major absorption peak emerging at ~595 ± 10 nm (**Figure 3.2a** and **Figure 3.S4,** Supporting Information).[16, 20-23] This “signal” peak was chosen to optimally overlap with the absorbance of the colorimetric indicator dye when it interacted with HCN. The second, “reference”, peak was chosen at around 690-740 nm, far from the absorbance of Cbi, to act as a ratiometric reference peak to provide an optical readout for remote detection. This dual-peak ratiometric readout is extremely useful for correcting changes in probe light intensity fluctuations which can lead to zero-point drift, but is not robust to index changes resulting from liquids or vapors infiltrating the porous medium, which is paramount for the Cbi indicator dye to accurately display a response coinciding with our engineered “signal” peak.[16, 18, 19] The photonic crystal sensors were then chemically modified with amine functional groups to facilitate the loading of the colorimetric indicator dye as well as the addition of a gatekeeper.

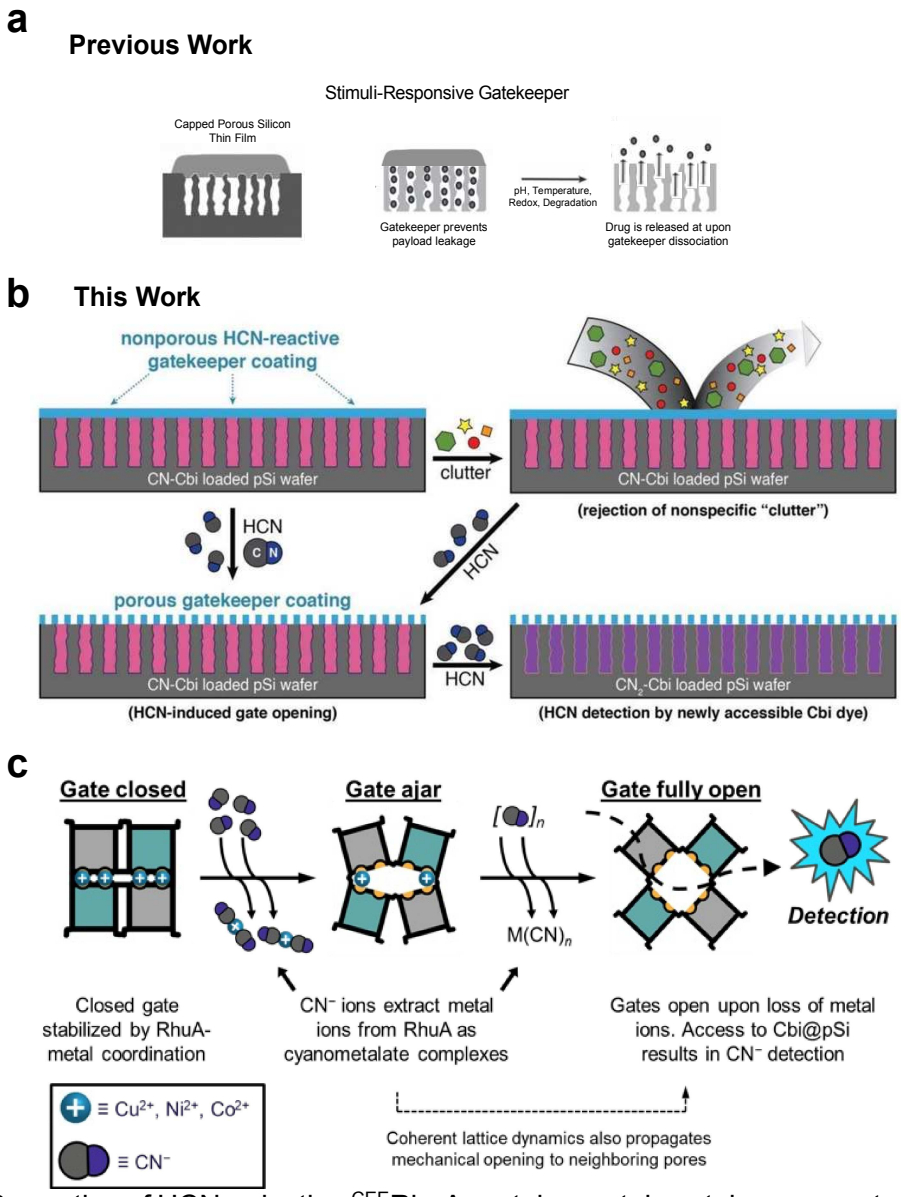

Figure 3.1: Properties of HCN-selective ^{CEE}RhuA protein crystals gatekeeper coated onto a pSi photonic crystal. (a) Schematic representation of previously reported gatekeeper-coated porous silicon-based systems. GPTMS-crosslinked chitosan is among many polymeric and lipid-based systems to protect the porous features and payload within the silicon substrate. pH, temperature, and redox potential conditions would trigger the release of the payload. This gatekeeping system is, however, limited for drug release applications. (b) Illustration of gatekeeping principle applied to the pSi sensor. The reactive coating yields a passive, continuous, broad-spectrum rejection of arbitrary clutter in the local environment, only being triggered "open" by the target analyte via chemical or mechanical means. c) Illustration of metal-bound ^{CEE}RhuA crystals that adopt a spring-loaded nonporous "gate closed" conformation, which is held under tension by metal ions chelated by geometrically opposed Glu sidechains, which neutralizes like-charge repulsion and structurally connects neighboring proteins. In the presence of HCN, these ions will be stripped from the lattices through the formation of cyano-complexes, releasing the spring to open the gate, allowing access to the underlying sensor.

We surmised that our gatekeeper must be able to: provide broad-spectrum rejection of chemical species by default (remaining in a nonporous state until exposure to HCN triggers the gate opening via a change in porosity), achieve high surface coverage of the substrate, yet still allow photons to pass through the coating to preserve remote detection, and function in air on a solid surface. These requirements indicated that the optimal gatekeeper would be two-dimensional, organic, and capable of switching between porous and nonporous states in a selective manner.

To meet these stringent requirements, we utilized a previously developed variant of L-Rhamnulose-1-phosphate aldolase, a square-shaped C4-symmetric protein bearing cysteine residues at its four corners and pairs of glutamate residues on each side (^{CEE}RhuA)[17, 24]. Under mildly reducing conditions, ^{CEE}RhuA undergoes solution self-assembly into checkerboard-like μm-scale porous 2D crystals via intermolecular disulfide bonding. The flexibility of the disulfide bonds permits them to act as hinges, enabling ^{CEE}RhuA crystals to undergo coherent structural dynamics that induce uniform changes in pore size from ~6 to <1 nm in diameter without losing crystallinity, while the introduction of glutamate residues on the protein surface endowed these materials with a porosity switch toggled by specific ions. Close-packing of the protein units (the nonporous conformation) was disfavored at thermodynamic equilibrium due to electrostatic repulsion but could be achieved upon the introduction of Ca^{2+} ions, which bind to and bridge neighboring carboxylate sidechains. Thus, the 2D morphology of ^{CEE}RhuA lattices, coupled with the ability to modulate their porosity through metal (un)binding, suggested that this material should fulfill all the requirements of the optimal gatekeeper coating (**Figure 3.2**).

As the nonporous conformation of ^{CEE}RhuA crystals is only accessible when bound to metal, we reasoned that displacement of the bridging ion by HCN (or CN^-) would provide the necessary gating mechanism (**Figure 3.1b**), as ^{CEE}RhuA crystals spontaneously open when Ca^{2+} is removed by dialysis or chelation with EDTA. However, $Ca(CN)_2$ is highly soluble in water, producing HCN gas even in moist air,[25] suggesting that chemical driving forces would render HCN sequestration thermodynamically impossible. In contrast, Co^{2+}—which exhibits the 2nd highest affinity for dicarboxylate coordinating ligands—readily forms water-stable inorganic salts with CN^-, namely $Co(CN)_2$ trihydrate and insoluble $K_4Co(CN)_6$ (in the presence of excess KCN). Animated by this concept, we first set out to establish whether this mechanism could be used to toggle lattice porosity in solution.

Following the methodology used to screen other ionic species, clarified suspensions (with uncrystallized protein monomers removed) of ^{CEE}RhuA lattices were mixed in 1:1 (v/v) ratios with Tris-buffered $CoCl_2$ solutions at twice the desired final Co^{2+} concentration and were allowed to stand for three days at 4 °C to ensure sufficient time for binding to occur. Direct visualization of the crystals by negative-stain transmission electron microscopy (ns-TEM) revealed that 25 mM $CoCl_2$ was sufficient to induce closure of the ^{CEE}RhuA crystal pores (**Figure 3.2e**). As seen previously with Ca^{2+}, vigorous mixing of the solution or dialysis to remove free ions both resulted in open-state crystals, suggesting that Co^{2+} indeed served as a surrogate bridging ion. Next, we investigated whether Co^{2+} could be displaced from closed lattices through competitive binding by CN^-. When Co^{2+}-bound ^{CEE}RhuA crystals were gently mixed with Tris-buffered KCN solutions to a Co:KCN stoichiometric ratio of 1:2, the ^{CEE}RhuA crystals remained nonporous after

3 days. However, when KCN was added to a final 1:6 stoichiometry, open-state ^{CEE}RhuA crystals were observed after 1 day (**Figure 3.3f**). This provided compelling evidence that not only could the nonporous conformation be stabilized by Co^{2+} ions, but also that Co^{2+}-binding could be rapidly reversed upon exposure to KCN, restoring crystal permeability.

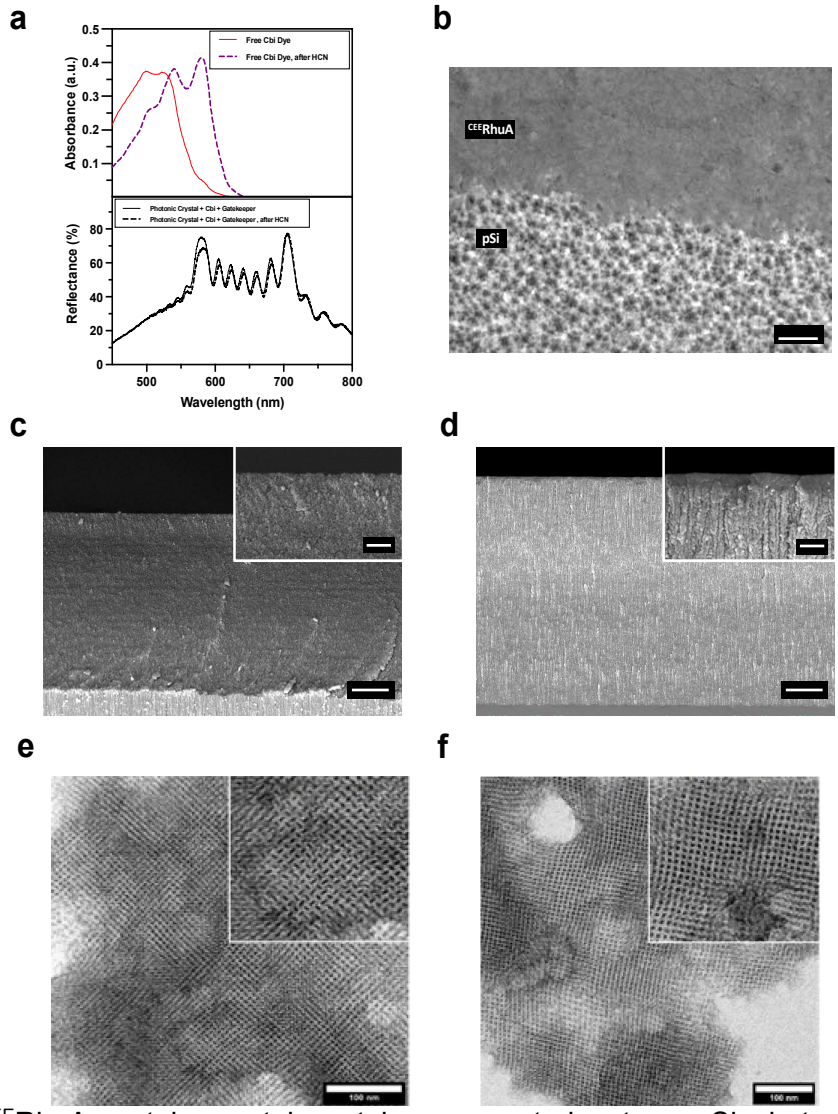

Figure 3.2: ^{CEE}RhuA protein crystals gatekeeper coated onto a pSi photonic crystal. (a) Representative visible absorbance spectra of cobinamide (Cbi), in solution (on top) and the optical reflectance spectrum of Cbi dye-impregnated, gatekeeper-coated pSi photonic crystal (on bottom), before and after exposure to 20 ppm hydrogen cyanide analyte vapors for 10 minutes. The absorbance spectrum was measured in a microplate reader normalized to a 1 cm path length cuvette using 500μM Cbi dye dissolved in ethanol, as described in the methods section of the text. The addition of cyanide was performed by the addition of concentrated aqueous KCN, sufficient to have achieve a final [CN^-] concentration of 500μM. The optical reflectance spectrum of the Cbi-loaded, gatekeeper-coated pSi photonic crystal is described below in the text, yielding a decrease in the intensity of the band ~590 nm. (b) Representative plan view scanning electron microscope (SEM) images of porous Si photonic crystal with partial deposition of the gatekeeper. Though the porous features of silicon are not visible with the gatekeeper coverage, the optical features remain intact. Representative scanning electron microscope (SEM) images of (c) as-etched pSi photonic crystal and (d) Cbi dye-impregnated, gatekeeper-coated pSi photonic crystal sensor (scale bar = 1000 nm); the insert shows a closer view of the photonic crystal (scale bar = 100 nm). The gatekeeper-coated pSi is estimated to be a thickness of 120 nm. TEM images of the of ^{CEE}RhuA protein crystals in both (e) closed and (f) open conformation (scale bar = 100 nm).

To structurally integrate the gatekeeper onto the sensor surface while still allowing for conformational motions of the protein subunits, we employed noncovalent electrostatic interactions as our attachment chemistry. It has previously been determined that the faces of 2D RhuA crystals are negatively charged, owing to the up-down orientation of the protein's C-terminal face, leading to preferential binding of crystals onto positively charged surfaces. To render the substrate surface charge positive, the pSi photonic crystals were functionalized with primary amines using cyclic azasilane reagent (2,2-dimethoxy-1,6-diaza-2-silacyclooctane; DMDASCO or "diazasilane) via a ring-opening click reaction, yielding "NH_2-pSi". This modification is performed without clogging the substrate pores, preserving efficient loading of the Cbi indicator dye. By utilizing RhuA crystal suspensions buffered at pH 6, which is below the surface amine pKa (~7.2) and above the ^{CEE}RhuA isoelectric point (~5.5), opposite-charge interactions were maximized. As-anodized pSi samples contained reactive Si-H species, which required the surface to be oxidized initially, to yield Si-O and Si-OH species. Attenuated total reflectance Fourier transform infrared (ATR-FTIR) spectra confirmed the presence of organic signatures assigned to the surface-grafted amine reagent (**Figure 3.S3**, Supplementary Information).

After loading the Cbi indicator dye into the pSi substrate, ^{CEE}RhuA suspensions (~5 μM protein concentration) were drop-cast onto both NH_2-pSi and untreated ("bare") pSi wafers and allowed to dry overnight. To verify the necessity of amine functionalization, initial wafers were washed with two 500 μL rinses of buffer. Scanning electron microscopy (SEM) imaging of the wafer surfaces clearly revealed extensive binding of well-resolved gatekeeper crystals distributed across the surface of NH_2-pSi wafers, in stark contrast to

untreated pSi chips, which were barren (**Figure 3.2b**, **Figure 3.S3b/c**, Supplementary Information). Subsequent wafers did not undergo any additional washing after drop-casting of the gatekeeper. Cross-sectional scanning electron microscope (SEM) images would show a ~120 nm thick gatekeeper layer coated on the top of a pSi photonic crystal (**Figure 3.2c/d**). Encouraged by these results, coupled with ns-TEM images of the gatekeeper in different conformations following CN^- exposure (**Figure 3.2e/f**), we carried out experiments to demonstrate the functionality of this bio-inorganic heterostructure.

Following previously developed methodologies for testing our photonic crystals, and detailed in the methodology section, we compared the basal response of Cbi-impregnated NH_2-pSi photonic crystals with and without the ^{CEE}RhuA gatekeeper to non-specific clutter materials, namely neat hexane (~3130 ppm) at a 50% RH value for 10 minutes. While the non-coated sensors indeed exhibited a shift in reflectance peak due to infiltration of gaseous clutter (**Figure 3.3a**), the reflectance spectrum for ^{CEE}RhuA-coated sensors remained constant (**Figure 3.3b**), indicating robust rejection of non-target species under “real-world” conditions in which both non-specific clutter and humidity were challenged onto the crystals. We then performed sequential 10-minute challenges of hexane, 10 ppm gaseous HCN, then hexane again at 50% RH to the gatekeeper sensors to assess their sensing properties (**Figure 3.3c**). As before, the spectrum remained constant during the initial hexane exposure, however upon HCN exposure we observed a decrease in the signal peak (consistent with an increase in absorbance due to HCN binding to Cbi) as well as a minor peak shift, indicating that HCN was able to pass through the gatekeeper layer. Finally, re-exposure to hexane resulted in a peak shift in the spectrum, indicating that the gatekeeper was in fact newly permeable to alkanes, rather

than simply selectively permeable to HCN. Together, these tests strongly suggest that the ^{CEE}RhuA gatekeeper can 1) prevent infiltration of non-specific clutter, 2) undergo the HCN-selective switching observed in solution while attached to the pSi sensor surface, and 3) preserve the sensing capabilities of the underlying substrate. The temporal signal response and peak shift are reported in **Figure 3.3d** for the corresponding reflectance spectra in **Figure 3.3c**, with the signal response quantified using **Eq. 1** to measure a ratiometric change from the "signal" peak of the photonic crystal, relative to the "reference" peak. The non-negative signal response in the second hexane exposure underscores the necessity of clutter rejection for robust sensing.

$$Response = \frac{R_t}{R_0} = (\frac{I_{signal}}{I_{reference}})_t / (\frac{I_{signal}}{I_{reference}})_0 \qquad \textbf{(1)}$$

In the above equation, which was used in previous sensing work, R_t is the ratio of intensities of the signal peak (I_{signal}) to the reference peak ($I_{reference}$) measured at time t, R_0 is the ratio of intensities of the signal band (I_{signal}) to the reference band ($I_{reference}$) measured before exposure (time t = 0).[16] Therefore, a decrease in the value of the response function would directly correspond to an increase in absorbance from the Cbi indicator dye that is correlated with HCN exposure, which can be measured temporally. In addition to this, the peak shift was calculated by measuring the temporal shift of the signal peak (in nm) after exposure to either HCN or non-specific clutter. As vapors infiltrate the pores of the pSi photonic crystal, they can change the index depending on whether the humidity level of the exposed vapor – red shift (positive nm peak shift) or blue shift (negative nm peak shift). It is expected that in a closed gatekeeper state, there would be no temporal response or peak shift, but once triggered open, as well as in a fully open gatekeeper state, could vapors infiltrate into the sensor.

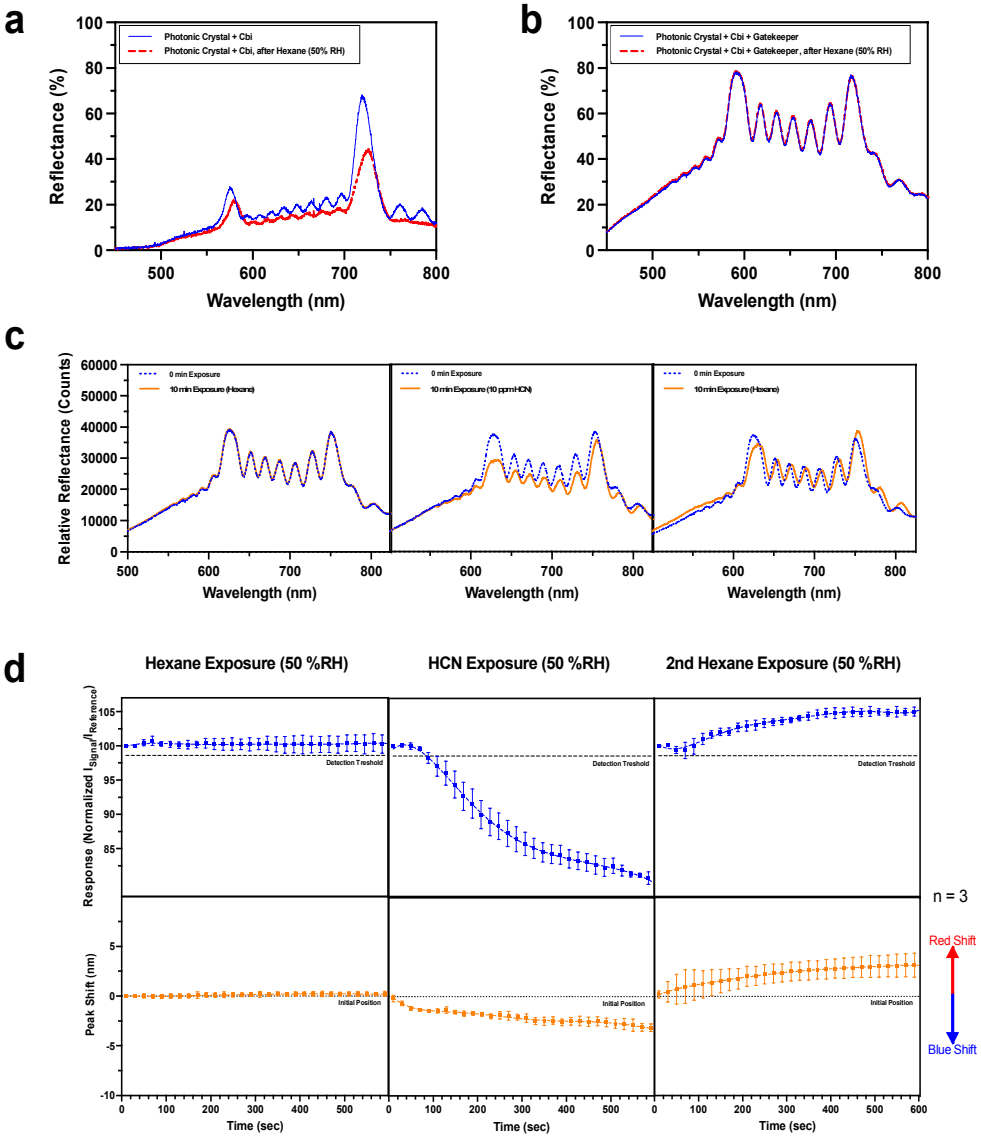

Figure 3.3: Optical response of gatekeeper-coated pSi photonic crystal sensors to analyte vapor challenges. Optical reflectance spectrum of Cbi-dye impregnated pSi photonic crystals (a) without the gatekeeper coating and (b) with the gatekeeper coating. The optical reflectance spectra on top for both (a) and (b) are the exposure of non-specific clutter (hexane vapor) for 10 minutes. The exposure of vapors are detailed in the methods section of the text. The presence of the gatekeeper prevents any spectral shift due to non-specific clutter exposure. (c) Optical reflectance spectra obtained after a 10-minute exposure to neat hexane (50% RH), 10 ppm $HCN_{(g)}$ (50% RH) and neat hexane (50% RH) once more (plotted chronologically). The exposure of both sets of vapors are detailed in the methods section of the text. The decrease in the signal peak with HCN exposure (~590 nm) indicates detection of HCN. The presence of the ^{CEE}RhuA gatekeeper only selectively opens after HCN exposure, enabling neat hexane to penetrate the pores. (d) Temporal response and temporal peak shift curves of Cbi-dye impregnated, gatekeeper-coated photonic crystal sensors upon exposure to the aforementioned vapors described in (c) neat hexane (50% RH), 10 ppm $HCN_{(g)}$ (50% RH) and neat hexane (50% RH) once more (plotted chronologically). Response metric is defined in Eq 1. Once again, responses and peak shifts are only seen after HCN exposure.

We next sought to augment our interpretation of the spectroscopic results by additional simulations and experiments. We performed all-atom molecular dynamics (MD) of infinitely periodic ^{C98}RhuA lattices (chosen to focus on steric effects, rather than the details of metal-carboxylate interactions challenging for classical MD forcefields) in the closed (Co^{2+}-bound), partially open ("ajar", post-HCN-exposure), and fully open states *in vacuo* to emulate conditions on the sensor surface. Solution-equilibrated structures of these lattices, plus their first hydration layer (expected to exist in the presence of ambient humidity), were extracted and held fixed in the center of the simulation box, and two sequential additions (or "boluses") of neat hexane at ~3000 ppm were added on one side of the lattice followed by equilibration. In the first bolus, we observed that there was a clear ordering of permeability from open to closed, as monitored by fraction of hexane molecules below the lattice after 25 ns of equilibration, with very few molecules permeating through the closed gatekeeper (**Figure 3.S5**, Supplementary Information). We also noticed that many of the hexanes adsorbed to the gatekeeper surface, as reflected in "lag times" of ~1, 2.5, and 4.5 ns for open, ajar, and closed states, respectively, so a second equivalent bolus was added to the system. After this second round of equilibration, the ajar and open states are nearly equivalent, indicating full permeability to hexanes in the HCN-exposed conformation, while the closed state is at least 2x less permeable, even for a single layer (**Figure 3.S6**, Supplementary Information). The transport rates in terms of total hexane molecules are >1 hex/ns for the open and ajar states, while it is ~8x lower for the closed state. As the thickness of the gatekeeper coating indicate 10-12 layers of ^{CEE}RhuA, the combined coating is likely

nearly totally impermeable, while even modest opening of the lattice pores is sufficient to reach equivalent porosity to the fully open state.

Encouraged by these results, we subsequently challenged the gatekeeper-coated pSi photonic crystals to a battery of non-specific interferant vapors, other than short-chain alkanes, to assess the selectivity of the gatekeeper and sensor to potential environmental clutter. This included humid air (H_2O), nitrogen (N_2), ammonia (NH_3), hexane and a complex air mixture containing 43 different volatile organic compounds defined by the US Environmental Protection Agency (EPA), referred to in this work as "TO-14A mix".[16] All interferents were diluted into a humidified air steam to final a humidity of 20%, 50% or 80% RH. The sensors were exposed to the flowing stream of potential interferents for 10 min and the responses are presented and compared with a 10 ppm of HCN(g) challenge in **Figure 3.4a**. As a reference, the response of non-gatekeeper coated sensors was also evaluated. A corresponding temporal response curve comparing both the interferent vapors and HCN was also calculated and plotted (Figure S6, SI). The gatekeeper-coated photonic crystal sensor showed no significant response to the vapor interferents at all values of %RH tested but showed very similar response to HCN compared to the non-gatekeeper coated pSi photonic crystals (**Figure 3.4a**).

To simulate real-world environments, the gatekeeper-coated sensors were exposed to HCN in the presence of a complex matrix containing multiple VOCs to determine if target analyte detection was obscured in the presence of this more complex mixture. The sensors were exposed to four different conditions in a sequential order for 10 minutes each: nitrogen (0% RH), nitrogen + water vapor at 50%RH, TO-14A mix at 50% RH, and finally 10 ppm HCN(g) spiked into air + TO-14A mix at 50% RH (**Figure**

3.4b). As expected, the ratiometric signal showed no response to any of the non-HCN containing streams. The sensors then displayed a strong response upon introduction of 10 ppm HCN(g) into a flowing stream containing the interferents. In addition to retaining their high-fidelity signal response to HCN, these results demonstrated that the integration of a specific protein-based gatekeeper onto the sensor indeed protected the substrate from the complex VOC mixture without impairing its sensitivity or selectivity.

Finally, to confirm that the all the major components are necessary for an integrated gatekeeping sensor, we tested a wide variety of controls, including different variations of RhuA gatekeepers, measured their temporal response and peak shift to ensure that only a Co^{2+}-bound ^{CEE}RhuA crystals provided the observed HCN-responsive gatekeeping properties (**Table S1**, Supplementary Information). The control experiments included the following:

1) Cbi-impregnanted NH_2-pSi sensors lacking the gatekeeper to assess the baseline response and peak shift of hexane infiltration (**Figure 3.S7**, Supplementary Information)
2) NH_2-pSi sensors + $CoCl_2$, to test if Co^{2+} ions on its own can provide a sensor response to 10 ppm HCN(g) exposure or that dried $CoCl_2$ salt blocked the pores to prevent gas infiltration (**Figure 3.S8**, Supplementary Information).
3) Disassembled ^{CEE}RhuA gatekeeper (reduced with TCEP) co-incubated with $CoCl_2$, all components of the "active" gatekeeper are intact, but ^{CEE}RhuA is not a crystal with metal-dependent porosity (**Figure 3.S9**, Supplementary Information).

4) Gently mixed ^{CEE}RhuA protein crystals without $CoCl_2$ co-incubation: a slightly porous gatekeeper (resembling the HCN-exposed conformation) without Co^{2+} ions to close the lattice (**Figure 3.S10**, Supplementary Information).
5) Vigorously mixed ^{CEE}RhuA protein crystals without $CoCl_2$: a fully porous gatekeeper without Co^{2+} ions to close the lattice (**Figure 3.S11**, Supplementary Information).
6) Gently mixed ^{C98}RhuA protein crystals without $CoCl_2$ co-incubation: a non-porous and non-HCN-responsive gatekeeper protein layer (**Figure 3.S12**, Supplementary Information).
7) Vigorously mixed ^{C98}RhuA protein crystals without $CoCl_2$ co-incubation: a fully porous non-HCN-responsive gatekeeper protein layer (**Figure 3.S13**, Supplementary).
8) ^{C98}RhuA protein crystals co-incubated with $CoCl_2$: identical in every way to the ^{CEE}RhuA gatekeeper, but non-HCN-responsive (**Figure 3.S14**, Supplementary Information).

All control experiments were conducted in identical fashion with the sequential vapor dosing procedure described above to directly compare their behavior to the fully integrated sensor. The observed results from **Table 3.S1** and **Figures 3.S7-14** indicated that all the gatekeeper variations and configurations did not behave in a closed, triggered and opened configuration as seen in **Figure 3.4b**, demonstrating that all components of the ^{CEE}RhuA gatekeeper system are necessary and sufficient to behave as designed.

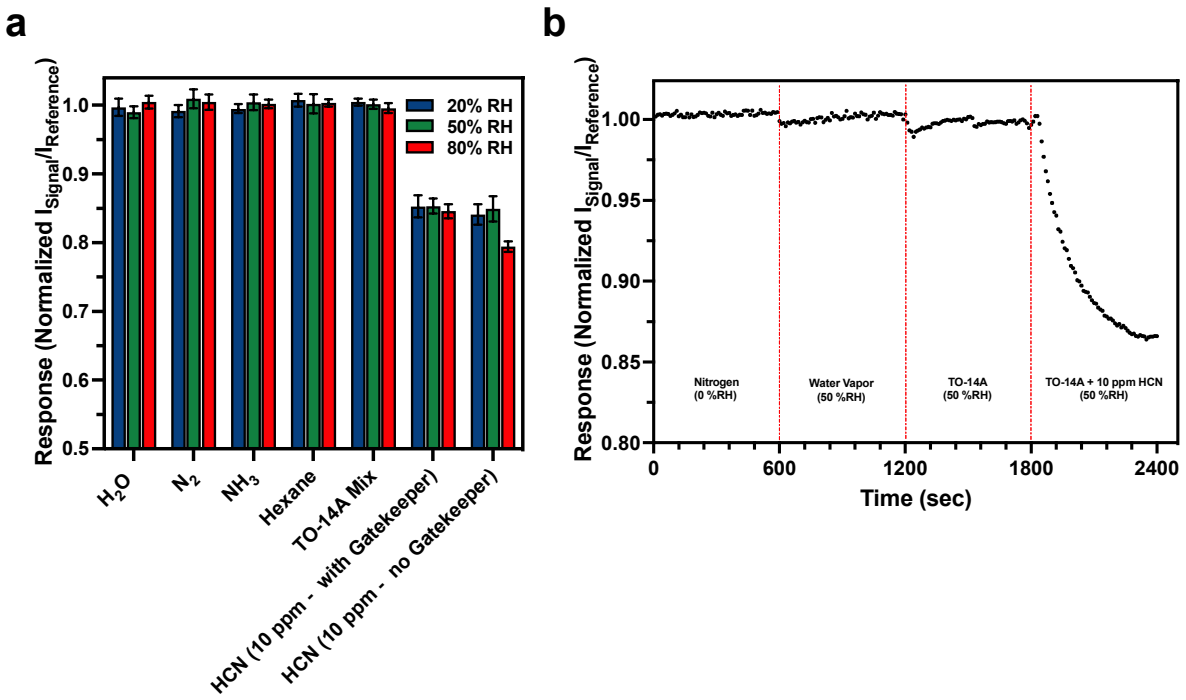

Figure 3.4: HCN sensing performance of Cbi-dye impregnated, gatekeeper-coated pSi photonic crystal sensors. (a) Selectivity studies of the Cbi-dye impregnated, gatekeeper-coated photonic crystal sensors challenged with the interferant vapors performed with carrier gas at 20%, 50% and 80% RH. Bars labeled "H_2O" represent air blanks at the indicated values of RH. Data were acquired 10 min after introduction of the indicated analyte or interferent agents. (b) Representative temporal response of Cbi-dye impregnated, gatekeeper-coated pSi photonic crystal sensors to sequential exposure of N_2 (time = 0−600 s); 50% RH air (time = 600−1200 s), TO-14A analyte mixture in 50% RH air (time = 1200−1800 s); 10 ppm of HCN in a carrier stream containing TO-14A analyte mixture in 50% RH air (time = 1800−2400 s). Each of the 43 VOC components of the TO-14A mixture was present in the air matrix at a nominal concentration of 0.5 ppm. The optical response (as defined in Eq. 1) was acquired every 10s.

3.3 Conclusion

We have reported here the development of a fully integrated pSi photonic crystal chemical sensor with high sensitivity and specificity to HCN that is enhanced with high chemical specificity afforded by a conformationally flexible engineered biological macromolecular gatekeeper. The resulting material serves as a passive indicator for HCN gas that can be assessed remotely from a safe distance through optical interferometric methods while remaining robust to ambient clutter. The rejection of non-HCN chemical species present in the environment was achieved using a crystalline biological

gatekeeper, a nonporous coating which only becomes permeable upon loss of specific chemical interactions (metal coordination) that are directly severed by HCN molecules. As a result, this sensor possesses resistance to erroneous readouts, demonstrating its promise as an unattended sentinel for the detection of noxious gas due to stability to non-specific interferents, humid air (H_2O), nitrogen (N_2), ammonia (NH_3), hexane and a complex air mixture of VOCs (EPA TO-14A) but showing a sensor response to 10 ppm $HCN_{(g)}$.

This work has demonstrated several of the principal advantages of using biological macromolecules as highly specific gatekeeping modalities in the form of one of the first integrated bio-inorganic heterostructures for the specific sensing of gases in ambient conditions. Protein engineering offers the possibility to create gatekeepers of arbitrary selectivity and behavior, which coupled with the high tunability of porous silicon and vast space of colorimetric indicator dyes, should make our approach an attractive general and versatile design strategy for the construction of next-generation chemical sensors with gatekeeper functionalities.

3.4 Materials & Instrumentation

All materials and reagents were used as received. Single-crystal highly doped p-type (B-doped) silicon wafers of resistivity 0.8 – 1 mΩ-cm, polished on the (100) face, were purchased from Siltronix Corp. 2,2-dimethoxy-1,6-diaza-2-silacyclooctane [DMDASCP]) was purchased from Gelest Inc. Premixed hydrogen cyanide (HCN) gas cylinders (10 and 20 ppm; balance gas nitrogen) were purchased from Gasco Inc. EPA TO-14A Calibration mix was purchased from Restek through Linde Spectra

Environmental Gases, catalogue #34432 and contained 1 ppm of each component. All other chemical reagents were purchased from Sigma-Aldrich.

Attenuated total reflectance Fourier transform infrared (ATR-FTIR) spectra were recorded on a Thermo Scientific Nicolet 6700 FTIR instrument fitted with a Smart iTR diamond ATR fixture. Scanning electron microscope (SEM) images were obtained with a Zeiss Sigma 500 in secondary electron imaging mode. Reflected light spectra were obtained in the visible-NIR spectral range with an Ocean Optics USB-4000 CCD spectrometer and a tungsten-halogen illumination source (Ocean Optics LS-1) connected with a Y-branch 600-μm-diameter, bifurcated multimode optical fiber. The common end of the bifurcated fiber was focused with an objective lens to a ~1 mm^2 spot and positioned with the optic axis normal to the sample surface. UV−vis absorbance spectra were obtained using a Molecular Devices SpectraMax 340PC384 Microplate Spectrophotometer with a 1 cm path length cuvette and 96-well microplate with normalized absorbance values to an equivalent 1 cm path length cuvette.

3.5 Methods

3.5a Preparation of Porous Silicon (pSi) Photonic Crystals

Single-crystal highly doped p-type (B-doped) silicon wafers of resistivity 0.8 – 1 mΩ-cm, polished on the (100) face, were purchased from Siltronix Corp. and were cleaved into square chips of size 2 cm x 2 cm and mounted inside a custom Teflon etching cell with a 1.2 cm^2 exposed circular surface area to an 3:1 (v/v) 48% aqueous hydrofluoric acid:ethanol electrolyte solution (CAUTION: HF is highly toxic and can cause severe burns on contact with the skin or eyes). The wafer was contacted on the backside with aluminum foil and anodized with a platinum coil counter-electrode. Prior to the preparation

of the stop-bands, the samples were cleaned using a “sacrificial etch” which was used to etch a thin porous layer into the chip at 400 mA cm^{-1} for 50s. The porous layer was subsequently removed by dissolution with a strong base of 2M aq. KOH. The cell was then rinsed with rinsed with water and ethanol three times and fresh HF electrolyte solution was added to prepare two stop-bands (dual peak pSi photonic crystal). The anodization waveform was generated using LabView software (National Instrument, Inc.) and the current was interfaced with a Keithley 2651A Sourcemeter power supply. A composite time-dependent current density waveform, J(t), used was created with Eq xx. With J_{max}= 4.167 mA/cm^2 and J_{min} = 4.167 mA/cm^2. For the preparation of the signal stop-band and reference stop-band, values of T_1 = 8.4 s and T_2 = 9.8 s were used. The composite waveform was applied for 300s, and the chips were subsequently rinsed with ethanol to remove any residual electrolyte.

3.5B Surface Functionalization of pSi Photonic Crystals

The as-etched pSi photonic crystals were chemically modified by subjecting the chips to an organotrialkoxysilane reagent to functionalize the surface with amine (NH_2). The pSi photonic crystals were initially incubated in in H_2O_2 (aqueous, 30% by mass) for 25 min at room temperature to generate a hydroxylated (Si-OH, Si-O-Si) porous Si films as described previously (ref). The crystals were then washed by sequential triplicate rinses with 100% ethanol, 50:50 ethanol:dichloromethane, and 100% dichloromethane, before submerging it in a glass vial containing 1.5 mL of heterocyclic silane (2,2-dimethoxy-1,6-diaza-2-silacyclooctane [DMDASCP]) for 3 hours under gentle stirring. Excess silane was removed, and the wafer was again subjected to serial triplicate rinses

in the reverse order (100% ethanol, 50:50 ethanol:dichloromethane, and 100% dichloromethane) and allowed to dry.

3.5C Synthesis and Loading of Monocyanocobinamide (MCbi)

Pure aquohydroxocobinamide ($OH(H_2O)Cbi$) was synthesized by base hydroloysis from hydroxocobalamin (Sigma-Aldrich) as described previously.[16, 20, 23] A stock solution of monocyanocobinamide ($CN(H_2O)Cbi$) was then prepared by reacting equimolar quantities of aquohydroxocobinamide (dissolved in aqueous 1M NaOH) with KCN (Fisher Scientific) for 6 hours under mild agitation at room temperature, which produced a dark red solution. Successful synthesis of monocyanocobinamide was verified by identification of the characteristic absorbance peak spanning 475–520 nm using a benchtop UV-Vis spectrometer (Molecular Devices Spectramax 340Pc384 Microplate Spectrophotometer), a distinct absorbance peak from 475-520 nm. The MCbi stock solution was diluted in ethanol until the concentration of the solution was 500 μM. A 100 μL aliquot of MCbi solution was subsequently drop-cast onto pSi-Si(NH_2) photonic crystal substrates and allowed to dry at room temperature for ~5 h or until the ethanol solvent appeared fully evaporated.

3.5D Synthesis, Preparation and Deposition of Gatekeeper Crystals onto pSi Photonic Crystals

^{CEE}RhuA protein was purified by published methods.[17] Briefly, ^{CEE}RhuA was overexpressed in E. coli cells which were grown to high density and lysed by sonication. The resulting solution was clarified by centrifugation, and subjected to multiple chromatographic steps, ultimately yielding approximately 10 mg pure protein per liter of cell culture. The purified protein was concentrated to 150 μM (~18 mg/mL) in the presence

of 10 mM β-mercaptoethanol and 1 mM $ZnCl_2$, conditions suitable for crystallization. 0.5 mL aliquots were flash frozen in liquid nitrogen and stored at −80 °C. Crystallization was induced by thawing the aliquots and leaving them on a shaking platform in the cold room at 4 °C for several days (up to several weeks). ^{CEE}RhuA crystal suspensions were clarified (unincorporated protein monomers were removed) by repeated cycles of gentle centrifugation (~3000 rpm) in a benchtop centrifuge for 30-60s, followed by replacement of the supernatant with fresh buffer solution containing 20 mM 2-(N-morpholino)ethanesulfonic acid (MES) pH 6 and 50 mM $CoCl_2$. 80-90% of the solution was replaced at each wash step, leading to complete exchange of the ^{CEE}RhuA crystals into the new buffer solution. After washing, the crystal suspensions typically contained protein concentrations of ~100 μM. Experimental screening determined that a protein concentration of 5 μM provided the functionally sufficient surface coverage of the sensor while preserving its optical reflectance spectrum. Crystal solutions were gently resuspended prior to deposition, using 50 μL to drop-cast onto 1.2 cm^2 square area chips. Amine functionalization of the pSi surface (described above) was found to be an essential prerequisite for effective crystal binding to the substrate. The pKAs of the amines in these chemical groups are estimated to be ~7.2, while the isoelectric point of the ^{CEE}RhuA protein is ~5.5, so drop- casting of the protein crystals was carried out using in the MES (pH 6) buffer introduced during the previous wash step, serving to promote binding by ensuring that the surface was positively charged while the protein remained negatively charged.

3.5E VAPOR DOSING EXPERIMENTS

The photonic crystals were challenged with various analyte streams of clutter vapors of fixed concentrations using mixed streams of dry, humidified compressed air, laboratory air or nitrogen gas. All stream flow rates were controlled using digital mass flow controllers (MFC) to tune the exact analyte concentrations. For water vapor and ammonia, aqueous solutions were prepared at a specified concentration and the vapors were generated by bubbling laboratory air until a vapor flow was transferred to the sample. Details are provided in **Figure 3.S5**. Hexane clutter vapor was generated through the bubbling of neat Hexane solutions. Both HCN and EPA TO-14A vapors were directly produced from certified gas cylinders mixed with humidified laboratory air to tune the correct concentration to be used. The concentrations of all the analytes that were used were calculated using their partial pressure values at 25°C for the aqueous solutions of H_2O and NH_3 as well as for neat hexane. The partial pressures were then subsequently converted to concentration values using previously described conversion methods.[16]

In that equation, $P_{analyte}$ is the partial pressure of the analyte vapor (Torr), $F_{analyte}$ is the flow rate of the analyte vapor stream (SCCM) and $F_{dilution,air}$ is the flow rate of the dilution air stream (SCCM). All RH values were verified using a probe hygrometer while sensing experiments were conducted with a net flow rate of 300 SCCM, as controlled using an MFC. Reflectance spectra measured from the pSi sensors were collected using an Ocean Optics USB-4000 CCD spectrometer, coupled to one end of a bifurcated fiber optic cable. The two other branches, combined towards a single fiber, connected towards a tungsten filament light source and a collimating lens, fitted to the distal end, and mounted 20 cm in from of the samples within its test chamber.

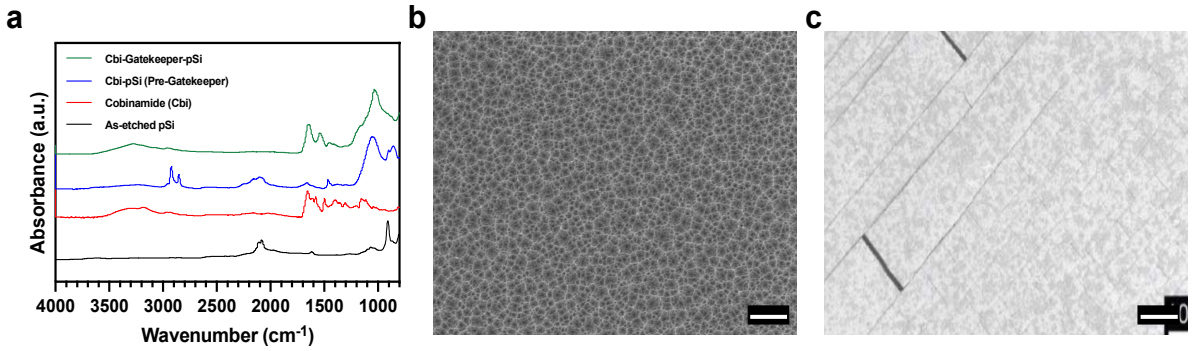

Figure 3.S1: Characterization and morphology of pSiNP surfaces of pSi and Gatekeeper-Cbi-pSi photonic crystal sensors. (a) Attenuated total reflectance Fourier-transform infrared (ATR-FTIR) spectra of photonic crystal samples from bottom to top: As-etched pSi (black trace), Cobinamide (Cbi) (red trace). Cbi-pSi (blue trace) and Gatekeeper-Cbi-pSi (green trace). Representative plan view scanning electron microscope (SEM) images of (b) as-etched porous Si photonic crystal, and (c) Gatekeeper-Cbi-pSi photonic crystal (scale bar = 100 nm). The addition of the gatekeeper coating covers the porous features of the silicon substrate, yet optical features are maintained.

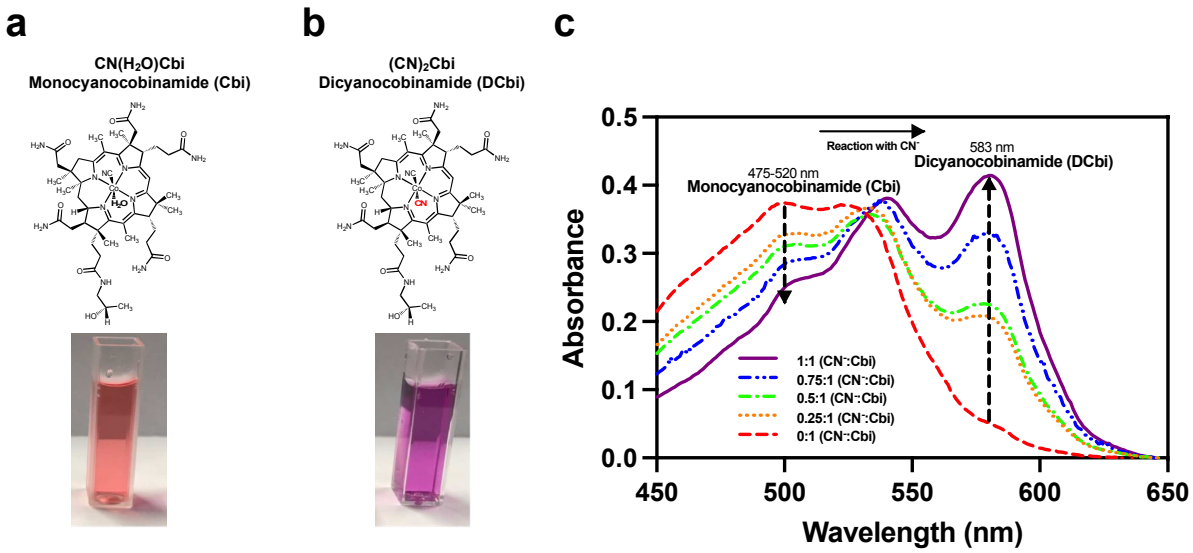

Figure 3.S2: Cobinamide structures and absorbance measurements. Molecular structures of the various cobinamide complexes, (a) monocyanocobinamide (Cbi) and (b) dicyanocobinamide (DCbi). Below shows photographs of corresponding cobinamide complexes dissolved in water inside of cuvettes. For these experiments, Monocyanocobinamide ("$CN(H_2O)Cbi$", or "Cbi") was used and prepared in-situ by reaction of an equimolar mixture of aquohydroxocobinamide and KCN following previous methods. DCbi is the fully saturated cobinamide complex after HCN exposure. a) Series of UV-vis absorbance spectra of monocyanocobinamide (Cbi) (500 μM) in water, upon titration with various ratiometruc concentrations of CN^- as indicated in the graph.

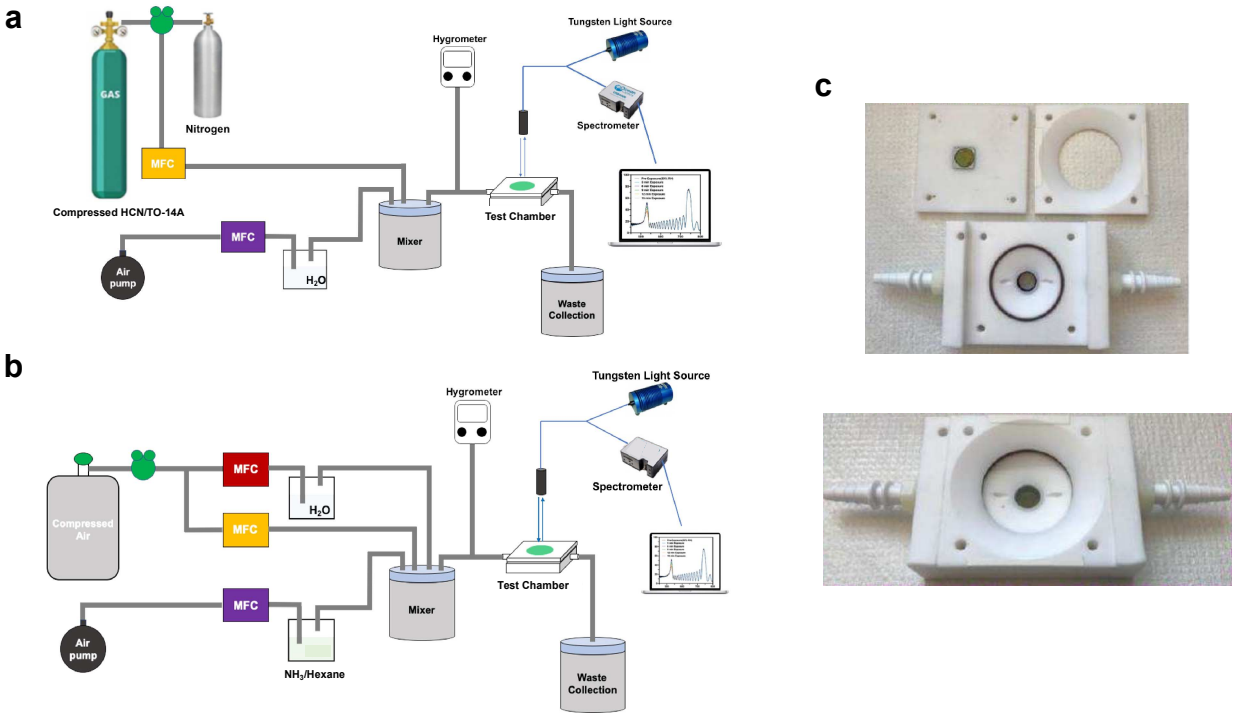

Figure 3.S3: Vapor dosing set-up and photonic crystal testing-chamber. (a) Schematic of vapor dosing setup for HCN and TO-14A sensing. The HCN source was from a certified gas cylinder containing 20 ppm HCN with nitrogen as a carrier gas. The %RH values reported were monitored with a commercial probe hygrometer. The HCN and TO-14A sensing experiments were conducted with a flow rate of 300 sccm. The use of mass flow controllers (MFCs) enabled the flexibility to tune the analyte concentration to be exposed on the chips, the %RH and the flow rate. Humid air, which was air bubbled through a water reservoir was adjusted to obtain the desired humidity and analyte concentrations within the mixer, that is eventually exposed to the sample testing chamber. The volume of the mixer is approximately 500.0 cc; with the concentration of analyte in the testing chamber was assumed to reach the steady-state, set-point concentration after 5 volumes passing through the chamber, corresponding to 5 x 500.0/300sccm = 8.3 min. (b) Schematic of vapor dosing setup for NH_3 and Hexane sensing. The set-up is the same as in (a), however it is modified to have aqueous solutions of NH_3 and Hexane analytes with the bubbling of a carrier gas through the solution. The aqueous concentration that is to provide the desired analyte concentration in the gas phase was chosen based on previous experiments and calculations.[16] (c) Teflon testing chamber used to house and test photonic crystal chips. The chamber is sealed for controlled vapor exposure, using inlet and outlet ports on the side, while the clear window enables optical measurements which can be measured by a CCD.

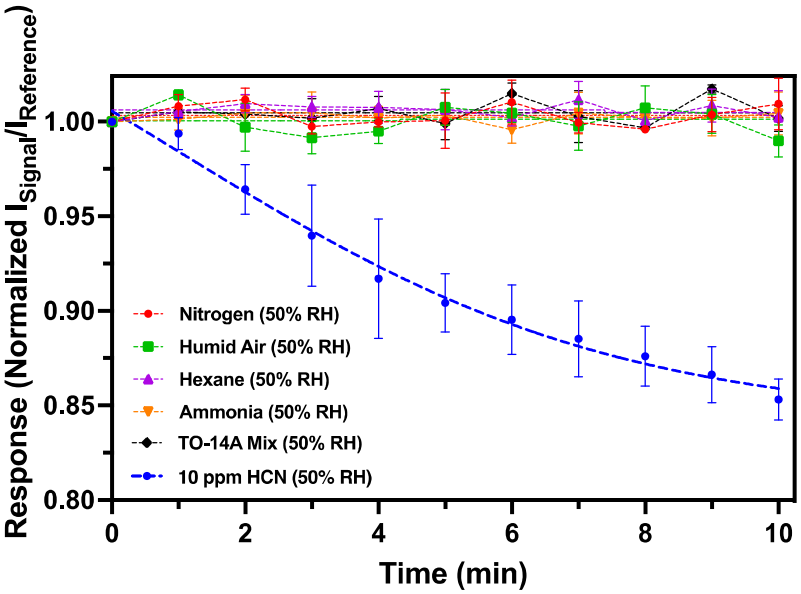

Figure 3.S4: Temporal responses of interferant vapors, including humid air (50% RH), neat hexane (50% RH), 100 ppm NH_3 (50% RH) and TO-14A mixture of VOCs (0.5 ppm of each component) compared to 10 ppm $HCN_{(g)}$ within 10 minutes.

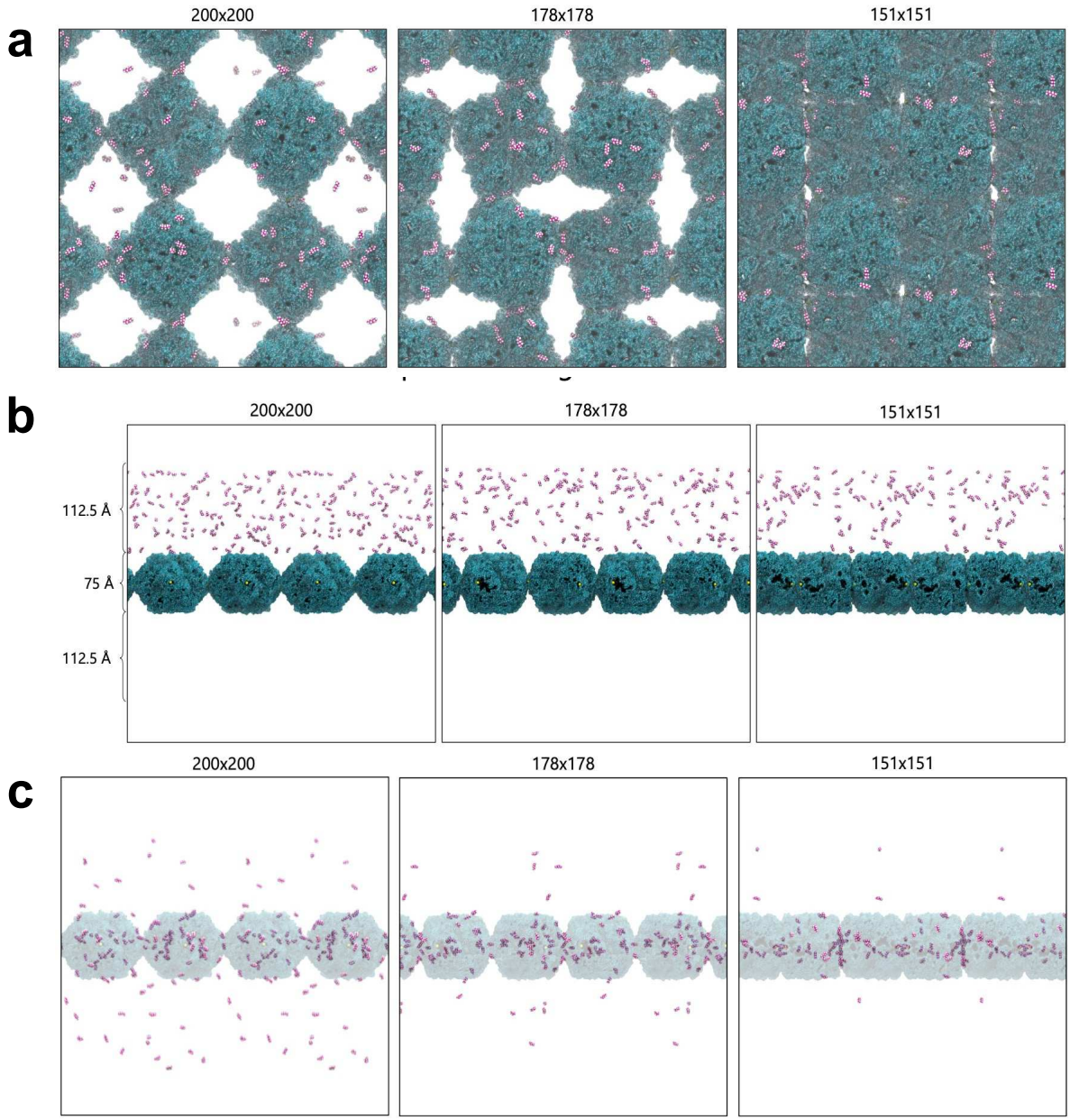

Figure 3.S5: All-atom molecular dynamics (MD) of infinitely periodic ^{C98}RhuA lattices (chosen to focus on steric effects, rather than the details of metal-carboxylate interactions challenging for classical MD forcefields) in the closed (Co^{2+}-bound), partially open ("ajar", post-HCN-exposure), and fully open states *in vacuo*.

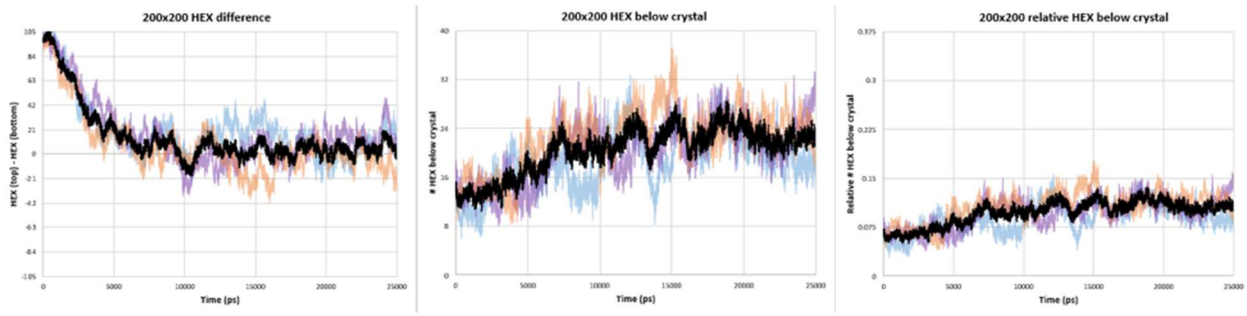

Figure 3.S6: Transport rates in terms of total hexane molecules. The values are >1 hex/ns for the open state within 10 minutes of exposure from **Figure 3.S5**.

Table 3.S1: Table of gatekeeper variations coated onto the photonic crystals. The table shows the various vapor dosing sequences, the expected effect and observed outcome after vapor dosing. The corresponding temporal dose response curves are listed as SI figures below.

Gatekeeper – pSi Sample	Vapors Dosed - Sequentially	Expected Effect	Observed Outcome	SI Figure #
^{CEE}RhuA Protein + $CoCl_2$ (Full Gatekeeper)	1. Hexane (50 %RH) – 10 min 2. 10 PPM HCN (50 %RH) – 10 min 3. Hexane (50 %RH) – 10 min	Full Gatekeeper should be impermeable to clutter vapors but show a response to HCN	Gatekeeper opens with HCN Exposure	**Figure 3.3c/d**
No Gatekeeper (pSi + Cbi)	Hexane (50 %RH) – 10 min	Peak Shift and/or change in response	Reflectance peak shift due to hexane	**Figure 3.S7**
$CoCl_2$	10 PPM HCN (50 %RH) – 10 min	$CoCl_2$ and HCN will not provide a change in response	No change in peak shift or response	**Figure 3.S8**
^{CEE}RhuA Protein (Reduced with TCEP) + $CoCl_2$	1. Hexane (50 %RH) – 10 min 2. 10 PPM HCN (50 %RH) – 10 min 3. Hexane (50 %RH) – 10 min	Disassembled ^{CEE}RhuA protein and Co^{2+} will either be fully permeable or impermeable to vapors	No change in peak shift or response	**Figure 3.S9**
Gently mixed ^{CEE}RhuA Protein (without $CoCl_2$)	1. Hexane (50 %RH) – 10 min 2. 10 PPM HCN (50 %RH) – 10 min 3. Hexane (50 %RH) – 10 min	^{CEE}RhuA protein without Co^{2+} will be permeable to vapors	Peak shift and response	**Figure 3.S10**
Vigorously mixed ^{CEE}RhuA Protein (without $CoCl_2$)	1. Hexane (50 %RH) – 10 min 2. 10 PPM HCN (50 %RH) – 10 min 3. Hexane (50 %RH) – 10 min	Vigorously mixed ^{CEE}RhuA protein without Co^{2+} will be permeable to vapors	Peak shift and response	**Figure 3.S11**
^{C98}RhuA Protein	1. Hexane (50 %RH) – 10 min 2. 10 PPM HCN (50 %RH) – 10 min 3. Hexane (50 %RH) – 10 min	Non-responsive ^{C98}RhuA protein should be fully impermeable to vapors	No change in peak shift or response	**Figure 3.S12**
Vigorously mixed ^{C98}RhuA Protein	1. Hexane (50 %RH) – 10 min 2. 10 PPM HCN (50 %RH) – 10 min 3. Hexane (50 %RH) – 10 min	Vigorously mixed non-responsive ^{C98}RhuA protein should be fully impermeable to vapors	Peak shift and response	**Figure 3.S13**
^{C98}RhuA Protein + $CoCl_2$	1. Hexane (50 %RH) – 10 min 2. 10 PPM HCN (50 %RH) – 10 min 3. Hexane (50 %RH) – 10 min	Non-responsive ^{C98}RhuA protein and Co^{2+} should be fully impermeable to vapors	No change in peak shift or response	**Figure 3.S14**

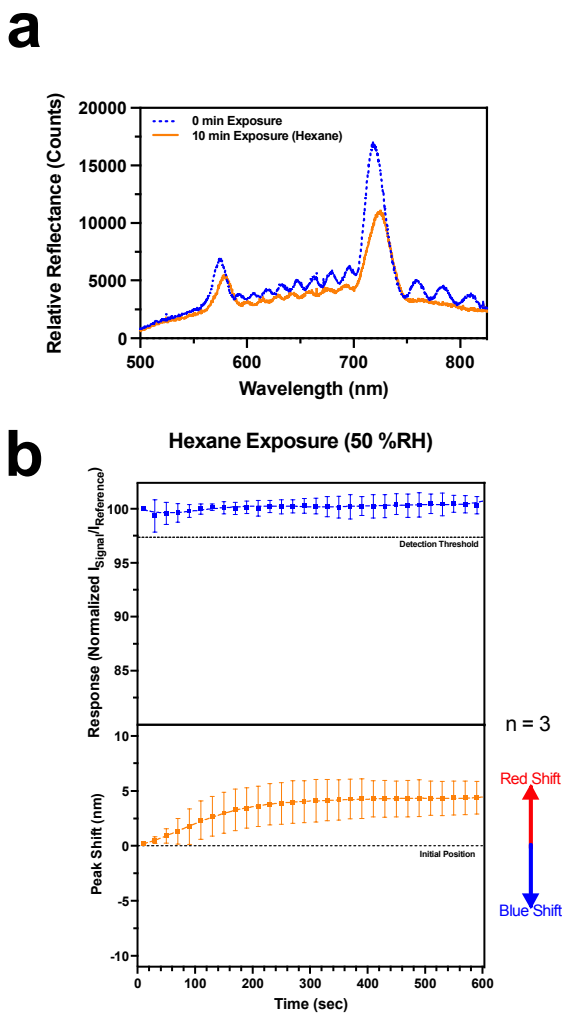

Figure 3.S7: Behavior of Cbi-dye impregnated pSi photonic crystal sensors without a ^{CEE}RhuA gatekeeper. (a) Optical reflectance spectra obtained after a 10-minute exposure to neat hexane (50% RH). The lack of the ^{CEE}RhuA gatekeeper enables neat hexane to penetrate the pores. (b) Temporal response and temporal peak shift curves of the photonic crystal sensors upon exposure to neat hexane (50% RH) described in (a). Response metric is defined in Eq. 1.

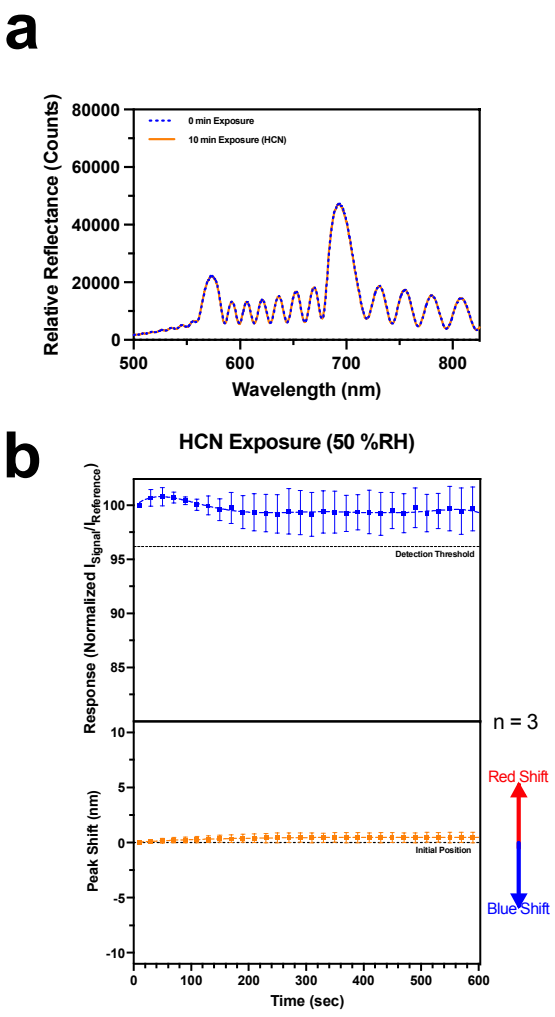

Figure 3.S8: Behavior of $CoCl_2$ coated pSi photonic crystal sensors. (a) Optical reflectance spectra obtained after a 10-minute exposure to 10 ppm $HCN_{(g)}$ (50% RH). As Co^{2+} is centered in both the ^{CEE}RhuA gatekeeper and the Cbi dye, this experiment was undertaken to confirm that the presence of the Cbi dye is necessary for HCN detection. (b) Temporal response and temporal peak shift curves of the photonic crystal sensors upon exposure to 10 ppm $HCN_{(g)}$ (50% RH) described in (a). Response metric is defined in Eq. 1.

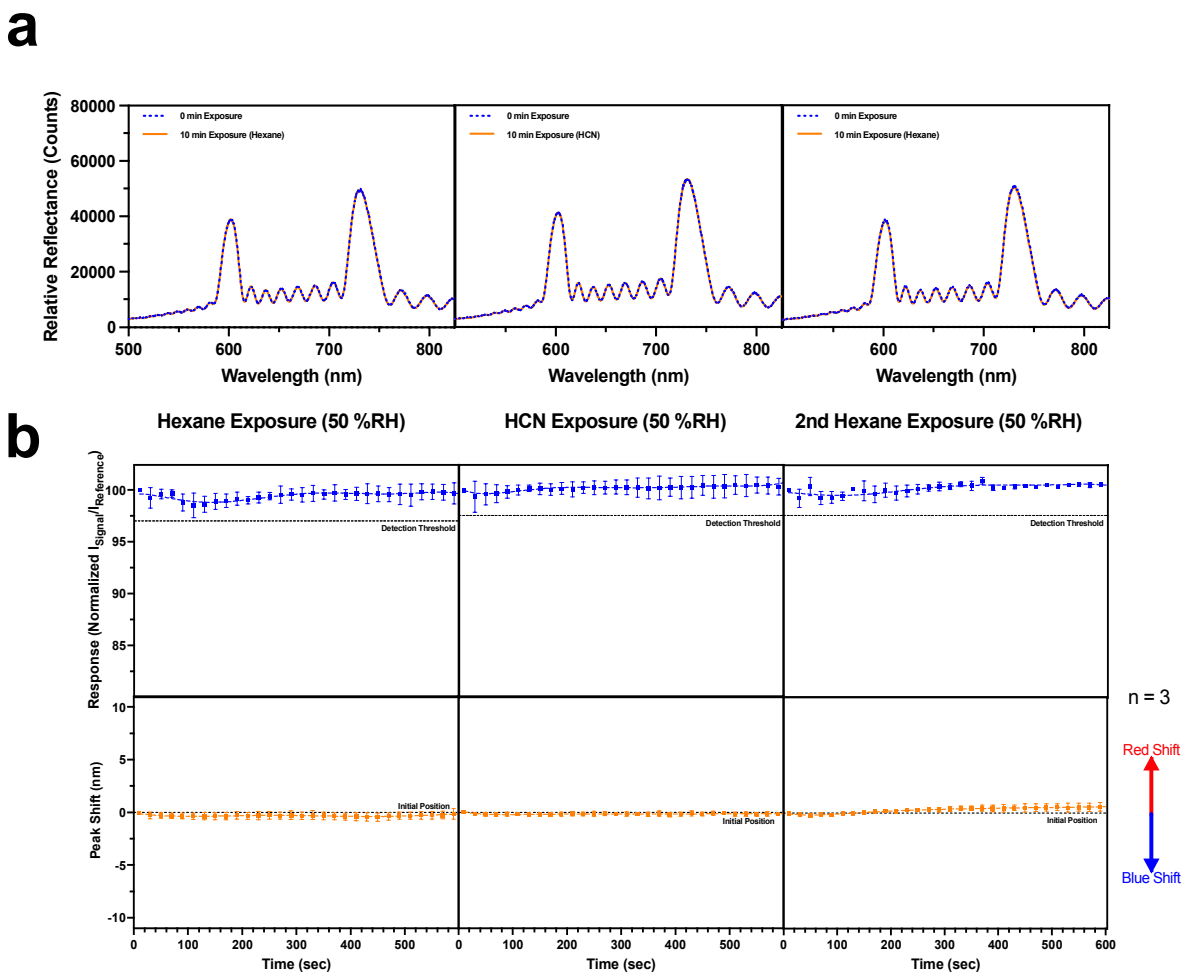

Figure 3.S9: Behavior of Cbi-dye impregnated pSi photonic crystal sensors with disassembled ^{CEE}RhuA proteins, co-incubated with $CoCl_2$. (a) Optical reflectance spectra obtained after a 10-minute exposure to neat hexane (50% RH), 10 ppm $HCN_{(g)}$ (50% RH) and neat hexane (50% RH) once more (plotted chronologically). The lack of signal response and peak shift indicates that the ^{CEE}RhuA protein must be fully assembled to provide a triggered and selective opening. (b) Temporal response and temporal peak shift curves of photonic crystal sensors upon exposure to the aforementioned vapors described in (a) neat hexane (50% RH), 10 ppm $HCN_{(g)}$ (50% RH) and neat hexane (50% RH) once more (plotted chronologically). Response metric is defined in Eq. 1.

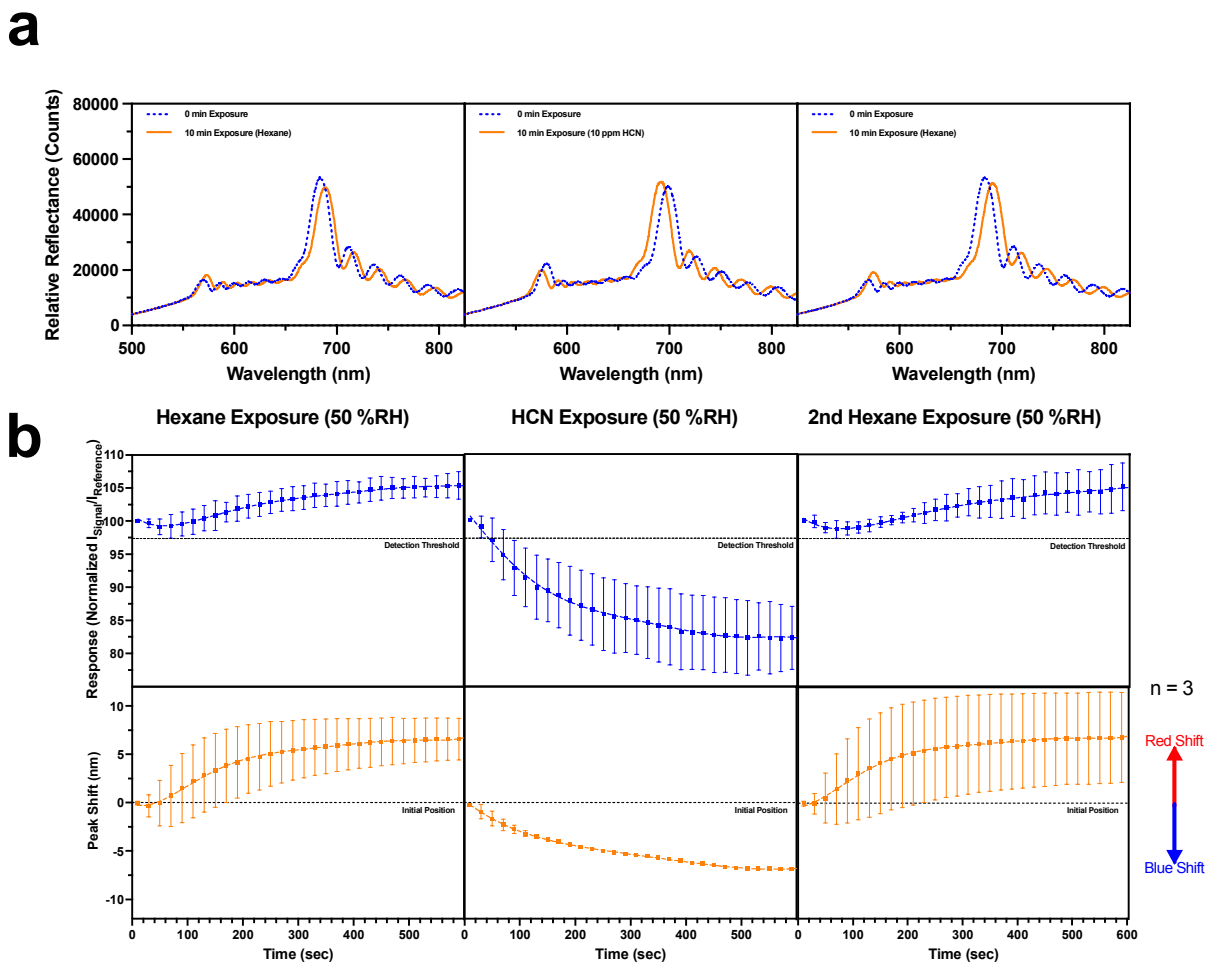

Figure 3.S10: Behavior of Cbi-dye impregnated photonic crystal sensors with a ^{CEE}RhuA protein (without $CoCl_2$ incubation) coating. (a) Optical reflectance spectra obtained after a 10-minute exposure to neat hexane (50% RH), 10 ppm $HCN_{(g)}$ (50% RH) and neat hexane (50% RH) once more (plotted chronologically). The change in the signal peak and corresponding peak shift with all vapors indicates the presence of $CoCl_2$ incubation is necessary for the gatekeeper to function as expected and reject vapors. The lack of metal to close the gatekeeper enables all vapors to penetrate the pores. (b) Temporal response and temporal peak shift curves of photonic crystal sensors upon exposure to the aforementioned vapors described in (a) neat hexane (50% RH), 10 ppm $HCN_{(g)}$ (50% RH) and neat hexane (50% RH) once more (plotted chronologically). Response metric is defined in Eq. 1.

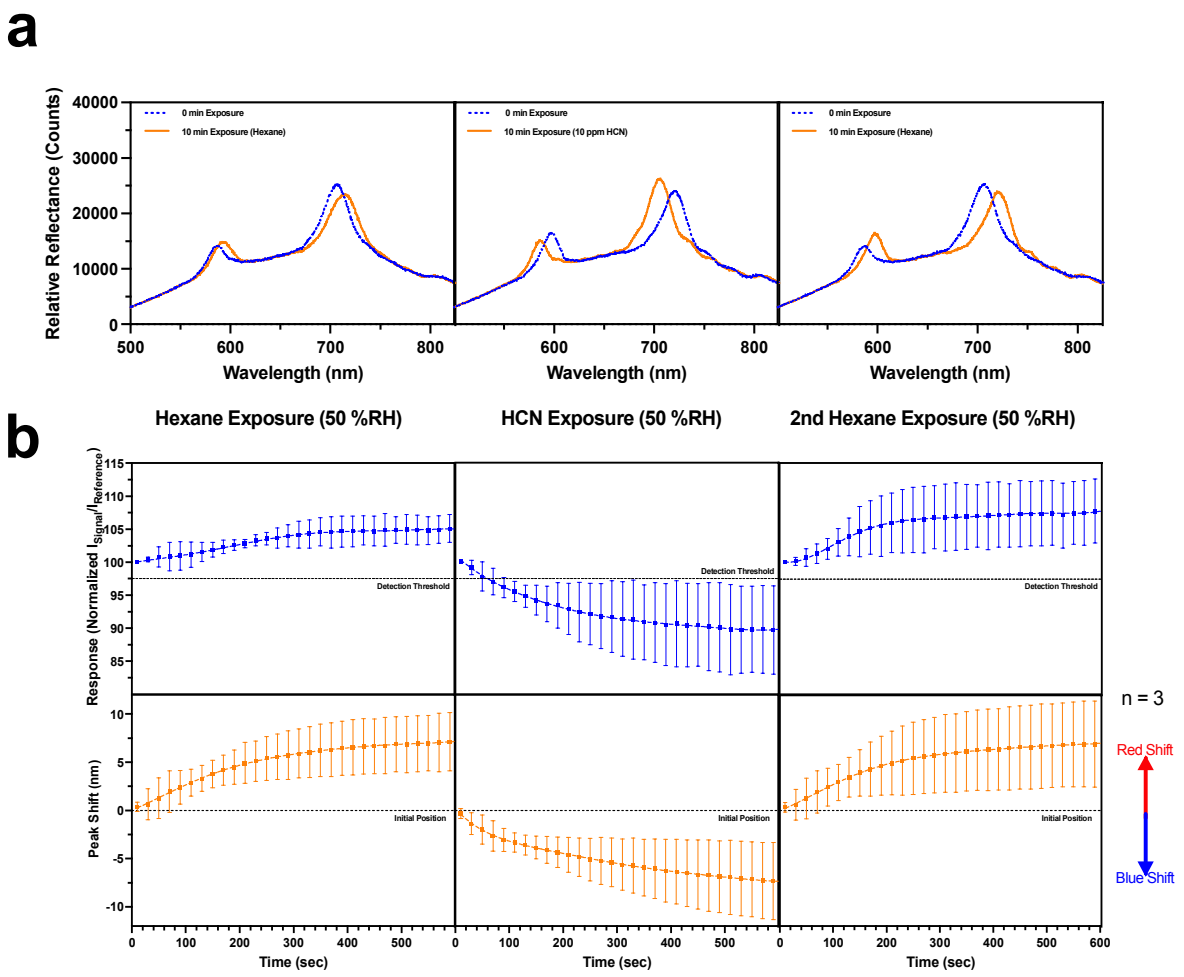

Figure 3.S11: Behavior of Cbi-dye impregnated photonic crystal sensors with a ^{CEE}RhuA protein (without $CoCl_2$ incubation) coating and vigorously mixed prior to deposition on the sensors. (a) Optical reflectance spectra obtained after a 10-minute exposure to neat hexane (50% RH), 10 ppm $HCN_{(g)}$ (50% RH) and neat hexane (50% RH) once more (plotted chronologically). The change in the signal peak and corresponding peak shift with all vapors indicates the presence of $CoCl_2$ incubation is necessary for the gatekeeper to function as expected and reject vapors. In addition, the vigorous mixing of the ^{CEE}RhuA protein does not yield any closed confirmation gatekeeper which can be triggered open as all vapors penetrate the pores. (b) Temporal response and temporal peak shift curves of photonic crystal sensors upon exposure to the aforementioned vapors described in (a) neat hexane (50% RH), 10 ppm $HCN_{(g)}$ (50% RH) and neat hexane (50% RH) once more (plotted chronologically). Response metric is defined in Eq. 1.

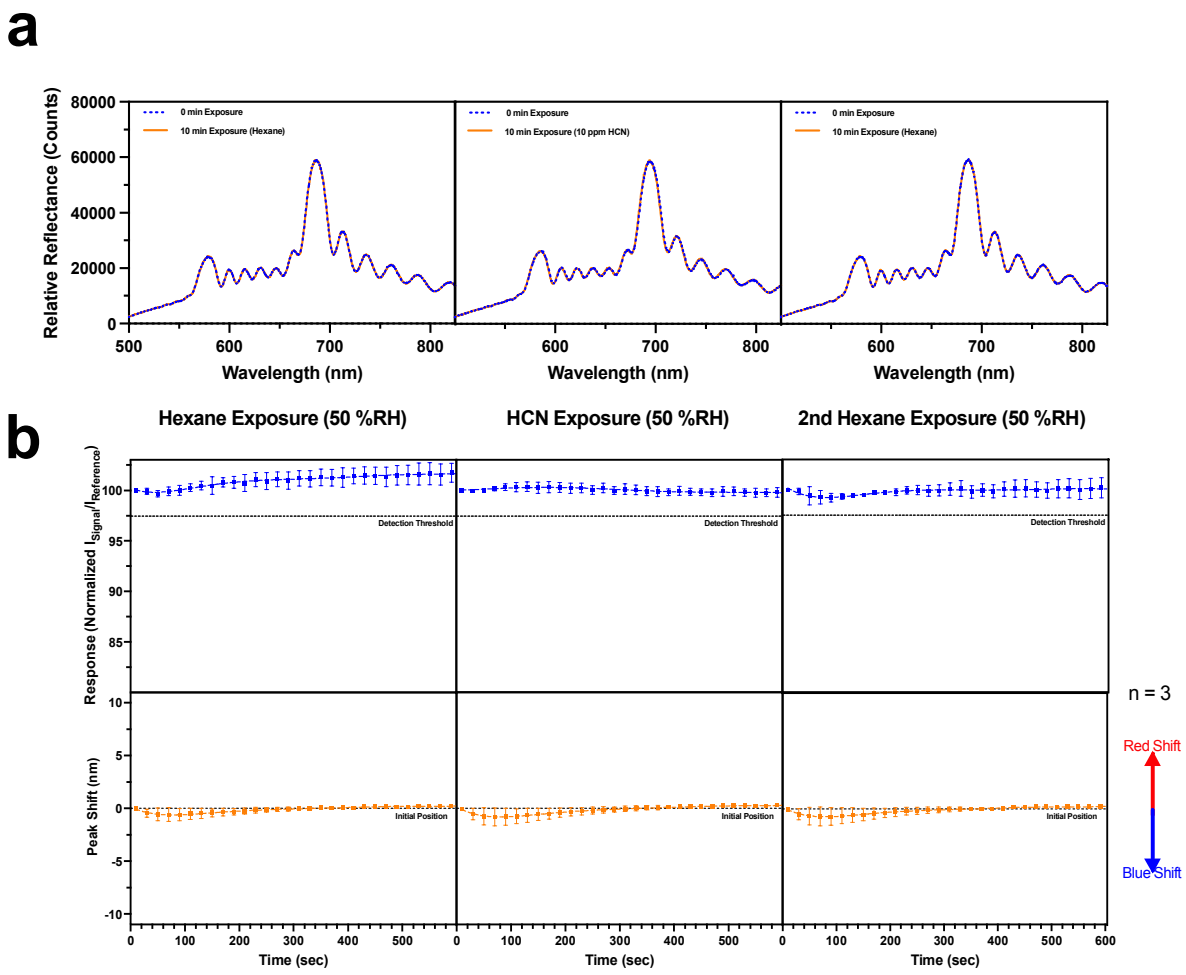

Figure 3.S12: Behavior of Cbi-dye impregnated photonic crystal sensors with a ^{C98}RhuA protein (without $CoCl_2$ incubation). (a) Optical reflectance spectra obtained after a 10-minute exposure to neat hexane (50% RH), 10 ppm $HCN_{(g)}$ (50% RH) and neat hexane (50% RH) once more (plotted chronologically). The lack of signal response and peak shift indicates that presence of ^{C98}RhuA protein does not behave as a selective gatekeeper. (b) Temporal response and temporal peak shift curves of photonic crystal sensors upon exposure to the aforementioned vapors described in (a) neat hexane (50% RH), 10 ppm $HCN_{(g)}$ (50% RH) and neat hexane (50% RH) once more (plotted chronologically). Response metric is defined in Eq. 1.

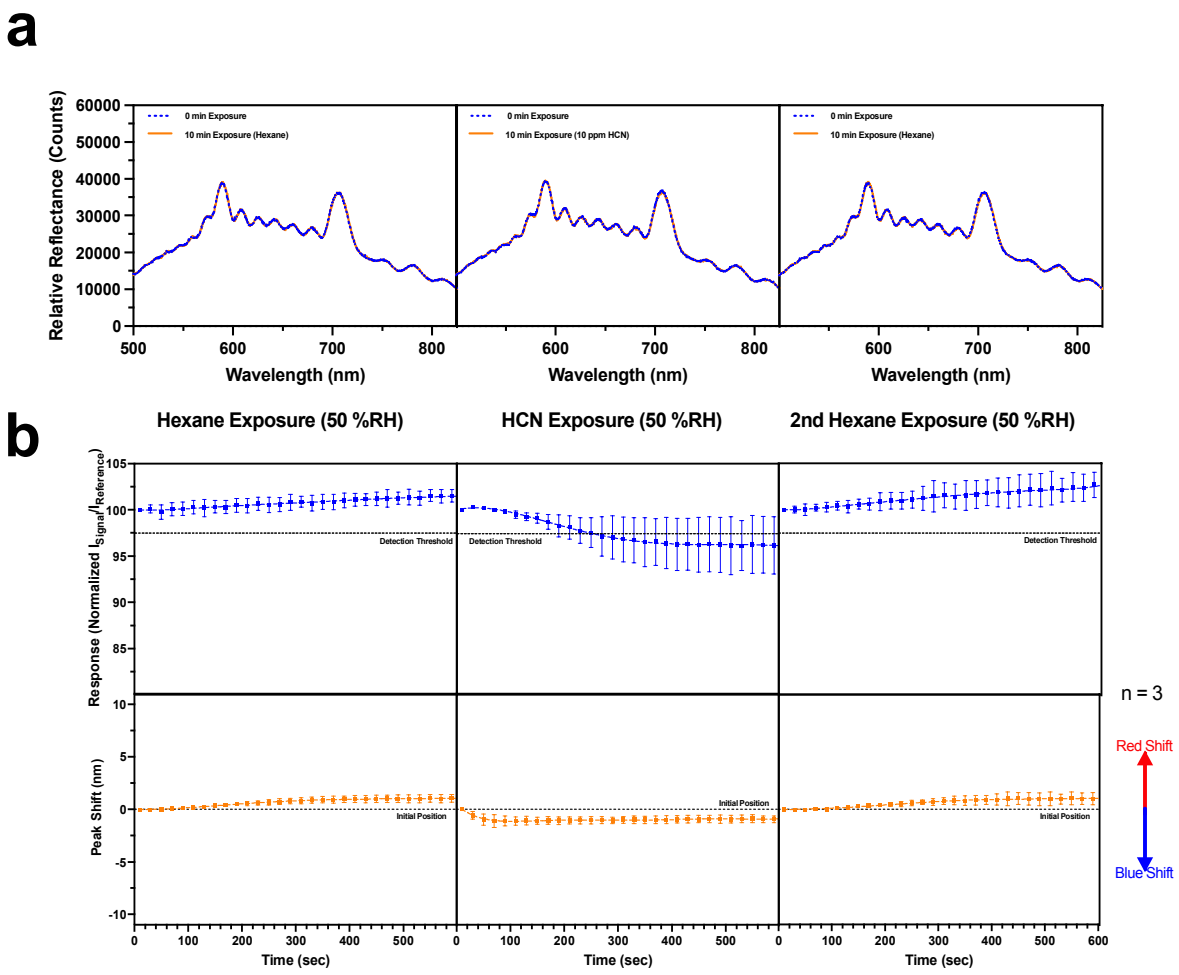

Figure 3.S13: Behavior of Cbi-dye impregnated photonic crystal sensors with a ^{C98}RhuA protein (without $CoCl_2$ incubation) and vigorously mixed prior to deposition. (a) Optical reflectance spectra obtained after a 10-minute exposure to neat hexane (50% RH), 10 ppm $HCN_{(g)}$ (50% RH) and neat hexane (50% RH) once more (plotted chronologically). The lack of signal response and peak shift indicates that presence of ^{C98}RhuA protein does not behave as a selective gatekeeper. In addition, the vigorous mixing of the ^{C98}RhuA protein does not yield gatekeeper which can be triggered open by $HCN_{(g)}$. (b) Temporal response and temporal peak shift curves of photonic crystal sensors upon exposure to the aforementioned vapors described in (a) neat hexane (50% RH), 10 ppm $HCN_{(g)}$ (50% RH) and neat hexane (50% RH) once more (plotted chronologically). Response metric is defined in Eq. 1.

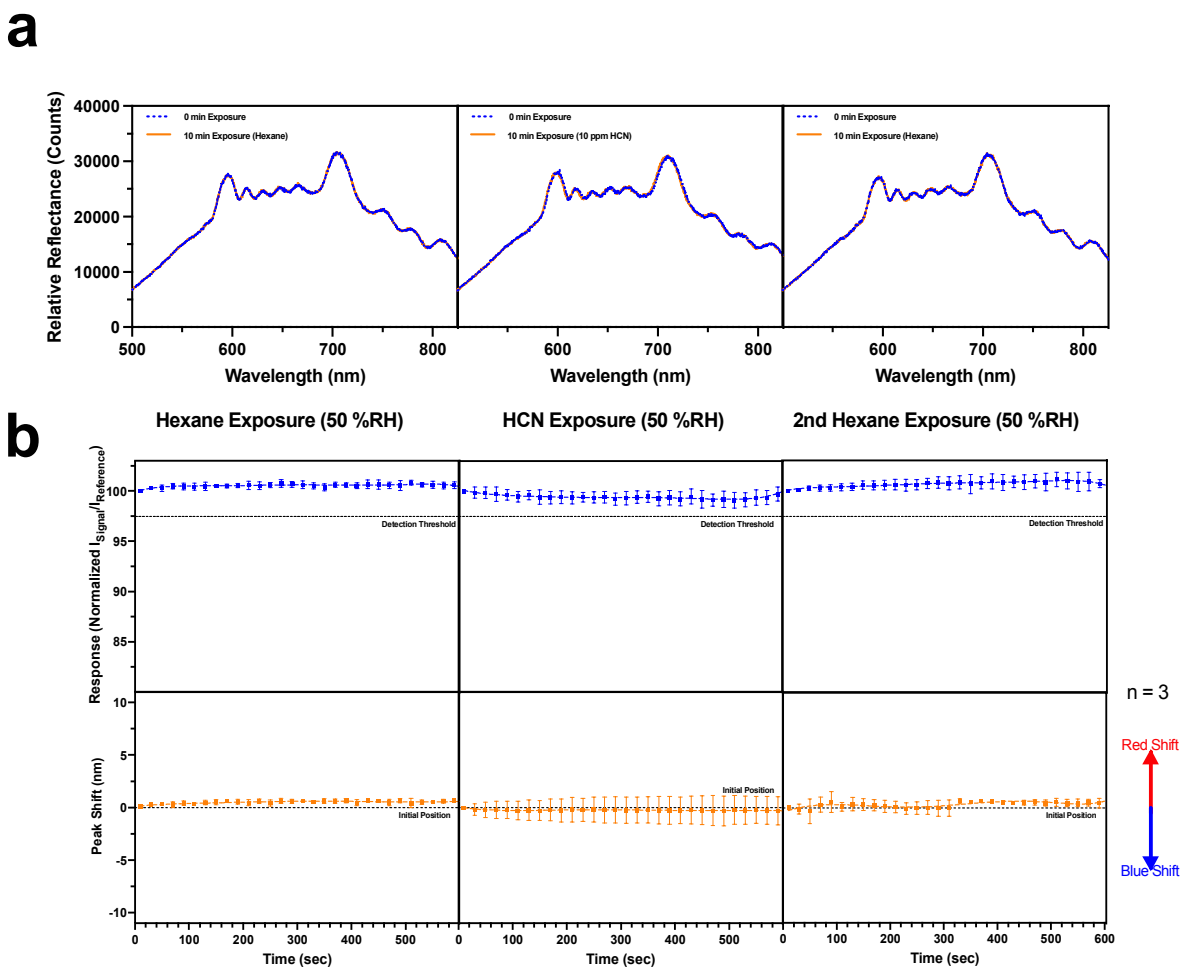

Figure 3.S14: Behavior of Cbi-dye impregnated photonic crystal sensors with a ^{C98}RhuA protein co-incubated $CoCl_2$ prior to deposition. (a) Optical reflectance spectra obtained after a 10-minute exposure to neat hexane (50% RH), 10 ppm $HCN_{(g)}$ (50% RH) and neat hexane (50% RH) once more (plotted chronologically). The lack of signal response and peak shift indicates that presence of ^{CEE}RhuA protein to behave as selective gatekeeper which can be triggered open by $HCN_{(g)}$. (b) Temporal response and temporal peak shift curves of photonic crystal sensors upon exposure to the aforementioned vapors described in (a) neat hexane (50% RH), 10 ppm $HCN_{(g)}$ (50% RH) and neat hexane (50% RH) once more (plotted chronologically). Response metric is defined in Eq. 1.

3.7 ACKNOWLEDGEMENTS

Chapter 3, in full, is currently being prepared for submission for publication of the material *Nature Nanotechnology*, 2022. Vijayakumar, S*., Alberstein, R.G*., Lu, Y.S., Chan, A., Wahl, C.E., Ha, J.S., Hunka, D.E., Boss, G.R., Tezcan, F.A., Sailor, M.J. "Photonic porous silicon sensor with integrated biological gatekeeper for remote detection of HCN vapors". The dissertation author was the primary researcher and author of this paper.

REFERENCES - CHAPTER 3

1. Y. Cai, T. Deng, Y. Pan and J. I. Zink, *Advanced Functional Materials*, 2020, **30**, 2002043.

2. W. Chen, C. A. Glackin, M. A. Horwitz and J. I. Zink, *Accounts of Chemical Research*, 2019, **52**, 1531-1542.

3. V. P. Torchilin, *Nature Reviews Drug Discovery*, 2014, **13**, 813-827.

4. M. Hamidi, A. Azadi and P. Rafiei, *Adv Drug Deliv Rev*, 2008, **60**, 1638-1649.

5. Y. Qiu and K. Park, *Adv Drug Deliv Rev*, 2001, **53**, 321-339.

6. J. Wen, K. Yang, F. Liu, H. Li, Y. Xu and S. Sun, *Chemical Society Reviews*, 2017, **46**, 6024-6045.

7. T. Jiang, A. Hall, M. Eres, Z. Hemmatian, B. Qiao, Y. Zhou, Z. Ruan, A. D. Couse, W. T. Heller, H. Huang, M. O. de la Cruz, M. Rolandi and T. Xu, *Nature*, 2020, **577**, 216-220.

8. Y.-M. Tu, W. Song, T. Ren, Y.-x. Shen, R. Chowdhury, P. Rajapaksha, T. E. Culp, L. Samineni, C. Lang, A. Thokkadam, D. Carson, Y. Dai, A. Mukthar, M. Zhang, A. Parshin, J. N. Sloand, S. H. Medina, M. Grzelakowski, D. Bhattacharya, W. A. Phillip, E. D. Gomez, R. J. Hickey, Y. Wei and M. Kumar, *Nature Materials*, 2020, **19**, 347-354.

9. T. Xu, N. Zhao, F. Ren, R. Hourani, M. T. Lee, J. Y. Shu, S. Mao and B. A. Helms, *ACS Nano*, 2011, **5**, 1376-1384.

10. C. A. Cheng, T. Deng, F. C. Lin, Y. Cai and J. I. Zink, *Theranostics*, 2019, **9**, 3341-3364.

11. W. Si, L. Chen, X.-B. Hu, G. Tang, Z. Chen, J.-L. Hou and Z.-T. Li, *Angewandte Chemie International Edition*, 2011, **50**, 12564-12568.

12. M. R. Ghadiri, J. R. Granja and L. K. Buehler, *Nature*, 1994, **369**, 301-304.

13. E. Ruoslahti, S. N. Bhatia and M. J. Sailor, *J Cell Biol*, 2010, **188**, 759-768.

14. H. Joh Nathan, T. Wang, P. Bhate Manasi, R. Acharya, Y. Wu, M. Grabe, M. Hong, G. Grigoryan and F. DeGrado William, *Science*, 2014, **346**, 1520-1524.

15. L. A. Weiss, N. Sakai, B. Ghebremariam, C. Ni and S. Matile, *Journal of the American Chemical Society*, 1997, **119**, 12142-12149.

16. Y.-S. Lu, S. Vijayakumar, A. Chaix, B. R. Pimentel, K. C. Bentz, S. Li, A. Chan, C. Wahl, J. S. Ha, D. E. Hunka, G. R. Boss, S. M. Cohen and M. J. Sailor, *ACS Sensors*, 2021, **6**, 418-428.

17. R. Alberstein, Y. Suzuki, F. Paesani and F. A. Tezcan, *Nature Chemistry*, 2018, **10**, 732-739.

18. A. M. Ruminski, G. Barillaro, C. Chaffin and M. J. Sailor, *Advanced Functional Materials*, 2011, **21**, 1511-1525.

19. B. H. King, A. Gramada, J. R. Link and M. J. Sailor, *Advanced Materials*, 2007, **19**, 4044-4048.

20. L. A. Greenawald, G. R. Boss, J. L. Snyder, A. Reeder and S. Bell, *ACS Sensors*, 2017, **2**, 1458-1466.

21. J. Lee, S. B. Mahon, D. Mukai, T. Burney, B. S. Katebian, A. Chan, V. S. Bebarta, D. Yoon, G. R. Boss and M. Brenner, *J Med Toxicol*, 2016, **12**, 370-379.

22. L. A. Greenawald, J. L. Snyder, N. L. Fry, M. J. Sailor, G. R. Boss, H. O. Finklea and S. Bell, *Sens Actuators B Chem*, 2015, **221**, 379-385.

23. J. Ma, P. K. Dasgupta, F. H. Zelder and G. R. Boss, *Anal Chim Acta*, 2012, **736**, 78-84.

24. Y. Suzuki, G. Cardone, D. Restrepo, P. D. Zavattieri, T. S. Baker and F. A. Tezcan, *Nature*, 2016, **533**, 369-373.

25. E. Gail, S. Gos, R. Kulzer, J. Lorösch, A. Rubo, M. Sauer, R. Kellens, J. Reddy, N. Steier and W. Hasenpusch, 2011, DOI: https://doi.org/10.1002/14356007.a08_159.pub3.

CHAPTER 4

ANTI-KIT- DNA APTAMER-CONJUGATED POROUS SILICON NANOPARTICLES FOR THE TARGETED DETECTIONS OF GASTROINTESTINAL STROMAL TUMORS

4.1 ABSTRACT

Evaluation of Gastrointestinal Stromal Tumors (GIST) during initial clinical staging, surgical intervention, and post-operative management can be challenging. Current imaging modalities (*e.g.*, PET and CT scans) lack both sensitivity and specificity. Therefore, advanced clinical imaging modalities that can provide clinically relevant images with high resolution would improve diagnosis. KIT is a tyrosine kinase receptor overexpressed on GIST. Here, the application of a specific DNA aptamer targeting KIT, decorated onto a fluorescently labeled porous silicon nanoparticle (pSiNP) is used for the *in vitro* & *in vivo* imaging of GIST. This nanoparticle platform provides high fidelity GIST imaging with minimal cellular toxicity. An *in vitro* analysis shows greater than 15-fold specific KIT protein targeting compared to the free KIT aptamer, while *in vivo* analyses of GIST-burdened mice that had been injected intravenously (IV) with aptamer-conjugated pSiNPs show extensive nanoparticle-to-tumor co-localization (>90 % of the injected dose) compared to controls. This provides an effective platform for which aptamer-conjugated pSiNP constructs can be used for the imaging of KIT-expressing cancers or for the targeted delivery of therapeutics.

4.2 INTRODUCTION

Gastrointestinal stromal tumor (GIST) is the most common sarcoma with ~6,000 new cases in the United States annually.[1] Conventional cross-sectional imaging techniques such as CT and MRI are routinely used for the evaluation of GIST and provide essential anatomic information for clinical staging and operative planning. Additional

functional information is provided by [^{18}F] fluorodeoxyglucose positron emission tomography (PET)[2] which non-specifically identifies the areas with increased glucose metabolism in the context of tumors, infection or inflammation. Unfortunately, these imaging modalities may fail to detect lesions or fail to differentiate GIST from benign tumors in the gastrointestinal tract including schwannomas, leiomyomas, and pancreatic rests leading to unnecessary biopsies and/or surgical resections. Therefore, non-invasive approaches with higher sensitivity and specificity are needed for: 1) initial radiological staging to identify subtle, but clinically relevant metastases; 2) improved recurrence detection after tumor resection; 3) the assessment of treatment responses in the neoadjuvant (i.e., preoperative) and metastatic settings, and 4) distinguishing GIST from other tumors that radiologically mimic GIST. To date, no such approach exists for the care of these patients.

GIST is diagnosed by overexpression of KIT, a receptor tyrosine kinase. Furthermore, approximately 60-70% of GIST are driven by oncogenic *KIT* gene mutations.[3, 4]The treatment of GIST provided the first proof of principle for precision medicine in solid tumors as driver mutations in the *KIT* gene were identified and effectively targeted with imatinib (IM; Gleevec, Novartis, Basel, Switzerland), a tyrosine kinase inhibitor (TKI). However, IM does not cure GIST. Therefore, R0 resection (*i.e.*, tumor-free margins) is the mainstay of curative treatment. Nevertheless, the risk of metastatic disease is substantial even in cases where tumor-free margins are achieved. The metastases frequently involve the peritoneal surfaces and/or liver due to peritoneal seeding and hematogenous spread, respectively. Therefore, methods to improve

visualization of metastases may be advantageous for more accurate radiographic staging and treatment decision making for patients with GIST.[5]

Currently, GIST diagnosis relies on analyzing tissue procured from either biopsy or surgical specimens. Although KIT-expressing GISTs are effectively diagnosed with immunohistochemical staining with anti-KIT antibodies, this approach requires maintaining hybridomas for production which is expensive and time consuming. Aptamers are a promising alternative to antibodies as a targeting species. Aptamers are single-stranded (ss) oligonucleotide (ssDNA or ssRNA) ligands that are selected against specific cell or protein targets through SELEX (Systematic Evolution of Ligands by Exponential Enrichment), an *in vitro* iterative process.[6, 7] Aptamers assume their structure through intra-molecular base-pairing between complementary nucleotides, and they assume secondary, then tertiary structures. These complex DNA structures can bind to their cognate targets with high affinity and specificity, with binding constants comparable to monoclonal antibodies. Due to their small size, aptamers have shown greater tissue penetration in comparison to antibodies as well as are non-immunogenic. Aptamers are also amenable to a variety of chemical modifications including conjugation with compounds such as fluorophores or drugs. Thus, modified aptamers have been proposed for several applications including *in vitro* and *in vivo* imaging, as well as targeted drug delivery.[8, 9]

Recently we published the first report to employ an anti-KIT aptamer for targeted labeling of GIST. We demonstrated that the aptamer bound to cancer cells in a KIT-dependent manner and was highly specific for GIST cell labelling *in vitro*. Functionally, the KIT aptamer bound extracellular KIT in a manner similar to KIT monoclonal antibody

staining and was trafficked intracellularly *in vitro*. The KIT aptamer bound dissociated primary human GIST cells. Additionally, the KIT aptamer specifically labeled intact human GIST tissue *ex vivo*, as well as peritoneal xenografts in mice with high sensitivity. These results represented the first application of an anti-KIT DNA aptamer-based method for targeted detection of GIST *in vitro* and *in vivo.*[10] However, the system needed improvement in two aspects in order to enable translation. These included increasing the binding affinity of the aptamer and improving the ability to detect this binding in a fashion that is amenable to intraoperative monitoring.

Traditional imaging approaches such as Computed Tomography (CT) or Magnetic Resonance Imaging (MRI) routinely fail to detect lesions, clinically relevant metastases, or to differentiate GIST from benign tumors leading to unnecessary biopsies and surgical resections.[10-12] PET and fluorescence-based approaches provide essential anatomic information for surgeons regarding clinical staging and operative planning, though they require a substantially high concentration of imaging agent. Fluorescent probes bring the added disadvantage that they can be easily photobleached.[13-15] Nanoparticles can overcome these issues by providing a vehicle in which a considerable concentration of imaging agent can be entrapped, which serves to protect the fluorescent payload from photobleaching while increasing its circulation time throughout the body until it reaches its target.[13, 15]

A challenge with GIST is the formation of metastases that is commonly associated with drainage tissues. It has been previously demonstrated that nanoparticle complexes are cleared by the renal system and/or the reticuloendothelial system (RES) including the liver, spleen, and lungs. Being able to specifically target metastatic regions, while limiting

non-specific endocytotic uptake by healthy cells and macrophages is a major challenge. Recent works have shown the effective use of nanoparticles for the imaging of GIST through MRI and near-IR fluorescence.[11, 16] However, these ultra-small (<10nm) nanoparticle complexes utilized the EPR effect to localize to the GIST tumors. Despite this promising work, relying on the EPR effect for targeting has been shown to be less effective than specific receptor targeting.[17-23]

The combination of targeting moieties and nanoparticles has been shown to be an effective platform in targeting tumors and other hard-to-reach organs. Nanoparticles provide an enhanced surface area in which multiple copies of a targeting moiety, such as monoclonal antibodies, peptides, or aptamers can be conjugated onto a single carrier, enhancing its specific targeting capabilities by providing multiple orientations in which the carrier could bind to the tumor receptor.[21, 22] Compared to free targeting counterparts, recent literature has shown up to an 30- to 40- fold greater targeting efficacy for nanosystems conjugated with targeting moieties.[17, 19, 21, 22] A wide range of nanocarriers are of interest, ranging from lipids and polymers to metallic particles. Porous silicon nanomaterials have been used extensively for the imaging and treatment of cancers due to their low-toxicity degradation pathway (that yields silicic acid end products which are readily excreted from the body), surface chemistry, and their tunable mesoporous features.[14, 17, 19, 20, 24] Porous silicon nanoparticles (pSiNP) have been previously used for the specific targeting of tumors with the surface-conjugation of peptides, antibodies and aptamers, and they have been used as a delivery vehicle for biological payloads and imaging agents, due to their large open pore volumes (typically 50-80%).[14, 15, 18, 19, 25-27]

This study was designed to develop a simple nanoparticle imaging construct that can be injected intravenously (IV) to GIST-burdened mice. Therefore, in this context, a porous silicon nanoparticle (pSiNP) would provide an attractive delivery platform due to the many tunable pore characteristics that can be used to load imaging agents while its very versatile surface chemistry can enable specific functionalization of targeting moieties. Utilizing *in vitro* experiments with KIT expressing cells, we demonstrated the enhanced multivalency effects of an aptamer-grafted nanoparticle compared to free KIT aptamers and KIT mAb. We reasoned that, by conjugating this aptamer onto a nanoparticle construct, its binding affinity can be increased by conjugating multiple aptamer-ligands onto a single particle.[21] We subsequently used human GIST injected mice for the *in vivo* labelling of GIST, isolating GIST liver metastases, and assessing tumor co-localization. We found that the KIT-aptamer conjugated pSiNPs can detect GIST cells with high affinity showing greater than 90% of tumor co-localization of visible metastases of nanoparticle to tumor signals within harvested *ex vivo* IVIS images of organs and fluorescence images of GIST-burdened liver sections when assessed through ImageJ. This study provided the first proof of principle that anti-KIT DNA aptamers conjugated onto pSiNPs can be a platform for the targeted imaging of GIST, which has implications for the targeted imaging and delivery of therapeutics for other KIT-expressing cancers.

4.3 Results & Discussion

4.3a Development of Aptamer-Conjugated Nanoparticles

The porous silicon nanoparticles (pSiNPs) were prepared as previously described.[28] The as-formed nanoparticles displayed an average hydrodynamic diameter of 156 ± 20 nm, as measured by dynamic light scattering (DLS). The specific surface area was 333 ± 14.71 m^2/g, the pore volume 1.38 ± 0.08 cm^3/g and the average pore size was 15 ± 0.13 nm, as determined from N_2 adsorption/desorption isotherms using the Brunauer-Emmett-Teller (BET) and Barrett–Joyner–Halenda (BJH) models (**Figure 4.2c & Table 4.S1**, Supporting Information). The nanoparticles were functionalized with heterocyclic-silanes (known as pSiNP-NH_2) and conjugated with fluorescent imaging labels Cy5.5 or fluorescein isothiocyanate (referred to here as pSiNP-NH_2-Cy5.5 or pSiNP-NH_2-FITC, respectively) onto the amine-terminated surface. The particles were subsequently PEGlyated with a bifunctional PEG linker (referred to here as pSiNP-NH_2-Cy5.5-PEG or pSiNP-NH_2-FITC-PEG, respectively). These multiple processes provided a slight increase in the hydrodynamic diameter and changes in pore size and pore volume (**Figure 4.2d & Table 4.S2**, Supporting Information).

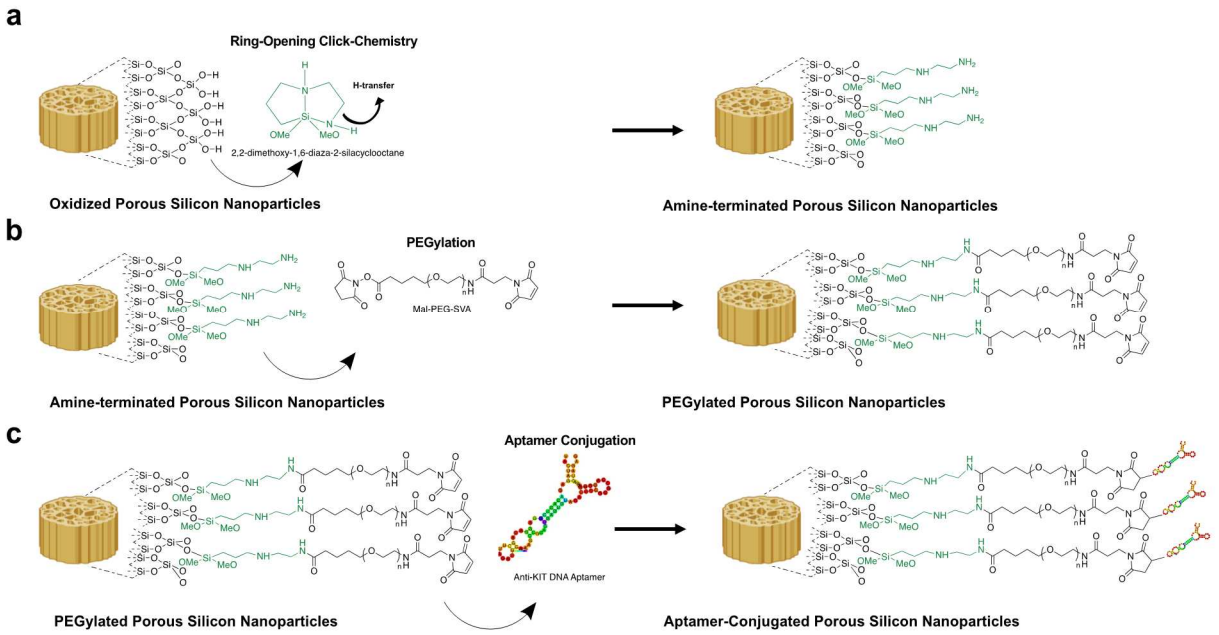

Figure 4.1: Preparation of silane-modified pSiNPs for the attachment of PEG and aptamers. (a) Schematic illustration of the ring-opening procedure to functionalize pSiNPs with primary amines for the attachment of PEG. (b) Schematic illustration of the attachment of Mal-PEG-SVA to enable circulation of the particles *in vivo* while also providing a surface for which the aptamer ligands could bind to the particle. (c) Schematic illustration of the KIT aptamer attachment. The SH- terminated aptamers bind covalently to the maleimide-terminated PEG on the pSiNPs through sulfhydryl- maleimide coupling.

The final nanoparticle construct had a coating of polyethylene glycol (PEG) with a functional tail that was used to attach the aptamer. The PEG coating was attached to the pSiNPs through the addition of a cyclic azasilane reagent (DMDASCO, 2,2-dimethoxy-1,6-diaza-2-silacyclooctane), which was used to functionalize primary amine groups easily and rapidly onto the pSiNP surface *via* a ring-opening click reaction (**Figure 4.1a**).[8] The successful functionalization of the silane was confirmed through Fourier transform infrared (FTIR) spectroscopy, dynamic light scattering (DLS) and ζ-potential measurements, indicating both N–H stretching and bending modes an increase in size and positive surface charge values (+18 ± 4 mV) (**Table 4.S2**). Both the positive charge and the amine terminal groups enabled a reactive surface for NHS ester-terminated

fluorophores to be grafted to the particle. This yielded a slight change in the ζ-potential measurements, but an increase in the particles' fluorescence for both Cy5.5 and FITC dyes (**Table 4.S2, Figure 4.S1 & Figure 4.S2**, Supporting Information). The remaining primary amine groups were used to graft PEG chains to the particle surface. A specialized PEG, maleimide-PEG-succinimidyl valerate (MAL-PEG-SVA) was utilized as a protective overcoat for the particles. This PEG formed amide bonds between the succinimidyl valerate and the surface primary amine groups of the pSiNPs, leaving a free maleimide group at the terminal end, used for aptamer attachment. The functionalization of the PEG group was also confirmed through FTIR spectroscopy and DLS measurements, yielding an increase in the hydrodynamic size and functional groups of strong aliphatic C–H stretching and amide C═O stretching bands (**Table 4.S2 & Figure 4.S2b**, Supporting Information). The KIT aptamer was subsequently grafted onto the nanoparticle using the terminal maleimide groups from the PEG (**Figure 4.1c**). The aptamer, with a thiol termination, was grafted using the commonly used sulfhydryl-maleimide reactive crosslinker coupling to form a covalent thioether bond (known as pSiNP-NH_2-Cy5.5-PEG-KIT or pSiNP-NH_2-FITC-PEG-KIT). Due to the presence of negatively charged aptamer ligands on the nanoparticles surface, the ζ-potential measurement decreased in value to +2.33 ± 1.02 mV (**Table 4.S2**, Supporting Information). Aptamers grafted to the pSiNP surface were also confirmed using FITC-labelled aptamers, with a 6-FAM label conjugated to the 3' end of the aptamer. By measurement of the optical absorbance of the supernatant (λ = 520), the amount of aptamer on the surface was found to be 32.52 ± 3.23 nmol/mg pSiNP (n = 3), which corresponds to a yield of 81.3 % of the added aptamer that became bound to the pSiNP surface (**Figure 4.S3**, Supporting Information).

Similarly, thermogravimetric analysis (TGA) measurements were used to assess the PEG surface coverage (**Figure 4.S4**, Supporting Information).

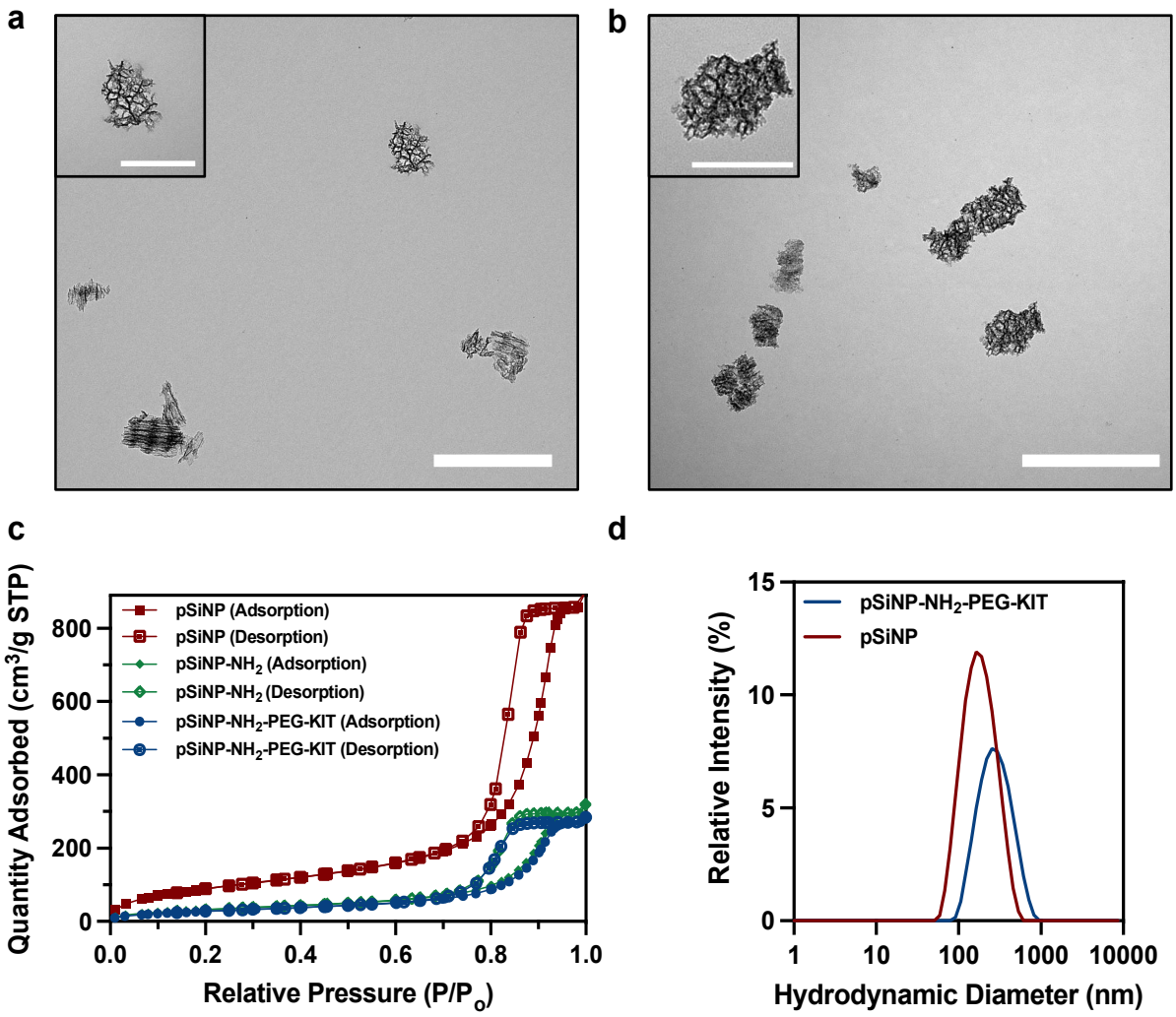

Figure 4.2: KIT-Aptamer conjugated porous silicon nanoparticles (KIT-pSiNP). Transmission Electron Microscopy (TEM) images of (a) freshly etched and (b) aptamer-conjugated particles (scale bar = 500 nm); the insert shows a closer view of a single nanoparticle (scale bar = 200 nm). (c) N_2 adsorption–desorption isotherms of the empty, unmodified pSiNPs, silane-functionalized pSiNPs and aptamer-conjugated, PEGylated pSiNPs. The isotherms are used to determine the pore size and pore volume of the particles. (d) Dynamic light scattering (DLS) data of freshly etched pSiNPs and PEGylated and aptamer-conjugated particles. There is an increase in hydrodynamic size due to the surface functionalization, PEGylation and aptamer conjugation of the particles.

4.3B *IN VITRO* CELLULAR TARGETING

Cellular targeting and imaging properties of the pSiNPs were screened using two cancer cell lines that overexpress KIT receptors, HMC-1.2 (Mastocytosis) and GIST-T1 (Gastrointestinal stromal tumor) as a preliminary model. We wanted to determine the specificity of the anti-KIT aptamer, conjugated to pSiNPs to bind to cells in a KIT-dependent manner. Initially, ssDNA KIT aptamers were obtained from previously published literature (5'-GAGGCATACCAGCTTATTCAAGGGGCCGGGGCAAGGGGGGGGTACCGTGGTAGG ACATAGTAAGTGCAATCTGCGAA-3').[10] In addition, a scrambled aptamer sequence was generated through a random oligonucleotide sequence generator, with the same free energy of the specific KIT aptamer sequence. The scramble sequence is as follows: (5'-TGACGGGAGACTTAAAACGCAAGGGGTGCAGCTATCGCGGAGGCCAAGGGTTCA AGTCGACGGGTAGCTA- GGTTGGA-3'; Oligo Calculator version 3.27, biotools.nubic.-northwestern.edu). Both the aptamer and scramble sequences were synthesized with a thiol modification on the 5' end and both an unmodified sequence and a 6-FAM fluorophore modification on the 3' end (Integrated DNA Technologies) for the various experimental applications. Though this KIT aptamer has previously displayed tumor-targeting properties, they have not been used as an active ligand mounted on pSiNPs targeting GIST cancers. For comparison, we have included in our experimental controls, the scramble aptamer target to measure specificity as well as free aptamer targets and a KIT-specific monoclonal antibody (mAb) as controls to measure multivalency effects of aptamer-conjugated pSiNP constructs as compared to free aptamer ligands and KIT mAb. Following the conjugation procedure, scramble aptamers were bound to the

fluorophore-labelled nanoparticles, while equivalent concentrations of free aptamer, anti-KIT specific and scramble, were used as individual controls. In addition, an anti-KIT mAb was used as another positive control to compare the binding of the KIT aptamer conjugated particles. Both HMC-1.2 and GIST-T1 cells were incubated with either the aptamer-nanoparticle constructs (pSiNP-NH_2-FITC-PEG-KIT, pSiNP-NH_2-FITC-PEG-SCR, pSiNP-NH_2-FITC-PEG), free aptamers (KIT-6-FAM & SCR-6-FAM), and antibody (KIT mAb) to confirm the intracellular localization of the labelled particles and aptamers after 1 hour and were subsequently quantified by flow cytometry (**Figure 4.3a & Figure 4.S5**, Supporting Information). Confocal micrographs were subsequently taken of the nanoparticle constructs and were consistent with the nanoparticle cellular uptake of the pSiNP-NH_2-FITC-PEG-KIT particles (**Figure 4.3b**). The significant difference of the FL1-A Fluorescence geometric mean (GM) of pSiNP-NH_2-FITC-PEG-KIT particles compared to the scramble-aptamer and non-aptamer conjugated pSiNP controls show that the pSiNP-NH_2-FITC-PEG-KIT are specific to both GIST-T1 (12.83-fold binding increase than pSiNP-NH_2-FITC-PEG-SCR & 12.92-fold binding increase than pSiNP-NH_2-FITC-PEG) and HMC-1.2 cell lines (17.41-fold binding increase than pSiNP-NH_2-FITC-PEG-SCR & 27.48-fold binding increase than pSiNP-NH_2-FITC-PEG). Compared to free KIT aptamers and a KIT mAb, the pSiNP-NH_2-FITC-PEG-KIT constructs showed a 5.24- and 5.64-fold binding increase for GIST-T1 cells and 5.39- and 5.70-fold increase with HMC-1.2 cells respectively (**Figure 4.3a & Figure 4.S5a**, Supporting Information) Due to the results of these experiments, we decided to go forth with *in vivo* studies.

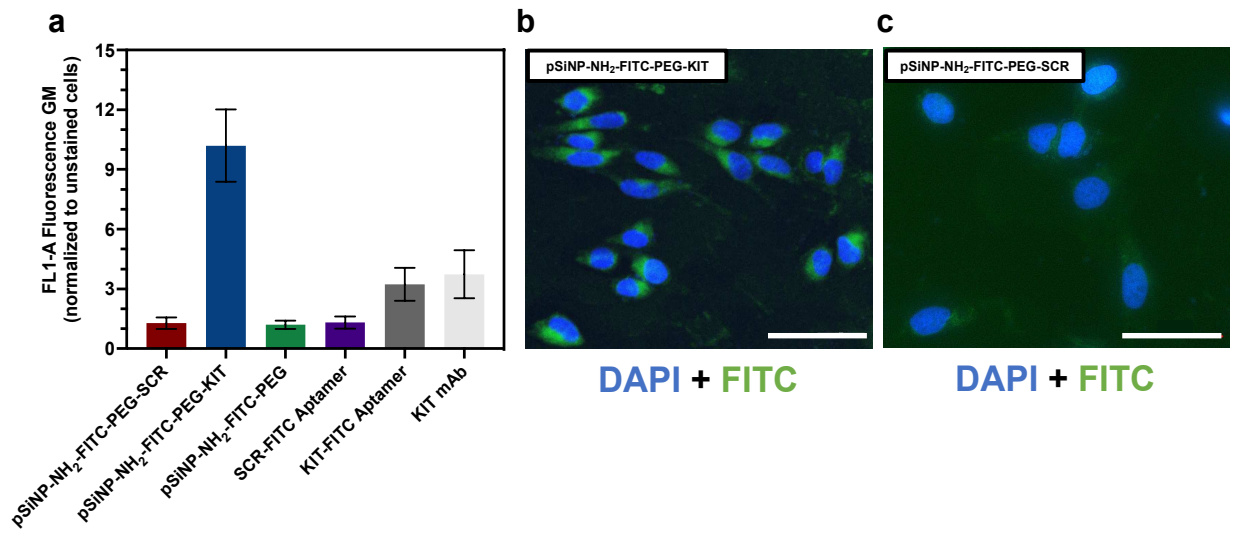

Figure 4.3: Investigation of cellular targeting of pSiNP constructs in a model GIST-T1 cancer cell line. (a) Interaction of GIST-T1 cells with pSiNP constructs quantified by flow cytometry (mean value ± SD, n = 3, $p < 0.05$). Confocal microscopy images of GIST-T1 cells incubated with (b) pSiNP-NH_2-FITC-PEG-KIT constructs and (c) pSiNP-NH_2-FITC-PEG-SCR. Both images are merged laser lines for DAPI and FITC (scale bar = 50 μm).

4.3C *IN VIVO* & *EX VIVO* CELLULAR TARGETING OF NANOPARTICLES

We next investigated the *in vivo* binding and localization of KIT-Aptamer conjugated particles and control nanoparticles. Following previously developed intrasplenic GIST-T1 models, we examined pSiNP-NH_2-Cy5.5-PEG-KIT binding to the tumors.[10, 12, 29-31] GIST-T1-GFP cells, co-injected with cancer associated fibroblasts (CAFs) were used in this model to visualize the tumor burden. We previously demonstrated that in the spleen-to-liver-GIST metastasis model used here, the CAFs can accelerate GIST growth and metastasis.[32] Three weeks after intrasplenic injection, mice underwent tail-vein injection of either pSiNP-NH_2-Cy5.5-PEG-KIT, pSiNP-NH_2-Cy5.5-PEG-SCR or pSiNP-NH_2-Cy5.5-PEG constructs at a concentration of 10 mg/kg. Binding of the constructs were assessed every hour for 5 hours, based on the intensity of the Cy5.5 signal for each mouse, using IVIS (In Vivo Imaging System) (**Figure 4.S6a**, Supporting Information). It is seen that the mean signal intensities of pSiNP-NH_2-Cy5.5-

PEG-SCR and pSiNP-NH_2-Cy5.5-PEG were lower than that of pSiNP-NH_2-Cy5.5-PEG-KIT signals. After 5 hours, the Cy5.5 intensities of all the pSiNP constructs were assessed to identify the greatest signal within the abdomen (**Figure 4.4**). As pSiNP-NH_2-Cy5.5-PEG-KIT constructs selectively bind to GIST-T1 tumors, any non-specific particle constructs, pSiNP-NH_2-Cy5.5-PEG-SCR and pSiNP-NH_2-Cy5.5-PEG, would be cleared out from the mice much more rapidly. Collectively, all these measurements suggest that the scrambled pSiNP-NH_2-Cy5.5-PEG-SCR and pSiNP-NH_2-Cy5.5-PEG constructs are non-selective due to their faster clearance from these RES tissues while the pSiNP-NH_2-Cy5.5-PEG-KIT had increased tumor detection due to the strong signal intensities at the multifocal disease sites.

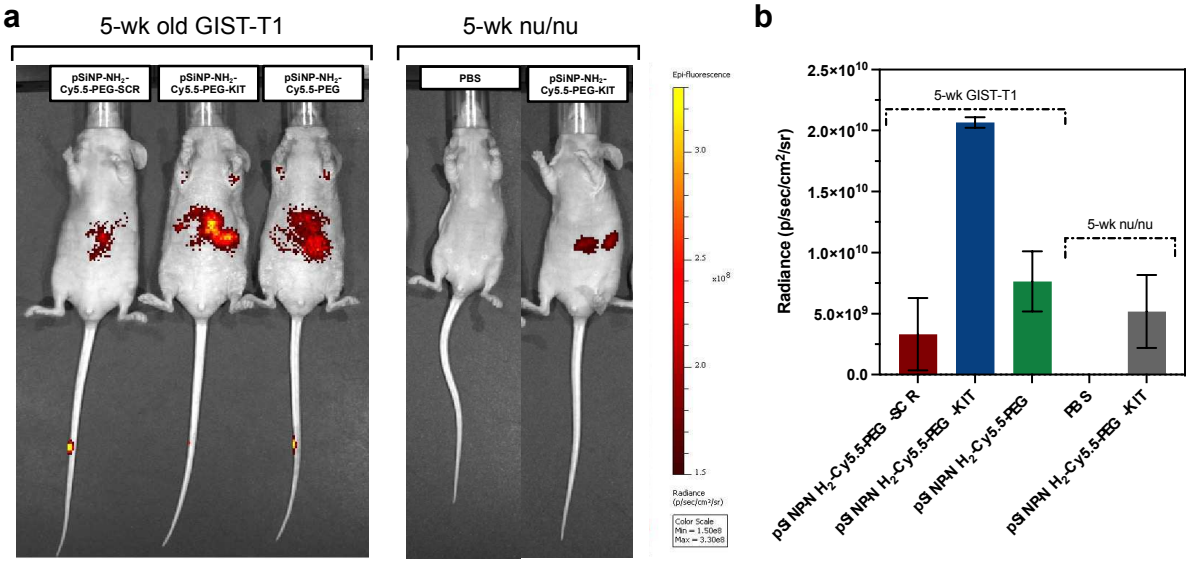

Figure 4.4: *in vivo* evaluation of targeted pSiNP constructs in GIST-T1 model. (a) IVIS images of both 5-week-old GIST-T1 and 5-week-old nu/nu mice injected with pSiNP constructs tail-vein. Cy5.5 signals, from fluorophores attached onto the pSiNP constructs were isolated within abdomen regions after 5 hours. (b) The IVIS signals were quantified for different construct groups indicating that injection of pSiNP-NH_2-Cy5.5-PEG-KIT particles produces the highest radiance signal (mean value ± SD, n = 3, $p < 0.05$).

We next evaluated the biodistribution of the nanoparticle constructs within our tumor-bearing mice. Analysis of the specific binding to these tumors were done by harvesting the organs after 5 hours post nanoparticle injection, for what we have named as *ex vivo* imaging for this study. Separately, the organs were imaged *ex vivo* by IVIS to isolate for the GIST-T1 metastases using a GFP signal. Subsequently, the Cy5.5 signal from the administered particles were also measured. Both signals were subsequently merged to isolate for the signal overlap. This step was repeated for all sets of particle constructs (**Figure 4.5a**). The merged GFP and Cy5.5 signal images were then assessed using ImageJ to analyze the signal overlap, known as GFP Co-Localization (%), to quantify the binding effectiveness of the pSiNP-NH_2-Cy5.5-PEG-KIT constructs towards GIST metastases (**Figure 4.5b & Figure 4.5c**). The importance of calculating the GFP co-localization is that our GIST model metastasizes within organs that are part of the reticuloendothelial system (RES) and mononuclear phagocyte system (MPS). As nanoparticles are cleared by phagocytes; hepatic clearance by Kupffer cells within the liver and the spleen and renal clearance by the kidneys, the importance of specific binding to GIST-T1 metastases that occur within these regions is paramount due to the potential of non-specific uptake in these organs. Active-targeted pSiNPs bearing KIT specific aptamers will bind to, and be internalized by these solid tumors, while non-active-targeted nanoparticles will be distributed within these organs non-specifically. The calculation of GFP co-localization will provide a quantitative measure of nanoparticle specificity (pSiNP-NH_2-Cy5.5-PEG-KIT) versus other non-GIST-specific nanoparticle controls (pSiNP-NH_2-Cy5.5-PEG-SCR and pSiNP-NH_2-Cy5.5-PEG). Through ImageJ, the specificity of pSiNP-NH_2-Cy5.5-PEG-KIT particles is significant, with greater than 90% in tumor co-localization

for both the liver and spleen (mean value ± SD, n = 3, *p < 0.05) while pSiNP-NH_2-Cy5.5-PEG-SCR and pSiNP-NH_2-Cy5.5-PEG controls yield very little non-specific uptake (15%> co-localization) due to its random distribution within the liver and spleen. From Figure 5a, there is no visible GIST metastases within the kidneys as well as a significantly lower nanoparticle distribution. The lack of GFP signal limited the quantification of pSiNP to GFP co-localization within this organ.

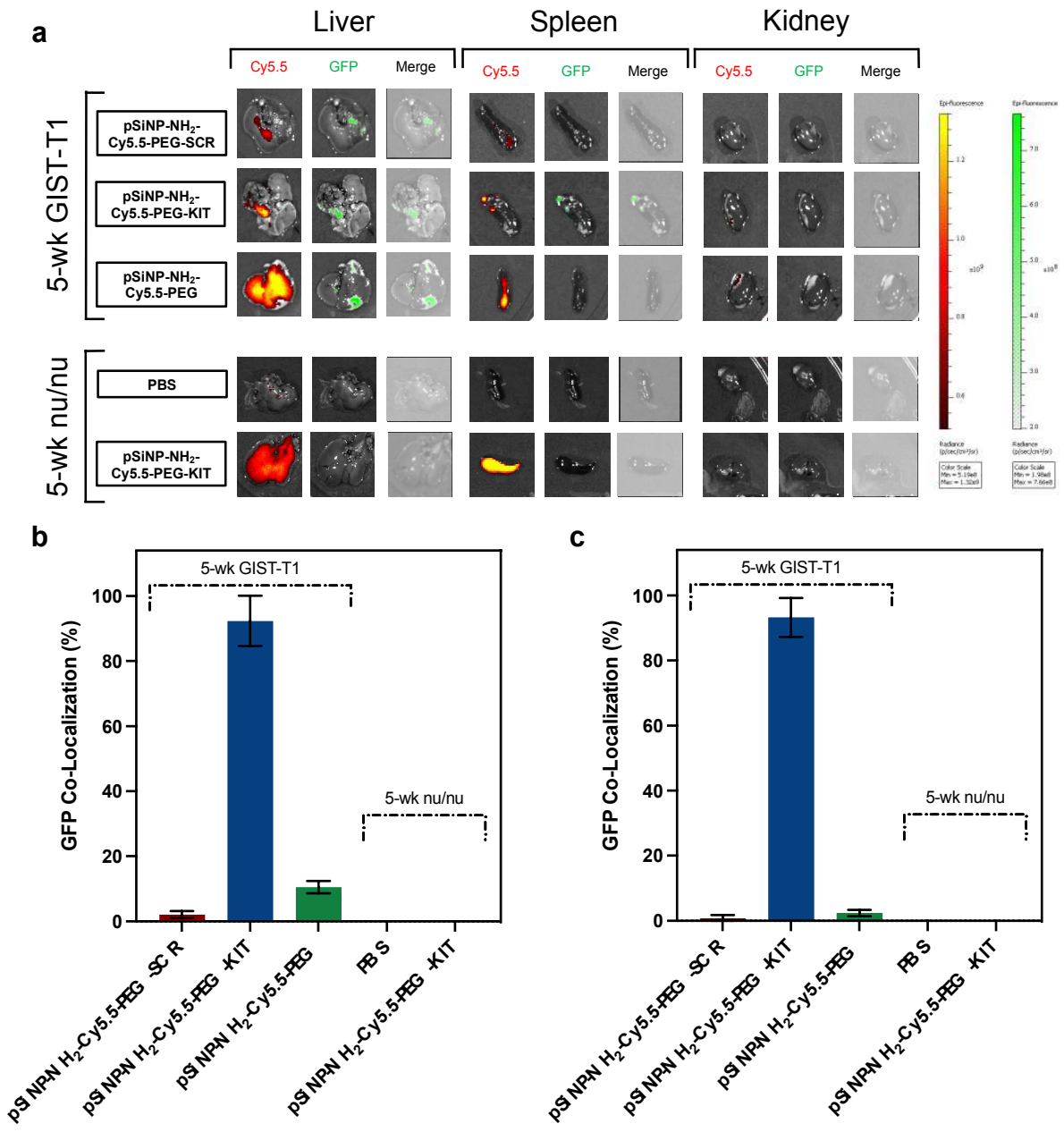

Figure 4.5: *ex vivo* imaging of abdominal organs following injection of pSiNP constructs. (a) IVIS images of harvested liver, spleen, and kidneys of GIST-T1 tumor burden and nu/nu mice. Both Cy5.5 signals from the injected pSiNP constructs and GFP signals from the GIST-T1-GFP metastases were imaged, and the signals were merged. GIST-T1-GFP co-localization for pSiNP constructs as assessed by ImageJ for (c) the liver and (d) spleen for GIST-T1 tumor burden and nu/nu mice (mean value ± SD, n = 3, $p < 0.05$). Kidneys were not assessed for co-localization as no visible GFP signal was measured in any of the mice.

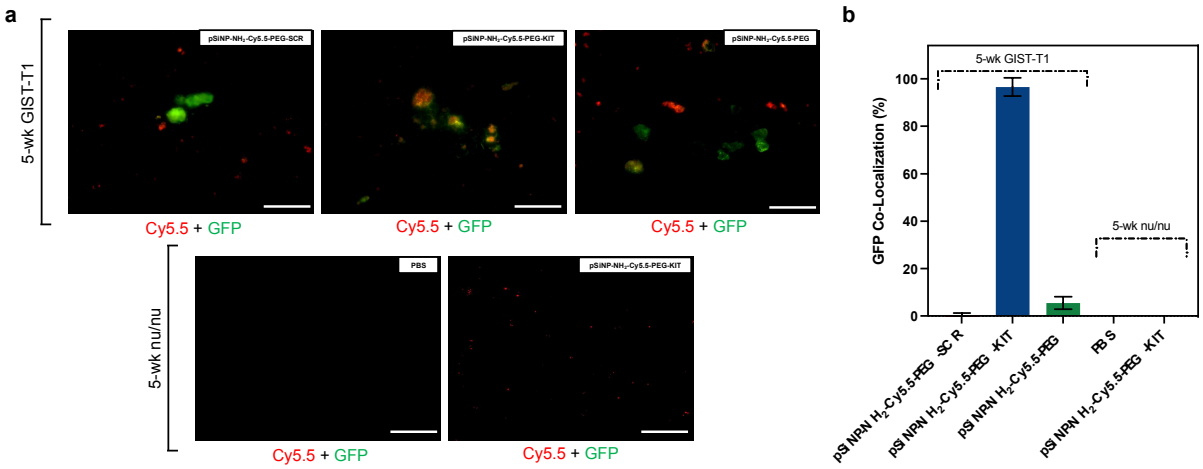

Figure 4.6: *ex vivo* imaging of frozen liver tissues. (a) Fluorescence images of frozen liver sections with merged Cy5.5 (red) and GFP (green) signals of GIST-T1 model containing metastasis that were sectioned and imaged by confocal microscopy. Frozen liver tissues of 5-wk old nu/nu mice were also imaged as a control to assess the distribution of pSiNP-NH_2-Cy5.5-PEG-KIT particles within the liver. Targeted KIT-aptamer conjugated pSiNPs showed an overlay of GFP and Cy5.5 signals confirming the presence of targeted pSiNPs within the metastasis tissues. (b) ImageJ was used to quantify the sliced samples for the GFP co-localization of the various pSiNP constructs (mean value ± SD, n = 5, $p < 0.05$).

Due to the significantly high GFP signal in the liver and the distribution of pSiNP constructs within the liver, further *ex vivo* analysis was undertaken to assess the specificity of the pSiNP-NH_2-Cy5.5-PEG-KIT constructs towards GIST tumors internalized within the organ. Fluorescence images of frozen liver sections were used to assess the specific targeting properties of the constructs when internalized within the liver in addition to assessing GIST metastases not visible on the liver surface (**Figure 4.6a**). As a control, frozen liver sections of healthy 5-wk old nu/nu mice were also imaged. This was done to confirm the lack of GFP signal within healthy mice as well as to assess the internalization and distribution of pSiNP-NH_2-Cy5.5-PEG-KIT within the liver due to RES clearance. Both Cy5.5 and GFP signals from the pSiNP constructs and the GIST-T1-GFP tumor metastases, respectively, were merged and GFP co-localization was used to quantify the KIT labelling to GIST (**Figure 4.6b**). Once again, there is significantly greater

co-localization of the pSiNP-NH_2-Cy5.5-PEG-KIT constructs than both pSiNP-NH_2-Cy5.5-PEG-SCR and pSiNP-NH_2-Cy5.5-PEG particles (mean value ± SD, n = 5, $p < 0.05$). Within the healthy control group, there is Cy5.5 signal due to pSiNP-NH_2-Cy5.5-PEG-KIT accumulation, which is also seen in Figure 5a. Similar to the *ex vivo* IVIS images of the harvested organs, there is some slight GFP co-localization from the control pSiNP-NH_2-Cy5.5-PEG constructs due to non-specific uptake of the particles. These results, combined with Figure 5, are consistent with the ability of the aptamer-conjugated particles to home to tumor cells within the RES- and MPS-related clearance organs and the active targeting properties are consistent within literature of similar pSiNP constructs that utilize peptide- and antibody-based targeting systems for other tumor models.[17, 19, 21]

4.3D BIOSAFETY OF NANOPARTICLES

Prior to the incubation of pSiNPs for *in vivo* imaging experiments, we assessed the cell cytotoxicity and histological evaluations of major organs to analyze the biosafety of the pSiNPs, cyclic-silane functionalization chemistry, the PEG overcoat, as well as the aptamer targeting moiety. The primary concern with the pSiNP construct was the heterocyclic silane chemistry which may induce a level of toxicity towards healthy cells. Though an effective chemistry to amminate nanoparticles, this cyclic-silane has had limited use for both *in vitro* and *in vivo* experiments. For *in vitro* biosafety analysis, RAW 264.7 macrophage cell lines were incubated for 48h with pSiNP formulations containing from 0.03125 mg to 0.5 mg of nanoparticles by total mass as well as a range of 1-16 ng of aptamer and an estimated 0.62-9.90 µg of azasilane reagent. These incubation concentrations were selected cover a range of masses of nanoparticles injected *in vivo* at a concentration of 10 mg/kg per mouse. A CCK8/WST-8 assay was used to determine

cell viability and results indicated >95% for all pSiNP constructs when compared to the media treated control (**Figure 4.S6a**, Supporting Information). To test *in vivo* biosafety, healthy 5- to 6-week-old nu/nu mice were injected tail-vein with the pSiNP-NH_2-Cy5.5-PEG-KIT constructs at doses corresponding to 10 mg/kg of pSiNP and ~32ng/mg pSiNP of aptamer and 198 μg/mg pSiNP of silane. After 5h of nanoparticle injection, the major organs of interest, liver, spleen and kidneys were harvested and sectioned for hematoxylin and eosin (H&E) histopathological evaluation (**Figure 4.7**). All major organs were found to show no histopathological findings (**Table 4.S3**, Supporting Information). In addition, the possibility of nanoparticle toxicity was assessed using an Alanine aminotransferase (ALT) assay, which was used to measure the pyruvate activity generated due to nanoparticle accumulation within the liver, where an increased pyruvate generation is generally associated with liver toxicity (**Figure 4.S7b-c**, Supporting Information). Blood serum was collected from *in vivo* histological experiments and following protocols from an ALT assay kit (Sigma), pSiNP-NH_2-Cy5.5-PEG-KIT constructs were compared to PBS-injected controls. It was found that pyruvate levels were equivalent for both pSiNP injections and PBS controls (**Figure 4.S7c**, Supporting Information), thereby indicating limited toxicity towards the liver.

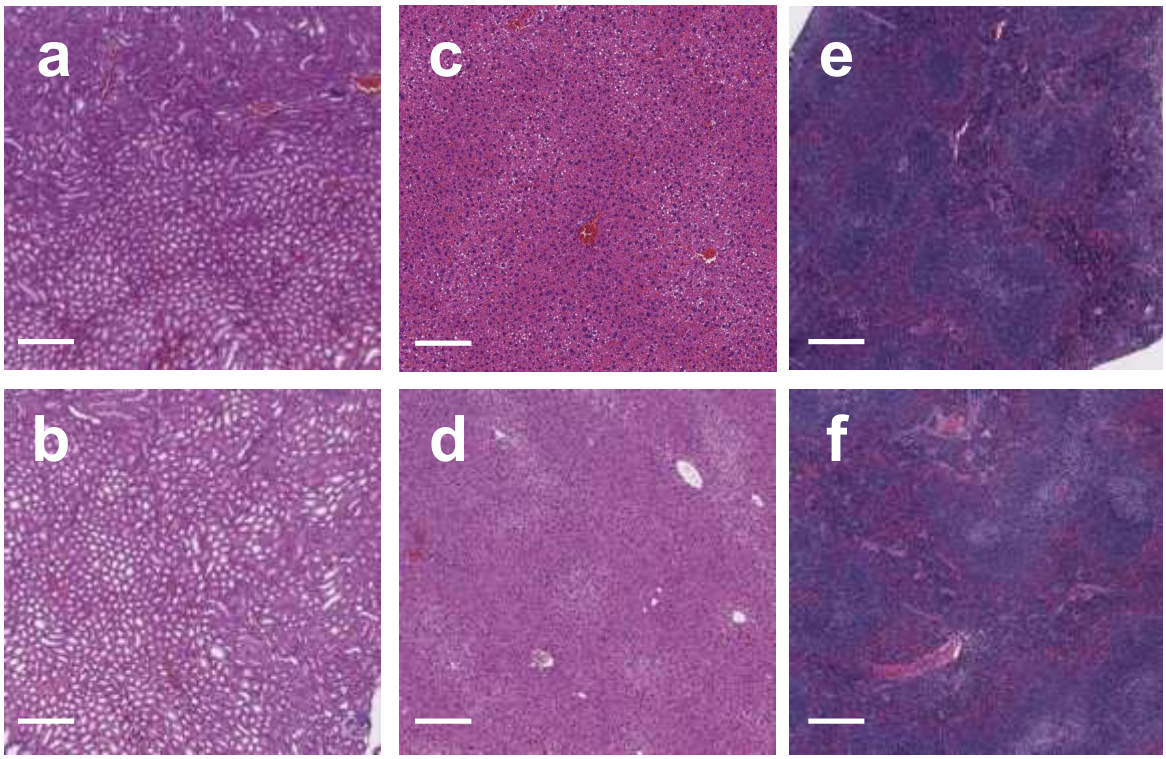

Figure 4.7: Histopathology of extracted organs 5 hours following injection of nanoparticles. No significant differences were observed between the control group that received PBS and the test group. H&E staining of major organs after 5 h of pSiNP construct circulation (10 mg/kg pSiNP, 8 ng/kg of Aptamer, 198 µg/kg of silane) in healthy nu/nu mice; (a & b) Kidney, (c & d) Liver, (e & f) Spleen. The top row of images were PBS injected mice while the bottom row was pSiNP-NH_2-Cy5.5-PEG-KIT injected mice. Histological analysis showed no major differences between the two sets or organs (**Table 4.S3**, Supporting Information).

Using nanoparticles for imaging or therapy of GIST has caught the attention of researchers recently. For instance, ultra-small (<10nm), renal-clearable zwitterionic organic nanocarriers were used for image-guided surgery. In another study microRNA (miRNA) was formulated in a polymeric nanoparticle (~110nm) to control the KIT expression. Although this work highlights the importance of KIT expression in management and therapy of GIST tumor, further animal studies are needed to evaluate the *in vivo* efficacy of the proposed formulation.[11, 33] Both strategies have yielded very promising data and have shown that these platforms can reach GIST targets with high affinity. In both cases, however, the particles rely on passive targeting effects, either

through retained circulation throughout the body or the enhanced permeability and retention (EPR) effect to reach the GIST target. To the best of our knowledge, only one group has utilized an active-targeting strategy with emulsion-polymer based nanoparticle conjugated with bevacizumab mAb for the diagnosis of GIST for CT imaging, however still relying significantly on the EPR effect for high-contrast imaging.[34] Our results have indicated that an active-targeted approach for the imaging of GIST using KIT-specific aptamers and pSiNPs can be very effective for *in vivo* based applications. The high stability and specificity, small size, versatile functional groups and low-cost of the KIT-specific aptamers provide a useful targeting moiety towards GIST compared to KIT mAb and peptides. More specifically, these results have indicated a very versatile platform for both the diagnostic and therapeutic-based applications. The porous nature of pSiNPs can enable the loading of various imaging agents and therapeutics from fluorophores to radiotracers, oligonucleotide payloads and small-molecule drugs while the facile conjugation of aptamers can open the door for this nanosystem to be used for various other hard-to-target cancers.

4.4 Experimental Section

4.4a Materials

Highly doped p-type doped p^{++}-type (B-doped) crystalline silicon wafers (~0.001 Ω cm resistivity, 100 mm diameter, 525 μm thickness) polished on the (100) face was purchased from Siltronix Corp. All reagents were used as received and purchased from Aldrich Chemicals, Inc. DMDASCO, 2,2-dimethoxy-1,6-diaza-2-silacyclooctane was purchased from Gelest, Inc. Maleimide-PEG-succinimidyl valerate (MAL-PEG-SVA) was purchased from Laysan Bio Inc. All buffer salts were purchased from Gibco Inc. The anti-

KIT DNA aptamer was purchased from Integrated DNA Technologies, following the 77 base-long binding regions following 5'-/5AmMC12/GAGGCATACCAGCTTATTCAAGGGGCCGGGGCAAGGGGGGGGTACC GTGGTAGGACATAGTAAGTGCAATCTGCGAA-3'. The aptamers were purchased with a 5'-thiol modifier and one specific batch contained a 3' 6-FAM fluorophore conjugation. 5-week-old nude mice were purchased from The Jackson Laboratory. Fluorophores were purchased from Lumiprobe. All other chemicals and media were purchased from Sigma and used as is.

4.4B Preparation of Porous Silicon Nanoparticles (pSiNP)

pSiNPs were prepared using a previously published "Perforated Etch" method as described previously.[20, 28] A highly doped p^{++}-type crystalline silicon wafer (~0.001 Ω cm resistivity, 100 mm diameter, 525 μm thickness, Siltronix, Inc.) was electrochemically etched in an electrolyte solution consisting of 3:1 (v:v) of 48% aqueous hydrofluoric acid (HF): to ethanol. (CAUTION: HF is highly toxic and can cause severe burns on contact with the skin or eyes). Prior to the preparation of the porous layer, the wafer was cleaned using a "sacrificial etch" consisting of etching a thin, porous layer into the wafer (400 mA cm^{-2} applied for 40 s) in the same electrolyte solution. The wafer was subsequently rinsed with ethanol and the porous layer was dissolved in a strong base (2M aqueous KOH). The cell was then rinsed with water and ethanol, before a fresh solution of 3:1 HF:ethanol electrolyte solution was added, to prepare the nanoparticles. The etching waveform for the particles was generated using LabView (National Instruments, Inc.), and the current was provided by a Keithley 2651A Sourcemeter power supply which was interfaced to LabView. The waveform used was composed of a square wave where a lower 46 mA/cm^2

current density was applied for 1.818 s, followed by a higher 365 mA/cm^2 current density pulse for 0.363 s. This waveform was repeated for 200 cycles, generating a thick, porous silicon film with thin regions of high porosity “perforations” that repeat approximately ever 200 nm through the porous layer. The electrolyte solution was subsequently removed, and the porous layer was washed three times with ethanol. This film was then removed from the silicon wafer through a “lift-off” with the application of a constant current density of 3.4 mA/cm^2 for 180 s in a 1:20 (v:v) 48% aqueous HF:ethanol electrolyte solution. The wafer was carefully transferred to a vial filled with deionized water and fragmented into nanoparticles by ultrasonication overnight in a ultrasonication bath. The resulting sonication yielded pSiNPs with an average diameter of 156.3 ± 6.5 as measured by dynamic light scattering (Z-average, intensity based, Zetasizer, Zs90, Malvern Instruments). Following this, the pSiNPs were centrifuged and resuspended in 100% ethanol for storage.

4.4C Surface Modification of pSiNPs

To track the porous silicon nanoparticles, two sets of fluorophores were used, FITC for the *in vitro* experiments and near-IR Cy5.5 dye for *in vivo* experiments. The surface of the nanoparticles were modified with a cyclic azasilane reagent (DMDASCO, 2,2-

dimethoxy-1,6-diaza-2-silacyclooctane), which generated primary amine groups on the particle surface via a ring-opening click reaction.[8] The azasilane reagent enabled the attachment of fluorophores and an overcoating of poly-ethylene glycol (MAL-PEG-SVA) to enable the conjugation of ssDNA aptamer constructs as well as to improve the circulation of the particles. For the azasilane attachment, pSiNPs in ethanol were centrifuged (15,000 rpm, 10 min) and the pSiNP pellet was washed in dimethyl sulfoxide

(DMSO) to remove protic solvents. Once washed, the nanoparticles (1 mg) were suspended in 400 µL of DMSO and an aliquot of cyclic-silane reagent (100 µL) was added. The pSiNP-silane mixture was allowed to mix for 3 hours. The resulting mix of particles were then washed and centrifuged 3 times with DMSO and finally resuspended in ethanol.

4.4D Loading of Fluorophores to pSiNPs

Two specific fluorophores, NHS Ester-FITC and NHS-Cy5.5 were used as imaging tags for the porous silicon nanoparticles. The fluorophores were bound to the amine terminated surface of the silane modified particles. Briefly, 10 µL of 5 mg/mL of fluorophore dissolved in DMSO was added to 1mg/mL of NH_2-terminated particles. The fluorophore was allowed to mix with the particles overnight, free from light. The particles were then washed 3 times with ethanol and centrifuged (15,000 rpm, 10 min) to remove any free fluorophore. The particles were then dispersed in ethanol and stored in dark.

4.4E Attachment of Poly-Ethylene Glycol (PEG) to pSiNPs

0.5 mg of the fluorophore-conjugated particles were then dispersed in 80 µL of ethanol and were mixed with a solution of (180 µL) of the heterofunctional linker maleimide-PEG-succinimidyl valerate (MAL-PEG-SVA, MW = 3400, Laysan Bio Inc.) in ethanol (5 mg/mL) following previous methods.[17] The PEG-nanoparticle mixture was incubated overnight at room temperature under mild shaking and free from light, to prevent bleaching of the fluorophore. Any unbound PEG was then removed with a triplicate wash in ethanol and centrifuged (15,000 rpm, 10 min). The particles were then dispersed in ethanol and stored in dark.

4.4F Attachment of DNA Aptamer Ligands to pSiNPs

For aptamer conjugation, a concentration of 3.4 mg/mL of particles were redispersed in DI water. Following this, 0.1 mg of the PEGylated particles were dispersed in a volume of 150 µL of DI water. After, 100 µL of aptamer (100 µM) that was pre-dispersed in DI water, following IDT protocols, was added to the nanoparticle solution. The particle-aptamer mixture was allowed to mix at 4°C for 2 hours and in dark. The particles were then washed 3 times with DI water and centrifuged (15,000 rpm, 10 min) to remove any unbound aptamer and were resuspended in PBS for immediate use (within 1-2 hrs) for *in vitro* cell incubation or *in vivo* injection.

4.4G Characterization of pSiNPs

Both the hydrodynamic diameter and the ζ-potential measurements were obtained on a Zetasizer, Zs90 (Malvern Instruments). Subsequent pSiNP size measurements were taken with particles dispersed in Dulbecco phosphate-buffer saline (DPBS), pH 7.4 while ζ-potential measurements were measured with particles dispersed in ethanol. The FTIR spectra of the particles were obtained by a Thermo Scientific Nicolet 6700 FTIR instrument fitted with a Smart iTR diamond ATR fixture. TEM images were obtained using a JEOL 1400 plus electron microscope (JEOL USA, Inc.) at 80KeV and subsequently imaged with a Gatan Oneview camera (Gatan, Inc.). Thermogravimetric analysis (TGA) data was obtained using a TA Instruments™ Discovery SDT 650™. Nanoparticle samples were heated from 100°C-800°C at a ramp rate of 10°C/min in nitrogen. Both weight (%) change and derivative heat flow values were assessed. Dye-loaded particle constructs were assessed using a Molecular Devices™ SpectraMax® iD5 Multi-Mode Microplate

Reader. N_2 adsorption/desorption isotherms were obtained using dry nanoparticles at a temperature of 77° K using a Micromeritics ASAP 202 instrument.

4.4H CELL CULTURE

GIST-T1 cells lines were obtained from T. Taguchi (Kochi Medical School, Nankoku, Japan), and the human mast cell line HMC 1.2 were obtained from I. Pass, Sanford Burnham Prebys Medical Discovery Institute, San Diego, CA. Both the cell lines were cultured following previous methods.[10] The GIST-T1 cell line was grown in Dulbecco's Modified Eagle Medium (DMEM) with 10% FBS, 1% penicillin/streptomycin (Sigma), and 2 mmol/L glutamine (Sigma). The human mast cell line HMC 1.2 were cultured in Iscove's modified Dulbecco's Medium (Gibco) with 10% FBS, 1% penicillin/streptomycin, and 1.2 mmol/L 1-Thioglycerol (Sigma).[10]

4.4I *IN VITRO* TOXICITY

Cellular viability of cells following nanoparticle treatment, was evaluated by using CCK8 assay kit purchased from abcam. Then, RAW264.7 macrophage cells were grown in DMEM media supplemented with FBS (10%) and PenStrep (1%) and it was seeded in a 96 well plate (10^4 cells per well) and stored in the incubator in the presence of CO_2 (5%) at 37 °C overnight. To measure in vitro toxicity, the cells were incubated with various concentrations of nanoparticles, ranging from 0.03125 mg/100µL to 0.5 mg/100µL for 48 hours. Following this, all buffer solution was removed, and the cells were washed in triplicates with PBS. Next, WST-8 / CCK8 solution was added directly to the cells following manufacturers protocols and the cells were allowed to incubate for 2 hours. The absorbance of the cells at 460 nm was subsequently measured using a Perkin-Elmer LS55 UV-Vis Spectrometer.

4.4J *IN VITRO* FLOW CYTOMETRY EXPERIMENTS AND CONFOCAL MICROSCOPY

HMC-1.2 cells were kept in suspension and approximately 1 x 10^6 cells were isolated and subsequently resuspended in cold DPBS buffer. Aptamer-conjugated pSiNPs were then incubated with the cells for 1 hour at 4°C. The cells were then washed thrice with DPBS and resuspended in a DPBS buffer for flow cytometry analysis.

GIST-T1 cells, approximately 1 x 10^6, were harvested from the cell cultures using trypsin Accutase (Sigma-Aldrich) and were subsequently washed in cold DPBS buffer. Aptamer-conjugated pSiNPs were then incubated with the cells for 1 hour at 4°C. The cells were then triplicated washed with DPBS and resuspended in a DPBS for flow cytometry analysis (BD Accuri C6). PE anti-human c-KIT antibody (Clone 104D2, BioLegend) was applied in 1:20 dilution for cell staining and as a control. All flow cytometry data was analyzed using FlowJo software.

HMC-1.2 and GIST-T1 cells, approximately 1 x 10^6 of each, were plated on glass bottom wells and cultured to 50% confluency. Once achieved, the cells were then washed three times with PBS and incubated with Aptamer-conjugated pSiNPs and free aptamer constructs for 1 hour at 4°C. The cells were then subsequently fixed in 4% paraformaldehyde (Thermo Fisher Scientific), washed, and counter-stained with DAPI (1:50,000, Thermo Fisher Scientific) to ensure cell staining.

4.4K ESTABLISHING THE SPLEEN-TO-LIVER GIST METASTASES MODEL

Five-week-old male nude mice were purchased from The Jackson Laboratory (Bar Harbor). A mixture of GFP-conjugated T1 (5 × 10^6 cells) and CAFs (1 × 10^6 cells), were suspended in 50 µL of Hanks' Balanced Salt Solution (HBSS). After the mice were anesthetized with isoflurane gas, ~1-cm incisions were made in the left abdominal flank,

and the cells were injected into the spleen. After 3 weeks, all mice were analyzed using the IVIS imaging system, and the signals were graphed by total photon flux (p/s). All animal experiments were conducted and approved in accordance with the Animal Care Committee of University of California, San Diego (S11020).

4.4L *IN VIVO* EXPERIMENTS

In vivo imaging was performed on GIST-T1-GFP induced mice. Prior to injection, the mice were weighed and a concentration of 10 mg/kg of particles (pSiNP-NH_2-Cy5.5-PEG-KIT, pSiNP-NH_2-Cy5.5-PEG-SCR, and pSiNP-NH_2-Cy5.5-PEG) per mouse was measured out. The mice were subsequently anesthetized using isoflurane gas and the mice were imaged prior to particle injection as a control using the IVIS. Cy5.5 signals were measured. Once the preliminary IVIS images were completed, the mice were anesthetized once more, and particles were then subsequently injected via tail-vein injection. Immediately, the mice abdomen was then imaged to measure the Cy5.5 signals. This process was repeated for all the mice with the respective control particles (pSiNP-NH_2-Cy5.5-PEG-SCR and pSiNP-NH_2-Cy5.5-PEG). Subsequently, every hour for five, the mice were anesthetized and imaged for the Cy5.5 signals to monitor both the intensity and distribution of the particles within the abdomen, particularly the region where the liver, spleen, and kidneys are located. After 5 hours, the mice were sacrificed following university protocols. Blood was collected for toxicity analysis. In addition, the organs of interest, liver, spleen, and kidneys were harvested for further *ex vivo* imaging and histology analysis.

4.4M *Ex vivo* Imaging

Five hours following the tail-vein injection of the nanoparticle constructs, the liver spleen and kidneys of the mice were harvested for further IVIS imaging. The images of the isolated organs were named as *ex vivo* imaging for the purpose of this study. Following the sacrifice of mice and the harvesting of the organs, all of the liver, spleen and kidneys were immediately washed with PBS buffer to remove excess blood. The organs were immediately imaged by IVIS to measure both Cy5.5 signals of the internalized particles and GFP signals from tumor metastases on the surface of the organs. This was repeated for the sets of organs for all the mice and the respective controls. GFP and Cy5.5 signals were imaged separately for ImageJ processing to assess signal overlap and GFP co-localization.

4.4N *In vivo* Toxicity & Histology Studies

Nanoparticle toxicity was assessed through blood toxicity using an Alanine aminotransferase (ALT) assay obtained from Sigma. Blood was collected 5 hours after nanoparticle administration from mice post *in vivo* experiments after the mice were sacrificed. The blood was immediately centrifuged at 4000 RPM for 5 minutes, to separate serum for ALT assay quantification. The serum from each of the mice blood samples were separated. Following the manufacturers protocol, ALT activity was measured utilizing serum samples from each mouse. Control serum samples with PBS-injected mice were utilized as a comparison.

Histological analysis was examined on the mice's liver, spleen, and kidneys post *ex vivo* imaging. Briefly, the organs were washed in PBS buffer and immediately transferred into labelled tissue cassettes before being immersed in a fixative solution,

10% Neutral buffered formalin (NBF) (Sigma) for 24 hours. Following this, the tissue cassettes were subsequently transferred into 70% ethanol for long-term storage. The tissue cassettes were then submitted to UCSD Moores Cancer Center Histology Core for tissue sectioning, plating, and H&E staining. All pathological analyses were completed by Dr. Valeria Estrada, MD from the Histology Core Facility.

4.4O Liver Section Imaging

Once liver samples were imaged *ex vivo*, the samples were subsequently sectioned to assess nanoparticle co-localization to GFP labeled metastases. Immediately after imaging, liver samples were washed in PBS and placed embedded in Tissue-Tek O.C.T. Compound (Sakura) and immediately frozen. The tissue samples were kept in the dark at -20°C until submitted to UCSD Moores Cancer Center Histology Core for tissue sectioning and plating. Following this, plated liver sections were imaged using a Keyence BZ-X710 where GFP and Cy5.5 signals were measured. GFP and Cy5.5 signals were imaged separately for ImageJ processing to assess signal overlap and GFP co-localization.

4.4P Image Analysis

All IVIS images were subsequently modified to remove all background noise using the IVIS proprietary software, Perkin Elmer Living Image. For all Cy5.5 signals for *in vivo* images, Radiance (p/sec/cm^2/sr) was assessed to a color scale from 1.50e8 to 3.30e8 (p/sec/cm^2/sr) to isolate the highest signals within the mouse abdomen, regions where the liver, spleen and kidney are physiologically located. These regions of interests were isolated to measure the total radiance value for each mouse at each respective time period and were plotted to measure the signal decay over time. For all *ex vivo* images,

the Cy5.5 signals were modified to a radiance scale from 5.19e8 to 1.32e9 (p/sec/cm^2/sr) and GFP signals were modified from 1.95e8 to 7.66e9 (p/sec/cm^2/sr). Cy5.5 and GFP signals of the organs were imaged separately.

To analyze co-localization of Cy5.5 and GFP signals, the normalized images were overlaid using ImageJ and the signals from both Cy5.5 and GFP images were merged. The overlap of Cy5.5 signal to total GFP signals enabled a quantitative value to calculate the signal overlap. The following equation was used to calculate GFP co-localization: $\text{GFP Co} - \text{localization } (\%) = \frac{\text{Total Merged Signal}}{\text{Total GFP Signal}} \times 100$. All co-localization calculations were only assessed within the imaged area of the tumor. Any Cy5.5 signal associated with the nanoparticle constructs that did not merge with the visible GFP signals from the organs were assumed to not bind with the GIST-T1 metastases. This same analysis was utilized for the frozen liver tissue section images where both Cy5.5 and GFP signals were measured.

4.4Q Statistical Analysis

All statistical analyses were assessed using GraphPad Prism 9. The investigators were not blinded throughout in vivo experiments or outcome assessment, except for the pathological assessments of tissues by Dr. Valeria Estrada, MD. Statistical significance was determined by both two-tailed unpaired Student *t* tests with Welch correction and one-way ANOVA for multiple comparisons when deemed appropriate.

4.5 Conclusions

In summary, porous silicon nanoparticles, decorated with anti-KIT DNA aptamers, showed highly effective labelling of human GIST cells in a clinically relevant GIST liver

metastasis model. This diagnostic platform showed clear multivalency effects relative to free KIT aptamers for targeting *in vitro*, and highly effective in *in vivo* and *ex vivo* targeting of GIST metastases in RES and MPS clearance tissues, the liver and spleen. The increased efficacy of tumor cell homing was attributed to the multivalent interactions that result from attaching multiple aptamer-targeting agents to a single nanoparticle. While this study focused on an imaging/diagnostic application, the results have implications for use of the aptamer-pSiNP system as a delivery vehicle for therapeutics.

4.6 SUPPORTING INFORMATION

Table 4.S1: Characteristics of pSiNP constructs for pore structure and internal surface area as calculated from cryogenic nitrogen adsorption isotherms. [a]Values determined using BET (Brunnauer–Emmett–Teller) analysis of the adsorption isotherms. [b]Values determined using BJH (Barret–Joyner–Halenda) analysis of the adsorption/desorption isotherms (mean value ± SD, n = 3).

N_2 Adsorption/Desorption Isotherms			
	pSiNP	**pSiNP-NH_2**	**pSiNP-NH_2-PEG-KIT**
Surface Area (m^2/g)[a]	333.43 ± 14.71	119.25 ± 22.76	102.04 ± 8,44
Pore Volume (cm^3/g)[b]	1.38 ± 0.08	0.46 ± 0.03	0.42 ± 0.07
Pore Size (nm)[b]	14.75 ± 0.13	14.13 ± 0.05	13.44 ± 0.10

Table 4.S2: Size & Surface Charge of pSiNP Constructs as assessed through Dynamic Light Scattering (mean value ± SD, n = 3).

Hydrodynamic Size & Surface Charge					
	pSiNP	**pSiNP-NH_2**	**pSiNP-NH_2-Cy5.5**	**pSiNP-NH_2-Cy5.5-PEG**	**pSiNP-NH_2-Cy5.5-PEG-KIT**
Z-Avg. Size (nm)	156.3 ± 6.5	168.4 ± 1.4	186.2 ± 8.6	228.2 ± 3.9	237.8 ± 1.1
ζ-Potential (mV)	-27.53 ± 1.63	14.22 ± 1.07	3.17 ± 0.67	6.65 ± 1.23	2.33 ±1.02

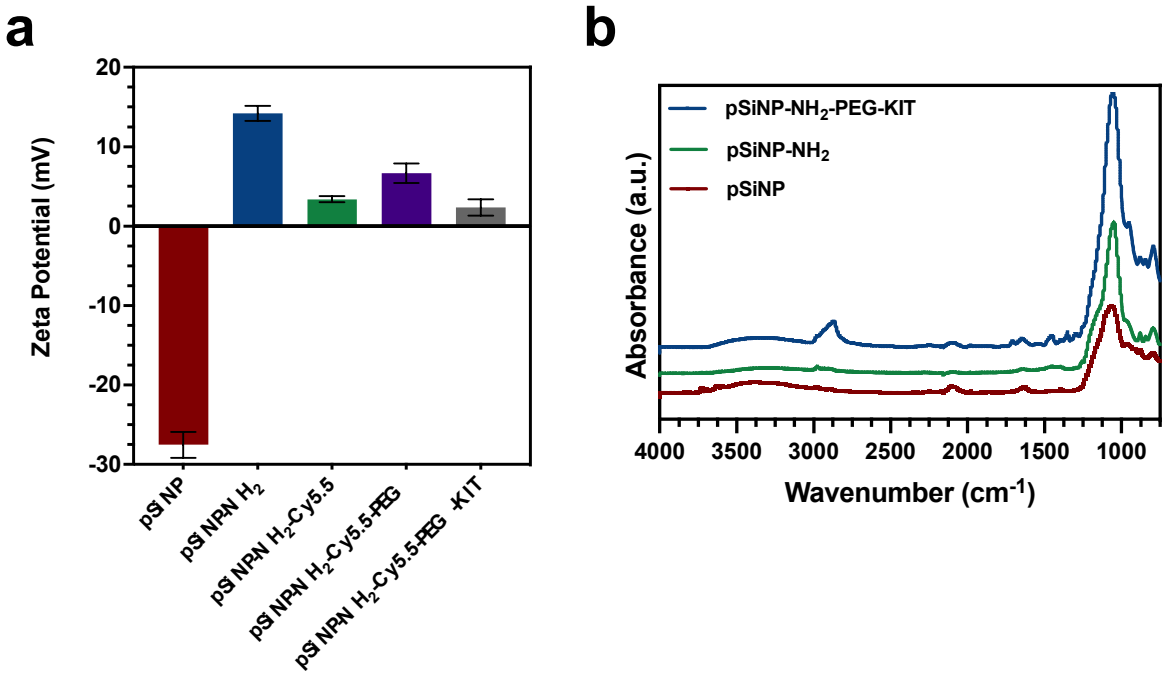

Figure 4.S1: Characterization of pSiNP constructs. (a) Zeta potential measurements of as-prepared pSiNPs, amine-functionalized pSiNPs (pSiNP-NH_2), dye-loaded amine-functionalized pSiNPs (pSiNP-NH_2-Dye), PEGylated pSiNPs (pSiNP-NH_2-Dye-PEG) and KIT-aptamer conjugated, dye-loaded PEGylated pSiNPs (pSiNP-NH_2-Dye-PEG-KIT) respectively (mean value ± SD, n = 3). Error bars represent standard deviation of three independently prepared samples. (b) Fourier Transform Infrared Spectroscopy (FTIR) spectra of pSiNPs functionalized with cyclic-silanes and PEG.

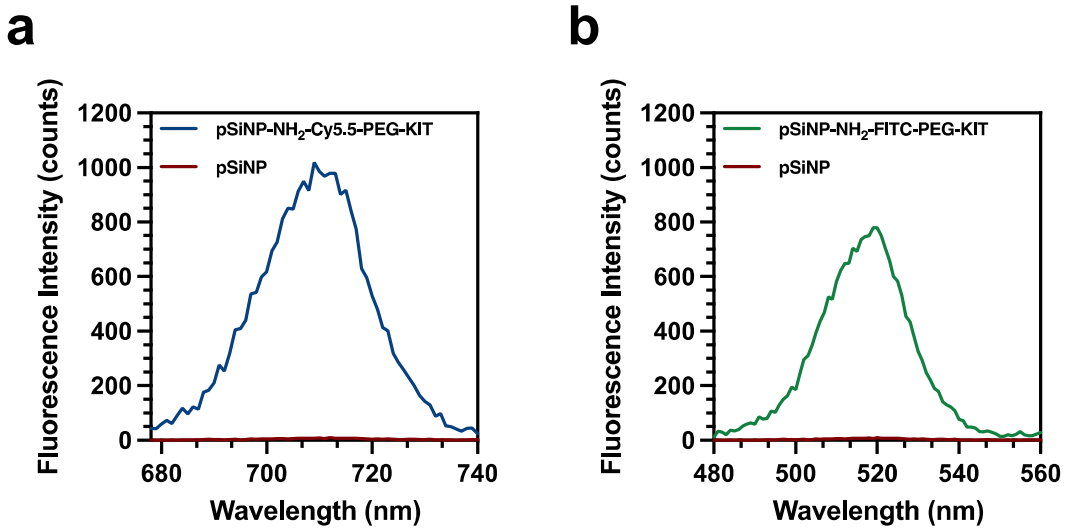

Figure 4.S2: Characterization of dye-conjugated pSiNPs. (a) Fluorescence measurement of Cy5.5 loaded pSiNPs. (b) Fluorescence measurement of FITC loaded pSiNPs.

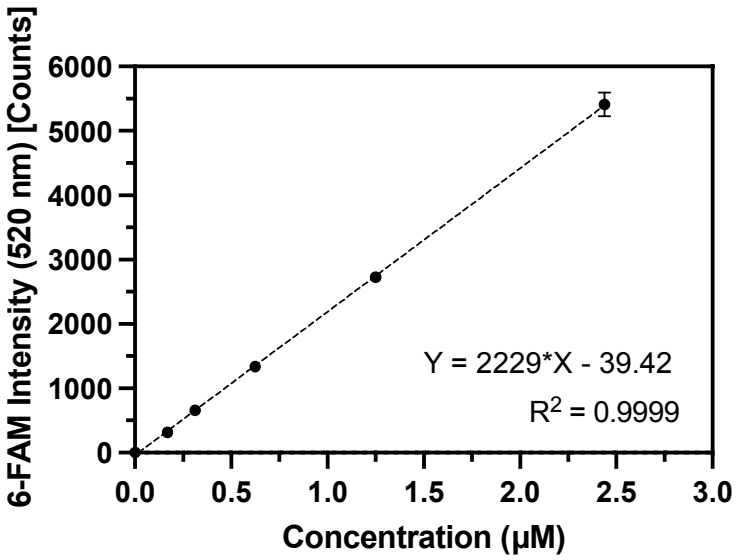

Figure 4.S3: Standard curve of 6-FAM-conjugated KIT-aptamer (mean value ± SD, n = 3). The aptamer concentration is correlated to the 6-FAM intensity at 520 nm and is used to quantify the concentration of aptamers bound to the pSiNPs.

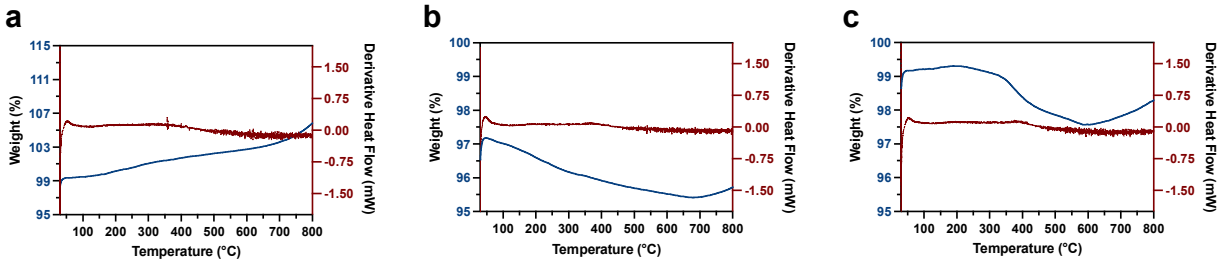

Figure 4.S4: Thermogravimetric analysis (TGA) measurements of (a) pSiNP, (b) pSiNP-NH_2 and (c) pSiNP-NH_2-PEG. The derivative heat flow indicates phase changes of the silane-coated and PEGylated particles while the weight (%) curve provides an estimate of the amount of conjugated material is available in a given amount of nanoparticles. The measurements indicated a weight percent loss of 1.98% (wt.) for the cyclic azasilane reagent which overlapped with a melting temperature from 71-73°C[1], as seen in (b) for the weight percent change. For (c), the determined weight percent loss for the MAL-PEG-SVA overcoat was 0.17% (wt.), determined by the melting point region from 182-287°C for the PEG[2]. These calculated values were used to determine levels of toxicity for the synthetic reagents for both *in vitro* and *in vivo* experiments.

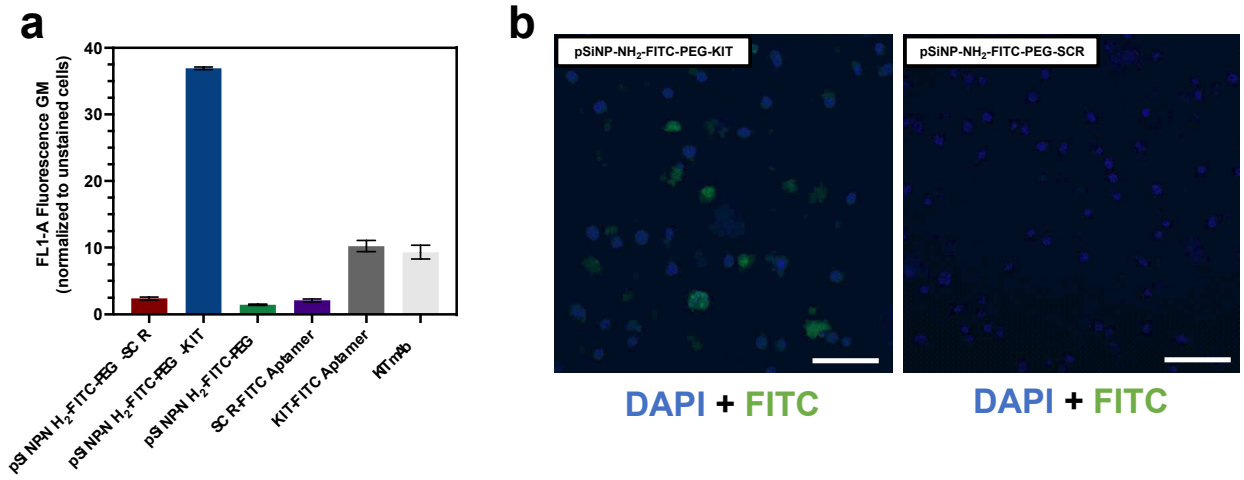

Figure 4.S5: Investigation of cellular targeting of aptamer-conjugated pSiNPs in a model HMC-1.2 cancer cell line. (a) Flow cytometry data evaluating the efficacy of the aptamer-conjugated pSiNP group to localize to GIST-T1 cells, quantified as a normalized FL1-A Fluorescence GM attached to the particles and aptamers, versus free KIT aptamer and scramble controls (mean value ± SD, n = 3, $p < 0.05$). Confocal microscopy images of HMC-1.2 cells incubated with (b) FITC-labelled, KIT-aptamer conjugated pSiNPs and (c) FITC-labelled, Scramble-aptamer control conjugated pSiNPs. Both images are merged laser lines for DAPI and FITC (scale bar = 100 µm).

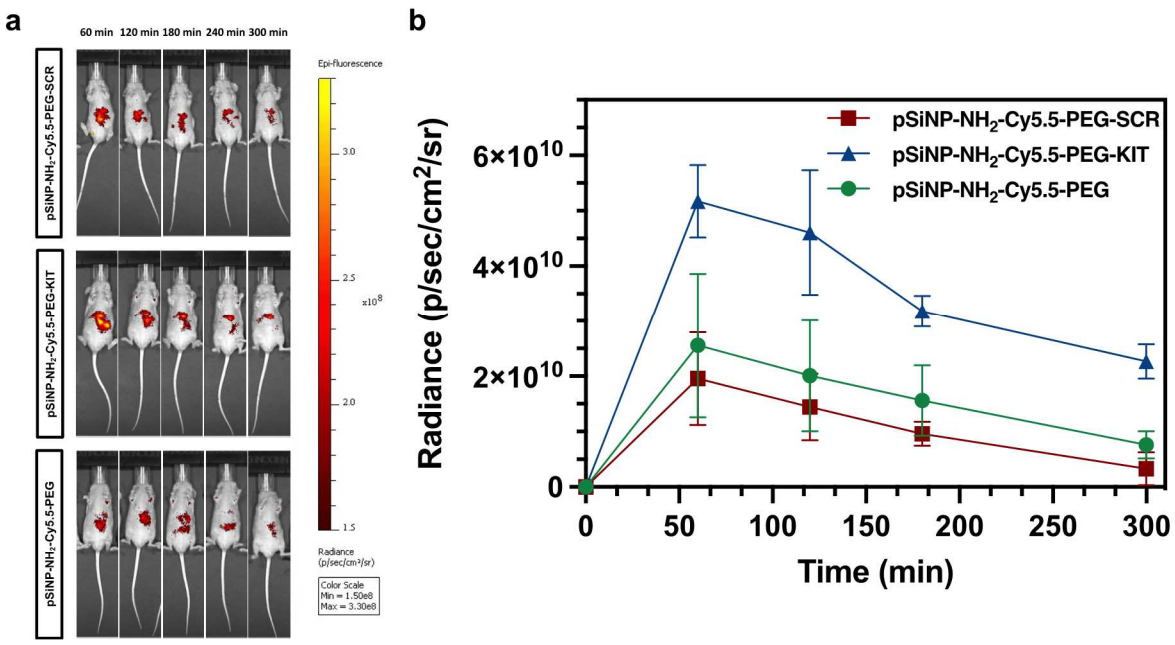

Figure 4.S6: Temporal *in vivo* IVIS imaging. (a) Temporal IVIS images of 5-week-old GIST-T1 mice injected with pSiNP constructs tail-vein. Cy5.5 signals, of the pSiNP constructs were isolated from abdomen regions after every hour for 5 hours. Isolated Cy5.5 signals from abdomen regions measuring (b) total radiance (p/sec/cm2/sr) for measured signals (mean value ± SD, n = 3).

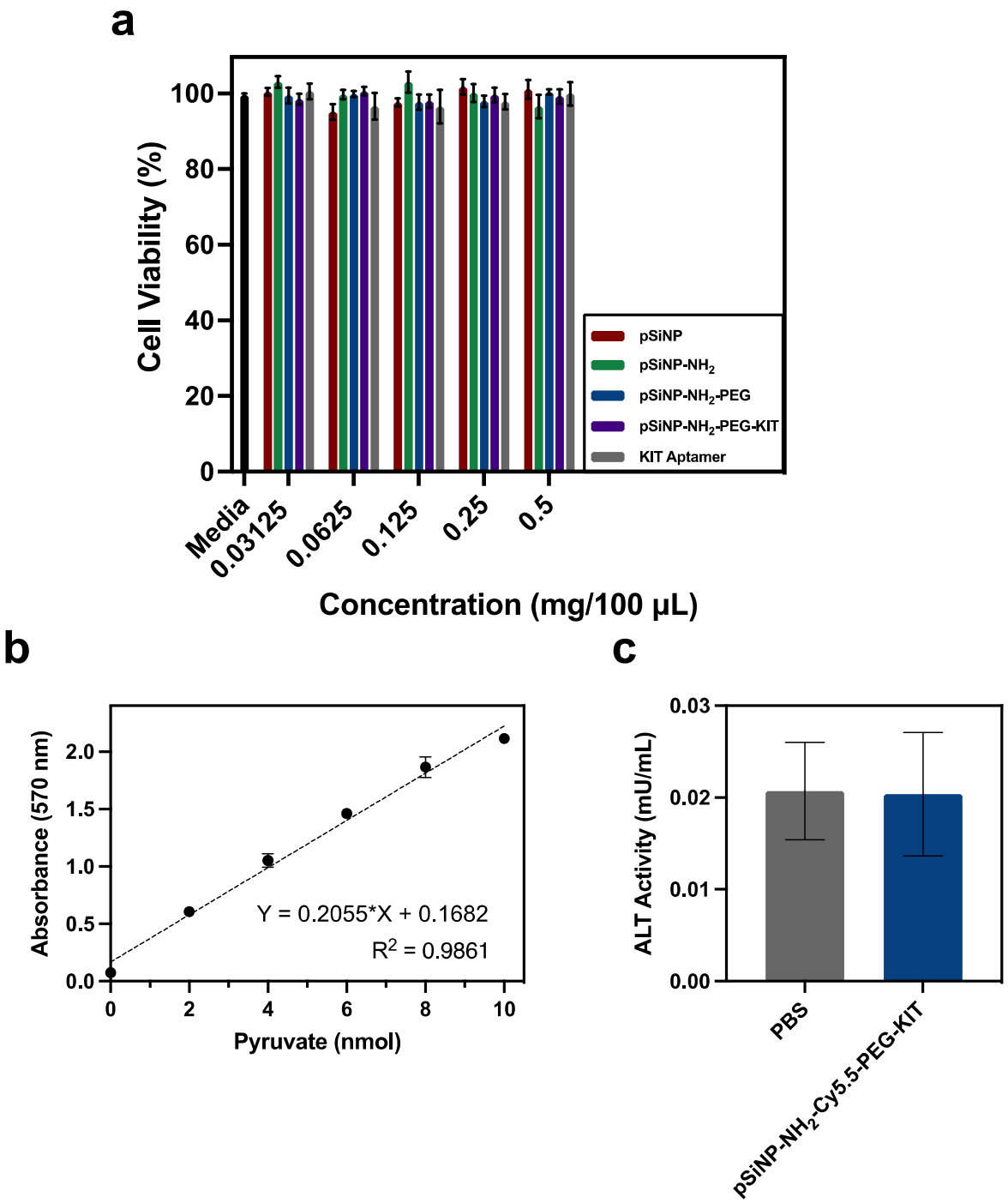

Figure 4.S7: Biosafety Analysis of pSiNP constructs. (a) Viability of RAW 264.7 macrophage cells incubated with various concentrations of pSiNP constructs for 48 hours. Error bars indicate SD (mean value ± SD, n = 3, $p < 0.05$). Serum ALT assay to measure liver toxicity due to pSiNP constructs. (b) Standard curve to assess Pyruvate activity and (c) ALT activity of serum collected from pSiNP-NH_2-Cy5.5-PEG-KIT and PBS injected mice (mean value ± SD, n = 3). Aptamer-pSiNP constructs showed no significant effects on ALT value when compared to PBS controls.

Table 4.S3: Histopathological analysis of harvested organs, liver, spleen, and kidneys of pSiNP injected mice compared to PBS controls. Analysis was completed by by Dr. Valeria Estrada, MD (UCSD Moores Cancer Center).

Histopathological Findings	
	Comments
Mouse 1 (PBS) - Kidney	No Pathological Findings
Mouse 1 (PBS) - Spleen	No Pathological Findings
Mouse 1 (PBS) - Liver	No Pathological Findings
Mouse 3 (pSiNP) - Kidney	No Pathological Findings
Mouse 3 (pSiNP) - Spleen	No Pathological Findings
Mouse 3 (pSiNP) - Liver	No Pathological Findings
Mouse 4 (pSiNP-KIT) - Kidney	No Pathological Findings
Mouse 4 (pSiNP-KIT) - Spleen	No Pathological Findings
Mouse 4 (pSiNP-KIT) - Liver	No Pathological Findings

4.6 Supporting Information – Literature Cited

1. D. Kim, J. M. Zuidema, J. Kang, Y. Pan, L. Wu, D. Warther, B. Arkles and M. J. Sailor, *Journal of the American Chemical Society*, 2016, **138**, 15106-15109.

2. S. Aksakal, R. Aksakal and C. R. Becer, 2021, DOI: https://doi.org/10.1002/9783527823819.ch7, 235-263.

4.7 Acknowledgements

Chapter 4, in full, has been submitted for publication of the material as it may appear in *Nanoscale*, 2022. Vijayakumar, S., Nasr, S.H., Davis, J.A., Wang, E., Zuidema, J.M., Lu, Y.S., Lo, Y-H., Sicklick, J.K., Sailor, M.J., Ray, P. "Anti-KIT DNA Aptamer-conjugated Porous Silicon Nanoparticles for the Targeted Detection of Gastrointestinal Stromal Tumors". The dissertation author was the primary researcher and author of this material.

REFERENCES - CHAPTER 4

1. G. L. Ma, J. D. Murphy, M. E. Martinez and J. K. Sicklick, *Cancer Epidemiol Biomarkers Prev*, 2015, **24**, 298-302.

2. Y. N. Kang, H. R. Jung and I. Hwang, *Cancer Res Treat*, 2010, **42**, 135-143.

3. C. L. Corless, C. M. Barnett and M. C. Heinrich, *Nature Reviews Cancer*, 2011, **11**, 865-878.

4. C. M. Barnett, C. L. Corless and M. C. Heinrich, *Hematology/Oncology Clinics of North America*, 2013, **27**, 871-888.

5. C. A. Metildi, C. M. Tang, S. Kaushal, S. Y. Leonard, P. Magistri, H. S. Tran Cao, R. M. Hoffman, M. Bouvet and J. K. Sicklick, *Ann Surg Oncol*, 2013, **20 Suppl 3**, S693-700.

6. C. Tuerk and L. Gold, *Science*, 1990, **249**, 505-510.

7. A. D. Ellington and J. W. Szostak, *Nature*, 1990, **346**, 818-822.

8. D. Kim, J. M. Zuidema, J. Kang, Y. Pan, L. Wu, D. Warther, B. Arkles and M. J. Sailor, *Journal of the American Chemical Society*, 2016, **138**, 15106-15109.

9. P. Ray, K. D. Viles, E. E. Soule and R. S. Woodruff, *Arch Immunol Ther Exp (Warsz)*, 2013, **61**, 255-271.

10. S. Banerjee, H. Yoon, M. Yebra, C.-M. Tang, M. Gilardi, J. S. Shankara Narayanan, R. R. White, J. K. Sicklick and P. Ray, *Molecular Cancer Therapeutics*, 2020, **19**, 1173.

11. H. Kang, W. R. Stiles, Y. Baek, S. Nomura, K. Bao, S. Hu, G. K. Park, M. J. Jo, H. I, J.-L. Coll, B. P. Rubin and H. S. Choi, *Advanced Materials*, 2020, **32**, 1905899.

12. C. A. Metildi, C.-M. Tang, S. Kaushal, S. Y. Leonard, P. Magistri, H. S. Tran Cao, R. M. Hoffman, M. Bouvet and J. K. Sicklick, *Annals of Surgical Oncology*, 2013, **20**, 693-700.

13. J. Tan, N. Yang, L. Zhong, J. Tan, Z. Hu, Q. Zhao, W. Gong, Z. Zhang, R. Zheng, Z. Lai, Y. Li, C. Zhou, G. Zhang, D. Zheng, Y. Zhang, S. Wu, X. Jiang, J. Zhong, Y. Huang, S. Zhou and Y. Zhao, *Theranostics*, 2017, **7**, 4862-4876.

14. D. Kim, J. Kang, T. Wang, H. G. Ryu, J. M. Zuidema, J. Joo, M. Kim, Y. Huh, J. Jung, K. H. Ahn, K. H. Kim and M. J. Sailor, *Advanced Materials*, 2017, **29**, 1703309.

15. J. Kang, D. Kim, J. Wang, Y. Han, J. M. Zuidema, A. Hariri, J.-H. Park, J. V. Jokerst and M. J. Sailor, *Advanced Materials*, 2018, **30**, 1800512.

16. K. Li, P. Li, Y. Wang and S. Han, *Frontiers in Oncology*, 2020, **10**.

17. A. Bertucci, K.-H. Kim, J. Kang, J. M. Zuidema, S. H. Lee, E. J. Kwon, D. Kim, S. B. Howell, F. Ricci, E. Ruoslahti, H.-J. Jang and M. J. Sailor, *ACS Applied Materials & Interfaces*, 2019, **11**, 23926-23937.

18. J. Kang, J. Joo, E. J. Kwon, M. Skalak, S. Hussain, Z.-G. She, E. Ruoslahti, S. N. Bhatia and M. J. Sailor, *Advanced Materials*, 2016, **28**, 7962-7969.

19. B. Kim, S. Sun, J. A. Varner, S. B. Howell, E. Ruoslahti and M. J. Sailor, *Advanced Materials*, 2019, **31**, 1902952.

20. M. J. Sailor, *Porous Silicon in Practice: Preparation, Characterization, and Applications*, Wiley-VCH, Weinheim, Germany, 2012.

21. L. Gu, L. E. Ruff, Z. Qin, M. Corr, S. M. Hedrick and M. J. Sailor, *Advanced Materials*, 2012, **24**, 3981-3987.

22. F. Chen, H. Hong, Y. Zhang, H. F. Valdovinos, S. Shi, G. S. Kwon, C. P. Theuer, T. E. Barnhart and W. Cai, *ACS Nano*, 2013, **7**, 9027-9039.

23. E. Secret, K. Smith, V. Dubljevic, E. Moore, P. Macardle, B. Delalat, M.-L. Rogers, T. G. Johns, J.-O. Durand, F. Cunin and N. H. Voelcker, *Advanced Healthcare Materials*, 2013, **2**, 718-727.

24. A. P. Mann, P. Scodeller, S. Hussain, J. Joo, E. Kwon, G. B. Braun, T. Mölder, Z.-G. She, V. R. Kotamraju, B. Ranscht, S. Krajewski, T. Teesalu, S. Bhatia, M. J. Sailor and E. Ruoslahti, *Nature Communications*, 2016, **7**, 11980.

25. B. Kim, J.-H. Park and M. J. Sailor, *Advanced Materials*, **0**, 1903637.

26. F. Zhang, A. Correia, E. Mäkilä, W. Li, J. Salonen, J. J. Hirvonen, H. Zhang and H. A. Santos, *ACS Appl Mater Interfaces*, 2017, **9**, 10034-10046.

27. M. Terracciano, I. Rea, N. Borbone, R. Moretta, G. Oliviero, G. Piccialli and L. De Stefano, *Molecules*, 2019, **24**.

28. Z. Qin, J. Joo, L. Gu and M. J. Sailor, *Particle & Particle Systems Characterization*, 2014, **31**, 252-256.

29. S. Banerjee, H. Yoon, S. Ting, C.-M. Tang, M. Yebra, A. T. Wenzel, H. Yeerna, J. P. Mesirov, R. J. Wechsler-Reya, P. Tamayo and J. K. Sicklick, *Molecular Cancer Therapeutics*, 2021, **20**, 2035-2048.

30. J. K. Sicklick, S. Y. Leonard, M. L. Babicky, C.-M. Tang, E. S. Mose, R. P. French, D. V. Jaquish, C. K. Hoh, M. Peterson, R. Schwab and A. M. Lowy, *Journal of Translational Medicine*, 2014, **12**, 41.

31. M. Yebra, S. Bhargava, A. Kumar, A. M. Burgoyne, C.-M. Tang, H. Yoon, S. Banerjee, J. Aguilera, T. Cordes, V. Sheth, S. Noh, R. Ustoy, S. Li, S. J. Advani, C. L. Corless, M. C. Heinrich, R. Kurzrock, S. M. Lippman, P. T. Fanta, O. Harismendy, C. Metallo and J. K. Sicklick, *Clinical Cancer Research*, 2022, **28**, 187-200.

32. H. Yoon, C.-M. Tang, S. Banerjee, M. Yebra, S. Noh, A. M. Burgoyne, J. D. l. Torre, M. D. Siena, M. Liu, L. R. Klug, Y. Y. Choi, M. Hosseini, A. L. Delgado, Z. Wang, R. P. French, A. Lowy, R. P. DeMatteo, M. C. Heinrich, A. A. Molinolo, J. S. Gutkind, O. Harismendy and J. K. Sicklick, *Oncogene*, 2021, **40**, 1957-1973.

33. M. Tanaka, H. Kataoka, S. Yano, H. Ohi, K. Moriwaki, H. Akashi, T. Taguchi, N. Hayashi, S. Hamano, Y. Mori, E. Kubota, S. Tanida and T. Joh, *Molecular Cancer Therapeutics*, 2014, **13**, 767-775.

34. T. B. Ligiero, C. Cerqueira-Coutinho, M. de Souza Albernaz, M. Szwed, E. S. Bernardes, M. A. V. Wasserman and R. Santos-Oliveira, *Biomedical Physics & Engineering Express*, 2016, **2**, 045017.

CHAPTER 5

MICROENVIRONMENT TARGETS AND RETINAL ANGIOGENIC BEHAVIOR OF ERUCAMIDE-LOADED POROUS SILICON NANOPARTICLES

5.1 ABSTRACT

Retinal photoreceptors, some of the most functionally dynamic and energetically demanding cells in the body, are nourished by the choriocapillaris, an extraretinal fenestrated capillary bed. Attenuation of the choriocapillaris induces photoreceptor atrophy and is characteristic of several eye diseases related to vision loss. These photoreceptors use a novel angiogenic pathway to maintain their primary blood supply and promote homeostasis. They accomplish this by generating the pro-angiogenic metabolite erucamide, a highly hydrophobic fatty acid amide, using peptidylglycine alpha-monooxygenase, an enzyme expressed in photoreceptor outer segments. Erucamide, maintains the structure and function of retinas, but its mechanism of action remains unknown. In this study we used a silane functionalized porous silicon nanoparticle (pSiNP) approach as a delivery vehicle for erucamide *in vitro* and *in vivo*. Using multiple nanoparticle and biochemical techniques, we identified erucamide's target cells, binding proteins, and potential mechanism of neurotrophic action. This study provides novel perspectives of neurovascular crosstalk and may inform future neurotrophic strategies for the treatment of neuro/vasculotrophic diseases of the eye.

5.2 MAIN TEXT

In phototransduction, photoreceptors are a major component in vision, whereby light is converted to electrical signals in the neurosensory retina as a connection between neuronal photoreceptors, the retinal pigment epithelium (RPE) and a specialized vascular plexus known as choriocapillaris.[1] It is known that the eye is one of the most vascularized

organs and that the choriocapillaris, which is a capillary network, is the primary blood supply for these photoreceptors.[2, 3] In fact, blood flow in these tissues is regulated by local factors from the vessels or associated neurons and/or glia in an autocrine or paracrine fashion or through neurovascular units.[4] However, the lack of the blood flow control is related to many neurodegenerative diseases including Parkinson's, Alzheimer's, amyotrophic lateral sclerosis, and cerebral palsy.[5]

Phototransduction is initiated within the photosensitive outer segments in both rod and cone receptors.[1, 4] RPE cell processes interdigitate with the sensitive outer segments and are able to perform critical functions for photoreceptor activity and survival.[1] The RPE can also separate the photoreceptors from the choriocapillaris and provide crucial vasculotrophic support by providing a steady stream of vascular endothelial growth factor (VEGF) and (Pigment epithelium-derived factor) PEDF to the choroid, and actively transport glucose and other metabolites to photoreceptors.[1, 2] Maintaining the homeostasis of both photoreceptors and choriocapillaris is not a simple task for RPE cells since perfusion rates of the choriocapillaris are similarly high as other parts of the body, and photoreceptors are the most numerous and energetically expensive cells in the retina.[6] However, based on these factors, photoreceptors are not believed to directly regulate local blood flow like other highly metabolically demanding neurons found in both the retina and the central nervous system (CNS).[7-10]

Generally, the functions of the choriocapillaris, RPE and photoreceptors are well balanced, except in cases such as postnatal development, where photoreceptors are forced to engage in a lethal competition for resources, and only enough photoreceptors that survive can be adequately nourished by the choriocapillaris.[6] In addition, initial

photoreceptor atrophy in early stages of degeneration results in nearly unmitigated oxygen flow into the retina (since photoreceptors are massive oxygen consumers), and the ensuing hyperoxia promotes exponential photoreceptor losses during late stages which lead to retinal diseases in its most severe forms, including neovascular age-related macular degeneration (AMD) and proliferative diabetic retinopathy (DR).[11, 12] Current therapeutic strategies to prevent photoreceptor atrophy have shown that interventions designed to improve circulation and/or photoreceptor nutrition can significantly delay the late-stage atrophy and examples include the delivery of general neurotrophic agents, RPE cell transplantation, or lifestyle changes.[13-15] Therefore, increasing the functionality of the choriocapillaris to increase circulation in early disease stages, but restricting blood flow in late disease states to prevent pathological angiogenesis may significantly enhance photoreceptor survival.

By gaining a better understanding of retinal degeneration, we hope to understand potential effective therapies to prevent the metabolic derangements that promote photoreceptor atrophy. Primary fatty acid amides (PAM), a family of endogenous chemical messengers, emerged as one of the most severely dysregulated class of metabolites in degenerating retinas.[16-18] Previous work has shown that erucamide (22:1, n-9; $C_{22}H_{43}NO$), was one of the most abundant metabolites detectable in wild-type rat eyes, and dramatically attenuated in multiple rodent models of photoreceptor atrophy, suggesting that it might be important for photoreceptor maintenance (**Fig. 5.S1**, Supporting Information). Erucamide is present in the central nervous system (and plasma) of many species including humans[16, 19, 20] and has been shown to regulate angiogenesis and water balance in skeletal muscles and the intestine.[19-21] However, its

function in the central nervous system, biosynthetic pathway, site of action, and potential signaling cascades are all unknown.

As erucamide is highly insoluble and hydrophobic, direct retinal injection is not possible as the fatty acid would aggregate locally and not disperse within the retina (**Fig. 5.1a**). We therefore utilized porous silicon nanoparticles (pSiNP) as a delivery vehicle. Porous silicon (pSi) based nanomaterials have been used extensively for drug delivery due to its biocompatibility and low toxicity within sensitive and hard-to-reach tissues.[22-26] pSi materials can degrade into silicic acid end products that can be excreted from the body. In addition, pSiNPs are very versatile due to their tunable size, and pores as well as readily functional surface which can aid with the loading of complex therapeutics. Previously, pSi particles have been used for the delivery of small-molecule drugs within the retina.[27, 28]

Motivated by the challenges of understanding erucamide's role as a neurotrophic factor as well as the versatile delivery features of pSiNPs, we designed a nanoparticle delivery construct for the retinal delivery of erucamide. In this study, we employed the use of surface functionalized pSiNPs for effective loading of the hydrophobic lipid fatty acid. The particles with nanoscale mesopores (nominal pore size, 10-15 nm) enabled effective loading of erucamide.

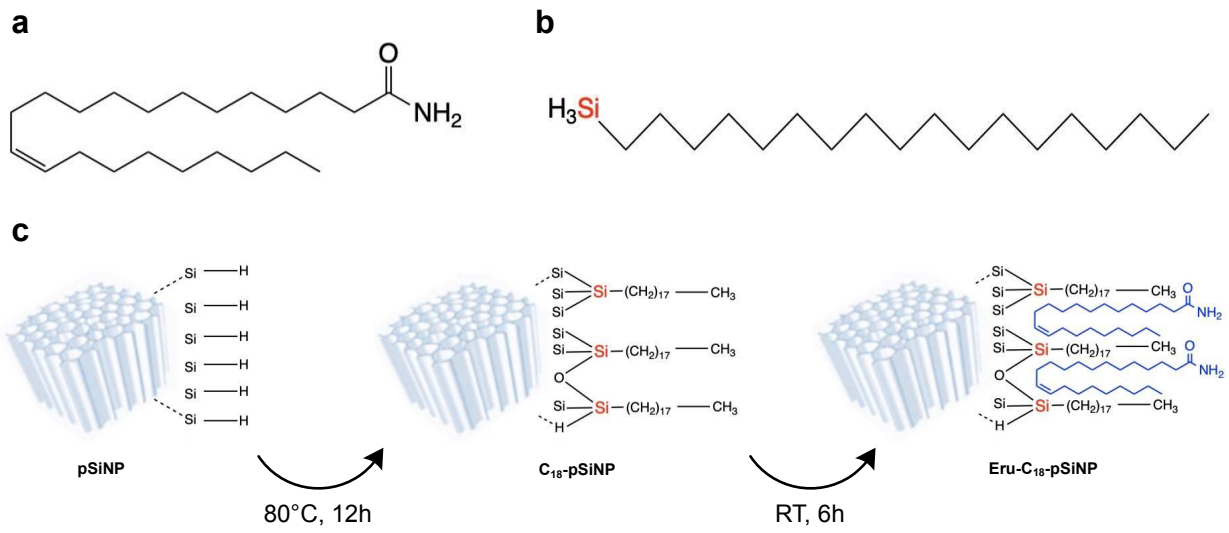

Figure 5.1: Preparation of silane-modified pSiNPs for erucamide loading. Schematic illustration of (a) erucamide, the hydrophobic lipid fatty acid amide and (b) the trihydridosilane, n-Octadecylsilane, to functionalize pSiNPs with long-chain hydrocarbons to render the particles hydrophobic. (c) Schematic illustration of the silane functionalization to the pSiNPs as well as erucamide loading to the C_{18}-pSiNPs.

Prior to erucamide loading, the pSiNPs were modified with a silane to provide a hydrophobic surface and interior, referred to in this work as C_{18}-pSiNP (**Figure 5.1**). The main use for this chemistry was to yield a stable hydrophobic surface to load erucamide through hydrobhoic-hydrophobic interactions. We used a thermal dehydrocoupling chemistry to prepare C_{18}-pSiNPs.[29] As-anodized pSi samples contain reactive Si-H species that can readily undergo dehydrocoupling reactions with organic species that contain a terminal -SiH_3 group.[26] Here, we chemically modified the pSiNPs with n-octadecylsilane ($H_3Si(CH_2)_{17}CH_3$), which has previously been shown to impart a highly hydrophobic character onto the particles (**Figure 5.1b/c**).[29] Attenuated total reflectance Fourier Transform Infrared (ATR-FTIR) spectroscopy was able to confirm the presence of the organic signatures assigned to the functionalized octadecylsilane species within the C_{18}-pSiNPs, including bands at 470 and 2850−2930 cm^{-1} assigned to the scissor and stretching modes of CH_2, respectively while a band at 1080 cm^{-1} for Si-O, in which the

thermally induced reaction generally produces quantities of silicon oxides (**Figure 5.S2c**, Supporting Information). In addition, dynamic light scattering (DLS) and ζ-potential measurements showed subtle changes in size and surface charge while N_2 adsorption–desorption isotherms showed changes in specific surface area, pore size and pore volume, associated with the dehydrocoupling reactions (**Figure 5.2**, **Figure 5.S2** & **Table 5.S1** & **5.S2**, Supporting Information).

Utilizing the C_{18}-pSiNPs, we subsequently loaded the particles with erucamide. C_{18}-pSiNPs were mixed for six hours with an equivalent mass ratio of erucamide and subsequently washed to remove any unbound erucamide. The loading was confirmed through DLS, FTIR, N_2 adsorption–desorption isotherms and thermogravimetric analysis (TGA) (**Figure 5.2d/e** & **Figure 5.S2c** & **5.S3**, Supporting Information). The increase in hydrodynamic size, stronger CH_2 stretching peaks, as well as the decrease in all of surface area, pore size and pore volume values, provided qualitative evidence of erucamide loading. TGA measurements indicated 14.75% (wt.%) of erucamide within the particles from the mass change within the temperature region from ~280°C to 573.19°C, the boiling point of erucamide (**Figure 5.S3**, Supporting Information). Beyond this temperature, any change in the weight of the particles, was not due to erucamide. This weight percent value provided an appropriate and accurate estimate to how much erucamide was loaded. This simultaneously enabled effective control of both nanoparticle and erucamide concentrations for both *in vitro* and *in vivo* experiments.

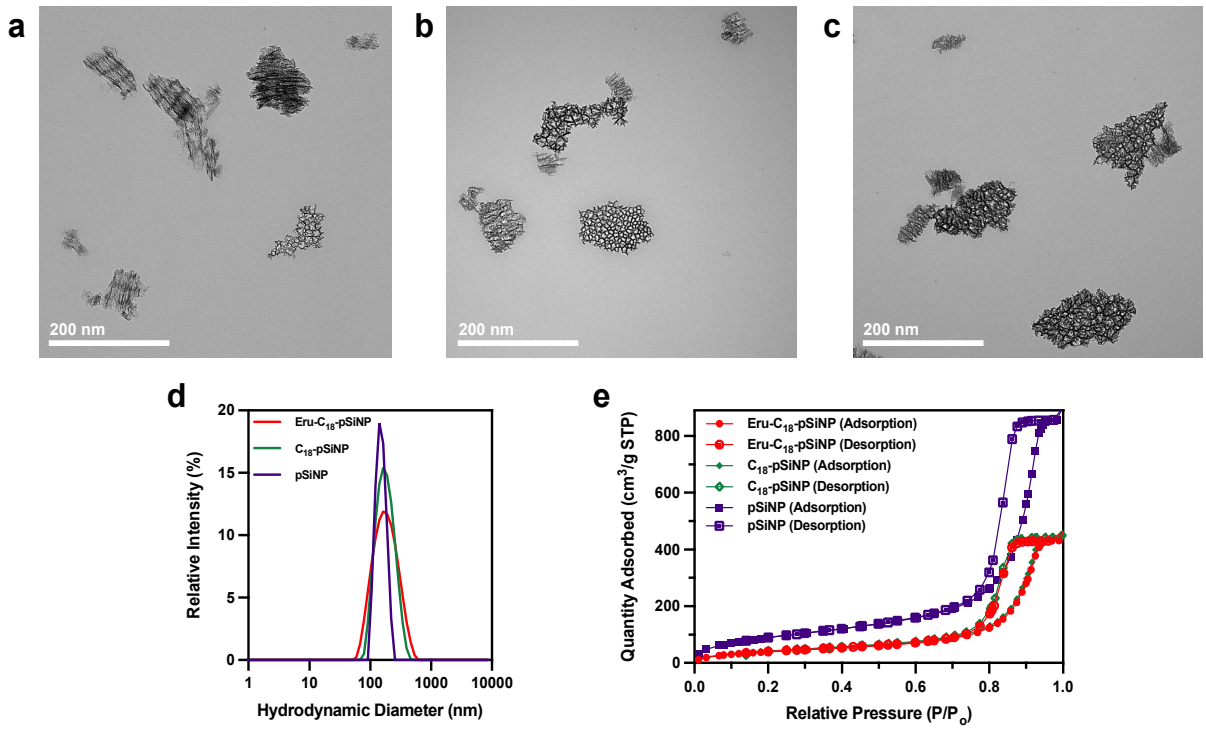

Figure 5.2: Characterization of Erucamided-loaded, silane-functionalized nanoparticles. Transmission Electron Microscopy (TEM) images of (a) freshly etched (pSiNP) and (b) octadecylsilane-functionalized (C_{18}-pSiNP) and (c) erucamided-loaded, octadecylsilane-functionalized particles (Eru-C_{18}-pSiNP) (scale bar = 200 nm). (d) Dynamic light scattering (DLS) data of freshly etched pSiNPs, silane-fuctionalized and erucamide-loaded, silane-functionalized particles. There is an increase in hydrodynamic size due to the surface functionalization and erucamide loading into the particles. (e) N_2 adsorption–desorption isotherms of the empty, unmodified pSiNPs, silane-functionalized pSiNPs and erucamide-loaded, silane-functionalized pSiNPs. The isotherms are used to determine the pore size and pore volume of the particles.

We then subsequently assessed the cell cytotoxicity and histological evaluations of retinal vessels to analyze the biosafety of the pSiNPs, and the silane functionalization. One of the initial concerns with the pSiNP construct was in regard to the silane chemistry, which may potentially induce toxicity towards healthy retinal cells. It is known that retinal tissues are very sensitive to external administration of inorganic nanoparticles, lipids and fatty acids. Though octadecylsilane is known to be an effective chemistry to impart hydrophobicity onto porous silicon, the silane has limited use for both *in vitro* and *in vivo* experiments. To assess *in vitro* biosafety both choroidal endothelial (hCh-Ecs) and retinal

endothelial cells were incubated for 48 h with concentrations of silane-modified pSiNPs (C_{18}-pSiNP) containing 0-10 µg/mL of particles. An alamarBlue assay was used to determine cell viability and results indicated >90% cell viability for all pSiNP constructs when compared to the media treated control (**Figure 5.S4**, Supporting Information).

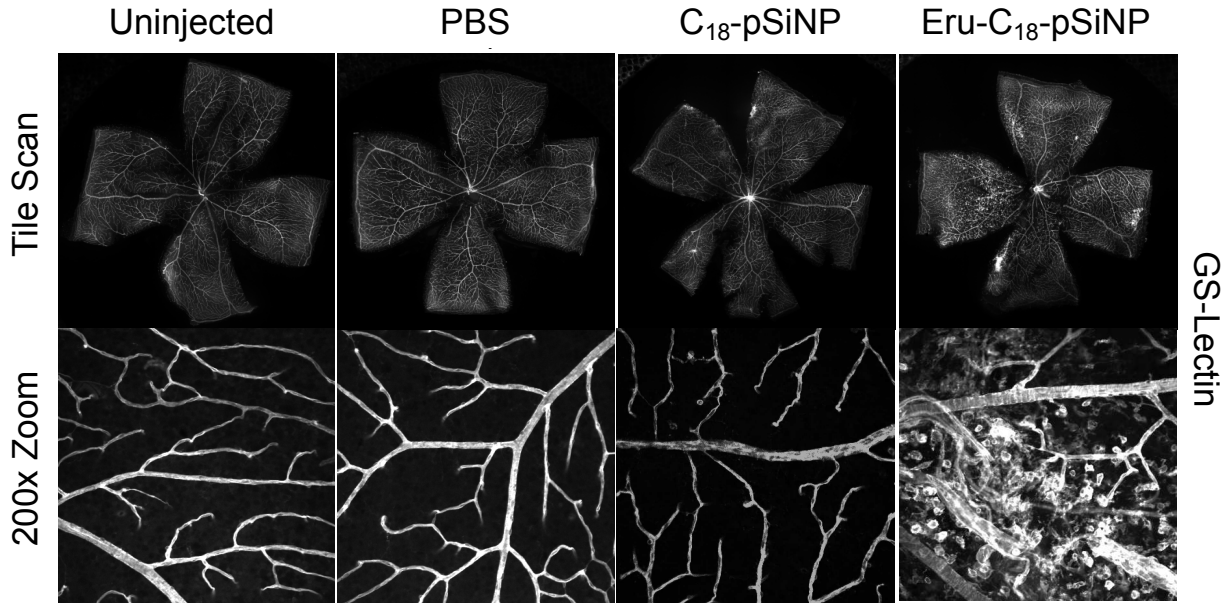

Figure 5.3: *in vivo* behaviour of pSiNP constructs. GS-lectin labeled retinal vessels at the superficial plexus after 72 hours post-injection of various pSiNP constructs in P27 mice. Only the injected Eru-C_{18}-pSiNP mice induced visible phenotype inflammation.

To examine the phenotype behavior of erucamide *in* vivo, retinal injections of pSiNP constructs (C_{18}-pSiNP) and erucamide-loaded pSiNP constructs (Eru-C_{18}-pSiNP) were compared to PBS controls. The retinal flat-mounts after lectin perfusion for both intravitreal and subretinal injection of Eru-C_{18}-pSiNP resulted in wide-spread activation of GS-Lectin positive cells, which was not seen with the controls (**Figure 5.3**). This was directly observed by evaluating the gross morphology of the retinal vessels from the flatmounts which clearly indicated the inflammation of infiltrated activated immune cell., The same inflammation of the vessels was not seen with the contralateral uninjected control eyes of the wild-type mice. Further assessment of the immunohistochemistry

(IHC) stained retinal sections also showed that there was a significant increase in the number of surviving rows of photoreceptors in P32 mice post injection of (**Figure 5.S5a**, Supporting Information). In addition, Eru-C_{18}-pSiNP prevented the photoreceptor atrophy in RD10 mice that occurred between P18 and P25 stages compared to uninjected controls (**Figure 5.S5b**, Supporting, Information). This evidence suggests that erucamide is a neurotrophic factor.

We subsequentially repeated the retinal injection experiments to identify the activated cells from the visible inflammation sites. In this experiment, retinal flat-mounts were stained with both Collagen IV (a specific endothelial cell marker) and CD11b+ markers. Since GS-Lectin stains for both endothelial and microglia/macrophage cells, it was necessary to separate the cell types to further determine which cells were inflamed. Eru-C_{18}-pSiNPs were shown to activate CD11+ microglia cells/macrophage precursors as the markers overlapped with the GS-Lectin-stained inflammation sites. This was, once again, not seen with the control C_{18}-pSiNPs. A secondary experiment using chemically synthesized fluorescent-dye (BODIPY) labelled erucamide (^{BDP}Eru) probe loaded within C_{18}-pSiNPs was repeated to facilitate the visualization of erucamide *in vivo*, and to identify if erucamide was uptaken by the activated CD11b+ cells (**Figure 5.4** & **Figure 5.S6**, Supporting Information). The co-localization between the BDP and the CD11b+ signals suggests that microglia is directly targeted by erucamide.

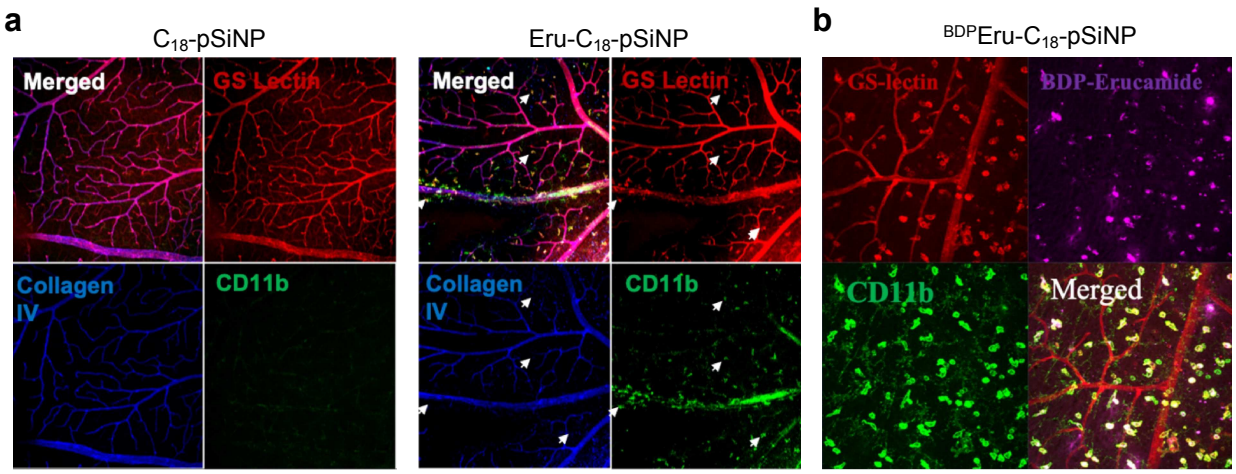

Figure 5.4: Vascularization of pSiNPs constructs to identify activated cells. (a) Retinal flat-mounts stained with GS-Lectin, Collagen IV and CD11b marker of retinal vessels at the superficial deep plexus after 72 hours post-injection of various pSiNP constructs in P27 mice. Only Eru-C_{18}-pSiNP constructs activate CD11b+ cells within the retina. (b) Retinal flat-mounts stained with GS-Lectin, and CD11b marker of retinal vessels at the superficial deep plexus after 72 hours post-injection of various BDP-labelled Erucamide-loaded (^{BDP}Eru) pSiNP constructs in P27 mice. ^{BDP}Eru-C_{18}-pSiNP particles overlap with CD11b+ cells, indicating that the cells uptake the particles.

With this in mind, the next step was to identify if euracamide had pro-angiogenic effects by identifying activated cytokines in both CD11b+ cells and human iPSC derived microglia. As microglia are the local immune cells in the retina and are activated during pathological conditions such as retinal degeneration and neovascularization, these cells migrate to affected sites and respond to inflammation phagocytic activity. This activity leads to the expression of inflammatory cytokines, as expressed by the visible microaneurysms. These activated CD11b+ cells and human iPSC derived microglia are commonly seen in different retinal degenerative, inflammatory and angiogenic diseases though, identifying the specific activated cytokines due to erucamide, is not yet understood. We subsequently sorted both CD11b+ cells and human iPSC derived microglia by flow cytometry after the addition of erucamide-loaded pSiNP constructs. We then evaluated the expression of pro-angiogenic genes within the sorted cells by qPCR

(**Figure 5.5**). We found that for CD11b+ cells, that the expression of PDGFα, CTGF, CX3CL1, Ang1 and PDGFβ were higher than the control particles. Within iPSC derived microglia, PDGFα, CX3CL1, Ang1, Ang2 and PDGFβ were significantly higher than the controls. With these experiments, it is suggested that the common angiogenic factors for both cell types, PDGFα, CX3CL1, Ang1 and PDGFβ are activated by the addition of erucamide.

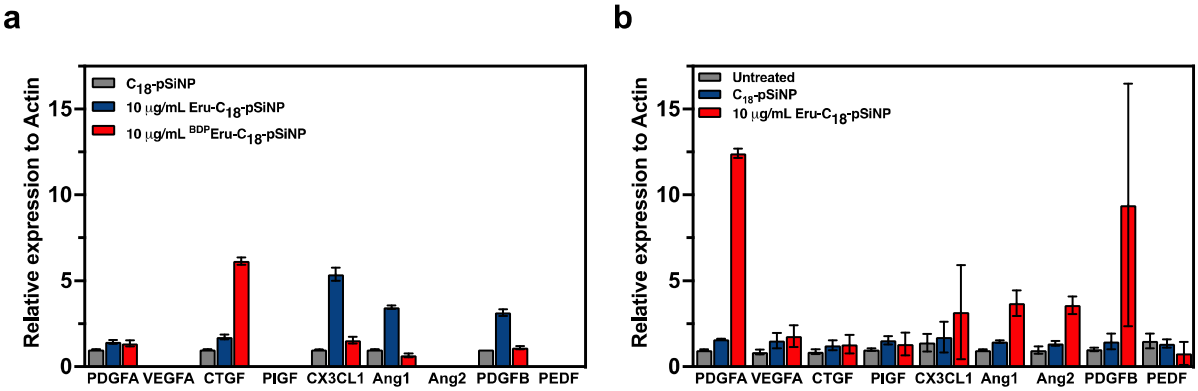

Figure 5.5: Proangiogenic factors activated by Eru-C_{18}-pSiNPs injection. Expression of factors upregulated by Eru-C_{18}-pSiNPs and ^{BDP}Eru-C_{18}-pSiNPs in (a) CD11b+ cells and (b) iPSC derived microglia cells determined by qPCR ($n = 3$, $p < 0.05$). In both cell types, erucamide activates similar angiogenic factors.

By identifying the various angiogenic factors activated by erucamide, we wanted to test a parallel experiment using other classes of hydrophobpic fatty acids, particularly two from the same PAM family, oleamide and palmitamide as well as a synthetically derived fatty acid, AFK-187 (**Figure 5.S7**, Supporting Information). One of the major reasons to identify the activated factors of similarly structured fatty acids is to see if this broader class of primary fatty acid amides would yield similar activated phenotypes. A synthetically modified AFK-187 was used as a novel analogue of erucamide to potentially act as more stable fatty acid for potential clinical use. In a similar fashion to erucamide, we loaded the particles with the various fatty acids and injected the constructs in P27

retinas. Retinal flat-mounts were subsequently stained with both GS-Lectin and CD11b+ markers to identify if the similar CD11b+ cells were activated. Both Oleamide and AFK-187 activated CD11b+ cells while palmitamide did not (**Figure 5.S8**, Supplementary Information). We also repeated the qPCR experiments on injected retinas to see if both oleamide and palmitamide activated similar angiogenic factors to erucamide (**Figure 5.S9**, Supporting Information). In both cases, the expression of the growth factors for both fatty acid amides do not show similar activation of proganiogenic factors to that of erucamide as well as the pSiNP controls. This data suggests that erucamide is unique as a PAM towards the activation of various angiogenic factors in CD11b+ cells.

To test the effectiveness of AFK-187 and compare the activation of angiogenic factors to erucamide, we added AFK-187 and erucamide-loaded pSiNPs to various siRNA knockdown cells We subsequently performed a qPCR analysis of mRNA isolated from iPSC microglia (**Figure 5.6**). We utilized a scrambled siRNA control while the other knockdown cells included genes for TMEM19, DRAM2 and TMBIM6. These were selected as they were potential binding proteins for erucamide as determined through photo-affinity labelling experiments (not shown). In all of the knockdown cells as well as the controls, AFK-187 shows greater angiogenic expression than erucamide. In addition, the activated angiogenic factors of VEGF, TNFα, CD11B and IL1B which mimic those of erucamide, suggest that the upregulation of proinflammatory cytokines could be used as an alternative for the rescue of PAM-knockout mice in further studies.

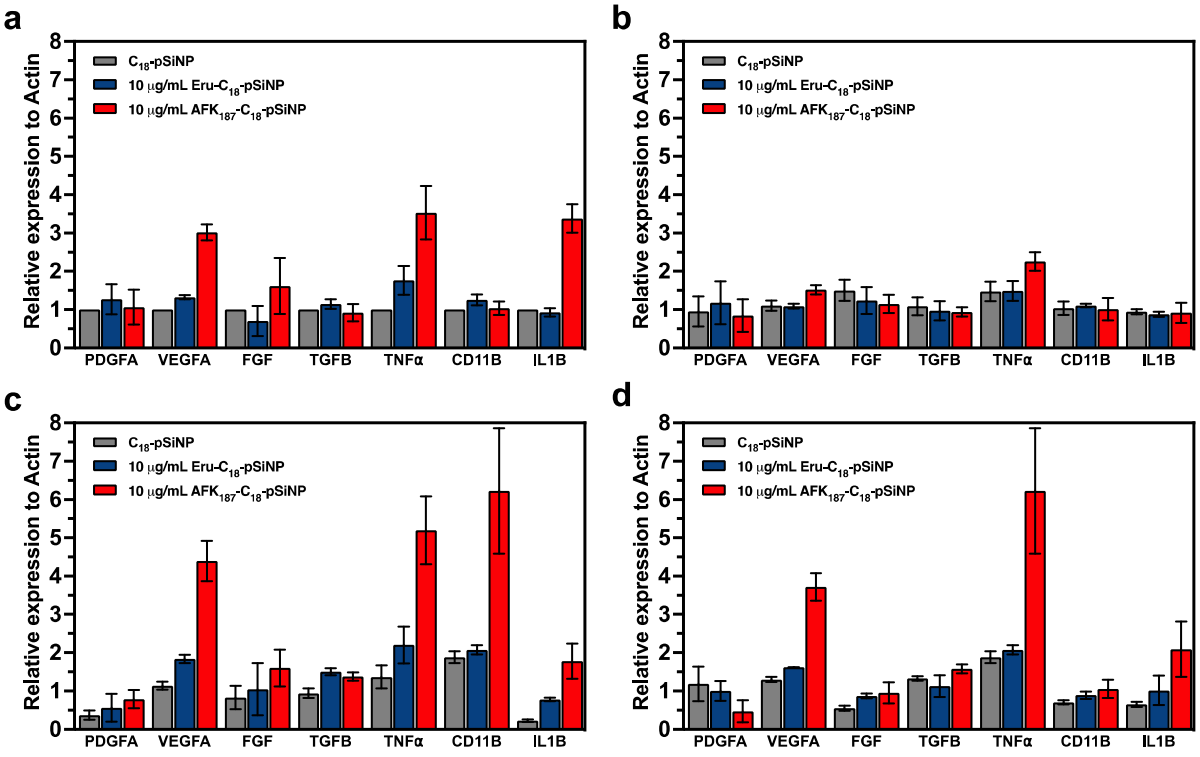

Figure 5.6: Proangiogenic factors activated by Eru-C_{18}-pSiNP and AFK-187-C_{18}-pSiNP injections. Expression of factors are evaluated by qPCR for iPSC derived microglia cells silenced with (a) scrambled siRNA control, (b) siTMEM19, (c) siDRAM2 and (d) siBI1 ($n = 3$, $p < 0.05$). For VEGFA, TNFα, CD11B and IL1B, both erucamide and AFK-187 yielded greater expression than C_{18}-pSiNP controls. In all cases, AFK-187 yielded greater expression of angiogenic factors than erucamide.

5.3 Conclusions

pSiNPs have provided an effective tool for the delivery of hydrophobic fatty acid amides within retinas. The surface functionalization of the particles through the addition of n-Octadecylsilane provides an increased hydrophobic surface to increase the loading capacity of erucamide. We can subsequently utilize this vehicle to better understand the *in vitro* and *in vivo* behavior of erucamide and other classes of PAMs. We hypothesize that, as a known angiogenic factor itself, erucamide may also work in a paracrine fashion to regulate and maintain a neurotrophic microenvironment in the retina. We have identified that decreased erucamide levels are associated with photoreceptor atrophy. In

addition, microglia can be a direct target of erucamide both *in vitro* and *in vivo*. This neurotrophic paracrine activity may be mediated by several novel microglial-associated erucamide-binding proteins that are responsible for the activation and angiogenic cytokine secretion from microglia cells. While more technical details remain, these observations may already provide valuable insight into neurovascular unit physiology, and the modulation of these pathways may represent novel targets for drug discovery in the treatment of neurovasculoglial degenerative retinal diseases.

5.4 Materials & Methods

5.4A Materials

Highly doped p-type doped p^{++}-type (B-doped) crystalline silicon wafers (~0.001 Ω cm resistivity, 100 mm diameter, 525 μm thickness) polished on the (100) face was purchased from Siltronix Corp. All reagents were used as received and purchased from Aldrich Chemicals, Inc. n-Octadecylsilane was purchased from Gelest, Inc. Fluorophores were purchased from Lumiprobe. All other chemicals and media were purchased from ThermoFisher and used as is.

5.4B Preparation of Porous Silicon Nanoparticles (pSiNP)

pSiNPs were prepared using a previously developed “Perforated Etch” method.[25, 30] A highly doped p^{++}-type crystalline silicon wafer (~0.001 Ω cm resistivity, 100 mm diameter, 525 μm thickness, Siltronix, Inc.) was electrochemically etched in a of 3:1 (v:v) ratio of 48% aqueous hydrofluoric acid (HF): to ethanol electrolyte solution. (CAUTION: HF is highly toxic and can cause severe burns on contact with the skin or eyes). Prior to the preparation of the porous layer, the wafer was cleaned using a “sacrificial etch” as previously described, which consists of etching a thin, porous layer into the wafer (400

mA cm^{-2} applied for 40s) using the aforementioned electrolyte solution. The wafer was subsequently rinsed with ethanol and the porous layer was dissolved in a strong base (2M aqueous KOH). The cell was then rinsed with water and ethanol three times, before a fresh solution of the electrolyte solution was added, to prepare the nanoparticles. The etching waveform for the particles was generated using LabView (National Instruments, Inc.), and the current was provided by a Keithley 2651A Sourcemeter power supply interfaced to LabView. The waveform used was composed of a square wave where a lower 46 mA/cm2 current density was applied for 1.818 s, followed by a higher 365 mA/cm2 current density pulse for 0.363 s. This waveform was repeated for 300 cycles, generating a thick, porous silicon film with thin regions of high porosity “perforations” that repeat approximately ever 200 nm through the porous layer. The electrolyte solution was subsequently removed, and the porous layer was washed three times with ethanol. This film was then removed from the silicon wafer through a “lift-off” with the application of a constant current density of 3.4 mA/cm2 for 180 s in a different electrolyte solution consisting of 1:20 (v:v) 48% aqueous HF:ethanol. The wafer was carefully transferred to a vial filled with ethanol. Prior to being fragmented into nanoparticles by ultrasonication overnight in a ultrasonication bath, the lift-off film was functionalized with silane as described in the following step.

5.4C Surface Modification of pSiNPs

The freestanding multi-layered pSi lift-off films were transferred into a 20 mL glass vial and 500µL ethanol and 1.5 mL of n-Octadecylsilane reagent was added. The vial was capped and freestanding pSi film, immersed in silane, was subject to ultrasonication and fragmented into nanoparticles overnight in a ultrasonication bath (Ultrasonic bath, model 97043-960, VWR International). The resulting particles were subsequently removed from the vial and centrifuged (15,000 rpm, 10 min) to remove any unbound silane. The particles were subsequently washed and centrifuged three times with n-hexane and three times with ethanol and finally and resuspended in 100% ethanol for storage.

5.4D Loading of fluorophores to pSiNPs

A specific fluorophore, Cy5.5 was used as an imaging tag for the tracking of porous silicon nanoparticles once injected *in vivo*. The fluorophores were bound surface modified particles through adsorption loading. Briefly, 10 µL of 5 mg/mL of Cy5.5 fluorophore dissolved in DMSO was added to 1mg/mL of C_{18}-terminated particles. The fluorophore was allowed to mix with the particles overnight, free from light. The particles were then washed 3 times with ethanol and centrifuged (15,000 rpm, 10 min) to remove any free fluorophore. The particles were then dispersed in ethanol and stored in dark.

5.4E Loading of Erucamide to pSiNPs

The lipid fatty acid, erucamide, was used for all *in vivo* experiments. A 10 mg/mL stock solution of erucamide was prepared by dissolving erucamide in ethanol overnight. Briefly, 1 mg/mL of C_{18}-pSiNPs was centrifuged (15,000 rpm, 10 min) to remove free ethanol and the particles were re-dispersed in the 1mL of the 10 mg/mL erucamide stock solution. The particles were then subsequently allowed to mix at 4°C for 6 hours. The

particles were then washed 3 times with ethanol and centrifuged (15,000 rpm, 10 min) to remove any unbound erucamide and were resuspended in ethanol for storage. The erucamide loaded particles were subsequently labelled as Eru-C_{18}-pSiNP. The same loading procedure was repeated for Oleamide, Palmitamide and AFK-187.

5.4F Characterization of pSiNPs

Hydrodynamic diameter (size) and the ζ-potential (surface charge) measurements were obtained on a Zetasizer, Zs90 (Malvern Instruments). All of pSiNP, C_{18}-pSiNP and Eru-C_{18}-pSiNP size measurements and ζ-potential measurements were measured with particles dispersed in ethanol. For hydrodynamic size, 300μL of 0.1mg/mL of particles were used while for ζ-potential, 800μL of 0.1mg/mL of particles were used. The FTIR spectra of the particles were obtained by a Thermo Scientific Nicolet 6700 FTIR instrument fitted with a Smart iTR diamond ATR fixture. TEM images were obtained using a JEOL 1400 plus electron microscope (JEOL USA, Inc.) at 80KeV and subsequently imaged with a Gatan Oneview camera (Gatan, Inc.). Thermogravimetric analysis (TGA) data was obtained using a TA Instruments™ Discovery SDT 650™. Nanoparticle samples were heated from 100°C-800°C at a ramp rate of 10°C/min in nitrogen. Both weight (%) change and derivative heat flow values were assessed. Dye-loaded particle constructs were assessed using a Molecular Devices™ SpectraMax® iD5 Multi-Mode Microplate Reader. N2 adsorption/desorption isotherms were obtained using dry nanoparticles at a temperature of 77 K using a Micromeritics ASAP 202 instrument.

5.4G Cell Culture

Induced pluripotent stem cell (iPSC) lines were derived from peripheral blood mononuclear cells from a female. The cell reprogramming was performed by the Harvard

iPS core facility utilizing a sendai virus for reprogramming factor delivery. All of the cell lines were obtained with verified normal karyotype and were contamination-free. iPSCs were maintained on Matrigel (BD Biosciences) coated plates immersed with mTeSR1 medium (STEMCELL Technologies). The cells were passaged every 3 days around 80% confluence. Colonies containing clearly visible differentiated cells were marked and manually removed prior to any subsequent passaging. All microglia precursors were generated using previously described methods.[31] The embryoid bodies (EBs) were formed using Aggrewells (STEMCELL Technologies), cultured with bone morphogenetic protein 4 (BMP4), vascular endothelial growth factor (VEGF), and stem cell factor (SCF), then plated into T175 flasks with Interleukin-3 and macrophage colony-stimulating factor (M-CSF). After 4 weeks, microglia precursors emerged within the supernatant. iPS derived Microglia precursors (pMG) were plated into 12 well plates containing X-VIVO15 with 100 ng/ml M-CSF, 2 mM Glutamax, 100 U/ml penicillin, and 100 µg/ml streptomycin for further in vitro assays. The cells were then stimulated with human recombinant Tgfβ1 (Peprotech, 100-21), 10 µM of SB525334 (Selleckchem, S1476), 200 µM of DMOG (Millipore sigma, D3695), then cell culture supernatant and cells were stored at −80°C for following qPCR and ELISA assays.

5.4H *IN VITRO* TOXICITY

Approximately 5000 cells in 300µL of Edothelial Growth Medium (EGM) of two specific cell lines including choroidal endothelial (hCh-Ecs) and retinal endothelial cells were plated into a 48 well plate. After 24 hours, 30µL of two specific concentrations of C_{18}-pSiNP, 1 mg/mL and 5 mg/mL, were added to each well of the plate in triplicates and were incubated for 24 hours at 37°C. Following this, a 10% (v/v) of alamarBlue™

(ThermoFisher, DAL1025) cell viability reagent (33μL) was added into each well. The plates were mixed through gentle rotation 2-3 times. After 6 hours, the fluorescence of each well was measured using an excitation at 540 nm and an emission at 590 nm. The cell viability was subsequently assessed using the fluorescence percentage of nanoparticle-treated wells compared to untreated control wells.

5.4I Mice and Animal Experimental Procedures

All animal protocols were approved by the IACUC committee at The Scripps Research Institute, La Jolla, California. All animals received food and water ad libitum. RD10 mice were obtained from The Scripps Research Institute animal facility. Mice were euthanized by cervical dislocation at varying time points, as indicated in the results. All animal protocols were approved by the IACUC committee at The Scripps Research Institute, La Jolla, California, and all federal animal experimentation guidelines were adhered to.

5.4J Immunohistochemistry of Whole-Mount Retinas

Enucleated eyes were placed in 4% paraformaldehyde (PFA) for 1 h. After fixation, the cornea, the lenses, the sclera, choroid, and the vitreous were removed and the retinas were laid flat with four radial relaxing incisions. Retinas were incubated in blocking buffer (PBS with 10% fetal bovine serum, 10% normal goat serum, and 0.2% Triton X-100) for 2 h at 4°C, following by an overnight incubation with primary antibodies in blocking buffer at 4°C. Tissue specimens were then washed and incubated with the corresponding Alexa fluorescent-conjugated secondary antibodies (Thermo Fisher) for 3 h. Retinas were washed in PBS and mounted with ProLong Diamond Antifade mounting medium (Thermo Fisher Scientific, P36965). Fluorescent-conjugated isolectin Griffonia Simplicifolia IB-4

(GS-lectin) (1:200; Thermo Fisher Scientific, I21413, I32450), Purified Rat Anti-CD11b (BD Biosciences, 550282) and RB X MS Collagen Type IV (EMD Millipore, AB756P) were used for labeling endothelial cells. For detecting hypoxic cells in vivo, 60 mg/kg bodyweight pimonidazole hydrochloride (Hypoxyprobe-1™ kit, hpi), diluted in PBS was administered by intraperitoneal injection 1 h prior to euthanasia. All images were acquired with a confocal laser scanning microscope (LSM 710, Zeiss) and processed with the ZEN 2010 software (Zeiss).

5.4K Retinal Microglia Isolation by Flow Cytometry

A postnatal neural dissociation kit (Miltenyi, 130-092-628) was used to prepare a single cell suspension from mouse retinas. Cells were centrifuged at 150*g* for 5 min at 4°C. The digested tissue was resuspended in 100 µl of 4% FBS in PBS containing an FITC antibody to CD11b (1:100; BioLegend, 101206) and incubated for 20 min on ice. The cells were washed and suspended with 1 ml of 4% FBS/PBS containing DAPI (1:2000; Thermo Fisher Scientific, 62248). Labeled retinal microglia (CD11b positive) were isolated by fluorescence-activated cell sorting (FACS) (MoFlo Astrios EQ; Beckman Coulter) at the Scripps Flow Cytometry Core Facility. Sorted cells were resuspend in 350ul of RLT buffer from RNeasy Micro Kit (QIAGEN) and stored at −80°C.

5.4L RNA Isolation and Real-Time PCR

For whole retina and culture cells, single retinas were collected in 500 µl of Trizol and total RNA was isolated using a PureLink RNA Mini Kit (Thermo Fisher Scientific) according to manufacturer's instructions. Seven hundred and fifty nanograms of RNA was used for RT-qPCR using a high-capacity cDNA reverse transcription kit (Thermo Fisher Scientific). For flow-sorted cells, total RNA was isolated from sorted cells using the

RNeasy Micro Kit (QIAGEN) and reverse transcribed using Maxima First Strand cDNA Synthesis Kit for RT-qPCR (Thermo Scientific). qPCR was performed using Power-up SYBR™ Green PCR Master Mix (Thermo Fisher Scientific) and primers on a Quantstudio 5 Real-Time PCR System (Thermo Fisher Scientific). β-actin (*Actb*) was used as the reference gene for all experiments. Levels of mRNA expression were normalized to those in controls as determined using the comparative CT (ΔΔ*CT*) method.

5.4M Statistical Analysis

All statistical analyses were assessed using GraphPad Prism 9. The investigators were not blinded throughout in vivo experiments or outcome assessment. Statistical significance was determined by both two-tailed unpaired Student *t* tests with Welch correction and one-way ANOVA for multiple comparisons when deemed appropriate.

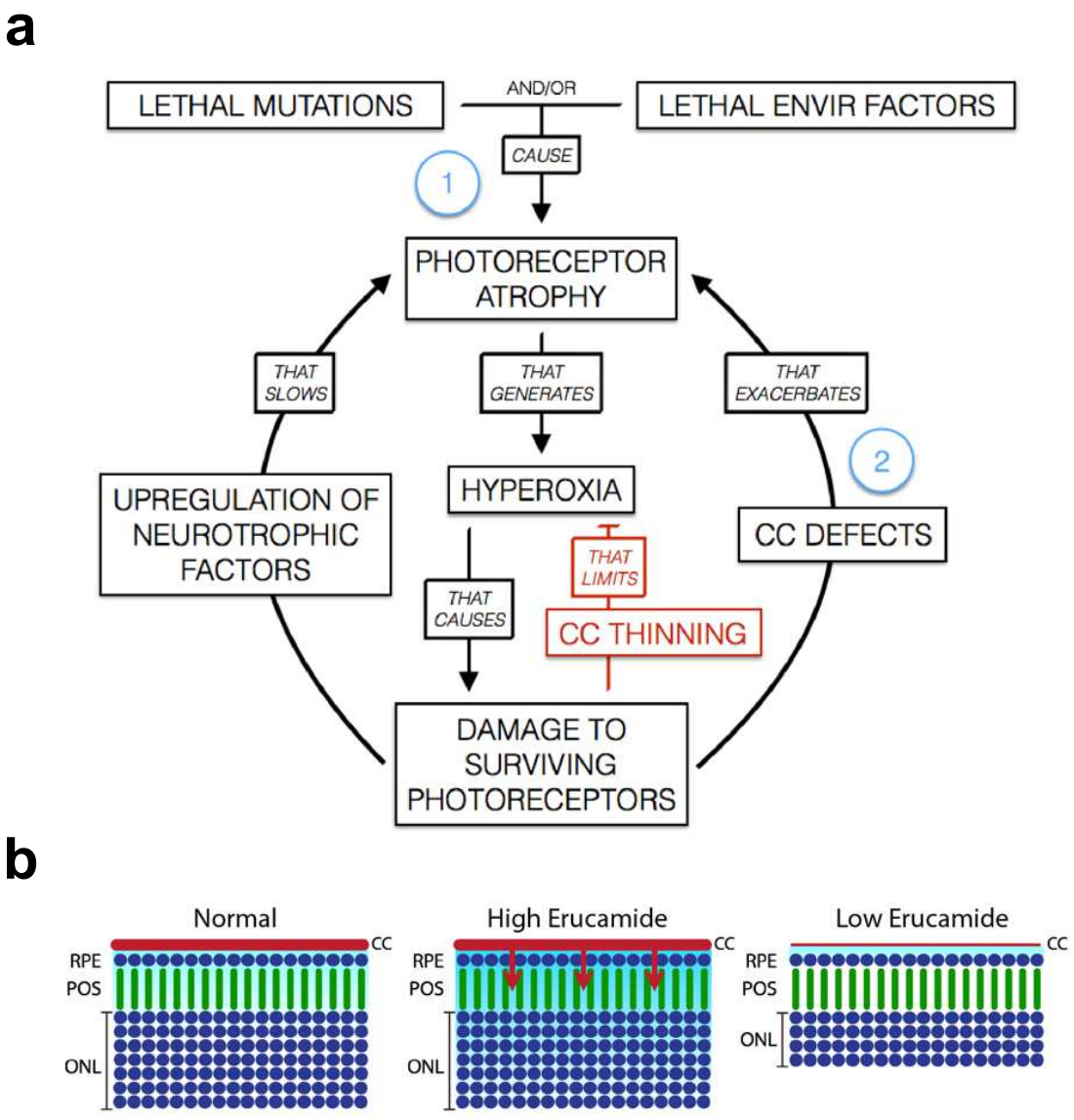

Figure 5.S1: Model for how erucamide may function within the retina. (a) Schematic of a modified two-stage model of retinal degeneration. A combination of various mutations and/or environmental factors induce potential early-stage photoreceptor atrophy, thereby ensuing hyperoxia, due to poorly regulated choriocapillaris. It is known that hyperoxia is a potent toxin that affect surviving photoreceptors. The red text indicates photoreceptor death and the subsequent loss in PAM/erucamide, would result in choriocapillaris constriction, which in turn locally limits the hyperoxia and subsequent damage to neighboring photoreceptors. (b) Schematic of erucamide levels and choriocapillaris. Normally high levels of erucamide are likely important in maintaining the proper size of the choriocapillaris. However, very high levels can induce abnormal vessel growth into the outer retina, while attenuated levels induce choriocapillaris constriction and are commonly associated with retinal degeneration diseases.

Table 5.S1: Size & Surface Charge of pSiNP Constructs as assessed through Dynamic Light Scattering (mean value ± SD, n = 3).

Hydrodynamic Size & Surface Charge			
	pSiNP	**C_{18}-pSiNP**	**Eru-C_{18}-pSiNP**
Z-Avg. Size (nm)	156.3 ± 6.5	168.4 ± 1.4	186.2 ± 8.6
ζ-Potential (mV)	-27.53 ± 1.63	14.22 ± 1.07	3.17 ± 0.67

Table 5.S2: Characteristics of pSiNP constructs for pore structure and internal surface area as calculated from cryogenic nitrogen adsorption isotherms. [a]Values determined using BET (Brunnauer–Emmett–Teller) analysis of the adsorption isotherms. [b]Values determined using BJH (Barret–Joyner–Halenda) analysis of the adsorption/desorption isotherms.

N_2 Adsorption Isotherms			
	pSiNP	**C_{18}-pSiNP**	**Eru-C_{18}-pSiNP**
Surface Area (m^2/g)[a]	357.563	158.373	150.859
Pore Volume (cm^3/g)[b]	1.33	0.69	0.65
Pore Size (nm)[b]	16.67	15.48	13.64

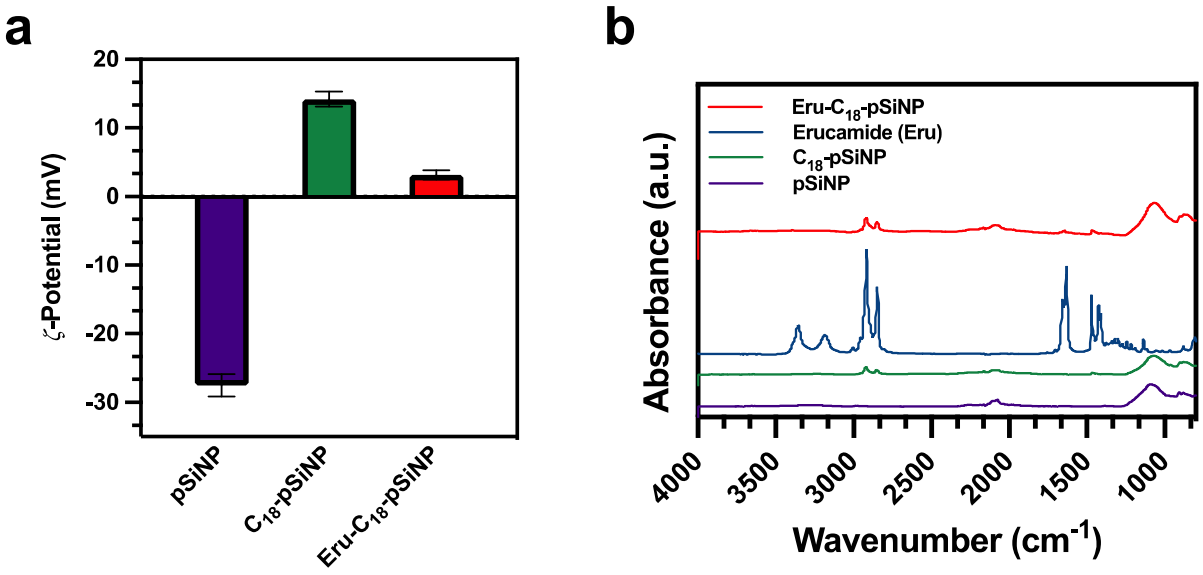

Figure 5.S2: Characterization of pSiNP constructs. (a) Zeta potential measurements of as-prepared pSiNPs, silane-functionalized pSiNPs (C_{18}-pSiNPs) and erucamide-loaded silane-functionalized pSiNPs (Eru-C_{18}-pSiNPs respectively (mean value ± SD, n = 3). Error bars represent standard deviation of three independently prepared samples. (b) Fourier Transform Infrared Spectroscopy (FTIR) spectra of pSiNPs functionalized with silanes and loaded with erucamide.

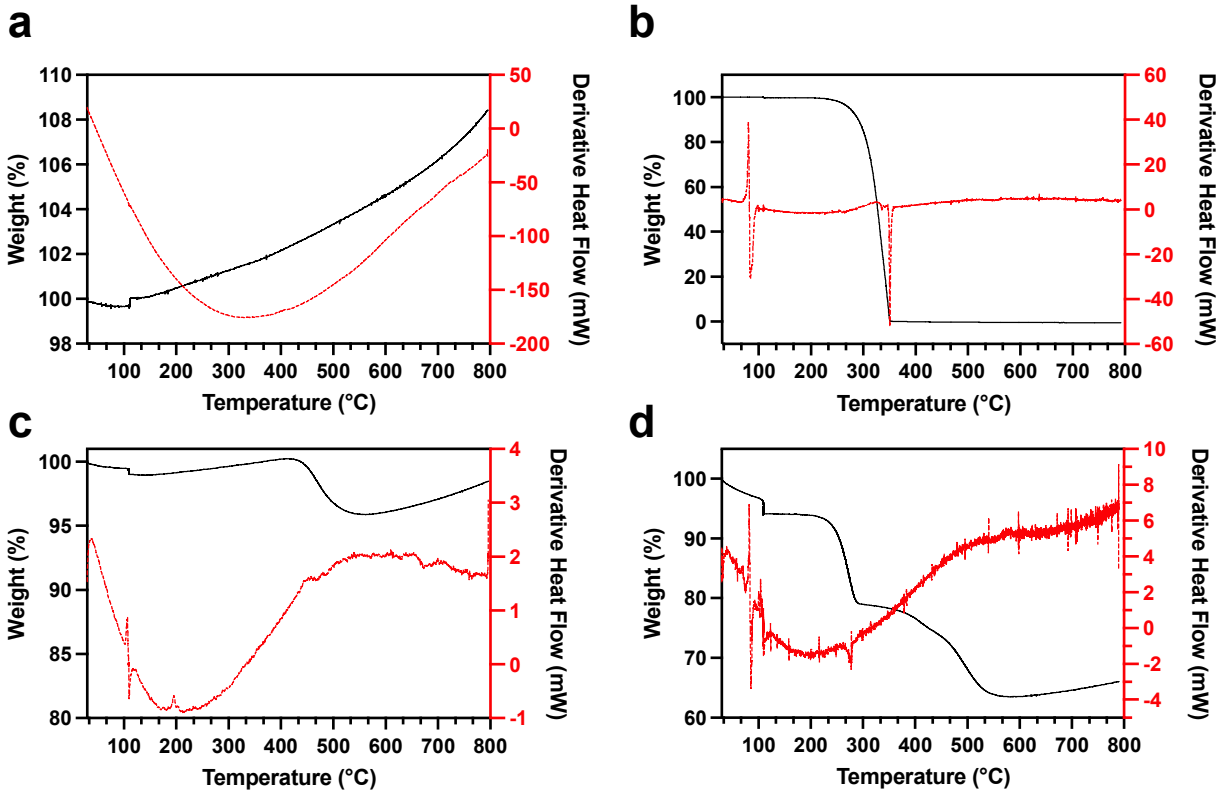

Figure 5.S3: Thermogravimetric analysis (TGA) measurements of (a) pSiNP, (b) Erucamide (c) C_{18}-pSiNP and (d) Eru-C_{18}-pSiNP. The derivative heat flow indicates phase changes of erucamide and the octadecylsilane reagent while the weight (%) curve provides an estimate of the amount of functionalized silane and loaded erucamide is available in a given amount of nanoparticles. The measurements indicated a weight percent loss of 14.75% (wt.%) of erucamide within the particles as a result of a mass change from ~280°C to 573.19°C in (d) resulting in the vaporization of erucamide. These calculated values were used to determine amounts of loaded fatty acid for both *in vitro* and *in vivo* experiments.

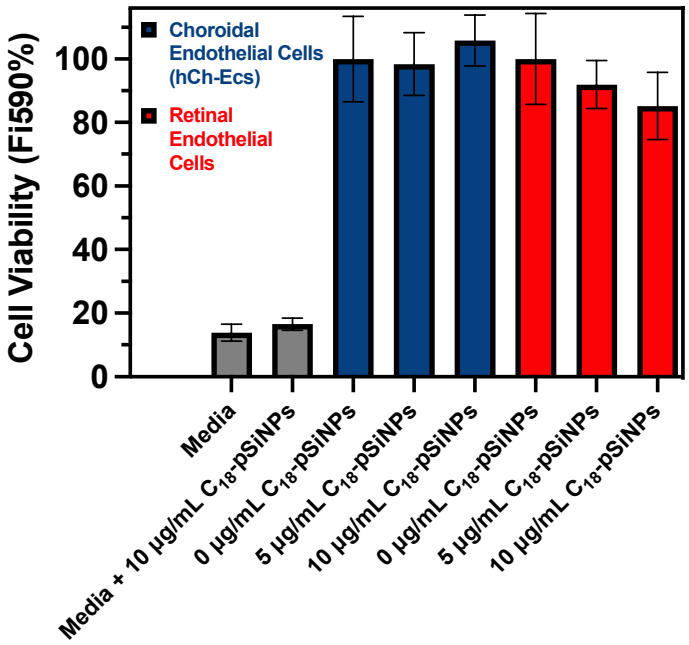

Figure 5.S4: *in vitro* toxicity of pSiNP constructs. Viability of both Choroidal Endothelial Cells (hCh-Ecs) and Retinal Endothelial Cells incubated with various concentrations of C_{18}-pSiNP constructs for 48 hours. The cell viability was assessed using an Alamar Blue assay following the manufacturer's protocol.

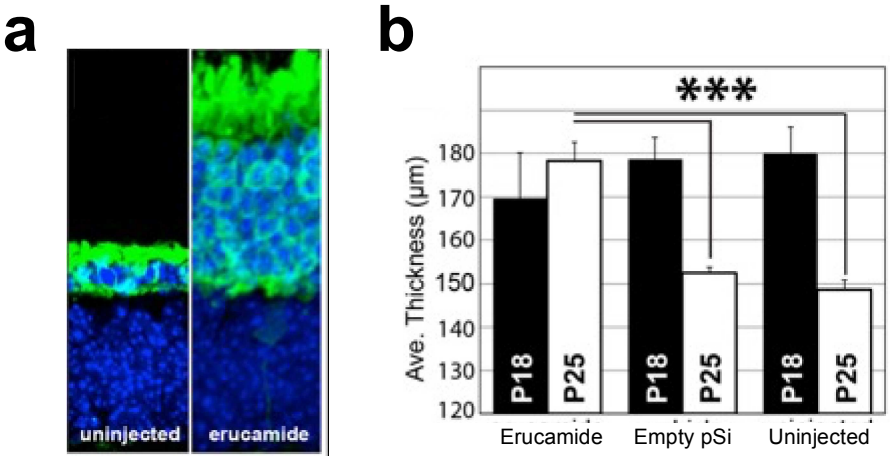

Figure 5.S5: Erucamide is neutrophic due to phenotypes changes. (a) Retinas from a P32 RD10 mouse (injected at P14). Photoreceptors were immunolabeled green (recoverin). Effects of erucamide injections quantified in (b) (n = 5; experiment repeated three times). Erucamide P18 vs erucamide P25, p = 0.76; erucamide P25 vs. vehicle P25, p = 9.57 x 10^{-7}; erucamide P25 vs uninjected P25, p = 3.57 x 10^{-7}. Error bars = max and min values, *** < 0.001.

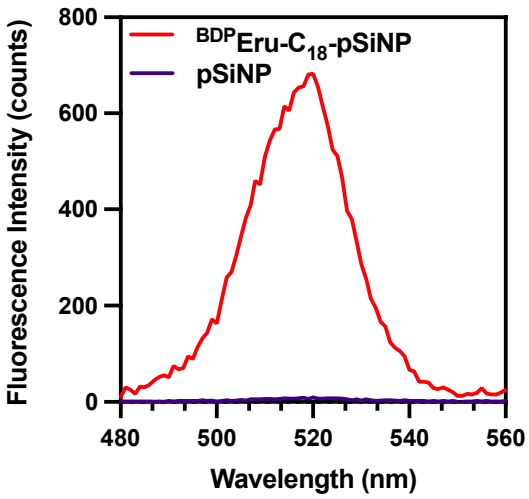

Figure 5.S6: Fluorescence measurement of bodipy-labelled erucamide-loaded, silane-functionalized pSiNPs (^{BDP}Eru-C_{18}-pSiNP). Unloaded pSiNPs show no fluorescence.

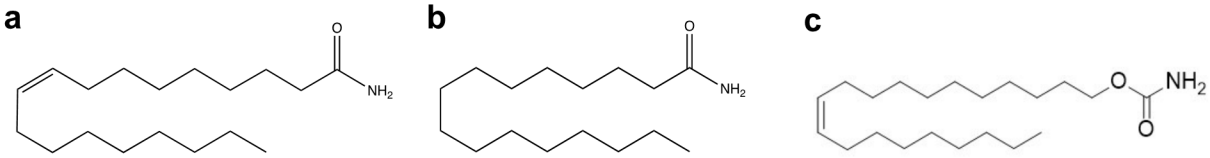

Figure 5.S7: Schematic illustration of erucamide derivatives within the same class of long chain fatty acids. The following show (a) oleamide, (b) palmitamide and (c) the synthetically derived AFK-187.

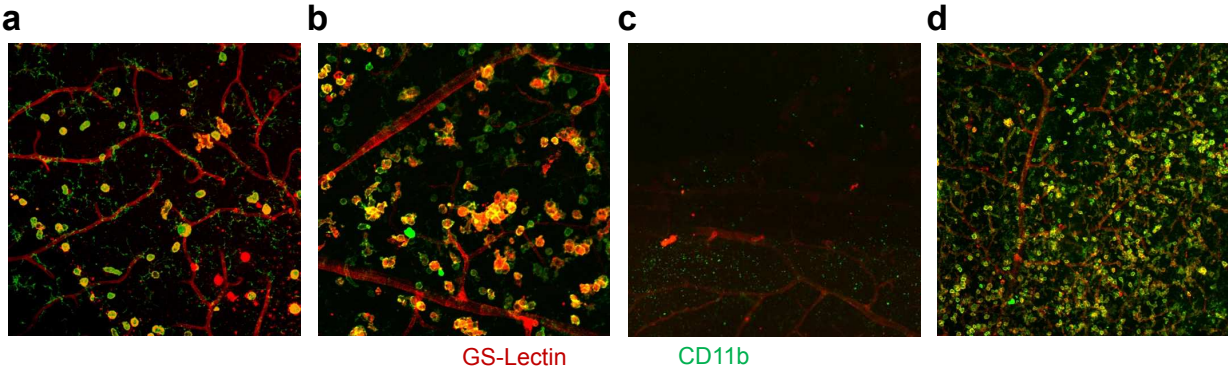

Figure 5.S8: Vascularization of loaded pSiNPs constructs to identify activated CD11b+ cells. Merged retinal flat-mounts stained with GS-Lectin and CD11b marker of retinal vessels at the superficial deep plexus after 72 hours post-injection of various pSiNP constructs in P27 mice including (a) erucamide (Eru-C_{18}-pSiNP), (b) oleamide (Ole-C_{18}-pSiNP), (c) palmitamide (Pal-C_{18}-pSiNP) and (d) AFK-187 (AFK-187-C_{18}-pSiNP). Both Ole-C_{18}-pSiNP and AFK-187-C_{18}-pSiNP constructs activate CD11b+ cells within the retina indicating that identifying the angiogenic factors is necessary for erucamide derivatives.

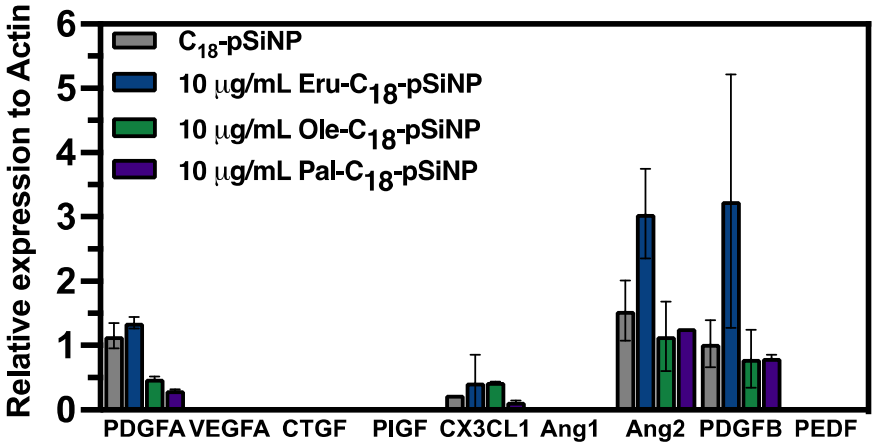

Figure 5.S9: Proangiogenic factors activated by erucamide-derivative loaded pSiNPs constructs. Expression of factors upregulated by Eru-C_{18}-pSiNPs, Ole-C_{18}-pSiNPs and Pal-C_{18}-pSiNPs in CD11b+ cells determined by qPCR (n = 3). Though oleamide and palmitamide express similar angiogenic factors to erucamide, its expression is not statistically significant compared to empty C_{18}-pSiNP controls.

5.5 Acknowledgements

Chapter 5, in part, is currently being prepared for submission for publication of the material in *Science*, 2023. Wei, G*., Chatterjee, S.*, Vijayakumar, S.*, Aguilar, E., Giles, S., Boger, D., Sailor, M.J., Friedlander, M. "Erucamide targets microglia to regulate the retinal angiogenic microenvironment and function as a neurotrophic factor". The dissertation author was a primary researcher and author of this chapter.

REFERENCES - CHAPTER 5

1. O. Strauss, *Physiological Reviews*, 2005, **85**, 845-881.

2. T. Kurihara, P. D. Westenskow, S. Bravo, E. Aguilar and M. Friedlander, *The Journal of Clinical Investigation*, 2012, **122**, 4213-4217.

3. M. Saint-Geniez, T. Kurihara, E. Sekiyama, E. Maldonado Angel and A. D'Amore Patricia, *Proceedings of the National Academy of Sciences*, 2009, **106**, 18751-18756.

4. A. Alm and A. Bill, *Experimental Eye Research*, 1973, **15**, 15-29.

5. E. Storkebaum, A. Quaegebeur, M. Vikkula and P. Carmeliet, *Nature Neuroscience*, 2011, **14**, 1390-1397.

6. J. Maslim, K. Valter, R. Egensperger, H. Holländer and J. Stone, *Investigative Ophthalmology & Visual Science*, 1997, **38**, 1667-1677.

7. K. Okabe, S. Kobayashi, T. Yamada, T. Kurihara, I. Tai-Nagara, T. Miyamoto, Y.-s. Mukouyama, Thomas N. Sato, T. Suda, M. Ema and Y. Kubota, *Cell*, 2014, **159**, 584-596.

8. D. B. Stanimirovic and A. Friedman, *Journal of Cerebral Blood Flow & Metabolism*, 2012, **32**, 1207-1221.

9. P. Sapieha, *Blood*, 2012, **120**, 2182-2194.

10. Y. Usui, P. D. Westenskow, T. Kurihara, E. Aguilar, S. Sakimoto, L. P. Paris, C. Wittgrove, D. Feitelberg, M. S. H. Friedlander, S. K. Moreno, M. I. Dorrell and M. Friedlander, *The Journal of Clinical Investigation*, 2015, **125**, 2335-2346.

11. Y. Ma, R. Kawasaki, L. P. Dobson, J. B. Ruddle, L. S. Kearns, T. Y. Wong and D. A. Mackey, *Investigative Ophthalmology & Visual Science*, 2012, **53**, 4306-4314.

12. M. E. Pennesi, S. Nishikawa, M. T. Matthes, D. Yasumura and M. M. LaVail, *Experimental Eye Research*, 2008, **87**, 561-570.

13. A.-J. F. Carr, M. J. K. Smart, C. M. Ramsden, M. B. Powner, L. da Cruz and P. J. Coffey, *Trends in Neurosciences*, 2013, **36**, 385-395.

14. E. Y. Chew, *Investigative Ophthalmology & Visual Science*, 2013, **54**, ORSF42-ORSF47.

15. K. Unsicker, *Cell and Tissue Research*, 2013, **353**, 205-218.

16. F. Cravatt Benjamin, O. Prospero-Garcia, G. Siuzdak, B. Gilula Norton, J. Henriksen Steven, L. Boger Dale and A. Lerner Richard, *Science*, 1995, **268**, 1506-1509.

17. C. Ezzili, K. Otrubova and D. L. Boger, *Bioorganic & Medicinal Chemistry Letters*, 2010, **20**, 5959-5968.

18. X. Guan, B. F. Cravatt, G. R. Ehring, J. E. Hall, D. L. Boger, R. A. Lerner and N. B. Gilula, *Journal of Cell Biology*, 1997, **139**, 1785-1792.

19. A. Hamberger and G. Stenhagen, *Neurochemical Research*, 2003, **28**, 177-185.

20. C. A. Mitchell, M. J. Davies, M. D. Grounds, J. K. McGeachie, G. J. Crawford, Y. Hong and T. V. Chirila, *Journal of Biomaterials Applications*, 1996, **10**, 230-249.

21. K. Wakamatsu, T. Masaki, F. Itoh, K. Kondo and K. Sudo, *Biochemical and Biophysical Research Communications*, 1990, **168**, 423-429.

22. B. Kim, S. Sun, J. A. Varner, S. B. Howell, E. Ruoslahti and M. J. Sailor, *Advanced Materials*, 2019, **31**, 1902952.

23. A. Bertucci, K.-H. Kim, J. Kang, J. M. Zuidema, S. H. Lee, E. J. Kwon, D. Kim, S. B. Howell, F. Ricci, E. Ruoslahti, H.-J. Jang and M. J. Sailor, *ACS Applied Materials & Interfaces*, 2019, **11**, 23926-23937.

24. B. Kim, H.-B. Pang, J. Kang, J.-H. Park, E. Ruoslahti and M. J. Sailor, *Nature Communications*, 2018, **9**, 1969.

25. J. Kang, J. Joo, E. J. Kwon, M. Skalak, S. Hussain, Z.-G. She, E. Ruoslahti, S. N. Bhatia and M. J. Sailor, *Advanced Materials*, 2016, **28**, 7962-7969.

26. M. J. Sailor, *Porous Silicon in Practice: Preparation, Characterization, and Applications*, Wiley-VCH, Weinheim, Germany, 2012.

27. D. Warther, Y. Xiao, F. Li, Y. Wang, K. Huffman, W. R. Freeman, M. Sailor and L. Cheng, *Drug Delivery*, 2018, **25**, 1537-1545.

28. K. Nan, F. Ma, H. Hou, W. R. Freeman, M. J. Sailor and L. Cheng, *Acta Biomaterialia*, 2014, **10**, 3505-3512.

29. D. Kim, J. Joo, Y. Pan, A. Boarino, Y. W. Jun, K. H. Ahn, B. Arkles and M. J. Sailor, *Angewandte Chemie*, 2016, **128**, 6533-6537.

30. Z. Qin, J. Joo, L. Gu and M. J. Sailor, *Particle & Particle Systems Characterization*, 2014, **31**, 252-256.

31. A. Usui-Ouchi, K. Eade, S. Giles, Y. Ideguchi, Y. Ouchi, E. Aguilar, G. Wei, K. V. Marra, R. B. Berlow and M. Friedlander, *Glia*, 2022, **70**, 1762-1776.

APPENDIX A

COBINAMIDE LOADED POROUS SILICON MICROPARTICLES FOR HCN DETECTION

Appendix A describes methods in loading cobinamide (Cbi) into porous silicon microparticles (pSiMP) and utilizing Cbi-loaded pSiMPs for the detection of HCN.

A.1 METHODS

A.1A PREPARATION OF POROUS SILICON MICROPARTICLES (PSIMPS)

Porous silicon microparticles were purchased from TruTags with the following conditions:

Lot# 200-2958
PRODUCT SPECIFICATION
Product Form: Microtags, unoxidized
Pore size: 10 - 20 nm
Tag size: 100 ± 25 µm (sieved to remove finer particles)
Particle thickness: 16 - 19 µm
Porosity: 80 ± 10 %
Microtag Thermal Oxidation: None (NOX)
Microtag Reflectance Spectrum, NOX: Two reflection peaks, target positions 540nm and 700nm.
Microtag Reflectance Spectrum Tolerance, NOX: 90% of material with first peak position between 530nm and 550 nm

Lot# 200-2956
PRODUCT SPECIFICATION
Product Form: Microtags, unoxidized
Pore size: 10 - 20 nm
Tag size: 100 ± 25 µm (sieved to remove finer particles)
Particle thickness: 16 - 19 µm
Porosity: 80 ± 10 %
Microtag Thermal Oxidation: None (NOX)
Microtag Reflectance Spectrum, NOX: Two reflection peaks, target positions 590nm and 700nm.
Microtag Reflectance Spectrum Tolerance, NOX: 90% of material with first peak position between 580nm and 600 nm

The above particles were purchased to have reflectance stop bands that at target positions that match the photonic crystal chips. The particles were kept sealed, inside a vacuum-desiccator to prevent any potential oxidation of the particles.

A.1B Surface Functionalization of pSiMPs

To render the surface of the microparticles, hydrophobic, thermally induced silane dehydrocoupling of n-octadecylsilane ($H_3Si\text{-}C_{18}H_{37}$) was functionalized onto the surface of microparticles.[1] 400-500 mg of microparticles were weighed and placed in a 20 mL glass vial. 750-1000µL of n-octadecylsilane was pipetted into the glass vial, enough to immerse all of the microparticles. The particles were then sealed and immersed in a silicone oil bath at 80°C for 12 hrs. Once reacted, the vial was removed from the oil bath and the particles were allowed to settle for 5 minutes. The particles were then cleaned by carefully pipetting out the n-octadecylsilane, without disturbing the settled particles. 5 mL of n-hexane was then placed in the solution and the particles were placed on a shaking table for 2 minutes for the n-hexane to infiltrate and wash all of the particles. The n-hexane was then removed after the particles were allowed to settle for 5 minutes. This step was repeated twice with n-hexane and three times with ethanol, to fully wash all of the particles. The particles were then transferred to a new glass vial and sealed in a desiccator to prevent exposure to the air.

A.1C Loading of Cobinamide to Fuctionalized pSiMPs

For a 20mg sample of microparticles, a 100µL aliquot of 50µM monocyanocobinamide was loaded. This equivalent amount was scaled up for a larger batch of particles. 400mg of surface-functionalized porous silicon microparticles were weighed out into a 20mL glass vial. 2mL of 50µM monocyanocobinamide was pipetted

into the vial, until all of the particles were fully immersed with monocyanocobinamide solution. A small piece of aluminum foil, punctured with holes, was covered over the opening of the vial. The vial was placed on a table shaker and allowed to dry at room temperature overnight, or until all of the ethanol solvent from the monocyanocobinamide solution was evaporated.[2]

A.1D Extraction Methodology of Cbi-Dye from pSiMPs

Below is the methodology for extracting Cbi from exposed pSi microparticles and analyzing its absorbance at 583 nm to quantify the amount of CN^- reacted with Cbi.

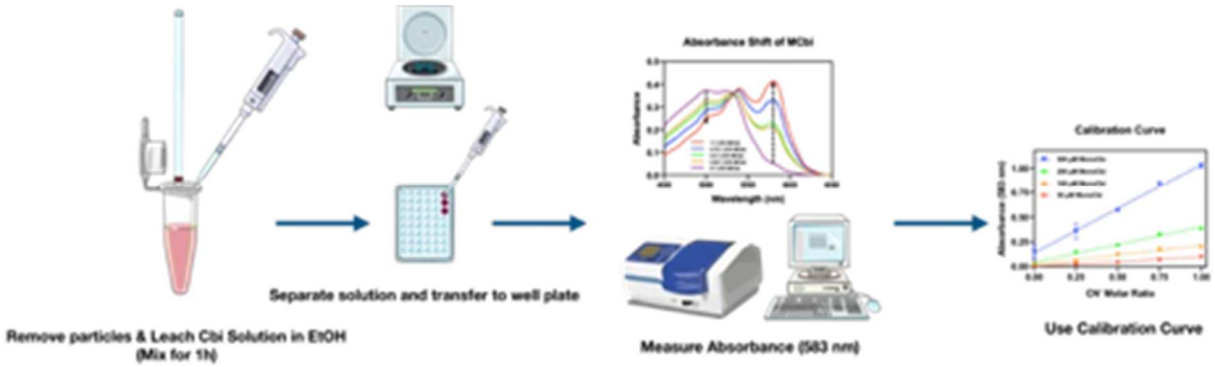

Figure A.1: Schematic of methodology in extracting cobinamide from pSiMPs for HCN measurements.

1. Once microparticles are exposed to the analyte, carefully remove the deactivated wool from the thermal desorption tube. Ensure that microparticles are not stuck to the wool so that the particles are not contaminated.

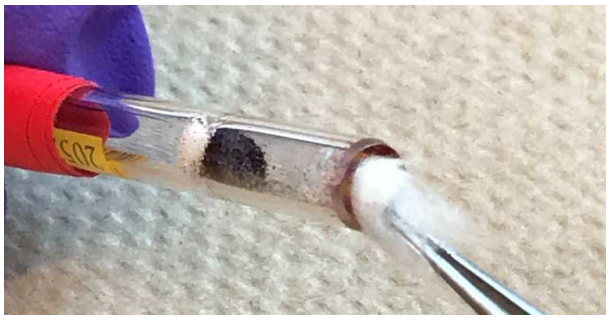

Figure A.2: Removing Cbi-loaded pSiMPs from thermal desorption tube.

2. Carefully transfer the microparticles from the thermal desorption tube into a clean Eppendorf™ tube. Ensure that microparticles do not get stuck to the tube walls as particles are charged.

Figure A.3: Transferring Cbi-loaded pSiMPs into Eppendorf™ tube.

3. Carefully add 500 µL of ethanol (EtOH) to the Eppendorf™ tube. Additional volumes of 1.75 mL, 2.5 mL or 5 mL can be added to the tube to either dilute the dye (should the dye solution be too concentrated) or to remove microparticles stuck to the tube walls. Note the volume of EtOH used.

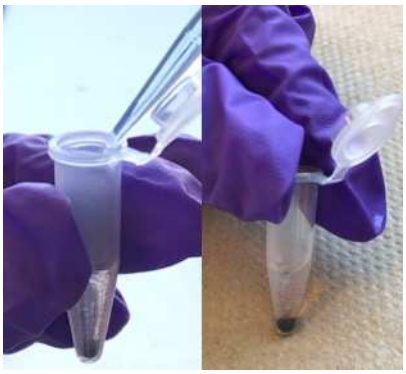

Figure A.4: Adding ethanol to Cbi-loaded pSiMPs.

4. Vortex the mixture for 1 hour, to ensure that the Cbi dye is extracted from the microparticles. The EtOH solution will change color as Cbi is extracted.

Figure A.5: Vortexing pSiMPs to remove Cbi from the particles.

5. To fully separate the microparticles from the Cbi-EtOH solution, centrifuge particles for at least 10 minutes at a minimum of 5000 RPM.

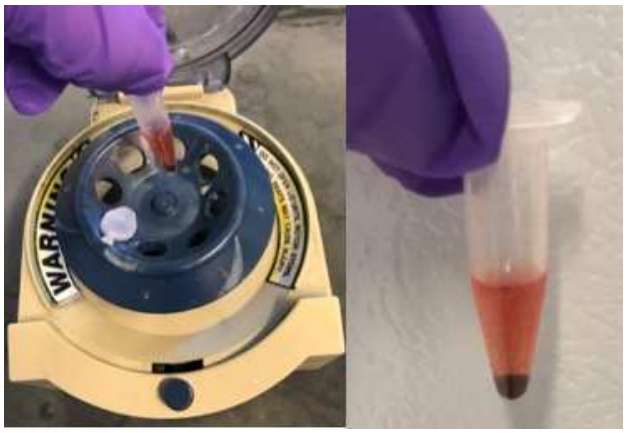

Figure A.6: Centrifuging the tube to remove the Cbi solution from pSiMPs.

6. Carefully pipette 100µL solution and transfer Cbi-solution to an absorbance well plate. By measuring triplicate solutions, accurate measurement of absorbances is ensured. Measure absorbance of the dye at 583 nm.

Figure A.7: Measuring the absorbance intensity of Cbi solution.

7. Compare the absorbance of the collected absorbance to the provided calibration curve.

A.2 Results & Discussion

A.2a Characterization of pSiMPs

Cobinamide-loaded porous silicon microparticles underwent a variety of tests to ensure that sensing and capture capabilities were maintained, despite the different material form-factor (microparticles vs. chip). The various characterization tests included optical reflectance, Fourier Transform Infrared Spectroscopy (FTIR), thermogravimetric analysis (TGA) and BET N_2 Adsorption/Desorption. The conditions from the tests as well as the results are given in the figures below.

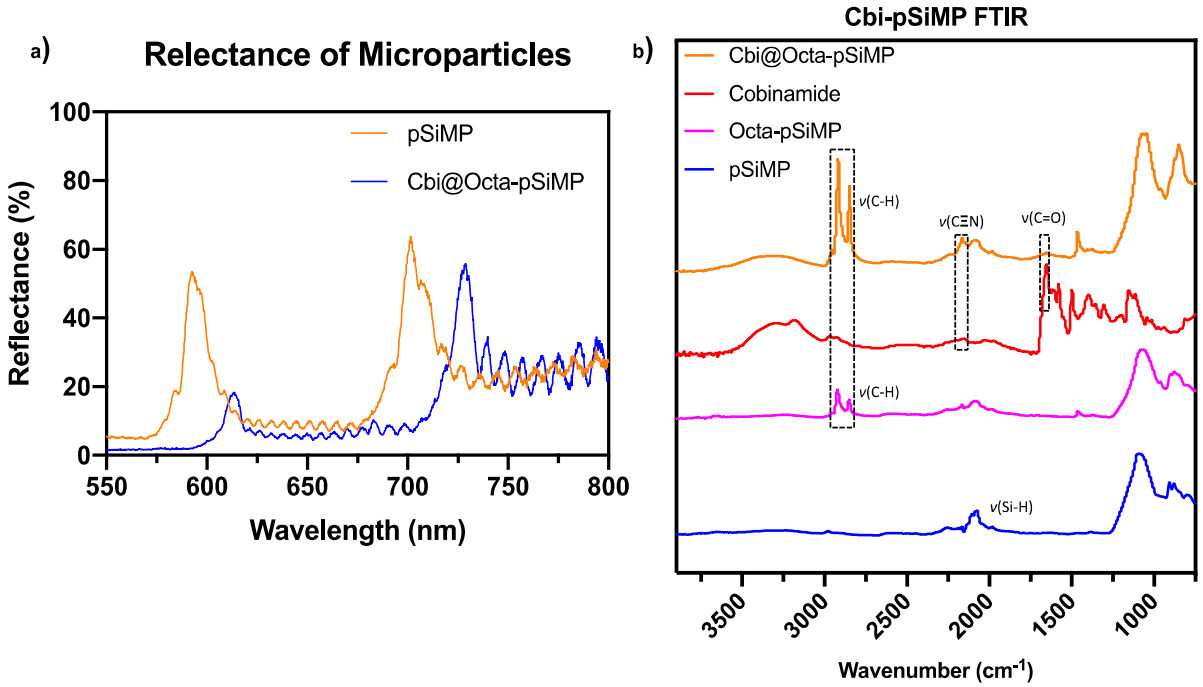

Figure A.8: Schematic of the characterization of cobinamide-loaded porous silicon microparticles. a) shows the reflectance of the microparticles before and after the surface functionalization and addition of cobinamide. b) shows the FTIR peaks of the various steps applied onto the porous silicon microparticles. The Cbi@Octa-pSiMP sample shows distinct peaks that match the surface functionalization of the n-octadecylsilane (2800-3100 cm^{-1}) and cobinamide (2140-2260 cm^{-1} and 1700-1750 cm^{-1}).

In **Figure A.8**, the optical reflectance of the microparticles was measured prior to and after surface functionalization and cobinamide loading. A noticeable red shift in

spectra can be seen, which is the same behavior with the porous silicon chips. In **Figure A.8b**, the FTIR spectra show noticeable peaks from 2800-3100 cm^{-1} which is indicative of a C-H stretch, that corresponds to the successful functionalization of n-octadecylsilane while also showing peaks from 2140-2260 cm^{-1} and 1700-1750 cm^{-1} that are indicative of the presence of cobinamide loading.[2, 3]

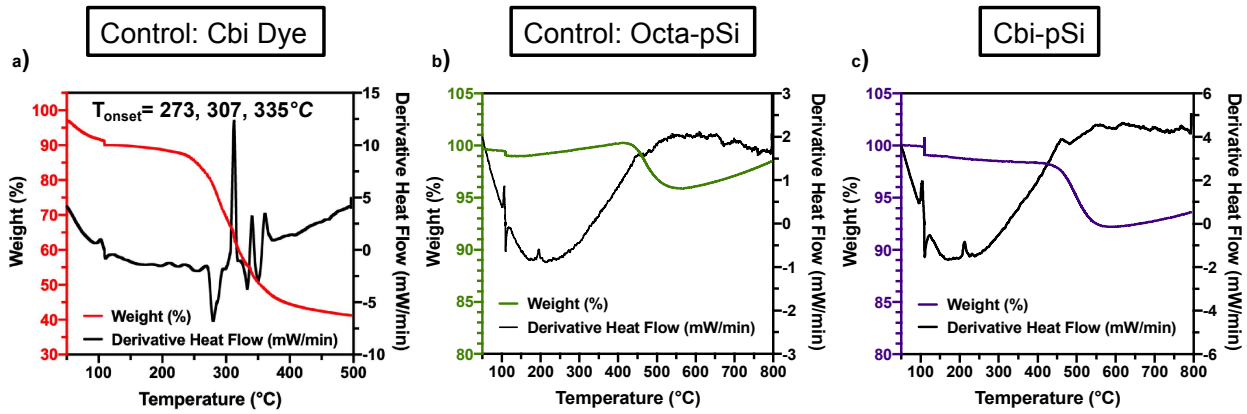

Figure A.9: Schematic of thermogravimetric analysis (TGA) tests of the Cbi-pSi microparticles. a) is the control run using cobinamide. There are distinct derivative heat flow peaks at 273°C, 307°C and 335°C with a change in weight % from 250-450°C. b) is another control run with surface modified microparticles (Octa-pSi). There is a noticeable change in weight from 400°C to 500°C, possibly due to the degradation of the n-octadecylsilane. c) is the TGA analysis of the cobinamide-loaded porous silicon microparticles.

In **Figure A.9**, TGA analysis of the various steps of the particles was undertaken. **Figure A.9a** and **Figure A.9b** were control measurements for the cobinamide and surface functionalized particles, respectively. For cobinamide, there are derivative heat flow peaks at 273°C, 307°C and 335°C, which are indicative of temperatures where the dye becomes unstable. It is also in this region that there is a significant weight % loss. With the Octa-pSi curve, there is no distinct peak for the derivative heat flow, but there is a noticeable decrease in weight % from 400°C to 500°C, which may be due to the degradation of the n-octadecylsilane. This weight loss matches the curve in **Figure A.9c** for the cobinamide-loaded porous silicon microparticles.

a)

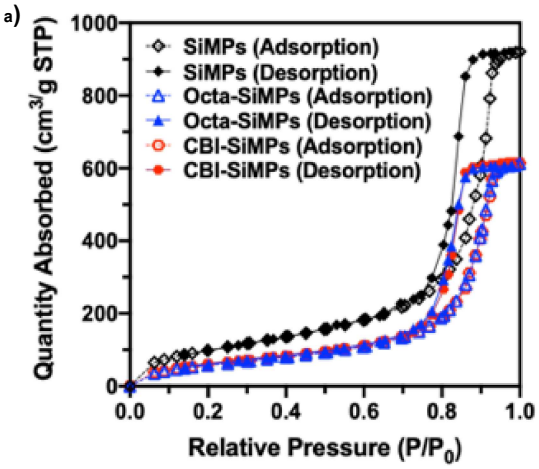

b)

	surface area (m^2/g)	Pore volume (cm^3/g)
SiMPs	383	1.43
Octa-SIMPs	231	0.95
CBI-SIMPs	235	0.95

n = 1

Figure A.10: Schematic of BET N_2 Adsorption/Desorption tests for porous silicon microparticles. a) shows the traces of the N_2 Adsorption/Desorption while b) is a table showing the calculated BET surface area and pore volume from the isotherms in a). There is a decrease in both BET surface area and pore volume due to the surface functionalization onto the microparticles, however there is no change due to the addition of cobinamide.

In **Figure A.10**, the BET N_2 Adsorption/Desorption isotherms are measured. There is noticeable change in the curves as shown in the table in **Figure A.10b**. Here the BET surface area and pore volume are measured for each step in the production of the microparticles. It is observed that there is a significant decrease in both surface area and pore volume due to the surface functionalization of n-octadecylsilane, however there is no change due to the addition of cobamamide. These measurements are to be repeated to ensure that the negligible change in BET surface area and pore volume due to the addition of cobinamide is accurate.

A.3 Conclusions

Cobinamide-loaded porous silicon can successfully be transferred to a microparticle-based form factor, without losing the spectral capabilities seen in porous silicon chips. Characterization tests of optical reflectance, FTIR, TGA and BET N_2 Adsorption/Desorption isotherms proved the surface functionalization and loading of

cobinamide to the porous silicon microparticles. Exposure of Cbi-pSiMP to HCN shows the detection and storage of HCN by measuring the change in absorbance through extracted cobinamide.

REFERENCES – APPENDIX A

1. D. Kim, J. Joo, Y. Pan, A. Boarino, Y. W. Jun, K. H. Ahn, B. Arkles and M. J. Sailor, *Angewandte Chemie International Edition*, 2016, **55**, 6423-6427.

2. N. L. Fry, G. R. Boss and M. J. Sailor, *Chem Mater*, 2014, **26**, 2758-2764.

3. L. A. Greenawald, J. L. Snyder, N. L. Fry, M. J. Sailor, G. R. Boss, H. O. Finklea and S. Bell, *Sensors and Actuators B: Chemical*, 2015, **221**, 379-385.

APPENDIX B

GATEKEEPER-COATED POROUS SILICON MICROPARTICLES

B.1 OVERVIEW

Bio-MOF deposition onto pSi microparticles (pSiMPs) proved to be exceptionally challenging and ultimately was not achieved with sufficient fidelity nor efficiency to permit regular experimentation. Most testing was performed at relatively small scales (2-10 mg pSiMPs), though a large scale-up (>400 mg) was performed as a M17 deliverable for testing. Small-scale testing typically involved 0.5-day incubations of pSiMPs with Bio-MOF crystals (and up to 3 days in solution). This is comparable to chip preparation, for which drying was completed overnight. For the M17 scale-up, a nearly 100% increase in mass was observed, likely due to oxidation of the pSiMP surface caused by the prolonged exposure to aqueous solution (>4 days). This represents a potentially serious limitation that would need to be addressed were this form factor pursued in the future, either through more complete passivation of the pSi surface or more efficient deposition methods of the Bio-MOF to limit exposure of pSiMPs to aqueous solutions.

Briefly, two major routes were pursued for attachment of Bio-MOF to pSiMPs. First was attempting binding of Bio-MOF to the pSiMP surface in solution, facilitated by mixing, to achieve an even coverage of Bio-MOF on both sides of the pSiMPs. The second was effectively an adaptation of the drop-cast method (as used for chips) directly onto pSiMPs. The latter method was pursued much more extensively owing to low solution-binding efficacy and possible destruction of Bio-MOF suspensions upon repeated collisions with suspended pSiMPs.

Screening for both routes included: MP amine functional group, absolute and relative quantities of both Bio-MOF and pSiMPs, choice of solvent (MES, diH2O, EtOH, MeOH) to modulate dielectric screening of electrostatic interactions, choice of substrate, as well as method of mixing (no mixing, orbital shaker, rotating wheel, rocker, manual pipetting). The rotating wheel was qualitatively determined to be most effective, but all methods and solution conditions consistently showed low binding. Organic solvents destroyed the Bio-MOF, so deposition was restricted to MES buffer or diH2O.

B.2 Results & Discussion

B.2a Solution binding of Bio-MOF to pSiMPs

Coating of both sides of the pSiMPs was a persistent concern for the manufacture of Bio-MOF@pSiMPs, as the MPs are porous throughout the entire of thickness of the particles, necessitating Bio-MOF coating on both surfaces to enable gatekeeping function. To address this, we originally attempted solution-phase binding of Bio-MOF to the pSiMPs. Binding was performed using aminated pSiMPs in 20 mM MES (pH 6) buffer or deionized water (pH 6), to enable electrostatic binding, with or without CoCl2. Initial results from a standing solution are shown in **Figure B.1** for relatively low quantities of Bio-MOF and pSiMPs. Comparable SEM images for different mixing techniques are shown in **Figure B.2**, though these are only partially representative due to the high variability observed between repeat samples. Additional representative screening results are shown in **Figure B.3** and **Figure B.4**.

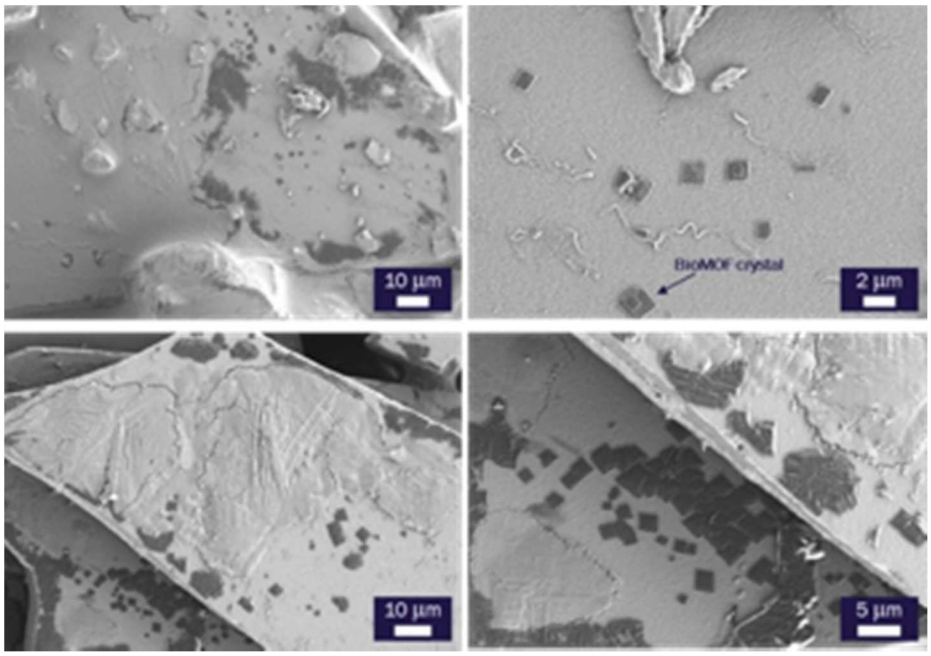

Figure B.1: SEM images of pSiMPs after overnight solution binding to Bio-MOF crystals. Here, the pSiMP:Bio-MOF mass ratios were 10:1 (0.2 mg:20 µg) (top), and 20:1 (0.2 mg:10 µg) (bottom). Bio-MOF crystals are clearly visible on the surface but are sparely populated.

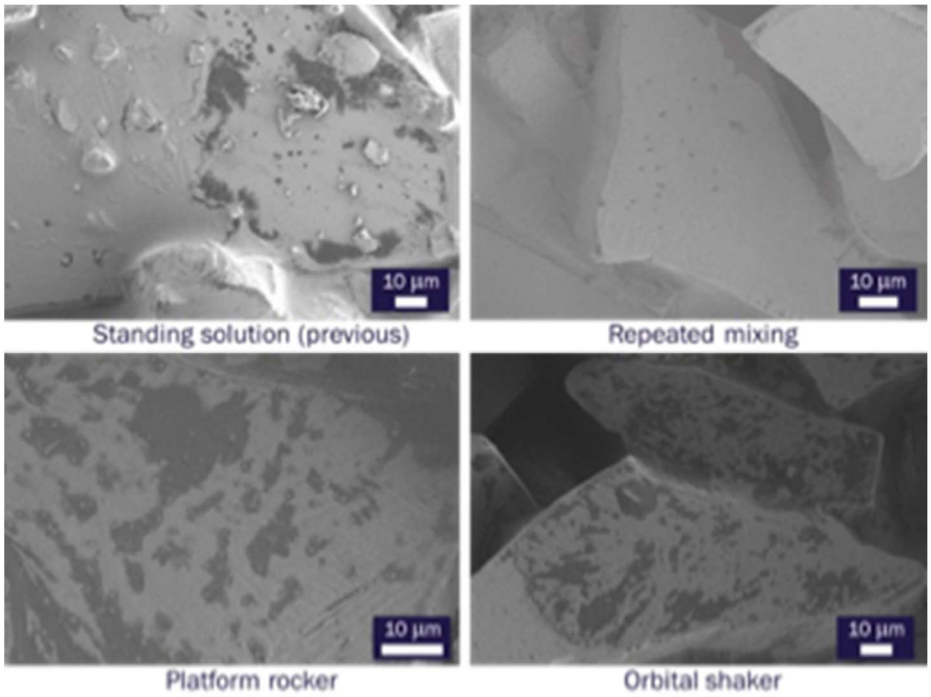

Figure B.2: SEM images of 10:1 (0.2 mg:20 µg) pSiMP:Bio-MOF samples under different mixing conditions. Coverage is low in all cases. For comparison, 30 µg of Bio-MOF covers a full 1.2 cm^2 pSi chip.

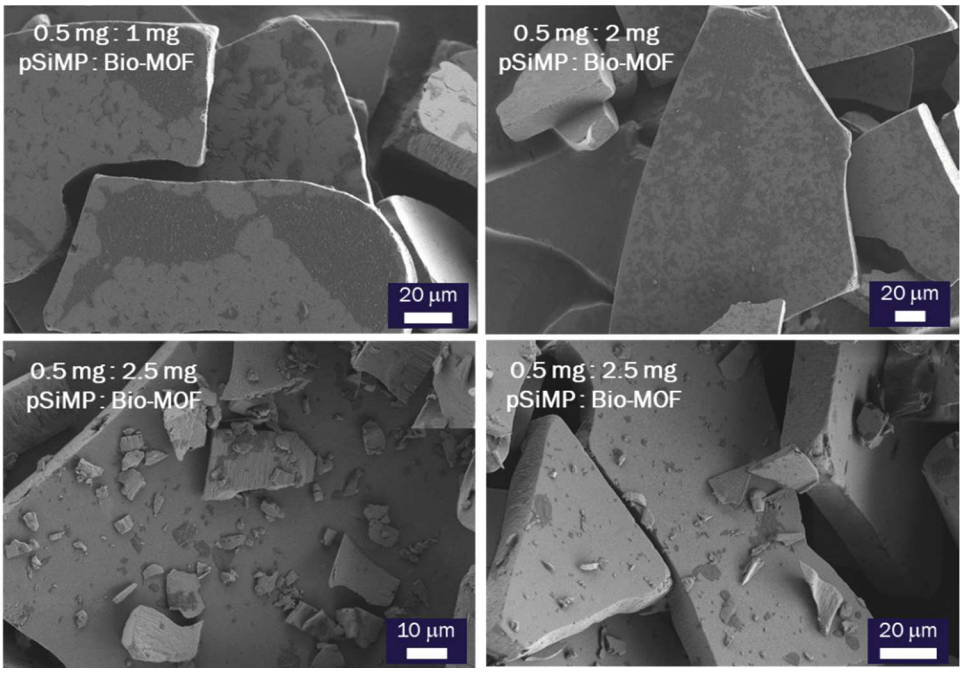

Figure B.3: SEM images of various mass ratios of 0.5 mg pSiMP vs Bio-MOF mixed via rotating wheel. Total Bio-MOF coverage does not follow any clear trend and breaking of the MPs is clear in the lower row. Compare to 30 µg of Bio-MOF per full 1.2 cm^2 pSi chip.

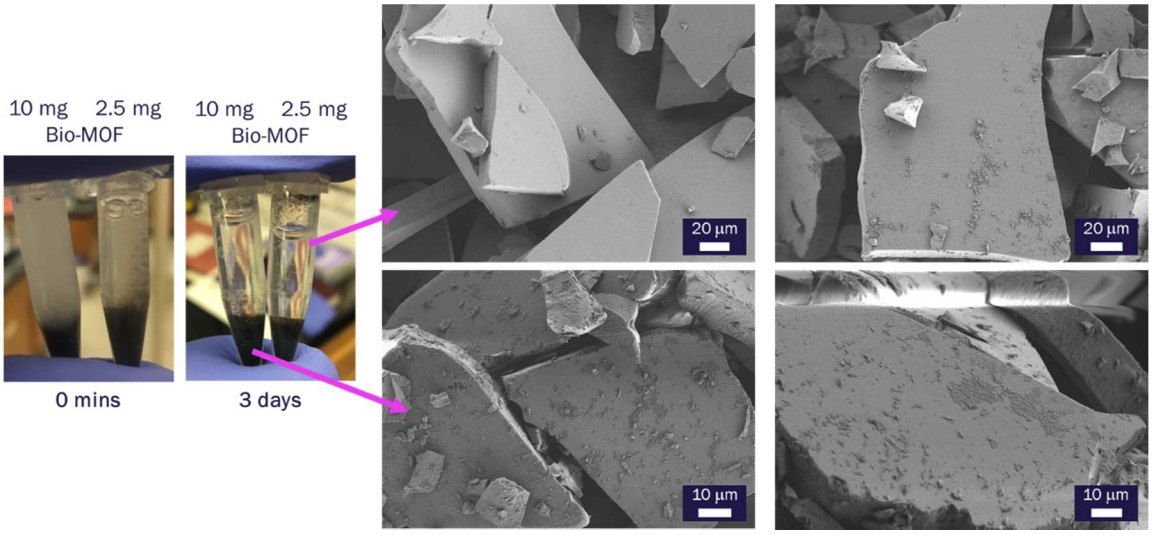

Figure B.4: 30 mg pSiMPs mixed with 10 or 2.5 mg Bio-MOF via rotating wheel mixer. Coverage is very low, and the MPs are likely highly oxidized after exposure to aqueous solution for 3 days. The large quantities of Bio-MOF tried here are prohibitively excessive for scale-up, suggesting that solution binding was not a promising route forward.

B.2B Drop-Casting" of Bio-MOF onto pSiMPs

To circumvent many of the difficulties associated with solution binding, we attempted to extend the drop-cast technique used for pSi chips to pSiMPs. First, solution-binding conditions were allowed to dry onto the MPs by slow evaporation while subject to mixing by rotating wheel (**Figure B.5**). This proved unsuccessful.

We then moved to direct deposition onto pSiMPs dispersed on solid substrates (glass and plastic vials or petri dishes) and in different solvents. We empirically determined that glass substrates worked better to improve dispersion of the MPs within the liquid drop, and petri dishes were used for their larger square area. Binding efficiency appeared to correlate with water content, but had no correlation to dielectric constant, indicating electrostatic interaction screening was not inhibiting binding (**Figure B.6**). Organic solvents deposited square-shaped Bio-MOF crystals, but by TEM these crystals were determined to have lost microscopic order, forcing the use of exclusively aqueous solvents.

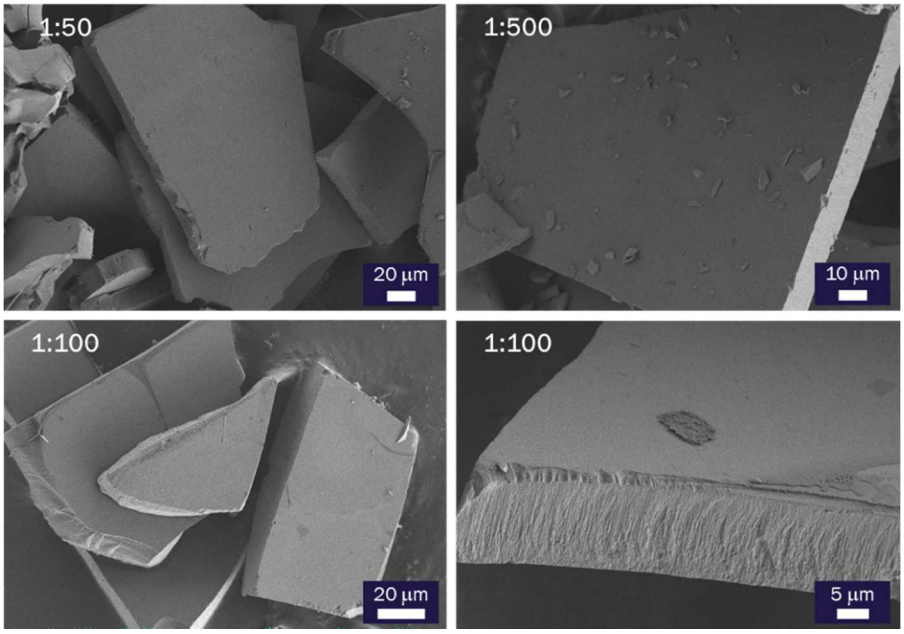

Figure B.5: 5 mg pSiMPs mixed with varying amounts of Bio-MOF (mass ratios given at top left) and allowed to dry while attached to a rotating wheel mixer for 2 days. A 1:100 ratio corresponds to 50 µg Bio-MOF. Coverage is nearly nonexistent at all concentrations, and the MPs are likely oxidized after 2 days in buffer.

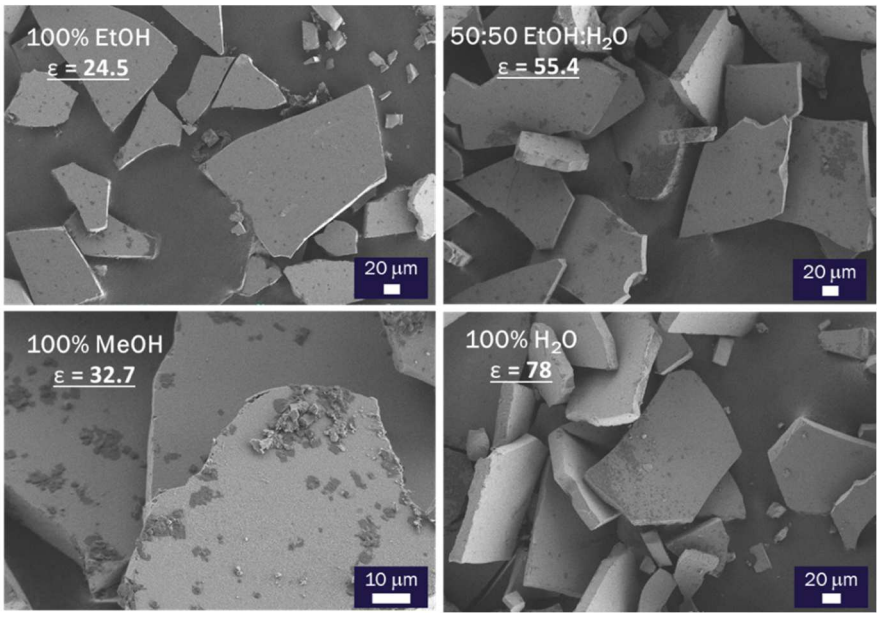

Figure B.6: SEM images of 30 µg Bio-MOF in different solvents drop-cast onto 2 mg pSiMPs and allowed to dry overnight. The solvent identity and dielectric constant are given the upper left corners. The expected trend would be increased binding at lower dielectric, but no clear trend emerged.

Now restricted to aqueous solvents, we attempted to tackle the issue of coating both sides of the pSiMPs. This largely involved drop-casting the Bio-MOF onto the pSiMPs once, inverting or randomizing the particle orientations/positions, then drop-casting a 2nd layer of Bio-MOF (**Figure B.7**). The variability of this method proved prohibitive for experimentation, both among particles within a sample and between deposition quantities. Finally, we attempted to improve localization of Bio-MOF crystals to the pSiMP surface through the use of hydrophobic substrates (**Figure B.8**), thus disfavoring Bio-MOF adsorption to the substrate. We also characterized a 3-layer "sandwich" method, consisting of drying a layer of Bio-MOF, depositing the pSiMPs onto that and allowing to dry, then another application of Bio-MOF, to intrinsically coat both sides of the pSiMPs with minimal experimental input (**Figure B.9**). Ultimately, the "sandwich method" on Teflon substrates, with Bio-MOF in MES (pH 6) + $CoCl_2$ was employed for the final scale-up to >400 mg pSiMPs (**Figures B.10-B.12**).

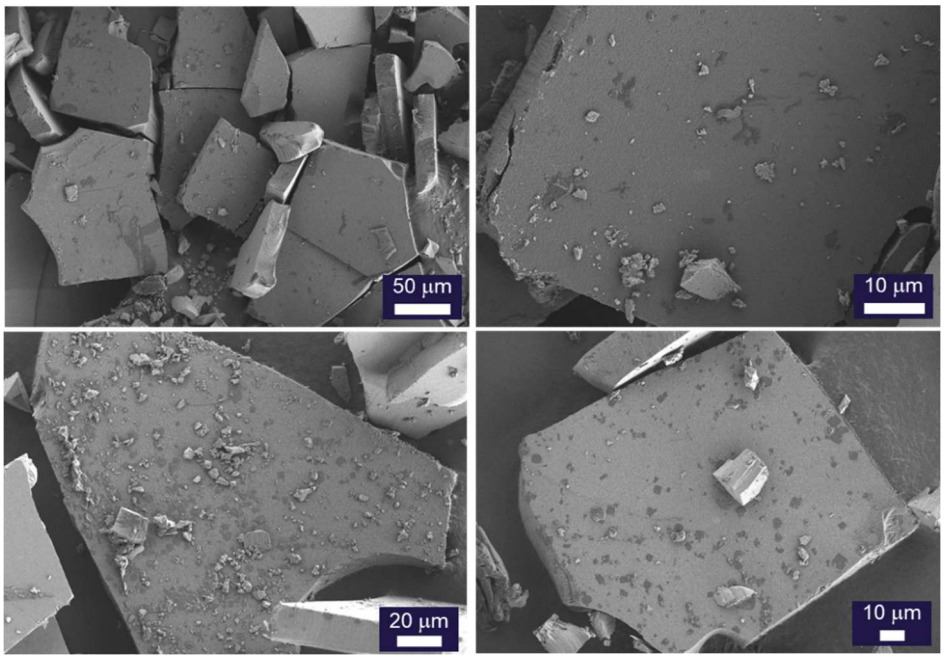

Figure B.7: Double application of Bio-MOF (2x 45 µg) onto 2 mg pSiMPs, either in H2O (top) or MES pH 6 (bottom), without added $CoCl_2$. After the first drop-cast step, the dried pSiMPs were gently overturned with a rubber policeman, then subjected to a second deposition. The inclusion of $CoCl_2$ did not appear to change binding behavior, so these images are representative of those conditions as well.

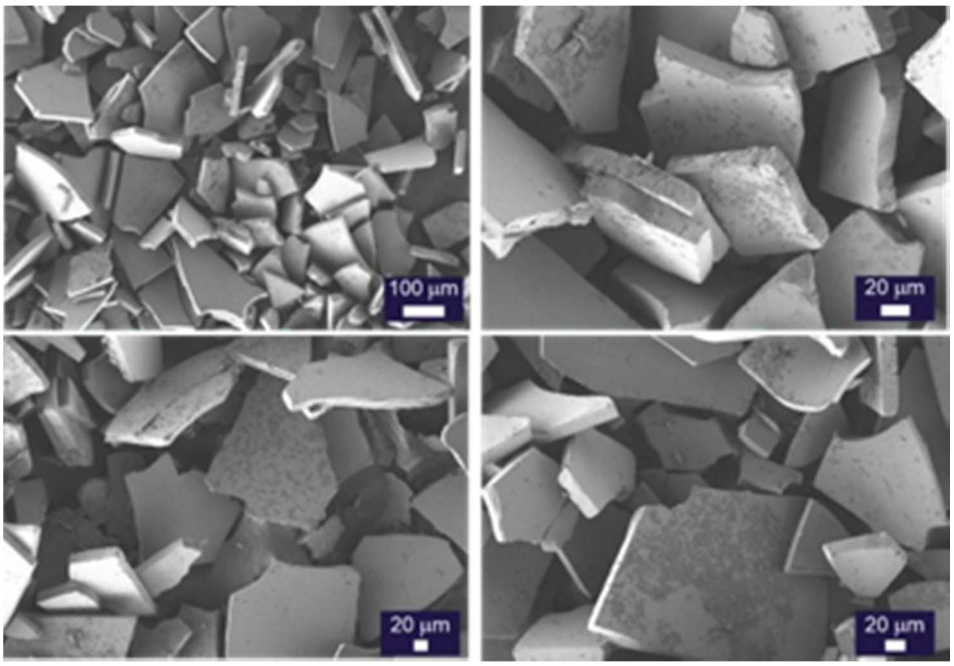

Figure B.8: 30 µg Bio-MOF in different solvents drop-cast onto pSiMPs atop a Teflon surface, to test whether the Bio-MOF suspension could be directed away from the Teflon and onto the particles. Moderate coverage is achieved, but it is very heterogeneous between particles within the same sample.

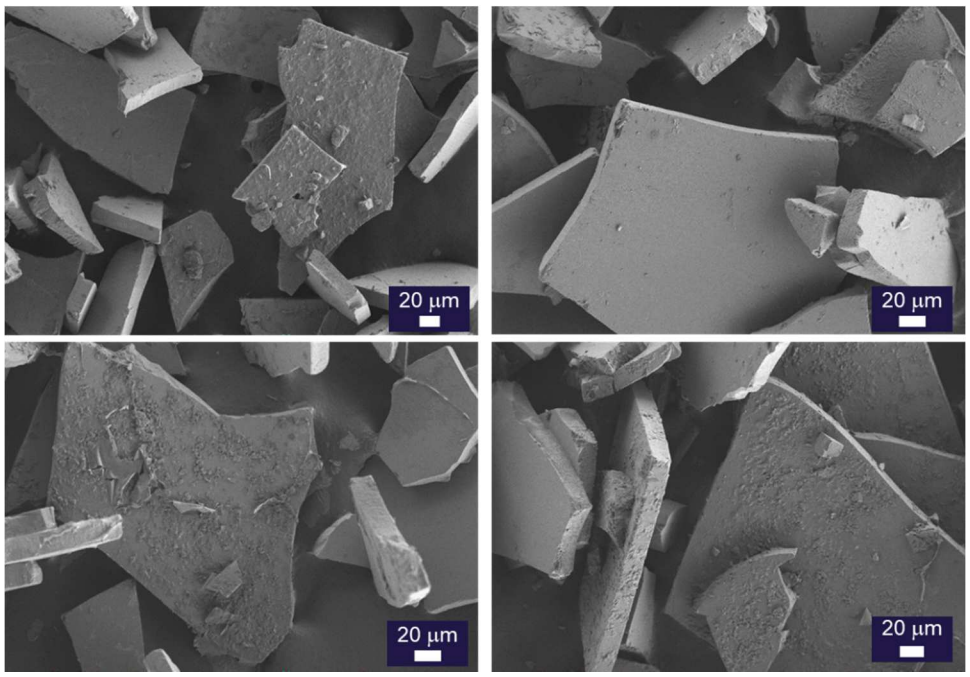

Figure B.9: Sandwich method on Teflon substrates. 2x15 µg Bio-MOF were deposited with 2 mg pSiMPs in water (top) or MES pH 6 buffer (bottom) + $CoCl_2$. Coverage was slightly better with MES, and $CoCl_2$ did not seem to impede binding.

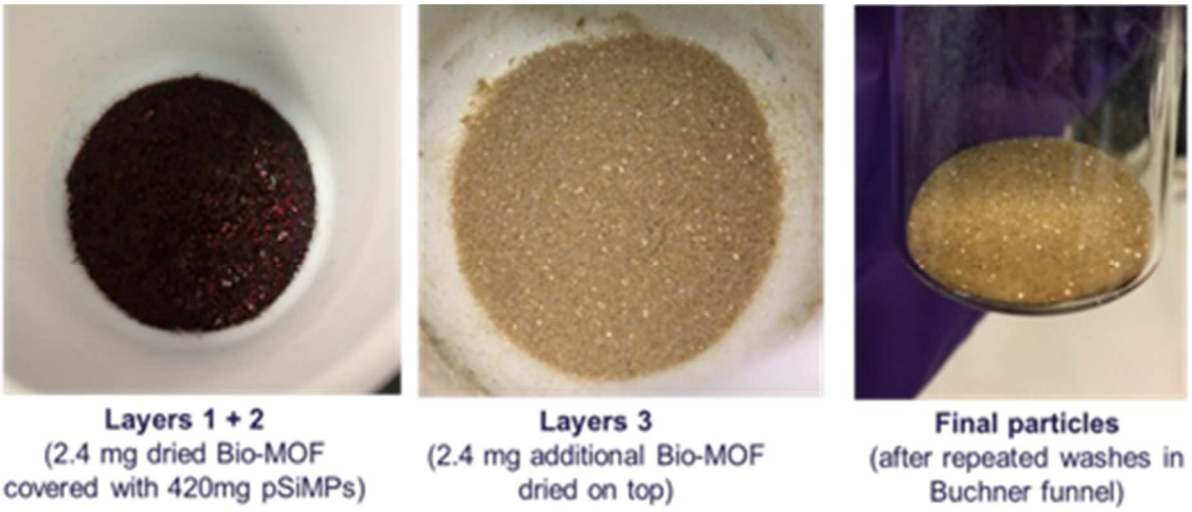

Figure B.10: Scale up of "sandwich method" on Teflon substrates. A total of 4.8 mg Bio-MOF was integrated with 420 mg pSiMPs in a multi-step deposition procedure to form layers 1-3. After production of the sandwich, the Bio-MOF@pSiMPs were washed repeatedly using MES+Co buffer to remove excess salts. The color change from red to brown results from a blueshift in the reflection bands due to oxidation of the pSiMP surface (seen in **Figure B.12**).

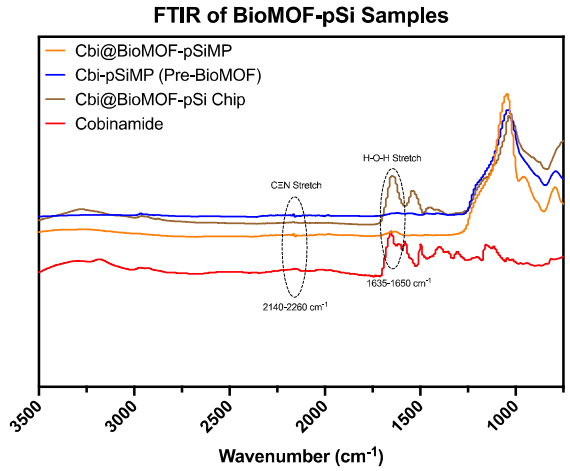

Figure B.11: Schematic of the FTIR peaks of the Bio-MOF-pSi samples before and after Bio-MOF deposition. A chip spectrum is included for reference. The visible C≡N stretch, seen in all pSi samples matches free Cbi.

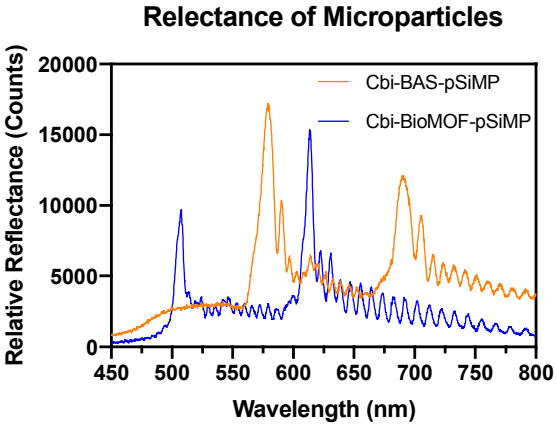

Figure B.12: Optical reflectance peaks of the Bio-MOF-pSi samples before and after Bio-MOF deposition.

B.3 Conclusions

Extensive screening over >6 months was carried out attempting to establish conditions which led to efficient Bio-MOF deposition onto pSi microparticles. These attempts proved relatively unsuccessful, however, consistently suffering from low coverage of Bio-MOF onto the particles. The underlying cause for this difficulty was never identified and was not resolved through exploratory deposition methods.